The impact of volcanic halogens, climate change, and sulfate aerosol geo-engineering on the atmospheric effects of volcanic eruptions

John Staunton Sykes

Supervisors:
Dr. Alex Archibald
Dr. Anja Schmidt

Department of Chemistry
University of Cambridge

This dissertation is submitted for the degree of
Doctor of Philosophy

Jesus College June 2021

Declaration

This thesis is the result of my own work and includes nothing which is the outcome of work done in collaboration except as declared in the preface and specified in the text. It is not substantially the same as any work that has already been submitted before for any degree or other qualification except as declared in the preface and specified in the text. It does not exceed the prescribed word limit for the Physics and Chemistry Degree Committee.

John Staunton Sykes
June 2021

Acknowledgments

Firstly, I'd like to thank my supervisors, Alex Archibald and Anja Schmidt, for all of their guidance and encouragement in both the writing of this thesis and the research that it contains. I'd like to especially thank Anja for welcoming me into her research group after my first year. I would not have got to this point without you and the Schmidt group.

I'd like to thank Thomas Aubry for being so generous with his time, effort, and ideas at every stage of this research. It has been so rewarding working with you. I'd also like to take this opportunity to apologise for asking you to proofread the earliest and most tortuous drafts of this thesis! My sincere thanks also go to Luke Abraham for his technical support, and to James Weber, Matt Shin, Lauren Marshall, and James Keeble for their willingness to discuss and help at the drop of a hat. I am also grateful to both Daniele Visioni and Clive Oppenheimer for the thought-provoking discussions during my viva and for their suggested revisions which have certainly improved this thesis.

Thank you to the Cambridge NERC DTP for funding this PhD, and to Mohit Dalvi for sponsoring my Met office collaboration, which allowed me access the Monsoon2 supercomputer.

Thanks to everyone who made working at Union Road interesting and enjoyable. Special thanks go to the members of G6 for putting up with the games of indoor tape ball cricket and the relentless pursuit of genuine edges or 'Gennys', as they became known.

At Jesus College, thanks to all the staff, especially the Porters and the Roost Café staff, who have kept me going, both in terms of mood and food, and to everyone with whom I have played tennis, football, hockey, squash, cricket, and pool or enjoyed long dinners and drinks. You have all helped to make this college the most wonderful place to live and work in over the last 8 years. I cannot describe how much I will miss this place.

I am incredibly grateful to my Mum and Dad for their unwavering support and for all the opportunities they have given me, which have enabled me to get to where I am now. To my siblings, friends from home and friends from university (Jesus, CUHC, The Hawks' Club, and The Rhads to name a few), thank you for showing a complete disinterest in my PhD and, instead, being a never-ending source of laughter and distraction. To Clemi, thank you for all the emotional support and sharing this journey with me. I've had the best time – more to come.

"I almost wish I hadn't gone down that rabbit-hole - and yet - and yet - it's rather curious, you know, this sort of life!"

But to business.

Abstract

The evolution of volcanic sulfur, stratospheric composition and radiative forcing following explosive volcanic eruptions injecting sulfur directly into the stratosphere is well understood. However, how the co-emission of volcanic halogens, climate change, and concurrent sulfate aerosol geo-engineering would alter the atmospheric effects of sulfur-only explosive volcanic eruptions has, previously, been under-researched. In this thesis, aerosol-chemistry-climate model simulations are utilised to show that the co-emission of volcanic halogens alongside sulfur (halogen co-emission) and climate change amplify the volcanic forcing of volcanic eruptions, mainly caused by a reduction in the aerosol lifetime and aerosol size. Stratospheric ozone is shown to be less vulnerable to sulfur-only eruptions, but more sensitive to halogen co-emission eruption scenarios in the future compared to the present-day, due to the projected decline in stratospheric halogen abundance and ozone recovery. An explosive volcanic eruption during stratospheric sulfate aerosol geo-engineering is found to lead to additional negative radiative forcing and total column ozone depletion, but the response is complex and non-additive.

This thesis emphasises the need to include volcanic halogen emissions when simulating the climate effects of past or future eruptions as well as the necessity to maintain space-borne observations of stratospheric compounds to better constrain the stratospheric injection estimates of volcanic eruptions. It identifies a novel climate-volcano feedback and highlights the need to re-evaluate the use of constant volcanic forcing typically used in future climate projections. Furthermore, this thesis demonstrates the difficulties associated with maintaining a stable level of radiative forcing in the event of an explosive volcanic eruption during sulfate aerosol geo-engineering.

Table of Contents

List of Tables

List of Figures

Abbreviations

ANOVA	**An**alysis **o**f **Va**riance
AOD	**A**erosol **O**ptical **D**epth
BDC	**B**rewer **D**obson **c**irculation
CCMI	**C**hemistry-**C**limate **M**odel **I**nitiative
CFC	**C**hloro**f**luoro**c**arbon
CH_4	Methane
CMIP6	**C**oupled **M**odel **I**ntercomparison **P**roject phase 6
CO_2	Carbon Dioxide
CTM	**C**hemical **T**ransport **M**odel
EESC	**E**quivalent **E**ffective **S**tratospheric **C**hlorine
ERF	**E**ffective **R**adiative **F**orcing
GeoMIP	**Geo**engineering **M**odel **I**ntercomparison **P**roject
GHG	**G**reen**h**ouse **G**as
GLOMAP	**GLO**bal **M**odel of **A**erosol **P**rocesses
GloSSAC	**Glo**bal **S**pace-based **S**tratospheric **A**erosol **C**limatology
H_2SO_4	Sulfuric Acid Vapour
HBr	Hydrogen Bromide
HCl	Hydrogen Chloride
HNO_3	Nitric Acid
IPCC	**I**ntergovernmental **P**anel on **C**limate **C**hange
LW	**L**ong**w**ave
MLS	**M**icrowave **L**imb **S**ounder
N_2	Nitrogen
NH	**N**orthern **H**emisphere
O_3	Ozone
O_3 RK	Ozone Radiative Kernel
OH	Hydroxyl Radical
PSCs	**P**olar **S**tratospheric **C**louds
RCP	**R**epresentative **C**oncentration **P**athways
R_{eff}	Aerosol Effective Radius
RF	**R**adiative **F**orcing
ScenarioMIP	**Scenario M**odel **I**ntercomparison **P**roject
SH	**S**outhern **H**emisphere
SO_2	Sulfur Dioxide
SRM	**S**olar **R**adiation **M**anagement
SSP	**S**hared **S**ocio-economic **P**athways
SST	**S**ea-**S**urface **T**emperature

SW	**S**hort**w**ave
SWV	**S**tratospheric **W**ater **V**apour
TCO	**T**otal **C**olumn **O**zone
TOA	**Top-of-atmosphere**
UKCA	**U**nited **K**ingdom **C**hemistry and **A**erosols
UKESM	**U**nited **K**ingdom **E**arth **S**ystem **M**odel
UM	**U**nified **M**odel
UV	**U**ltra**v**iolet
VEI	**V**olcanic **E**xplosivity **I**ndex
VolMIP	**M**odel **I**ntercomparison **P**roject on the climatic response to **V**olcanic **f**orcing
VSL	**V**ery **S**hort **L**ived
WHO	**W**orld **H**ealth **O**rganisation
WMO	**W**orld **M**eteorological **O**rganisation

Chapter 1

Introduction

This doctoral dissertation includes one published paper and three chapters in preparation for submission. Consequently, this introduction gives an overview of the motivation, key concepts, and layout of the dissertation and each results chapter includes a detailed and specific introduction to the relevant research question.

1.1 Motivation

Throughout Earth's history, explosive volcanic eruptions have been a major driver of year-to-year variability in Earth's climate and atmospheric composition, with wide reaching consequences for society and ecosystems globally. Explosive volcanic eruptions have been linked to crop failure, famines, disease pandemics, wars, regime changes and civilisation collapse (e.g. Antonopoulos, 1992; Guillet et al., 2017; Manning et al., 2017; McConnell et al., 2020). Sulfur dioxide (SO_2) emitted during volcanic eruptions is oxidised by the hydroxyl radical (OH) to sulfuric acid vapour (H_2SO_4) which condenses to form sulfate aerosol particles. Sulfate aerosol particles scatter shortwave radiation (SW) and absorb longwave radiation (LW), resulting in net surface and tropospheric cooling and stratospheric heating (Labitzke and McCormick, 1992). In the stratosphere, sulfate aerosols are quickly advected globally with an average lifetime of 1 to 2 years before being deposited to the surface, but the climate response can be prolonged by ocean feedbacks resulting in multi-decadal impacts (e.g., Free and Robock, 1999; Gupta and Marshall, 2018; Stenchikov et al., 2009). Volcanic aerosols also have the potential to alter stratospheric ozone. The addition of large amounts of volcanic aerosols into the stratosphere increases the surface area on which heterogeneous chemical reactions which result in the destruction in ozone can take place (Solomon, 1999). Ozone depletion induced by volcanic sulfate aerosols alters the radiative heating of the lower stratosphere and the flux of harmful UV to the surface, which could cause DNA damage to animals and plants, and increase the occurrences of skin cancers, eye damage and immune system deficiencies among the population (World Health Organization, 1994).

The effects of volcanic sulfur emissions from explosive eruptions on climate and stratospheric ozone are well understood. However, petrological data suggest that volcanic eruptions in some geological settings often release substantial amounts of halogen gases into the atmosphere (Krüger et al., 2015; Kutterolf et al., 2013, 2015) and, although volcanic halogens are efficiently scavenged by hydrometeors in the plume, direct stratospheric injection of volcanic halogens is predicted theoretically (Textor et al., 2003) and has been observed following eruptions in the satellite era (Carn et al., 2016; Hunton et al., 2005; Prata et al., 2007; Read et al., 2009; Rose et al., 2006). Datasets currently available suggest that the stratospheric injection of volcanic halogens is highly variable, however, it is clear that volcanic halogens are injected into the stratosphere after some volcanic eruptions but there is very limited research into how the co-emission of volcanic halogens may alter the life cycle of volcanic sulfate aerosol, the chemical composition of the stratosphere, and the magnitude of the volcanic forcing.

Earth's climate has changed noticeably over the last century impacting ecosystems and societies around the world. Global average land and ocean temperatures have warmed, glaciers and ice sheets have decreased in size and sea

levels have risen. Furthermore, the frequency and intensity of extreme weather events, such as drought or heavy rainfall have increased (IPCC, 2018). The best available evidence indicates that this climate change is predominantly driven by the anthropogenic emission of greenhouse gases like carbon dioxide, enhancing the natural greenhouse effect of Earth's atmosphere. Understanding how volcanic eruptions can alter the climate has been a topic of study for over a century (e.g. Humphreys, 1913). In contrast, understanding how climate change may in turn impact volcanic processes and their climate impact has received less attention. Climate-volcano feedbacks have been shown to impact the magnitude, location, and frequency of volcanic eruptions (e.g. Jellinek et al., 2004) but how climate change alters the processes that govern the volcanic sulfur lifetime, the associated aerosol optical properties, and volcanic forcing remains largely unexplored. For example, climate change is expected to result in a cooler stratosphere and slower stratospheric reaction kinetics, but also greater stratospheric water vapour concentration, which will lead to higher OH concentrations and faster oxidation of SO_2 (Collins et al., 2013). Furthermore, climate change will lead to an acceleration of the Brewer-Dobson circulation which can be expected to reduce the lifetime of stratospheric sulfate aerosol (Butchart, 2014; Collins et al., 2013; Griffiths et al., 2021). Over the next century continued anthropogenic emission of greenhouse gases will result in further climate change. To fully understand the consequences of climate change, or indeed projects designed to mitigate climate change, we need to account for the knock-on effects that climate change may have on major drivers of internal variability, including volcanic eruptions. It is therefore vital to identify climate-volcano feedbacks and quantify the effect these feedbacks may have on climate variability.

The aim of this thesis is to explore how the co-emission of volcanic sulfur and halogens, climate-volcano feedbacks, and concurrent sulfate aerosol geo-engineering alter the life cycle of volcanic sulfur, the chemical composition of the stratosphere, and the magnitude of the volcanic forcing. Recent advances in the capabilities of aerosol-climate models to interactively simulate volcanic emissions and aerosol microphysics, and the inclusion of these modules in Earth system models, allow us to effectively explore the interactions of volcanic eruptions, climate, and chemistry in this thesis (Mills et al, 2016; Schmidt et al., 2018).

1.2 Volcanic Sulfur

1.2.1 Emissions

Volcanic eruptions can inject large amounts of particles and gases into the atmosphere. The major component of volcanic eruptions is magmatic material, otherwise known as ash or tephra, which falls out of the atmosphere on the timescale of minutes to a few weeks (Symons, 1888; Vernier et al., 2016). Volcanic eruptions can also emit a significant amount of gases, predominantly in the form of H_2O, CO_2, and N_2 (Sigurdsson et al., 2000). The volcanic emission of these gases over Earth's history is the origin of the Earth's ocean and atmosphere. Although both H_2O and CO_2 are strong greenhouse gases, emissions from individual eruptions have little impact on their atmospheric concentration or radiative forcing on seasonal to centennial timescales because the emission rate is small relative to the atmospheric concentration. Instead, at these timescales, it is the emissions of sulfur species, mainly in the form of SO_2, that are most relevant for climate (Pollack et al., 1976).

1.2.2 Stratospheric Aerosols

In the stratosphere between approximately 15 km and 25 km altitude lies the 'Junge' layer (Junge, Chagnon, and Manson, 1961), a layer of stratospheric aerosol composed mostly of aqueous sulfuric acid (H_2SO_4) solution droplets (hereafter referred to as sulfate aerosol) with small contributions from non-sulfate matter (Kremser et al., 2016). In volcanically quiescent periods, the sulfate aerosol in the Junge layer is maintained mainly by natural and anthropogenic emissions of sulfate precursor gases such as SO_2, carbonyl sulfide (OCS) and dimethyl sulfide (DMS) which are transported into the stratosphere through the tropical tropopause (Kremser et al., 2016; SPARC, 2006). During explosive volcanic eruptions large quantities of SO_2 gas can be injected directly into the stratosphere. In the stratosphere, the volcanic SO_2 is oxidised to form H_2SO_4 vapour primarily by reaction with OH and H_2O via Eq. 1.1-1.3 with a lifetime of days to weeks (e.g. Bluth et al., 1992):

$$SO_2 + OH + M \rightarrow HSO_3 + M \qquad \text{(Eq. 1.1)}$$

$$HSO_3 + O_2 \rightarrow SO_3 + HO_2 \qquad \text{(Eq. 1.2)}$$

$$SO_3 + H_2O + M \rightarrow H_2SO_4 + M. \qquad \text{(Eq. 1.3)}$$

The rate determining step in the oxidation of SO_2 is Eq. 1.1 and, as such, the concentration of OH in the stratosphere determines the rate of sulfate aerosol production following volcanic eruptions. Bekki (1995) and Robock et al. (2009) reported that OH can become depleted in the volcanic plume following large volcanic eruptions, resulting in the lengthening of the SO_2 lifetime and delaying the formation of H_2SO_4. H_2SO_4 vapour condenses easily even at the low pressures in the stratosphere to form either new sulfate aerosols via binary homogeneous nucleation, whereby H_2SO_4 and H_2O condense forming H_2SO_4-H_2O droplets, or via heterogeneous nucleation, whereby H_2SO_4 condenses onto an existing aerosol, including existing sulfate aerosol (Kremser et al., 2016). Volcanic sulfate aerosol particles grow further by coagulation. A detailed description of aerosol microphysics can be found in SPARC (2006).

Balloon-borne measurements show that in volcanically quiescent periods the typical stratospheric particle number concentration is between 5 cm^{-3} and 10 cm^{-3}, and most particles have a radius smaller than 0.1 μm. In comparison, after large explosive eruptions, stratospheric volcanic sulfate aerosol typically have a radius of between 0.4 μm and 0.5 μm and a particle number concentrations of around 2 cm^{-3} (Schmidt and Carn, in press). However, the processes of aerosol nucleation and growth mean that the sulfate aerosol size and number concentrations can be distributed over several orders of magnitude following volcanic eruptions. Volcanic sulfate aerosols are described using an aerosol size distribution in either a 'sectional' or 'modal' aerosol scheme. A 'sectional' aerosol scheme reformulates the continuous aerosol size distribution into a discrete set of bins sizes. Whereas, 'modal' aerosol schemes, such as the one used in this thesis, groups aerosols into 'modes' based on their size (Mann et al., 2012). These modes are well-represented by log-normal distributions and have different physical properties, lifetimes and impacts on radiation and chemistry (Steinfeld, 1998). Nucleation of new sulfate aerosols results in new nucleation sized (<0.01 μm) sulfate aerosol, whereas condensation of H_2SO_4 onto the surface of another aerosol leads to the growth of Aitken (~0.01 to ~0.1 μm) sized aerosols. Further condensation and/or coalescence leads to the formation of accumulation (~0.1 to ~2.5 μm) and, eventually, coarse (>2.5 μm in diameter) sized aerosols. As a result, only nucleation of new particles increases the number of aerosols, and most volcanic aerosols reside

in the accumulation mode. Modal aerosol schemes are less computationally expensive than sectional schemes but do not resolve the aerosol size distribution as well. A detailed comparison of sectional and modal aerosol microphysics schemes can be found in Mann et al. (2012).

A typical size distribution of volcanic particles is shown in Figure 1.1, but the specific size ranges or each mode is specific to the model used in this thesis (see Section 2.1).

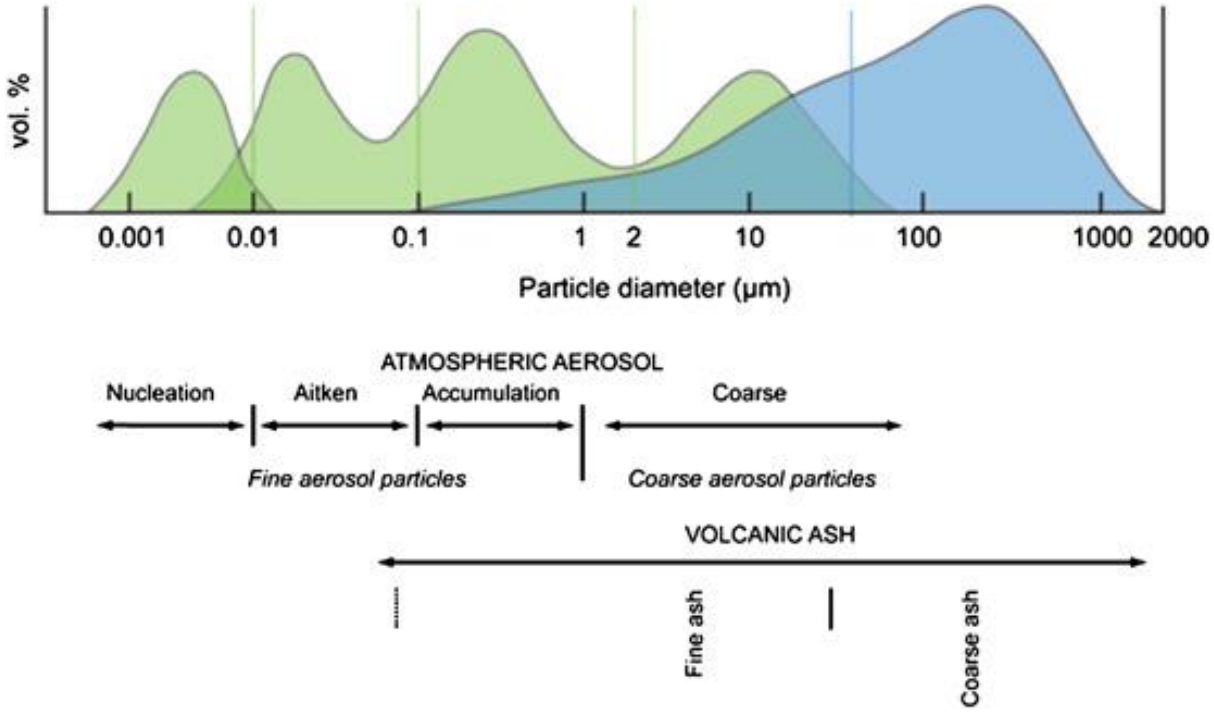

Figure 1.1 The size distribution of aerosols in Earth's atmosphere can typically be described using lognormal distributions with different physical properties. An illustrative size distribution of volcanic particles, aerosol (green) and ash (blue). Figure from Durant, A.J., Bonadonna, C., Horwell, C.J., 2010. Atmospheric and Environmental Impacts of Volcanic Particulates: Elements, vol. 6 (4), 235–240).

The lifetime of volcanic sulfate aerosol is primarily determined by the rate at which they are transferred from the stratosphere into the troposphere, which, in turn, depends on the aerosol settling velocity, with more massive (e.g. coarse mode) particles sedimenting faster, and the transport of aerosol via large-scale stratospheric circulation (described in section 1.3). Once in the troposphere, sulfate aerosols are rapidly removed by incorporation into water droplets either in clouds (rainout) or by falling precipitation below the cloud (washout), collectively known as wet deposition, as well as dry deposition e.g. over ice sheets (Marshall, 2018).

1.3 Stratospheric Transport

The lowest distinct layer of the atmosphere is called the troposphere, bounded by the surface of the earth at the bottom and the tropopause at the top, a boundary marked by a temperature inversion with warmer air above cooler air. The globally averaged tropopause height is ~12 km but this varies from ~8 km at the poles to ~17 km in the

tropics. Above the troposphere lies the stratosphere bounded by the tropopause at the bottom and the stratopause at ~50 km.

The troposphere and stratosphere are essentially separate regions of the atmosphere with differing photochemical and transport processes. The troposphere is heated largely from the Earth's surface below, meaning that the air immediately above the surface is typically the warmest and temperature reduces with altitude. This temperature profile is inherently unstable as a parcel of air at the surface is less dense than the air above it and tends to rise, driving overturning and rapid vertical transport on the order of days to weeks. By contrast, the stratosphere is heated from above through the absorption of solar radiation by O_3. This leads to inherently very stable conditions and, as a result, the stratosphere has very slow vertical transport on the order of months to years. The stratosphere acts as a lid on the less stable troposphere and the tropopause acts as a barrier limiting transport between the two regimes.

In the stratosphere, zonal winds transport volcanic aerosol across all latitudes within 3 weeks, whereas the vertical and meridional transport of volcanic aerosol is slow and occurs over the course of months (Robock and Matson, 1983). Meridional transport in the stratosphere is dominated by the Brewer-Dobson circulation (BDC), a large-scale single celled circulation pattern spanning from the tropics to the poles. Stratospheric circulation via the BDC can be split into four regimes: the summer hemisphere, the tropical pipe, the surf zone, and the polar winter vortex (Figure 1.2).

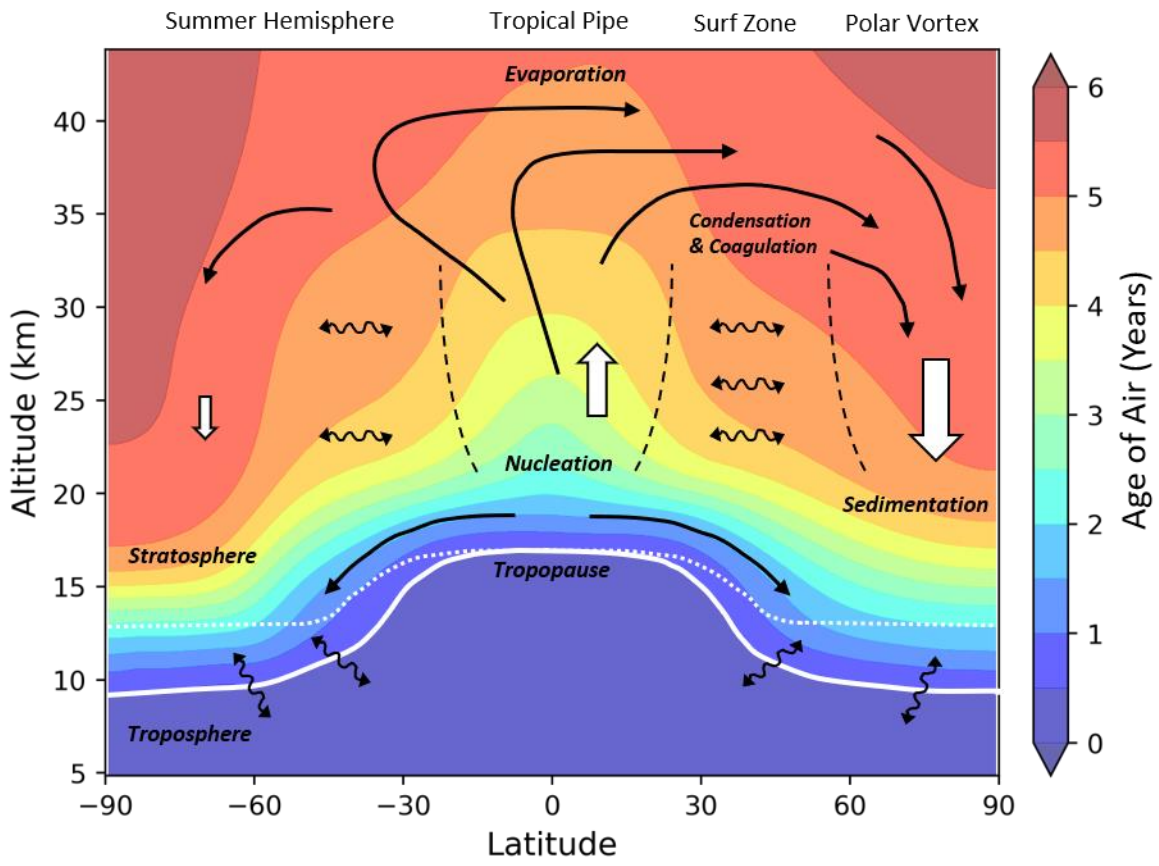

Figure 1.2 Schematic cross-section of the BDC during the northern hemisphere winter adapted from Holton et al. (1995) and Bönisch et al. (2011) overprinted onto an age-of-air cross-section. Solid arrows represent mean circulations and depict the upper (~35km) and lower (immediately above the tropopause) branches of the BDC. Dashed vertical lines represent regions of reduced transport and mark the edges of the 'leaky topical pipe' (Plumb, 1996) and the polar vortex. The solid white line marks the tropopause, and the dotted white line bounds the region where isentropic surfaces span the tropopause. Wiggly arrows depict transport along isentropes. Microphysical processes are displayed in italics.

The BDC is characterised by upwelling in the tropics, poleward transport, and descent at the poles (Butchart, 2014; Holton et al., 1995) and is predominantly driven by the release of energy as Rossby waves break in the stratosphere during a phenomenon known as Rossby wave pumping. Rossby wave pumping has a strong seasonal dependence which results in a BDC with stronger transport towards the winter hemisphere and stronger descent over the winter polar vortex (Holton et al., 1995). The meridional transport in the mid-latitude includes horizontal mixing resulting from the dissipation of wave energy in the 'surf zone'.

Meridional transport from the tropics to the mid-latitudes is restricted by a subtropical (15° to 30° latitude) transport barrier located between ~20 km and 30 km, forming what is often referred to as the 'leaky tropical pipe' (Neu and Plumb, 1999; Plumb, 1996). This leaky tropical pipe leads to a build-up of aerosol in the stratospheric subtropics following explosive tropical eruptions (Trepte and Hitchman, 1992). The BDC is characterised by faster, lower altitude branches that transport air poleward below the tropical pipe acting all year in both hemispheres, and a slower, higher altitude branch predominantly in the direction of the winter hemisphere (Butchart, 2014; Plumb, 2002). This means that particles and gases below roughly 20 km can be transferred out

of the stratosphere faster with a shorter lifetime than those higher up. The residual mean circulation in the stratosphere is relatively slow, meaning that aerosol reaching the stratosphere via the tropical pipe can remain in the stratosphere for 1-2 years (Figure 1.2). Once outside the tropical pipe or for aerosol introduced into the stratosphere at higher latitudes the stratospheric aerosol lifetime is much shorter (e.g. Kremser et al., 2016).

Meridional transport is modulated by the phase of the Quasi-biennial Oscillation (QBO) (e.g. Punge et al., 2009), an oscillation of the equatorial zonal wind alternating between easterlies and westerlies in the tropical stratosphere, with a mean period of between 28 and 29 months. The amplitude of the easterly phase (~40 ms^{-1}) is roughly twice as strong as the westerly phase (~20 ms^{-1}). The easterly phase is characterised by a stronger sub-tropical barrier, increased ascent within the tropical pipe, and weaker transport to the poles compared to a westerly phase (Hitchman et al., 1994).

The winter polar vortex is a persistent, large-scale area of cold, rotating air encircling the polar regions, extending from the middle troposphere to well into the stratosphere. These vortices rotate clockwise at the South Pole and anticlockwise at the North Pole. The lateral flow of air at the edges of the winter polar vortices helps to isolate cold, dry air over the poles forming an additional meridional transport barrier (e.g. Niemeier and Schmidt, 2017). Polar vortices can be weakened or strengthened when the Equator to pole temperature gradient increases or decreases, respectively. Polar vortex strength is an important driver of ozone depletion, with stronger polar vortexes leading to enhanced polar ozone depletion (Solomon, 1999; Zuev and Savelieva, 2019). For example, Lawrence et al. (2020) linked an unusually strong Arctic polar vortex with the record-breaking ozone loss observed in the 2019/2020 Arctic winter.

1.4 Radiative Forcing

Radiative forcing is defined as the net (SW + LW) radiative flux at the top of the atmosphere caused by an externally imposed perturbation in the Earth's radiative energy budget. Examples of perturbations that can lead to radiative forcing include changes in the solar constant, changes in surface reflection properties, and changes in the concentrations of radiatively active species (e.g., CO_2, aerosols) (IPCC, 1990). Stratospheric sulfate aerosols strongly perturb the Earth's radiative balance (Pollack et al., 1976) because the small particle radii of around 0.05 to 1 μm makes them very efficient at scattering incoming solar radiation (Mie, 1908). As a result, sulfate aerosols in the stratosphere lead to an enhancement of the planetary albedo, a reduction in the incident solar flux at the Earth's surface, and radiative cooling at the surface (Schmidt and Carn, in press). In contrast, aerosols absorb infrared radiation which is re-emitted in all directions, resulting in stratospheric and surface warming which partially offsets the surface cooling. For example, the 1991 eruption of Mt. Pinatubo injected 18 ± 4 Tg of sulfur (Guo et al., 2004) directly into the stratosphere and resulted in peak global mean shortwave radiative forcing of -4 to -5 Wm^{-2} and a peak global mean longwave radiative forcing of +1 to +3 Wm^{-2} (Soden et al., 2002).

Assuming aerosols are perfect spheres, Mie theory can be used to estimate the scattering and absorption of radiation by sulfate aerosols, using the incident radiation wavelength, sulfate aerosol size, and the optical properties of sulfate aerosol, enabling the aerosol extinction and aerosol optical depth (AOD) to be calculated

(Steinfeld, 1998). Aerosol extinction is the sum of aerosol scattering and absorption (i.e. it is the total attenuation of incident radiation due to the aerosol) and the AOD is the vertical integral of the aerosol extinction. Mie theory predicts that aerosol extinction is most efficient per unit mass when the particles are similar in size to the wavelength of incident radiation, as such, the radiative impact of sulfate aerosols depends on the aerosol size distribution which is collectively described by the effective radius (R_{eff}) (e.g. Timmreck et al., 2010). R_{eff} is the surface-area-density-weighted mean radius of the aerosol distribution and in practice is calculated as three times the total aerosol volume concentration divided by the total aerosol surface area concentration. Lacis (2015) used Mie scattering theory to determine that volcanic sulfate aerosol with a radius of ~0.20 μm has the largest aerosol extinction per unit mass at 550 nm, with a substantial drop off for aerosols both larger and smaller. In a sensitivity study considering the large 1257 eruption of Mt. Samalas, Timmreck et al. (2009) investigated the impact of volcanic sulfate aerosol size on the radiative forcing and climate impact. They found differences of 10 Wm^{-2} in the global mean top of the atmosphere radiative flux anomalies and 1.4°C in the global mean surface temperature when they varied the aerosol effective radius from 0.2 μm to 1.3 μm whilst keeping the volcanic sulfur burden constant.

Aerosol R_{eff} plays a significant role in determining the magnitude and duration of the radiative forcing following explosive volcanic eruptions. Assuming the same total sulfur burden, aerosols that grow larger are less efficient at scattering SW radiation and sediment out of the stratosphere faster (see Section 1.2.2), resulting in a smaller SW radiative forcing and faster recovery. This complex relationship between R_{eff} and radiative forcing is central to some of the results in this study.

1.5 Volcanic aerosol and ozone

Volcanic eruptions can also perturb stratospheric composition, and in particular ozone through heterogeneous reactions on the aerosol surface. The stratospheric ozone layer absorbs a large fraction of the biologically harmful ultraviolet (UV) radiation from the sun. In doing so, it protects life on Earth from DNA damage and reduces the occurrences of skin cancers, eye damage and immune system deficiencies (WHO, 1994). The key stratospheric ozone (O_3) reactions are detailed in this section.

The presence of stratospheric ozone was first determined in the 1920s from observations of the solar UV spectrum (McElroy and Fogal, 2008). A theory for the source of this ozone layer was proposed by Chapman (1930) in what is now commonly known as the Chapman mechanism:

$$O_2 + h\nu \rightarrow O + O \qquad \text{(Eq. 1.4)}$$

$$O_3 + h\nu \rightarrow O + O_2 \qquad \text{(Eq. 1.5)}$$

$$O + O_2 + M \rightarrow O_3 + M \qquad \text{(Eq. 1.6)}$$

$$O + O_3 \rightarrow O_2 + O_2 \qquad \text{(Eq. 1.7)}$$

Although the Chapman mechanism is successful in producing the general profile of stratospheric ozone, it overestimates the observed concentrations by a factor of two due to the omission of several additional stratospheric

ozone sinks. Gradually over the following decades the additional loss sinks were identified as chemical catalytic loss cycles.

The first of these catalytic cycles was identified by Bates and Nicolet (1950) and is commonly known as the HO_x ($OH + HO_2$) cycle. The HO_x cycle comprises of:

$$OH + O_3 \rightarrow HO_2 + O_2 \qquad \text{(Eq. 1.8)}$$
$$HO_2 + O \rightarrow OH + O_2 \qquad \text{(Eq. 1.9)}$$
$$\text{Net: } O_3 + O \rightarrow 2O_2.$$

in the middle stratosphere, or alternatively:

$$H + O_3 \rightarrow OH + O_2 \qquad \text{(Eq. 1.10)}$$
$$OH + O \rightarrow H + O_2 \qquad \text{(Eq. 1.11)}$$
$$\text{Net: } O + O \rightarrow O_2$$

in the upper stratosphere.

The main source of HO_x species is from the oxidation of water vapour via Eq 1.12. Water vapour is present in low concentrations in the stratosphere, it has two main sources: transport from the troposphere and chemical production from methane (Löffler et al., 2016).

$$H_2O + O \rightarrow 2OH \qquad \text{(Eq. 1.12)}$$

The next catalytic loss cycle to be identified was the NO_x (NO and NO_2) cycle (Crutzen, 1970):

$$NO + O_3 \rightarrow NO_2 + O_2 \qquad \text{(Eq. 1.13)}$$
$$NO_2 + O \rightarrow NO + O_2 \qquad \text{(Eq. 1.14)}$$
$$\text{Net: } O_3 + O \rightarrow O_2 + O_2$$

The major source of NO_x is from N_2O via reaction with O in Eq. 1.15.

$$N_2O + O \rightarrow 2NO \qquad \text{(Eq. 1.15)}$$

It was first suggested that halogens could lead to stratospheric ozone loss in Molina and Rowland (1974). Since then, several catalytic cycles through which chlorine and bromine destroy stratospheric ozone have been identified. Including through the chlorine loss reactions proposed by Stolarski and Cicerone (1974):

$$Cl + O_3 \rightarrow ClO + O_2 \qquad \text{(Eq. 1.16)}$$
$$ClO + O \rightarrow Cl + O_2 \qquad \text{(Eq. 1.17)}$$

Net: $O_3 + O \rightarrow 2O_2$

the bromine equivalent (Staehelin et al., 2018)(WMO,1999):

$Br + O_3 \rightarrow BrO + O_2$ (Eq. 1.18)

$BrO + O \rightarrow Brl + O_2$ (Eq. 1.19)

Net: $O_3 + O \rightarrow 2O_2$

the ClO dimer reactions proposed by Molina and Molina (1987):

$2(Cl + O_3 \rightarrow ClO + O_2)$ (Eq. 1.20)

$ClO + ClO + M \rightarrow Cl2O_2 + M$ (Eq. 1.21)

$Cl_2O_2 + h\nu \rightarrow Cl + ClO_2$ (Eq. 1.22)

$ClO_2 + M \rightarrow Cl + O_2 + M$ (Eq. 1.23)

Net: $2O_3 \rightarrow 3O_2$

and through the chlorine and bromine cross-coupling reaction schemes proposed by McElroy et al. (1986), for example:

$BrO + ClO \rightarrow Br + ClO_2$ (Eq. 1.24)

Active species from the HO_x, NO_x, ClO_x and BrO_x catalytic loss cycles have corresponding reservoir species, and we refer to the family of active and reservoir species combined as HO_y, NO_y, ClO_y, and BrO_y, respectively. Some key reactions important for the transfer of species between reactive and reservoir forms are outlined below (Solomon, 1999):

$ClO + NO \rightarrow Cl + NO_2$ (Eq. 1.25)

$Cl + CH_4 \rightarrow HCl + CH_3$ (Eq. 1.26)

$HO_2 + ClO \rightarrow HOCl + O_2$ (Eq. 1.27)

$ClO + NO_2 + M \rightarrow ClONO_2 + M$ (Eq. 1.28)

$OH + NO_2 + M \rightarrow HNO_3 + M.$ (Eq. 1.29)

Heterogeneous reactions play an important role in cycling of species between reactive and reservoir forms. Heterogeneous reactions are reactions that involve species of more than one phase, here the term refers to the reaction of gas phase reactants on the surface of aerosols. Some key heterogeneous reactions are outlined below:

$HCl + ClONO_2 \rightarrow HNO_3 + Cl_2$ (Eq. 1.30)

$N_2O_5 + H_2O \rightarrow 2HNO_3$ (Eq. 1.31)

$ClONO_2 + H_2O \rightarrow HNO_3 + HOCl$ (Eq. 1.32)

$HCl + HOCl \rightarrow H_2O + Cl_2$ (Eq. 1.33)

$$BrONO_2 + H_2O \rightarrow H_2O + HOBr \quad \text{(Eq. 1.34)}$$

$$HCl + BrONO_2 \rightarrow HNO_3 + BrCl \quad \text{(Eq. 1.35)}$$

$$HCl + HOBr \rightarrow H_2O + BrCl \quad \text{(Eq. 1.36)}$$

The surface area required to facilitate these heterogeneous reactions is provided by polar stratospheric clouds (PSCs) or by sulfate aerosols following volcanic eruptions (Solomon, 1999). There are two types of PSCs, consisting of water and nitric acid (Type I) or water only (Type II), but both types only occur in the extremely cold temperatures inside the winter polar vortex. Volcanic aerosols, on the other hand, provide surfaces for heterogeneous reactions at all latitudes and at all times of the year. Heterogeneous reactions reduce the levels of active NO_x species but increase the levels of active ClO_x and BrO_x species. N_2O_5 (a reactive nitrogen intermediate) reacts with water vapour via Eq 1.29 on these surfaces to form HNO_3. This sequesters reactive NO_x species into a long-lived reservoir and limits the availability of NO_x radicals to take part in the catalytic loss cycles which deplete stratospheric ozone, reducing the chemical destruction of ozone (Crutzen, 1970; Johnston, 1971). In contrast, these reactions liberate reactive ClO_x and BrO_x species from their long-lived reservoirs via Eq. 1.30-1.36, increasing the chemical destruction of ozone (Aquila et al., 2013; Solomon, 1999; Solomon et al., 1996).

The net chemical impact of volcanic sulfate aerosol loading on stratospheric ozone is dependent on the atmospheric equivalent effective stratospheric chlorine (EESC) concentration. EESC is a measure of the ozone destruction potential and includes weighted chlorine and bromine contributions; EESC = $[Cl_y]$ + 60 x $[Br_y]$ (Cadoux et al., 2015; Montzka et al., 2011; Sinnhuber et al., 2009). A large volcanic eruption in low-EESC atmospheric conditions, such as a pre-industrial or future atmosphere, is expected to result in a net stratospheric ozone increase (Langematz, 2018); however, when the EESC loading of the stratosphere is high, an eruption will lead to a net stratospheric ozone decrease (e.g. Tie and Brasseur, 1995). The present-day atmosphere is currently in a window of elevated EESC caused by the anthropogenic release of halogens into the atmosphere during the second half of the twentieth century. During this window, large explosive eruptions that inject sulfur into the stratosphere (hereafter sulfur-only) will result in stratospheric ozone depletion, but in the future and pre-industrial, when EESC concentrations are low, sulfur-only explosive volcanic eruptions will have the opposite effect and result in an increase in stratospheric ozone. EESC concentrations peaked in the late 1990s after the use of halogen bearing compounds were gradually phased out by the 1987 Montreal Protocol (Anderson et al., 2000). Since then, atmospheric EESC concentrations have fallen substantially and are expected to continue to fall eventually reaching pre-industrial levels at some point in the future, see Figure 1.3 (Dhomse et al., 2018). However, the timing of this transition is poorly constrained, with previous estimates ranging from 2015 to beyond 2040 (Naik et al., 2017; Rosenfield, 2003; Tie and Brasseur, 1995), see Chapter 5 for more details.

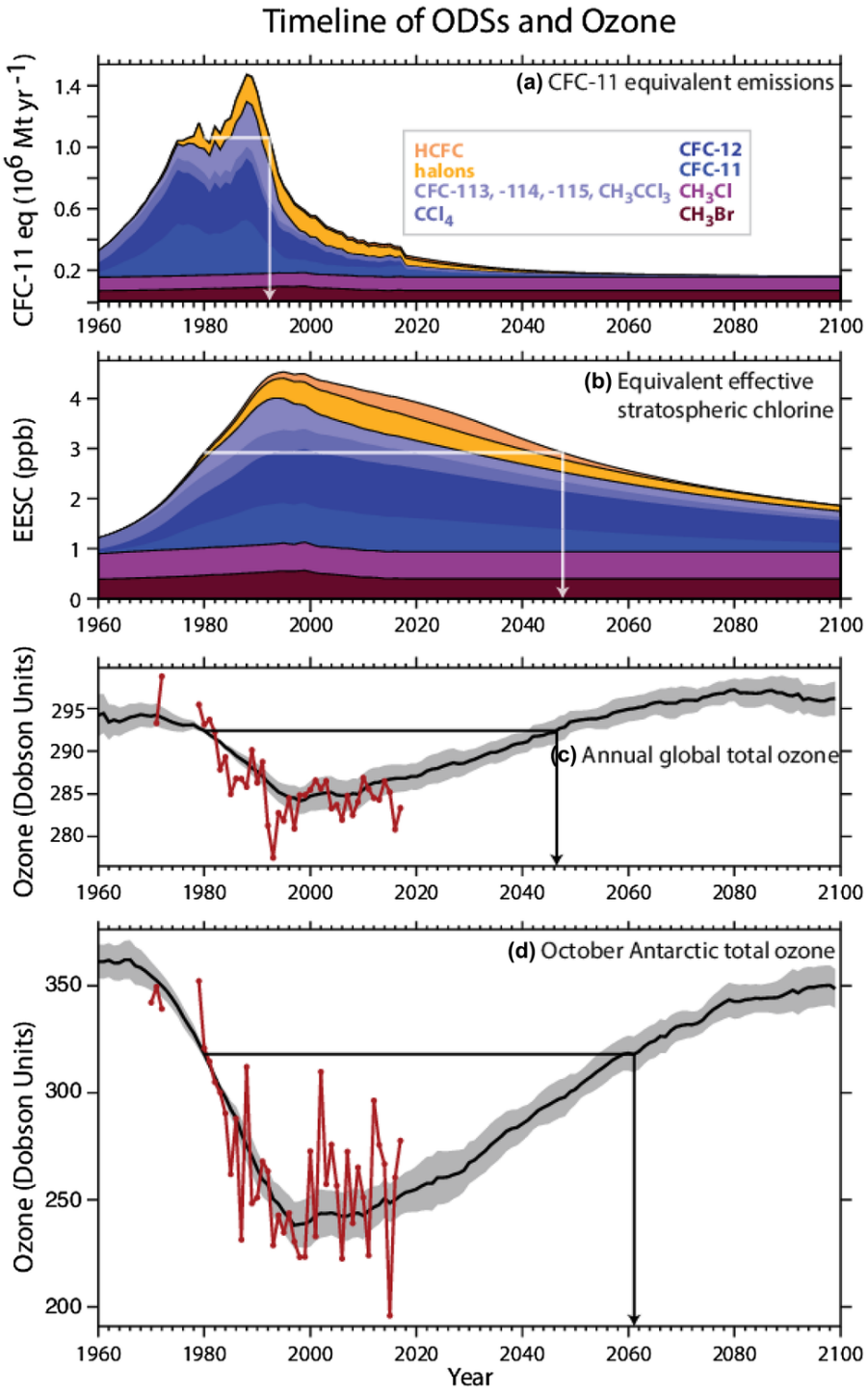

Figure 1.3 Time series of (a) CFC-11-equivalent emissions, (b) EESC concentration (ppb), (c) global mean total column ozone, and (d) October Antarctic total column ozone. Future projections assume full compliance with the Montreal Protocol and use standard methodologies based on production rates, and release rates from inventory banks. The lines with arrows indicate where values return to their 1980 reference values. This figure and the caption are taken from WMO (2018).

1.6 Volcanic Halogens

Petrological data suggest that volcanic eruptions may also release substantial amounts of halogen gases into the atmosphere, resulting in a temporary elevation of the atmospheric EESC concentration (Krüger et al., 2015; Kutterolf et al., 2013, 2015). After water, CO_2, and sulfur gases (e.g. SO_2 and H_2S), halogens are often the most abundant gases emitted during volcanic eruptions. The main halogen component of volcanic emissions is chlorine (as hydrogen chloride (HCl)), with small amounts of bromine, fluorine, and iodine (as hydrogen bromide (HBr), hydrogen fluoride (HF), and hydrogen iodide (HI)) (Textor et al., 2004). Petrological analysis of the 1257 Mt. Samalas eruption suggests as much as 227 Tg of hydrogen chloride (HCl) and 1.3 Tg of hydrogen bromide (HBr) could have been emitted into the atmosphere alongside 158 Tg of sulfur dioxide (SO_2) (Vidal et al., 2016). Similarly, petrological estimates suggested up to 675 Tg of Cl and 1.5 Tg of Br could have been degassed in the 1500 BCE eruption of Mt. Santorini (Cadoux et al., 2015). However, the portion of the halogens erupted at the vent that reach the stratosphere (hereafter halogen injection efficiency) is not well constrained and has been the subject of debate in the community for decades. Halogens are soluble (especially HCl) and may be scavenged by water, ice hydrometeors and ash in the volcanic plume (Halmer et al., 2002). Despite efficient scavenging, direct stratospheric injection of volcanic halogens is predicted theoretically, and sophisticated plume models suggest that between 10% and 20% of the HCl emitted at the vent of large explosive eruptions could reach the stratosphere (Textor et al., 2003).

In situ measurements from aircraft following the 2000 Mt. Hekla eruption in Iceland showed that 75% of the HCl emitted at the vent entered the lower stratosphere and was still present 35 hours after the eruption, suggesting that little scrubbing took place in the tropospheric eruption column (Hunton et al., 2005; Rose et al., 2006). Read et al. (2009) used retrievals from the Microwave Limb Sounder (MLS) satellite to show that SO_2 and HCl was injected directly into the lower stratosphere during the 2004 Manam, 2007 Anatahan, 2008 Soufrière Hills, 2008 Okmok, 2008 Kasatochi, 2009 Redoubt, and 2009 Sarychev eruptions. Using retrievals from MLS, Prata et al. (2007) reported HCl at ~20 km in the volcanic plume of the 2006 Soufrière Hills eruption, with stratospheric HCl:SO_2 gas ratios <0.1 (relative mixing ratios). Carn et al. (2016) reported MLS stratospheric HCl:SO_2 gas ratios of 0.01–0.03 for 14 small eruptions in the period between 2005 and 2014 (Table 1.1). Limitations with the field of view and spatial sampling of MLS mean these observed ratios are likely an underestimate (Carn et al., 2016).

Volcano	Eruption Date	HCl (ppbv)	SO_2 (ppbv)	HCl/SO_2
Manam	Jan 27, 2005	5	279	0.01
Anatahan	Apr 6, 2005	3.5	133	0.02
Soufrière Hills	May 20, 2006	3	200	0.01
Chaitén	May 6, 2008	1.6	28	0.03
Okmok	Jul 12, 2008	5	212	0.01–0.02
Kasatochi	Aug 7, 2008	5.5	392	0.01–0.014
Redoubt	Mar 26, 2009	4.5	175	0.02
Sarychev Peak	Jun 15, 2009	8	529	0.03
Merapi	Nov 5, 2010	6.5	172	0.03
Cordón Caulle1	Jun 4, 2011	2.5	77	0.03
Nabro	Jun 15, 2011	9	306	0.03
Paluweh	Feb 2, 2013	2.2	129	0.01
Kelut	Feb 14, 2014	7	398	0.01
Sangeang Api	May 31, 2014	2.5	53	0.03

Table 1.1 HCl and SO_2 mixing ratios measured by MLS in volcanic clouds, data from Carn et al. (2016).

Petrological analysis in Bacon et al. (1992) suggested that the Volcanic Explosivity Index (VEI) 7, 7.6 kya eruption of Mt. Mazama degassed ~100 Tg of Cl, and the ice core record of the same eruption suggested 8.1 Tg Cl and 57.5 Tg SO_2 were injected into the stratosphere with a halogen injection efficiency of 8.1% and a stratospheric HCl:SO_2 molar ratio of ~0.3 (Zdanowicz et al., 1999).

Despite both effectively scavenging halogens in the eruptive column of Plinian volcanic eruptions, Textor et al. (2003) reported that liquid water hydrometeors have a higher scavenging efficiency compared with solid water (ice) hydrometeors. As such, an eruption with a higher availability of total water or higher ratio of liquid water to ice will have an increased overall scavenging efficiency and will thus result in reduced stratospheric halogen injection. Water in the plume may be sourced from the magma itself or be entrained from ambient air in an atmosphere. The exact ratio of liquid water to ice in the plume is determined by the temperature distribution within the eruption column, however, typically only a small fraction of the total water exists as liquid water due to the low temperatures in Plinian volcanic eruptions where much of the eruption column is below -35ºC (Textor et al. 2003).

The two largest eruptions in the satellite era, 1991 Mt. Pinatubo and 1982 El Chichón, highlight the variability in stratospheric halogen injection following explosive volcanic eruptions. Both eruptions released relatively small amounts of halogens, 4.5 Tg and 1.8 Tg (Varekamp et al., 1984) of chlorine respectively, with HCl:SO_2 molar

ratios of ~0.4 (Mankin et al., 1992). Despite emitting more Cl into the atmosphere than El Chichón, observations following the 1991 Mt. Pinatubo eruption showed minimal stratospheric halogen injection, as the halogens were more efficiently scavenged in the eruption cloud (Wallace and Livingston, 1992). The Pinatubo eruption occurred at the same time and in the same location as a typhoon in the Philippines, and it is thought these very wet tropospheric conditions led to more efficient washout of halogens (Gerlach et al., 1996; McCormick et al., 1995; Self et al., 1996).

In comparison, spectroscopic measurements of the 1982 El Chichón stratospheric eruption plume indicated an HCl increase of 40% compared to measurements taken prior to the eruption, with a stratospheric injection of >0.04 Tg of HCl and a halogen injection efficiency of at least 2.5% (Mankin et al., 1992; Woods et al., 1985). Woods et al. (1985) measured NaCl salt particles in the lower stratospheric eruption cloud of El Chichón derived from the chlorine-rich magma. They hypothesised that the rapid ascent of large Plinian eruption phases led to the formation of ice-bearing crystals and salt particles, which would lower the halogen scrubbing efficiency and preserve the halogens for stratospheric release. In the stratosphere, these salt particles may react with volcanic sulfuric acid leading to the formation of secondary HCl, via Equation 1.37:

$$2\ NaCl + H_2SO_4 \rightarrow NaSO_4 + 2\ HCl \qquad \text{(Eq. 1.37)}$$

Overall, current datasets show that the stratospheric injection of volcanic halogens is highly variable and depends on both the total mass of halogens released at the vent and the degree of scavenging, which is determined by the geochemistry of the volcano and the prevailing atmospheric conditions during the eruption, particularly the humidity. It is clear, however, that volcanic halogens are injected into the stratosphere after some volcanic eruptions, but there is limited research into how these volcanic halogens may alter the volcanic aerosol microphysics, stratospheric chemistry, and volcanic forcing.

Lurton et al. (2018) simulated the 2009 Sarychev Peak eruption and showed how inclusion of co-emitted halogens resulted in a lengthening of the SO_2 lifetime, due to the further depletion of OH, and a corresponding delay in the formation of aerosols, giving better agreement between modelled and observed SO_2 burden and showing how co-emitted halogens could impact volcanic sulfur processing. Brenna et al. (2020) simulated a delay in SO_2 oxidation but the same total sulfur lifetime and aerosol effective radius resulting in a 20% smaller radiative forcing in simulations of a super-eruption with co-emitted volcanic sulfur and halogens compared to volcanic sulfur only. Research into the role of co-emitted halogens on total column ozone has predominantly been carried out in pre-industrial climate states (e.g. Brenna et al., 2019; Cadoux et al., 2015; Ming et al., 2020), only Klobas et al. (2017) has investigated the response in future climate states. See Section 3.1 for more details.

1.7 Climate Change

Earth's climate has changed measurably over the last century impacting ecosystems and societies globally. Global average land and ocean temperatures have warmed, glaciers and ice sheets have decreased in size and sea levels have risen. Furthermore, the frequency and intensity of extreme weather events, such as drought or heavy rainfall

has increased (IPCC, 2019). Global climate has varied dramatically throughout Earth's history, but the recent changes are occurring at an unprecedented rate (IPCC, 2018). The best available evidence indicates this is predominantly driven by the anthropogenic emission of greenhouse gases such as carbon dioxide. According to the IPCC Assessment Report (AR5), in 2017 the troposphere has warmed and the stratosphere has cooled by 1°C compared to pre-industrial levels (1850-1900 average) and is changing by roughly 0.2°C per decade. Continued anthropogenic emission of greenhouse gases will produce further climate change and further changes to the Earth's physical environment and ecosystems, but how much depends on the future rates of emissions. Limiting global warming to 1.5 °C compared to 2 °C is projected to significantly reduce the climate-related risks for natural and human systems (IPCC, 2018). At the current rate, global warming is projected to reach 1.5°C between 2030 and 2050, but 20-40% of the human population already live in regions where warming has surpassed this threshold (IPCC, 2018). A global warming of less than 1.5°C is geophysically possible, but whether warming is kept below this threshold depends on the future rates of anthropogenic emissions and mitigation projects.

Climate change may alter the climate effects of volcanic eruptions in several ways, including:

1) By altering the distribution of volcanic eruptions in terms of magnitude, location, and frequency e.g. as a consequence of glaciation-deglaciation cycles (Jellinek et al., 2004; Swindles et al., 2018; Watt et al., 2013).
2) By altering background climatic conditions into which the volcanic eruption takes place, e.g more stratified ocean (Fasullo et al., 2017) and atmosphere (Aubry et al., 2016, 2019).
3) By directly altering the processes that govern the volcanic sulfur cycle and, in turn, the associated aerosol optical properties and radiative forcing. For example, climate change is expected to result in a cooler stratosphere and slower stratospheric reaction kinetics, but also greater stratospheric water vapour concentration which will lead to higher OH concentrations and faster oxidation of SO_2 (Collins et al., 2013). Furthermore, climate change will lead to an acceleration of the Brewer-Dobson circulation which can be expected to reduce the lifetime of stratospheric sulfate aerosol (Butchart, 2014; Collins et al., 2013; Griffiths et al., 2021).

There is substantial evidence linking the frequency, location, and magnitude of volcanic eruptions to the deglaciation of ice-covered volcanoes (e.g. Jellinek et al., 2004). However, as the time-lag between ice retreat and volcanic response has been constrained to between 500 and 2000 years (Jellinek et al., 2004; Watt et al., 2013), it is unlikely such impacts are relevant on the timescale of climate projections (up to 2100 and occasionally 2300) (Swindles et al., 2018). Fasullo et al. (2017) reported that, as the Earth warms and the ocean becomes increasingly stratified in the future, the surface temperature response to volcanic eruptions may penetrate less deep into the ocean, resulting in enhanced cooling of the surface ocean and air. However, Hopcroft et al. (2018) used simulations of a Mt. Tambora sized eruption in 2040 RCP6.0 conditions to show that future volcanic eruptions would result in reduced surface cooling. Aubry et al. (2016) and Aubry et al. (2019) reported that the volcanic plume height and the fraction of volcanic sulfur that is injected into the stratosphere is sensitive to climate change due to the increased atmospheric stratification and tropopause height. Aubry et al. (under review) is the only study to explore the impacts of climate change on the processes that directly govern the stratospheric volcano sulfur

cycle. They found that climate change increased the TOA radiative forcing, stratospheric warming, and surface cooling of explosive volcanic eruptions with respect to the historical period, primarily due to a decrease in aerosol size driven by the acceleration of the Brewer-Dobson circulation and further modulated by a higher SO_2 injection height, see Section 4.1 for more details.

Scenarios describing potential future pathways of anthropogenic climate change drivers, such as emissions and land use, are vital to climate change research. These scenarios enable researchers to assess the likely changes to the climate system, quantify the direct impacts on ecosystems and society as well as potentially important feedbacks that may exacerbate or dampen the impacts of climate change. In 2007, a process for producing future scenarios was developed and resulted in the creation of the Representative Concentration Pathways (RCPs) (van Vuuren et al., 2011), a set of four possible future pathways of land use change and greenhouse gas and air pollutant emissions from the year 2000 to 2100. The four scenarios spanned a wide range of future outcomes, resulting in radiative forcings of 2.6, 4.5, 6.0, and 8.5 Wm^{-2}. More recently, scenarios were developed for the Scenario Model Intercomparison Project (ScenarioMIP) (O'Neill et al., 2016). These are driven by a new set of land use and emissions projections based on future pathways of societal development and are referred to as Shared Socioeconomic Pathways of societal development (SSPs). SSPs have been designed to integrate research across scientific communities and to address specific research and policy questions. The ScenarioMIP model design is summarised in Figure 1.4. It introduces four SSP-based scenarios which update the existing RCPs and achieve the same forcing levels by 2100 (e.g. 2.6, 4.5, 6.0, and 8.5 Wm^{-2}) and four new scenarios that plug the gaps in the forcing pathways defined by the RCPs. The two SSPs that are used extensively in this work are SSP2-4.5 and SSP5-8.5, both of which are updated RCP pathways. SSP2-4.5 represents a moderate future forcing pathway, whereas SSP5-8.5 represents a high-end future forcing pathway.

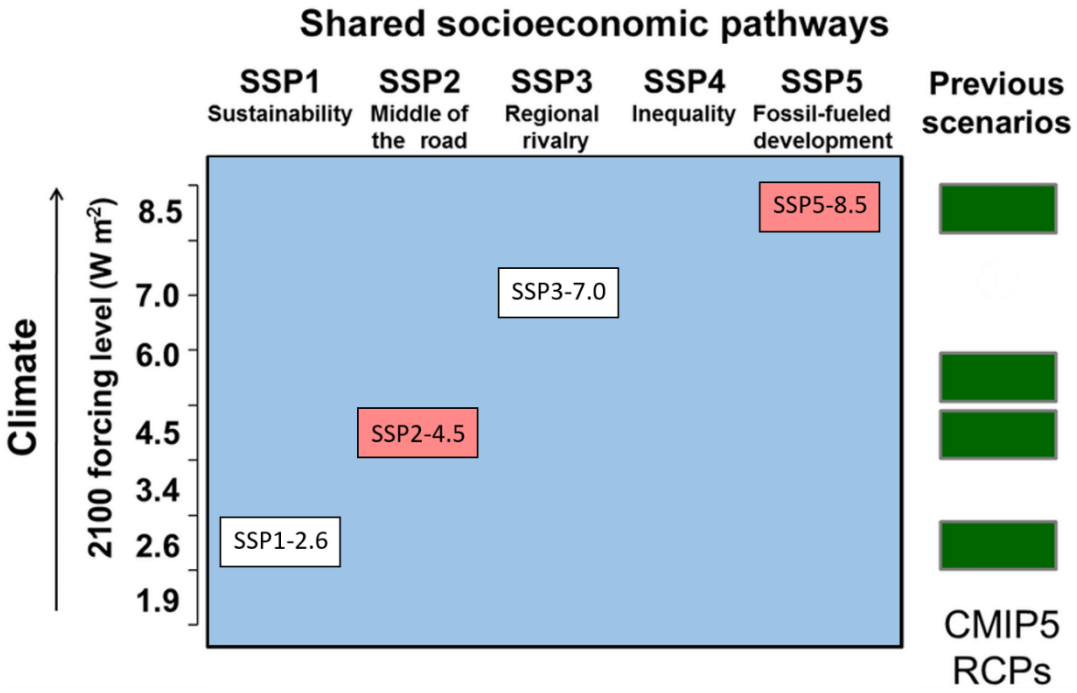

Figure 1.4 SSP-RCP scenario matrix summarising the ScenarioMIP simulations, adapted from O'Neill et al. (2016). Each cell in the matrix represents a combination of SSP and climate outcome (Wm^{-2}) based on a particular forcing pathway. Pink cells indicate scenarios used extensively in this thesis.

Future forcing scenarios also enable us to assess the effectiveness of proposed adaptation or mitigation response actions. The Geo-engineering Model Intercomparison project (GeoMIP) (Kravitz et al., 2015) and has proposed several experiments to assess the effectiveness of implementing large scale geo-engineering projects. GeoMIP proposes to apply geo-engineering measures to a SSP5-8.5 forcing projection baseline with the aim of reducing the forcing down to the levels in a SSP2-4.5 forcing projection. Four different mechanisms of geo-engineering are to be explored in GeoMIP but the most relevant to this work is G6Sulfur which attempts to reduce the radiative forcing through direct injections of SO_2 into the tropical stratosphere -- so called solar radiation management (SRM). SRM by direct stratospheric aerosol injection is one of the most discussed methods of SRM as it would likely be effective, affordable, and logistically scalable. Furthermore, the impacts are thought to be predictable as we have well studied natural analogues in the form of explosive volcanic eruptions, see Chapter 6 for more details.

1.8 Aims and Research Questions

1.8.1 Thesis Aims

This thesis consists of four studies with the objective of understanding how the co-emission of volcanic halogens and sulfur (halogen co-emission), climate-volcano feedbacks, and concurrent sulfate aerosol geo-engineering modify the effects of explosive sulfur-only volcanic eruptions. Specifically, this work intends to address the following scientific questions:

1. How is the volcanic radiative forcing and stratospheric composition altered by the co-emission of volcanic halogens and sulfur from large tropical explosive volcanic eruptions?
    - How does the co-emission of volcanic halogens modify the volcanic sulfur life cycle?
    - How does the co-emission of volcanic halogens affect stratospheric composition and compositional forcing?
    - How does the co-emission of volcanic halogens alter the volcanic effective radiative forcing (defined in Section 2.3)?

2. How will climate change alter the effects of tropical explosive sulfur-only and halogen co-emission volcanic eruptions?
    - How will climate change impact the volcanic sulfur life cycle and forcing of future tropical explosive volcanic eruptions?
    - Can statistical models be developed to generalise the change in volcanic forcing under a wide range of CO_2 concentrations?
    - How sensitive and vulnerable is total column ozone to explosive volcanic eruptions in future climate states?

3. How will sulfate aerosol geo-engineering alter the atmospheric effects of explosive sulfur-only and halogen co-emission volcanic eruptions?
    - How are the volcanic sulfur life cycle and radiative forcing effects of explosive tropical volcanic eruptions altered in a climate state which has been geo-engineered by direct stratospheric SO_2?
    - How is the sensitivity and vulnerability of total column ozone to explosive volcanic eruptions altered by concurrent sulfate aerosol geo-engineering?

1.8.2 Thesis Structure and Publication Work

Firstly, this thesis describes the only published study to comprehensively investigate and quantify the impacts of co-emitted volcanic halogens on volcanic effective radiative forcing (Chapter 3, Staunton Sykes et al., 2021). Secondly, we describe how climate change amplifies the volcanic aerosol forcing of both sulfur-only and halogen co-emission eruption scenarios in future climate states and develop novel statistical models to generalise the results of this climate-volcano feedback. (Chapter 4, Staunton Sykes et al., in prep). Thirdly, we present findings to suggest that the total ozone column in future climate states is less vulnerable to sulfur-only eruption scenarios,

as expected, but more vulnerable to halogen co-emission scenarios (Chapter 5). Lastly, we explore how the effects of explosive volcanic eruptions will be changed when they erupt into a climate state which has been geo-engineered by direct stratospheric SO_2 emission (Chapter 6, Staunton Sykes et al. (in prep)).

In addition to the papers/chapters contained within this thesis, I have contributed to two further published works:

Aubry, T. A., **Staunton Sykes, J**., Marshall, L. R., Haywood, J., Abraham, N. L., Schmidt, A.: Climate change strongly modulates the stratospheric volcanic sulfate aerosol life cycle and radiative forcing, Nature Communications, https://doi.org/10.1038/s41467-021-24943-7, 2021

Weber, J.*, Shin, Y. M.*, **Staunton Sykes, J**.*, Archer-Nicholls, S., Abraham, N. L., Archibald, A. T.: Minimal climate impacts from short-lived climate forcers following emission reductions related to the COVID-19 pandemic, Geophysical Research Letters., https://doi.org/10.1029/2020GL090326, 2020

Where * indicates equal contribution.

Chapter 2

Methods and Models

This section describes the methods and models used in the publications and chapters contained in this dissertation. Each chapter also includes a specific methods section tailored to the relevant research question.

2.1 UKESM-AMIP

2.1.1 Model Description

All simulations performed in this thesis utilise UKESM-AMIP, the atmosphere-only configuration of the UK Earth System Model UKESM1.0 (Sellar et al., 2019) including coupled aerosol-chemistry-climate components consisting of the UK Met Office Unified Model (UM) and the United Kingdom Chemistry and Aerosol (UKCA) module. The UKCA module is run at UM version 11.2 with the combined stratosphere and troposphere chemistry (StratTrop) scheme which simulates 84 species competing in 291 reactions (Archibald et al., 2020). The model is free running in the atmosphere but forced by surface boundary conditions (sea ice and sea surface temperatures), like the UK Earth system model (UKESM1) Atmospheric Model Intercomparison Project (AMIP) simulation submitted to the Coupled Model Intercomparison Project Phase 6 (CMIP6) (Sellar et al., 2019, 2020). The resolution was 1.875° longitude by 1.25° latitude with 85 vertical levels extending from the surface to 85 km. The dynamics of the stratosphere have previously been shown to be well represented in this model, and it has an internally generated Quasi-Biennial Oscillation (QBO) (Osprey et al., 2013). The model includes the fully interactive stratospheric GLOMAP-mode aerosol scheme (Dhomse et al., 2014; Mann et al., 2010). GLOMAP-mode is a comprehensive aerosol microphysics model that simulates size resolved aerosol mass and number concentrations in seven log-normal modes: four soluble modes (nucleation, Aitken, accumulation and coarse) and three insoluble modes (Aitken, accumulation and coarse). It includes the full aerosol life cycle comprising emissions, nucleation, condensation, coagulation, cloud processing, gravitational settling, and wet and dry deposition. GLOMAP-mode also calculates aerosol optical properties online which are used to calculate direct and indirect radiative effects (Mulcahy et al., 2020).

In UKCA, the concentration of stratospheric ozone is determined by photochemical reactions as well as catalytic loss cycles which destroy ozone involving chlorine, bromine, nitrogen, and hydrogen radical species (Archibald et al., 2020). Photolysis reactions in UKCA utilise rates calculated from either the FAST-JX scheme or look-up tables (Telford et al., 2013). Ozone-depleting radical species are produced by the photolysis of compounds containing chlorine or bromine reacting on the surface of stratospheric aerosols, including hydrochloric acid (HCl), hydrogen bromide (HBr), chlorine nitrate ($ClONO_2$), and bromine nitrate ($BrONO_2$). Heterogeneous reactions facilitated by polar stratospheric clouds (PSCs) in the polar lower stratosphere or sulfate aerosol following explosive volcanic eruptions are also important for stratospheric ozone concentrations. Eight additional heterogeneous reactions involving chlorine and bromine species were added as described in Ming et al. (2020), with the main change being the explicit treatment of the reactions of four additional chemical species: Cl_2, Br_2, $ClNO_2$, and $BrNO_2$ which are photolysed to produce Cl and Br radicals. Comparison with the National Institute

of Water and Atmospheric Research - Bodeker Scientific (NIWA-BS) total column ozone dataset shows that the inclusion of these additional heterogeneous reactions improves the simulation of springtime total column ozone (Dennison et al., 2019).

2.1.2 Model Validation

UKESM1 has previously been shown to perform well, it has a stable pre-industrial state and gives good agreement with observations throughout simulations of the historical period, although it has a high equilibrium climate sensitivity (5.4 K) relative to the previous model generation (3.2 K) and other CMIP5 models (<4.7 K) (Sellar et al., 2019). UKESM1 contains a stratosphere-troposphere chemical scheme (UKCA StratTrop) which is fully coupled to an aerosol scheme (GLOMAP-mode). The UKCA StratTrop chemical mechanism is a merger of previously well-evaluated tropospheric and stratospheric chemical and aerosol mechanisms. UKCA StratTrop performs well when compared to a wide array of observations, including stratospheric ozone (Archibald et al., 2020) and it has previously been shown to give good agreement with total column ozone observations throughout the recent historical period in a multi-model study carried out as part of the Chemistry-Climate Model Initiative (CCMI) (Dhomse et al., 2018). GLOMAP-mode has been shown to perform well against datasets in simulating concentrations of aerosol precursors gases and chemically speciated aerosol mass and number in the troposphere. The evolution of simulated global burden, lifetime, and removal of sulfate aerosol lies very close the multi-model median from the AEROCOM mode intercomparison exercise (Mann et al., 2010, 2012).

The use of GLOMAP-mode for simulating explosive volcanic eruptions has been comprehensively validated by Dhomse et al. (2014), who found it performs similarly to other aerosol-composition climate models and gives good agreement with observations of the sulfate burden, aerosol optical depth, aerosol size distribution and stratospheric heating following the 1991 Mt Pinatubo eruption (M. Toohey et al., 2011; Mills et al., 2016), and also by Dhomse et al. (2020) following the 1963 eruption of Mt Agung, the 1982 eruption of El Chicon, and the 1991 eruption of Mt Pinatubo. Mode merging from the accumulation to coarse modes is turned off above 100 hPa as described in Dhomse et al. (2014). This ensures that aerosol in the accumulation mode can continue to grow within the accumulation mode rather than be transferred into the coarse mode. This technique was found to result in a better fit of aerosol size distributions compared to a reference sectional aerosol scheme and observations following the 1991 eruption of Mt. Pinatubo (Kokkola et al., 2009; Niemeier et al., 2009).

2.1.3 Model Development

Several developments to the UKESM-AMIP model were made to facilitate the research in this thesis. By default UKESM utilises prescribed volcanic properties. This was modified instead to allow the direct injection of volcanic SO_2, and, for the first time, the direct injection of volcanic HCl and HBr, replicating developments used in previous versions of UKCA. As part of the collaborative work with Aubry et al. (2021) the distribution of volcanic gas emissions was modified to reflect a more realistic Gaussian distribution. The width of the Gaussian distribution was calibrated to 10% of the injection height in accordance with Aubry et al. (2019).

Eight additional heterogeneous reactions involving chlorine and bromine species were added as described in Ming et al. (2020), with the main change being the explicit treatment of the reactions of four additional chemical species: Cl_2, Br_2, $ClNO_2$, and $BrNO_2$ which are photolysed to produce Cl and Br radicals. The inclusion of these reactions was shown to improve the stratospheric halogen and ozone chemistry by accounting for inter-halogen reactivation in Braesicke et al. (2013). Model output diagnostics were created to track the abundances and reaction fluxes of the chemical families that are important for stratospheric ozone, including: HO_x, HO_y, NO_x, NO_y, ClO_x, Cl_y, BrO_x, and Br_y.

2.2 Experimental design

Across the four results chapters in this thesis, we utilise results from volcanic eruption simulations carried out in four different background climate states. The first is a historical climate state representative of the 1990s (hereafter HIST) (Eyring et al., 2016), the second and third are two future climate states representative of the 2050s driven by moderate (SSP2-4.5) and high-end (SSP5-8.5) emission projections of greenhouse gases and halocarbons (hereafter SSP2 and SSP5) (O'Neill et al., 2016), and finally, a geo-engineered future climate state representative of the 2050s, defined by G6Sulf (hereafter G6_SRM) which applies geo-engineering measures to a SSP5-8.5 forcing projection baseline with the aim of reducing the forcing down to the levels in a SSP2-4.5 forcing projection (Kravitz et al., 2015). We utilise atmosphere-only, time-slice experiments whereby the sea surface temperature (SST), sea ice fraction and depth, surface emissions and lower boundary conditions are prescribed using decadal-average climatologies. In HIST simulations, the climatologies are calculated using data from the fully coupled UKESM1.0 historical runs produced for CMIP6 (Eyring et al., 2016) and averaged over the years 1990 to 2000. The control simulation was initialised from the January 1995 initialisation file taken from the same UKESM1.0 historical scenario simulation. In SSP2 and SSP5 simulations, the climatologies are calculated using data from the fully coupled UKESM1.0 ScenarioMIP runs produced for CMIP6 and averaged over the years 2050 to 2060, the control simulations were initialised from the January 2055 initialisation file taken from the respective ScenarioMIP simulation (Eyring et al., 2016). The model set-up used for G6_SRM simulations was identical to SSP5, except with an additional emissions file to incorporate the direct emission of SO_2. The injection strength required to reduce the SSP5-8.5 forcing down to the levels of SSP2-4.5 was found by trial and as part of Jones et al. (2021).

By averaging over the decade the atmosphere-only simulations are forced with boundary conditions typical of the period but not a specific date within that decade. The fully coupled transient simulations had internally generated El Niño and La Niña cycles, however, the decadal mean SSTs had a permanent neutral signal (see Figure A1). In each case, the model was allowed to spin up for 15 years and the control was run for a further 20 years. The effect of explosive volcanic eruptions was investigated by running a series of 10-year volcanic perturbation simulations initialised from different years in the control run to sample the variability in QBO states. Changes are plotted as the difference between the average of the ensembles and a climatology derived from the 20-year control run. Cumulative forcings are calculated as the time-integrated forcing across the Earth's surface and represent the total energy loss as a result of the volcanic eruption (J). The ensemble range is included as an envelope on timeseries plots and utilised in significance testing where appropriate (see Section 2.5).

The volcanic emissions are prescribed by direct injection of SO_2, HCl and HBr into the stratosphere with a Gaussian plume vertical distribution centred on 21 km and a width of 2.1 km (10% of the height) (Aubry et al., 2019), lasting for 24 hours on July 1st. An injection altitude of 21 km was chosen as, allowing for lofting, this results in a volcanic sulfate altitude consistent with the 1991 eruption of Mt Pinatubo (Guo et al., 2004). The gases were injected in the tropics (5ºS latitude and 0º longitude) to represent a typical tropical explosive eruption (Newhall et al., 2018). The impacts of very-short-lived Bromine species are accounted for by adding a fixed contribution of 5 pptv into the CH_3Br surface concentration.

Since historical stratospheric volcanic SO_2 fluxes are variable and the volcanic flux of HCl and HBr into the stratosphere remains uncertain, we developed a simulation matrix that spans a range of possible explosive volcanic emissions. The four sets of experiments have one large SO_2 (10 Tg), and one very-large SO_2 (56 Tg) emission scenario both with (H10 and H56) and without halogens (S10 and S56), as shown in Table 2.1.

Scenario	SO_2 (Tg)	HCl (Tg)	HBr (Tg)	HCl:SO_2
S10	10	-	-	-
H10	10	1.5	0.0086	0.26
S56	56	-	-	-
H56	56	15	0.086	0.47

Table 2.1 Showing the eruption masses of SO_2, HCl and HBr in Tg and HCl:SO_2 (relative mixing ratio) for the four sets of experiments used in this thesis.

These eruption sizes (10 Tg SO_2 and 56 Tg SO_2) are hypothetical, but they are comparable to a VEI 6 (e.g. 1991 Mt. Pinatubo) and VEI 7 (e.g. 1257 Mt. Samalas) eruption, representing 1-in-50-100-year and 1-in-500-1000-year events respectively (Newhall et al., 2018). VEI is used here to provide context of the recurrence rates but is not used as an index representative of climate impact. H56 utilises the 1257 Mt. Samalas HCl and HBr emission estimates from Vidal et al. (2016) and assumes a conservative ~5% stratospheric halogen injection efficiency, less than the 10-20% predicted by plume modelling in Textor et al. (2003) and closer to the observed efficiency following El Chichón (>2.5%) and in the ice core record of Mt. Mazama (8%), as well as the fraction supported by Wade et al. (2020). HIST_H10 has a SO_2 injection similar to that found to reproduce the spatial and temporal evolution of stratospheric aerosol optical depth (SAOD) following 1991 Pinatubo (Mills et al., 2016) and 10-times-smaller HCl and HBr flux than HIST_H56. This results in a HCl:SO_2 ratio of ~0.26 and ~0.47 in HIST_H10 and HIST_H56 respectively, similar to the estimated stratospheric injection ratio for Mt. Mazama (0.3) (Zdanowicz et al., 1999) and the ratios used in Ming et al. (2020), and Brenna et al. (2020) but smaller than the ratio used in (Cadoux et al., 2015). Experiment identifiers used throughout this thesis are formed by combining the background climate and eruption scenario identifiers, as shown in Table 2.2.

Simulation Key	**Climate Scenario**			
Eruption Scenario	**HIST**	**SSP2**	**SSP5**	**G6_SRM**
S10	HIST_S10	SSP2_S10	SSP5_S10	G6_S10
H10	HIST_H10	SSP2_H10	SSP5_H10	G6_H10
S56	HIST_S56	SSP2_S56	SSP5_S56	G6_S56
H56	HIST_H56	SSP2_H56	SSP5_H56	G6_H56

Table 2.2 Showing the full simulation matrix utilised in this thesis. Experiment identifiers are formed by combining the climate scenarios (column headings) and emission scenarios (rows)

2.3 Radiative Energy Budget Decomposition

Volcanic effective radiative forcing (hereafter ERF) is calculated as the difference (Δ) in the net (SW+LW) top-of-atmosphere (TOA) radiative fluxes (*F*) between perturbed and control simulations, as follows:

$$ERF = \Delta F \quad \text{(Eq. 2.1)}$$

Volcanic ERF is decomposed as described in Schmidt et al. (2018) and Ghan (2013), as follows:

$$ERF = \Delta(F - F_{clean}) + \Delta(F_{clean} - F_{clear,clean}) + \Delta F_{clear,clean} \quad \text{(Eq. 2.2)}$$

$$= ERF_{ari} + ERF_{aci} + ERF_{clear,clean} \quad \text{(Eq. 2.3)}$$

This decomposition is enabled by implementing extra calls to the radiation scheme as recommended by Ghan (2013) to obtain F_{clean} and $F_{clear,clean}$, where F_{clean} denotes a radiation flux diagnostic calculation without aerosol radiation interactions but including aerosol-cloud interactions through microphysics, and $F_{clear,clean}$ denotes a radiation flux diagnostic calculation that ignores both aerosol-radiation and cloud-radiation interactions. Thus, $F - F_{clean}$, determines the impact of all aerosols and $\Delta(F - F_{clean})$ is an estimate of the forcing from volcanic aerosol-radiation interactions (ERF_{ari}). The second term $\Delta(F_{clean} - F_{clean,clear})$ represents the difference in the clean-sky cloud radiative forcing, and is an estimate of the aerosol-cloud interactions (ERF_{aci}) due to volcanic emissions. The third term, $ERF_{clear,clean}$ accounts for changes not directly due to aerosol or cloud interactions, largely the result of changes in surface albedo and atmospheric composition. In this study, we fix sea-surface temperature and sea-ice fields meaning that surface albedo is expected to be unchanged and any $F_{clear,clean}$ changes are the result of atmospheric compositional changes.

2.4 Ozone Radiative Kernel

To calculate the resulting radiative forcing from the ozone changes simulated in this thesis, we use the ozone radiative kernel (O_3 RK) technique based on Rap et al. (2015) and updated for the whole atmosphere as outlined in Iglesias-Suarez et al. (2018). The O_3 RK is constructed by calculating the change in LW and SW flux caused

by a 1 ppb perturbation in ozone added to each atmospheric layer in turn. The change in SW and LW flux is diagnosed using the offline version of the Suite Of Community RAdiative Transfer (SOCRATES) model, based on Edwards and Slingo (1996). All other variables are defined using climatologies and are kept constant. The LW component of the O_3 RK (Fig. 2.1c) is positive throughout the atmosphere, with a maximum in the tropical upper troposphere lower stratosphere. The SW component (Fig. 2.1c) is negative above ~12 km altitude and positive below ~12 km altitude. This results in a net O_3 RK (Fig. 2.1a) 510 which is positive everywhere except above ~25 km between 60ºS and 60ºN. A more detailed description of the ozone radiative kernel can be found in Rap et al. (2015).

Rap et al. (2015) proposed the O_3 RK as an efficient and accurate method to estimate ozone RFs and suggested it was particularly well suited for multi-model intercomparison activities. Iglesias-Suarez et al. (2018) compared the ozone radiative forcing estimated using the O_3 RK (i.e. by multiplying the simulated ozone change by the net O_3 RK) with the corresponding radiative forcing calculated directly with the SOCRATES radiative transfer model and found a good agreement between the two methods (global mean difference of 0.01 Wm^{-2}).

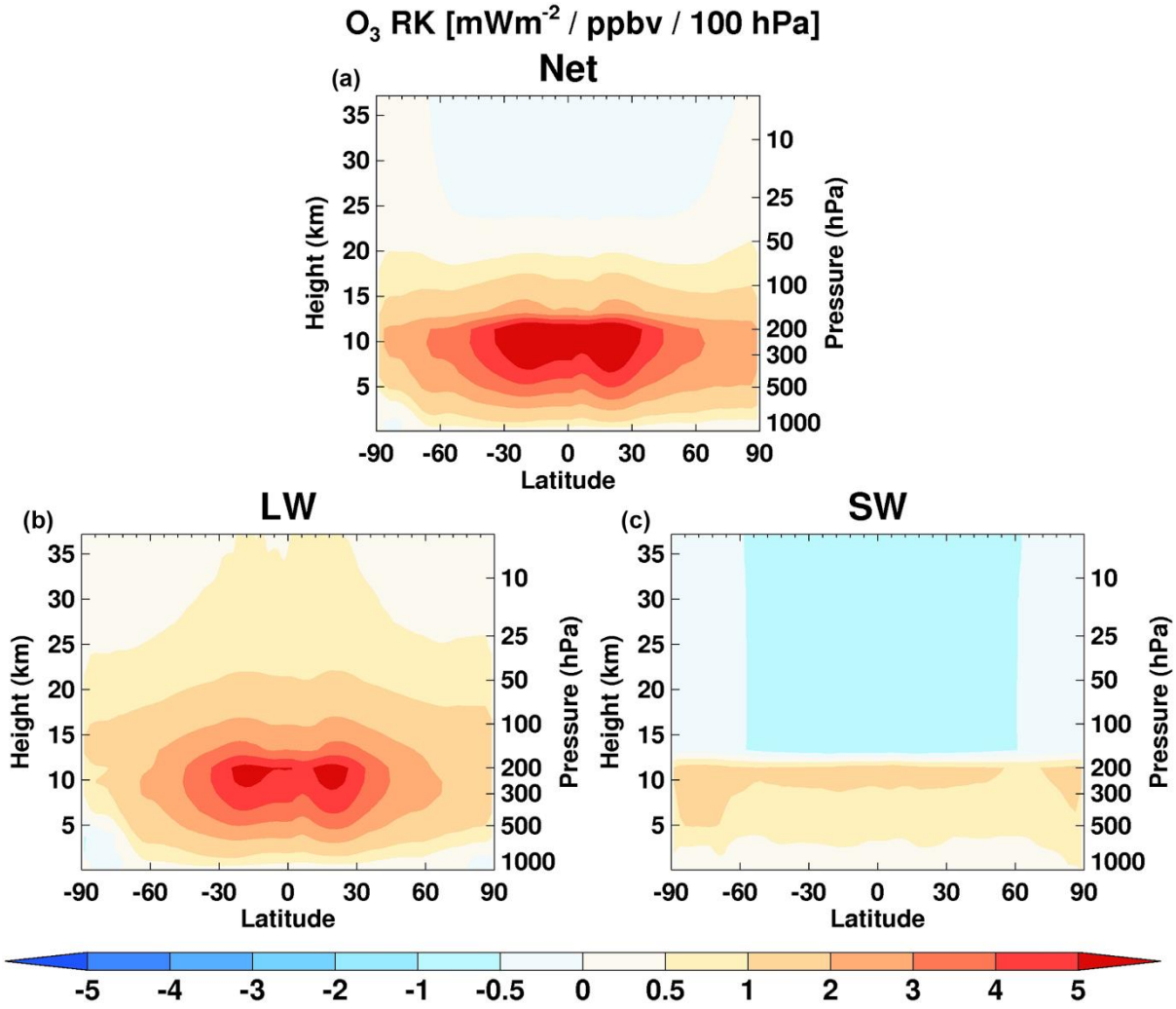

Figure 2.1 Annual zonal mean whole atmosphere ozone radiative kernel under all-sky conditions for (a) net (LW + SW), (b) LW, and (c) SW components. Figure taken from Iglesias-Suarez et al. (2018).

2.5 Statistical Methods

2.5.1 Statistical Significance

A result is statistically significant if there is a very low chance it can be explained solely by chance or random effects. This thesis uses the probability value, hereafter p value, to indicate the statistical significance of a finding. An extremely low p value indicates high statistical significance, while a high p value means low or no statistical significance. A significance level of 0.05 or less is considered the statistically significant threshold in this study. That means there is a 5% or lower chance of our results occurring solely due to chance or random effects.

In this thesis data are analysed through null hypothesis significance testing, the formal procedure for assessing whether a relationship between variables or a difference between groups is statistically significant. Research questions are phrased as two main hypotheses:

- **Null hypothesis (H0)** there is no true effect, no relationship between variables, or no difference between groups.
- **Alternative hypothesis (H1)** there is a true effect, a relationship between variables, or a difference between groups.

Hypothesis testing in this thesis starts with the assumption that the null hypothesis is true. Statistical tests are used to assess the likelihood (probability) of obtaining our results under this assumption. We reject or retain the null hypothesis depending on whether the p value is below or above the significance level (0.05), respectively. We used two statistical tests in this thesis, explained in more detail in the following subsections.

2.5.2 Mann-Whitney

The Mann–Whitney U test is a nonparametric test of the null hypothesis that, for randomly selected values ‘A’ and ‘B’ from two populations, the probability of ‘A’ being greater than ‘B’ is equal to the probability of ‘B’ being greater than ‘A’. The Mann-Whitney U test is the nonparametric alternative to the independent t-test. The Mann-Whitney U test is used in this study as it is does not require the data to be normally distributed. It is difficult to confirm normality when the sample size (number of ensembles) is small. Mann-Whitney U tests were carried out using the ‘mannwhitneyu’ function from the ‘scipy’ package at version 1.5.2.

2.5.3 Analysis of variance (ANOVA)

Analysis of variance (ANOVA) is the name given to a collection of statistical models and their associated estimation procedures used to analyse the differences among means. ANOVA provides a statistical test of whether the means of two or more populations are equal, and therefore generalizes the t-test beyond two means. In this thesis, 3-way ANOVA is used to determine whether three independent predictor variables have a significant effect on a continuous dependent variable and any interactions therein. ANOVA was carried out using the ‘ols’ and ‘anova_lm’ function from the ‘statsmodels’ package at version 10.1.

Chapter 3

Co-emission of volcanic sulfur and halogens amplifies volcanic effective radiative forcing

The results from this chapter were published in Atmospheric Chemistry and Physics in June 2021.

Staunton-Sykes, J., Aubry, T. J., Shin, Y. M., Weber, J., Marshall, L. R., Luke Abraham, N., Archibald, A., and Schmidt, A.: Co-emission of volcanic sulfur and halogens amplifies volcanic effective radiative forcing, Atmos. Chem. Phys., 21, 9009–9029, https://doi.org/10.5194/acp-21-9009-2021, 2021

JSS designed the study, ran the UKESM1-AMIP experiments, analysed the results, and wrote the manuscript. AS and AA provided support for designing the study and analysing the results. TJA, LRM, and NLA provided support for running the experiments, and TJA, YMS, and JW, provided support for the analysis. All authors contributed to revising the manuscript.

Abstract

The evolution of volcanic sulfur and the resulting radiative forcing following explosive volcanic eruptions is well understood. Petrological evidence suggests that significant amounts of halogens may be co-emitted alongside sulfur in some explosive volcanic eruptions, and satellite evidence indicates that detectable amounts of these halogens may reach the stratosphere. In this study, we utilise an aerosol-chemistry-climate model to simulate stratospheric volcanic eruption emission scenarios of two sizes, both with and without co-emission of volcanic halogens, in order to understand how co-emitted halogens may alter the life cycle of volcanic sulfur, stratospheric chemistry and the resulting radiative forcing. We simulate a large (10 Tg of SO_2) and very large (56 Tg of SO_2) sulfur-only eruption scenario and a corresponding large (10 Tg SO_2, 1.5 Tg HCl, 0.0086 Tg HBr) and very large (56 Tg SO_2, 15 Tg HCl, 0.086 Tg HBr) co-emission eruption scenario. The eruption scenarios simulated in this work are hypothetical, but they are comparable to Volcanic Explosivity Index (VEI) 6 (e.g. 1991 Mt. Pinatubo) and VEI 7 (e.g. 1257 Mt. Samalas) eruptions, representing 1-in-50-100-year and 1-in-500-1000-year events respectively, with plausible amounts of co-emitted halogens based on satellite observations and volcanic plume modelling.

We show that co-emission of volcanic halogens and sulfur into the stratosphere increases the volcanic effective radiative forcing (ERF) by 24% and 30% in large and very large co-emission scenarios compared to sulfur-only emission. This is caused by an increase in both the forcing from volcanic aerosol-radiation interactions (ERF_{ari}) and composition of the stratosphere ($ERF_{clear,clean}$). Volcanic halogens catalyse the destruction of stratospheric ozone, which results in significant stratospheric cooling, offsetting the aerosol heating simulated in sulfur-only scenarios and resulting in net stratospheric cooling. The ozone-induced stratospheric cooling prevents aerosol self-lofting and keeps the volcanic aerosol lower in the stratosphere with a shorter lifetime. This results in reduced growth by condensation and coagulation and a smaller peak global mean effective radius compared to sulfur-only simulations. The smaller effective radius found in both co-emission scenarios is closer to the peak scattering

efficiency radius of sulfate aerosol, and thus, co-emission of halogens results in larger peak global mean ERF_{ari} (6% and 8%). Co-emission of volcanic halogens results in significant stratospheric ozone, methane and water vapour reductions, resulting in significant increases in peak global mean $ERF_{clear,clean}$ (>100%), predominantly due to ozone loss. The dramatic global mean ozone depletion simulated in large (22%) and very-large (57%) co-emission scenarios would result in very high levels of UV exposure on the Earth's surface, with important implications for society and the biosphere.

This work shows for the first time that co-emission of plausible amounts of volcanic halogens can amplify the volcanic ERF in simulations of explosive eruptions. It highlights the need to include volcanic halogen emissions when simulating the climate impacts of past or future eruptions as well as the necessity to maintain space-borne observations of stratospheric compounds to better constrain the stratospheric injection estimates of volcanic eruptions.

3.1 Introduction

Sulfur gases emitted into the atmosphere by volcanic eruptions have a strong direct climate impact through the formation of sulfuric acid aerosol, which reflect incoming sunlight and cool the Earth's surface (Robock, 2000). Petrological data suggest that volcanic eruptions in some geological settings may also release substantial amounts of halogen gases into the atmosphere (Krüger et al., 2015; Kutterolf et al., 2013, 2015). Petrological analysis of the 1257 Mt. Samalas eruption suggests as much as 227 Tg of hydrogen chloride (HCl) and 1.3 Tg of hydrogen bromide (HBr) could have been emitted into the atmosphere alongside 158 Tg of sulfur dioxide (SO_2) (Vidal et al., 2016). The portion of the halogens erupted at the vent that reach the stratosphere (hereafter halogen injection efficiency) is not well constrained and has been the subject of debate in the community for decades. Halogens are soluble (especially HCl) and may be scavenged by water, ice hydrometeors and ash in the volcanic plume (Halmer et al., 2002). Despite efficient scavenging, direct stratospheric injection of volcanic halogens is predicted theoretically, and sophisticated plume models suggest that between 10% and 20% of the HCl emitted at the vent of large explosive eruptions could reach the stratosphere (Textor et al., 2003).

Aircraft measurements following the 2000 Mt. Hekla eruption in Iceland showed that 75% of the HCl emitted at the vent entered the lower stratosphere and was still present 35 hours after the eruption, suggesting that little scrubbing took place in the tropospheric eruption column (Hunton et al., 2005; Rose et al., 2006). Read et al. (2009) used retrievals from the Microwave Limb Sounder (MLS) to show that SO_2 and HCl was injected directly into the lower stratosphere during the 2004 Manam, 2007 Anatahan, 2008 Soufrière Hills, 2008 Okmok, 2008 Kasatochi, 2009 Redoubt, and 2009 Sarychev eruptions. Using retrievals from MLS, Prata et al. (2007) reported HCl at ~20 km in the volcanic plume of the 2006 Soufrière Hills eruption, with stratospheric HCl:SO_2 gas ratios <0.1. Carn et al. (2016) reported MLS stratospheric HCl:SO_2 gas ratios of 0.01–0.03 (relative mixing ratios) for 14 small eruptions in the period between 2005 and 2014. Limitations with the field of view and spatial sampling of MLS mean these observed ratios are likely an underestimate (Carn et al., 2016).

Petrological analysis in Bacon et al. (1992) suggested that the considerably larger, Volcanic Explosivity Index (VEI) 7, 7.6 kya eruption of Mt. Mazama degassed ~100 Tg of Cl, and the ice core record of the same eruption

suggested 8.1 Tg Cl and 57.5 Tg SO_2 were injected into the stratosphere with a halogen injection efficiency of 8.1% and a stratospheric HCl:SO_2 molar ratio of ~0.3 (Zdanowicz et al., 1999). The two largest eruptions in the satellite era, 1982 El Chichón and 1991 Mt. Pinatubo, highlight the variability in stratospheric halogen injection following explosive volcanic eruptions. Both eruptions released relatively small amounts of halogens, 1.8 Tg (Varekamp et al., 1984) and 4.5 Tg of chlorine respectively, with HCl:SO_2 molar ratios of ~0.4 (Mankin et al., 1992). Spectroscopic measurements of the El Chichón stratospheric eruption plume indicated an HCl increase of 40% compared to measurements taken prior to the eruption, with a stratospheric injection of >0.04 Tg of HCl and a halogen injection efficiency of at least 2.5% (Mankin and Coffey, 1984; Woods et al., 1985). Woods et al. (1985) measured NaCl salt particles in the lower stratospheric eruption cloud of El Chichón derived from the chlorine-rich magma. They hypothesised that the rapid ascent of large Plinian eruption phases led to the formation of ice-bearing crystals and salt particles, which would lower the halogen scrubbing efficiency and preserve the halogens for stratospheric release. In the stratosphere, these salt particles may react with volcanic sulfuric acid leading to the formation of secondary HCl. In contrast, despite emitting more Cl into the atmosphere than El Chichón, observations following the 1991 Mt. Pinatubo eruption showed minimal stratospheric halogen injection, due to the fact that halogens were more efficiently scavenged in the eruption cloud (Wallace and Livingston, 1992). The Pinatubo eruption occurred at the same time and in the same location as a typhoon in the Philippines, and it is thought these very wet tropospheric conditions led to the effective washout of halogens (Gerlach et al., 1996; McCormick et al., 1995; Self S et al., 1996).

Overall, current datasets show that the stratospheric injection of volcanic halogens is highly variable and depends on both the total mass of halogens released at the vent and the degree of scavenging, which is determined by the geochemistry of the volcano and the prevailing atmospheric conditions during the eruption, particularly the humidity. It is clear, however, that volcanic halogens are injected into the stratosphere after some volcanic eruptions, but there is limited research into how these volcanic halogens may alter the volcanic aerosol microphysics, stratospheric chemistry, and volcanic forcing.

Lurton et al. (2018) simulated the 2009 Sarychev Peak eruption (0.9 Tg of SO_2) in CESM1(WACCM) (Community Earth-System Model, Whole Atmosphere Community Climate Model) and showed how inclusion of co-emitted halogens (27 Gg of HCl) resulted in a lengthening of the SO_2 lifetime, due to the further depletion of OH, and a corresponding delay in the formation of aerosols, giving better agreement between modelled and observed SO_2 burden and showing how co-emitted halogens could impact volcanic sulfur processing.

Tie and Brasseur (1995) utilised model calculations to show how background atmospheric chlorine loadings altered the ozone response to volcanic sulfur injections. In conditions typical of the pre-1980 period, the ozone column abundance was shown to increase after a large volcanic eruption. The increase in column abundance was the result of suppression of the NO_x-catalysed ozone loss cycle, which was driven by the sequestration of reactive nitrogen to its reservoir species via heterogeneous reactions on the surface of volcanic aerosol. The ozone response was shown to be independent of the magnitude of the eruption, as the heterogeneous conversion of active nitrogen to its reservoir was saturated. However, after 1980, higher background chlorine levels resulting from the anthropogenic emissions of chlorofluorocarbons, meant that the ozone response became negative in winter at mid

and high latitudes. The suppression of NO_x-catalysed ozone loss was counterbalanced by an increase in the ClO_x-catalysed ozone loss, resulting in a transition in the total column ozone response. Unlike in pre-industrial conditions, the ozone response was dependent on the eruption size as the heterogeneous conversion of chlorine species from reservoir to reactive was not saturated. Since then, a number of studies have investigated the impact of volcanic halogens on stratospheric ozone. Cadoux et al. (2015) petrologically determined chlorine and bromine degassing budgets for the Bronze Age (~1600 BCE) Santorini eruption and, using a halogen injection efficiency of 2%, input 36 Tg S, 13.5 Tg Cl and 0.02 Tg Br uniformly between the tropopause and 35 km in a pre-industrial background state within a 2D chemical transport model (CTM). They simulated ozone depletion lasting a decade with a peak global mean of 20-90% over the northern hemisphere. The molar ratio of HCl and SO_2 injected into the stratosphere ($HCl:SO_2$) in this study was 0.64, considerably larger than observations from MLS (<0.1) and ice core records of Mt. Mazama (<0.3). Klobas et al. (2017) also used a 2D CTM to study the impact that co-emission of volcanic halogens has on total column ozone in contemporary and future background states. They simulated hypothetical Pinatubo sized eruptions with a $HCl:SO_2$ of ~0.14 and reported global ozone depletion lasting ~2-3 years with a peak of 20%. These CTM studies used prescribed wind fields and, as a result, do not include the important interactive feedbacks of radiation and dynamics which alter the transport of tracers and thus the composition of the atmosphere. Ming et al. (2020) simulated explosive tropical eruptions in a chemistry-climate model which consisted of the UK Met Office Unified Model (UM) together with the United Kingdom Chemistry and Aerosol (UKCA) scheme, including the interactive stratospheric aerosol model GLOMAP-mode (Mann et al., 2010). They simulated 6 sets of experiments: low-SO_2 (10 Tg) and high-SO_2 (100 Tg) eruptions paired with no HCl, low-HCl (0.02 Tg) and high-HCl (2 Tg), and reported significant ozone depletion over both poles for at least four years in the high-SO_2 and high-HCl experiment. Brenna et al. (2019) used CESM1(WACCM) with prescribed volcanic aerosols and sea surface temperatures (SSTs) to simulate an average eruption of a Central American Volcanic Arc volcano in a pre-industrial background state, with a 10% halogen injection efficiency (2.5 Tg Cl, 9.5 Gg Br). They found ozone depletion of up to 20% globally for 10 years, with ozone hole conditions over the tropics and Antarctica. Consequently, UV radiation increases of >80% were simulated in the tropics, averaging to >40% for 2 years.

However, these studies did not investigate how volcanic halogens may interact with the sulfur aerosol life cycle and modulate volcanic forcing. Brenna et al. (2020) used the Community Earth System Model 2 (WACCM6) to investigate the coupling and feedback between volcanic aerosol, chemistry, radiation and climate pre-industrial background state. They investigate the combined effect of the sulfur (523 Tg S) and halogen (120 Tg Cl, 0.2 Tg Br) emissions of the Los Chocoyos super-eruption, assuming a 10% halogen injection efficiency resulting in a stratospheric $HCl:SO_2$ molar ratio ~0.4, on volcanic gases, ozone and surface UV. Compared to simulations with sulfur-only injections, they simulate a lower peak sulfate burden attributed to the delay in SO_2 oxidation but with the same total sulfur lifetime and aerosol effective radius. Thus, the co-emission of halogens results in a smaller radiative forcing; 20% lower compared to sulfur-only. Wade et al. (2020) compared HadGEM3-ES (Earth System configuration of the Hadley Centre Global Environment Model version 3) simulations of the 1257 Mt. Samalas eruption, utilising the halogen degassing estimates from Vidal et al. (2016) and stratospheric halogen injection efficiencies of 20% and 1%, with the available surface temperature proxies. Their results suggest it is unlikely

that 20% of degassed halogens reached the stratosphere, but smaller fractions gave good agreement with multi-proxy surface temperature records.

The aim of this study is to simulate hypothetical large- and very-large-sized eruptions, both with and without halogens, in a coupled chemistry-aerosol model in order to investigate how the co-emission of volcanic sulfur and halogens alters the evolution of volcanic aerosol, ozone, stratospheric composition, and the consequential radiative forcing and UV flux.

3.2 Data and Methods

3.2.1 Experimental Design

Our study utilises the HIST UKESM-AMIP time-slice experiments as described in Chapter 2. The HIST control simulation was run using the January 1995 initialisation file and climatologies calculated using data from the fully coupled UKESM1.0 historical runs produced for CMIP6 (Eyring et al., 2016) and averaged over the years 1990 to 2000. By averaging over a decade, the atmosphere-only simulations are forced with boundary conditions typical of the period but not a specific date within that decade. The fully coupled transient simulations had internally generated El Niño and La Niña cycles, however, averaging the SSTs over the 1990 to 2000 period resulted in a permanent neutral signal in the SST pattern (see Figure A1). The 1990s, and thus these time slices, were characterised by high background halogen levels due to anthropogenic emissions of chlorofluorocarbons (CFCs) throughout the preceding decade. The impacts of very-short-lived Bromine species are accounted for by adding a fixed contribution of 5 pptv into the CH_3Br surface concentration. The model was allowed to spin up for 15 years and the control was run for a further 20 years. The effect of explosive volcanic eruptions was investigated by running a series of 10-year volcanic perturbation simulations initialised from 6 different years in the control run to sample the variability in QBO states. Changes are plotted as the difference between the average of the 6 ensemble members and a climatology derived from the 20-year control run. Ensemble ranges are included as envelopes where appropriate. Cumulative forcings are calculated as the time-integrated forcing across the Earth's surface and represent the total energy loss (J) as a result of the volcanic eruption.

Volcanic effective radiative forcings (hereafter ERF*)* are calculated as differences (*Δ*) in the net top-of-atmosphere (TOA) radiative fluxes (*F*) between perturbed and control climatologies as follows:

$$ERF = \Delta F \qquad (Eq. 3.1)$$

Volcanic ERF is decomposed as described in Schmidt et al. (2018) and Ghan (2013), as follows:

$$ERF = \Delta(F - F_{clean}) + \Delta\left(F_{clean} - F_{clear,clean}\right) + \Delta F_{clear,clean} \qquad (Eq. 3.2)$$

$$= ERF_{ari} + ERF_{aci} + ERF_{clear,clean} \qquad (Eq. 3.3)$$

This decomposition is enabled by implementing extra calls to the radiation scheme as recommended by Ghan (2013) to obtain F_{clean} and $F_{clear,clean}$, where F_{clean} denotes a radiation flux diagnostic calculation without aerosol-radiation interactions but including aerosol-cloud interactions through microphysics, and $F_{clear,clean}$ denotes a radiation flux diagnostic calculation that ignores both aerosol-radiation and cloud-radiation interactions. Thus, $F - F_{clean}$, determines the impact of all aerosols and $\Delta(F - F_{clean})$ is an estimate of the forcing from volcanic aerosol-radiation interactions (ERF_{ari}). The second term $\Delta(F_{clean} - F_{clean,clear})$ represents the difference in the clean-sky cloud radiative forcing, and is an estimate of the aerosol-cloud interactions (ERF_{aci}) due to volcanic emissions. The third term, $ERF_{clear,clean}$ accounts for changes not directly due to aerosol or cloud interactions, largely the result of changes in surface albedo and atmospheric composition.

The volcanic emissions are prescribed by direct injection of SO_2, HCl and HBr into the stratosphere with a Gaussian vertical distribution centred on 21 km and a width of 2.1 km (10% of the height) (Aubry et al., 2019), lasting for 24 hours on July 1st. An injection altitude of 21 km was chosen as, allowing for lofting, this results in a volcanic plume altitude consistent with the 1991 eruption of Mt Pinatubo (Guo et al., 2004). The gases were injected in the tropics (5ºS latitude and 0º longitude) to represent a typical tropical explosive eruption (Newhall et al., 2018).

Since historical stratospheric volcanic SO_2 fluxes are variable and the volcanic flux of HCl and HBr into the stratosphere remains uncertain, we developed a simulation matrix that spans a range of possible explosive volcanic emissions, as outlined in Chapter 2. The four sets of experiments have one large SO_2 (10 Tg), and one very-large SO_2 (56 Tg) emission scenario both with (HIST_H10 and HIST_H56) and without halogens (HIST_S10 and HIST_S56), as shown in Table 3.1. These eruption sizes (10 and 56 Tg SO_2) are hypothetical, but they are comparable to a VEI 6 (e.g. 1991 Mt. Pinatubo) and VEI 7 (e.g. 1257 Mt. Samalas) eruption, representing 1-in-50-100-year and 1-in-500-1000-year events respectively (Newhall et al., 2018).

Scenario	SO_2 (Tg)	HCl (Tg)	HBr (Tg)	HCl:SO_2
HIST_S56	56	-	-	-
HIST_H56	56	15	0.086	0.47
HIST_S10	10	-	-	-
HIST_H10	10	1.5	0.0086	0.26

Table 3.1 Showing the eruption masses of SO_2, HCl and HBr in Tg for the four sets of experiments.

3.3 Results

3.3.1 Sulfur Microphysics and ERF_{ari}

Atmospheric burdens of volcanic sulfur species are summarised in Figure 3.1. As shown by Lurton et al. (2018), volcanic halogens deplete the hydroxyl radical (OH) via equation 3.4

$$HCl + OH \rightarrow Cl + H_2O \qquad \text{(Eq. 3.4)}$$

which limits the availability of OH for SO_2 oxidation, leading to slower destruction of volcanic SO_2 and an increase in SO_2 e-folding time of 21% and 40% in HIST_H10 and HIST_H56 compared to HIST_S10 and HIST_S56, respectively. As the rate of formation of sulfuric acid is decreased, we simulate a corresponding delay in the formation of sulfate aerosol and a reduction in the peak sulfate aerosol burden by 8% in both HIST_H10 and HIST_H56.

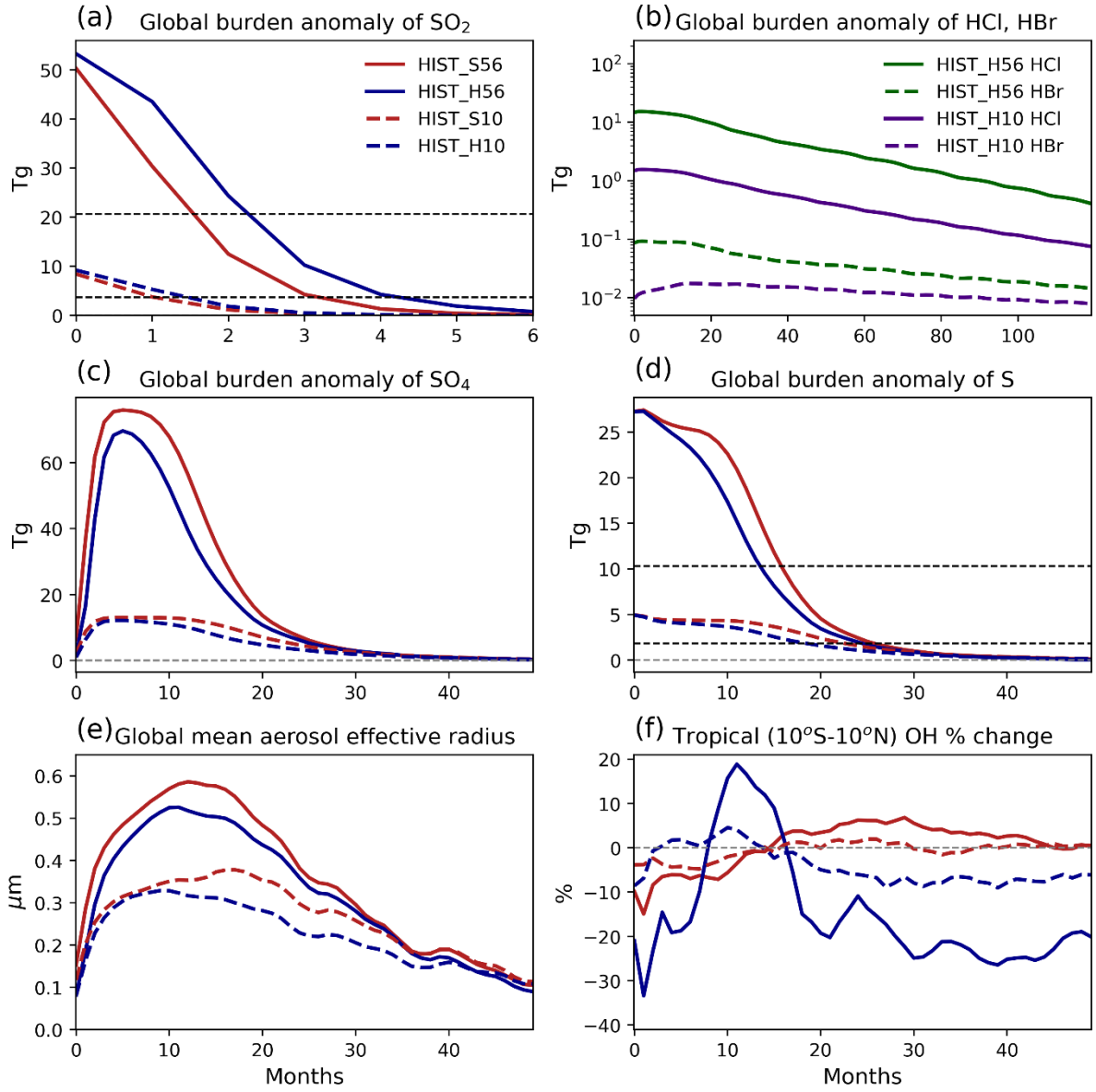

Figure 3.1 Evolution of sulfur, halogens, aerosol effective radius and OH for the HIST_S10, HIST_H10, HIST_S56 and HIST_H56 simulations relative to the control climatology. (a) Global SO_2 burden anomalies. (b) Global HCl and HBr burden anomalies on a log scale. (c) Global sulfate aerosol burden anomalies. (d) Global total sulfur burden anomalies. (e) Global mean aerosol effective radius, weighted by aerosol surface area density. (f) Tropical (10°N-10°S) stratospheric OH change (%). Dashed horizontal lines in panels (a) (b) and (d) represent the mass remaining after one e-folding time. Note the different axis scales.

Despite the slower rate of SO_2 oxidation, the co-emission of halogens reduces the e-folding lifetime of the sulfur burden to 17.3 and 11.7 months in HIST_H10 and HIST_H56, compared with 21.2 and 13.6 months in HIST_S10 and HIST_S56, a decrease of 18% and 14% respectively. This indicates that co-emission of halogens alters the rate at which sulfur is removed from the atmosphere. Significant differences in stratospheric temperature change are simulated between the sulfur-only and halogen simulations. In sulfur-only simulations, strong positive temperature anomalies (~3 K) due to sulfate aerosol absorption of infra-red radiation are simulated across the tropical stratosphere (Figure 3.2). This aerosol heating increases the vertical ascent (Figure A2) and lofts volcanic aerosol to altitudes higher than the initial injection height in the model. By contrast, co-emission of volcanic halogens results in significant stratospheric ozone depletion of 22-57% (see section 3.2) and, in turn, this results in large negative temperature anomalies (~ -3 K) over most of the lower and middle stratosphere (Figure 3.2). Ozone generates heat in the stratosphere by absorbing both incoming shortwave (SW) radiation from the Sun and by absorbing upwelling longwave (LW) radiation from the troposphere. Thus, decreasing stratospheric ozone results in stratospheric cooling, offsetting the volcanic aerosol heating and resulting in net stratospheric cooling. This stratospheric cooling decreases the vertical ascent in the tropics (Figure A2) and prevents volcanic sulfate aerosol being self-lofted in HIST_H10 and HIST_H56. The volcanic sulfate aerosol thus remains at significantly lower altitudes in HIST_H10 and HIST_H56 (~21-22 km) compared with HIST_S10 and HIST_S56 (~24-25 km) (Figure 3.2e,f). Lower altitude aerosol remains in a faster region of the Brewer-Dobson circulation (Figure A3) which results in faster transport to high latitudes and removal from the stratosphere (Figure 3.1d).

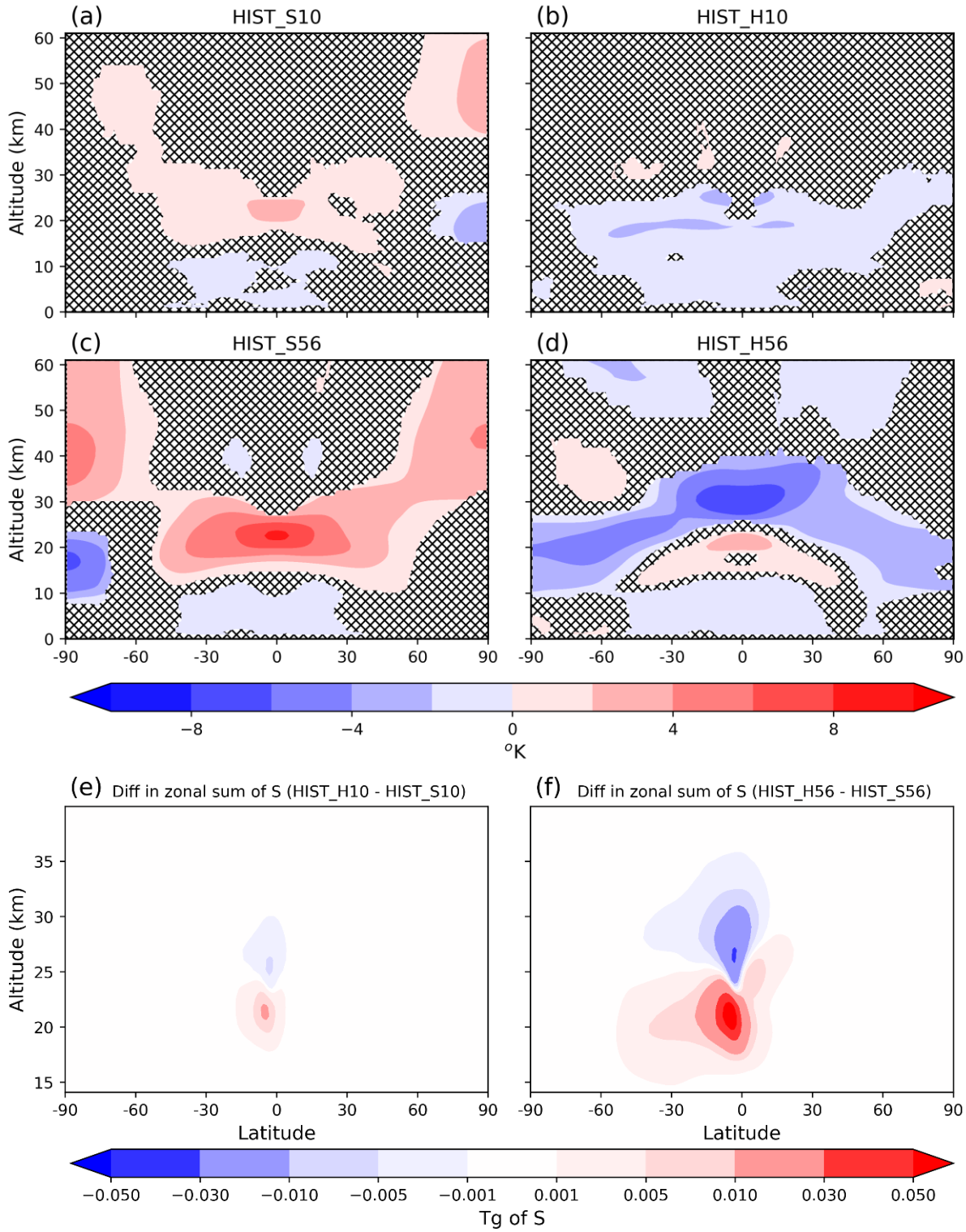

Figure 3.2 Zonal mean temperature anomaly (K) averaged over the first post-eruption year relative to the control climatology (a) HIST_S10, (b) HIST_H10, (c) HIST_S56, and (d) HIST_H56. Differences that are not significant at the 95% confidence interval according to a Mann–Whitney U test are indicated with hatches. Difference in zonal sum of total sulfur averaged over the first-year post-eruption (e) HIST_H10 – HIST_S10, and (f) HIST_H56 – HIST_S56.

The maximum global mean aerosol effective radii (R_{eff}) is 0.38 μm and 0.59 μm in HIST_S10 and HIST_S56, respectively. The maximum global mean R_{eff} simulated in HIST_S10 is similar to that derived from measurements following 1991 Pinatubo, with an estimate of 0.4 - 0.5 μm from balloon-borne measurements (Deshler et al., 1997) and 0.45 μm obtained from GloSSAC satellite observations (GloSSAC, version 1.1; Thomason et al., 2018). The shorter lifetime of sulfur in the atmosphere following HIST_H10 and HIST_H56 eruptions results in reduced aerosol growth and smaller aerosol R_{eff}. The peak global mean R_{eff} is ~15% and ~10% smaller in HIST_H10 and HIST_H56 compared to their equivalent SULF simulations (Figure 3.1e). This aerosol growth stunting effect is a direct result of the shorter sulfur lifetime, rapid spreading, and removal of aerosol. Volcanic sulfate aerosols grow through microphysical processes of condensation and coagulation (Kremser et al., 2016). The faster removal of sulfate aerosol in HIST_H10 and HIST_H56 reduces the growth via condensation and coagulation and results in smaller peak global mean aerosol R_{eff}. This theory is supported by Figure 3.3 which shows a scatter plot of the 3-year averaged global mean aerosol effective radius as a function of the global sulfur burden e-folding lifetime for each individual ensemble member, with a significant correlation within both 10 Tg (r=0.88) and 56 Tg (r=0.95) eruption ensembles. The positive correlation between these two variables holds only for each eruption size scenario. To a first order, the aerosol R_{eff} is determined by the magnitude of the volcanic sulfur injection. The larger SO_2 injection in HIST_H56 and HIST_S56 ensemble simulations leads to larger-sized sulfate aerosols, faster sedimentation and shorter removal time compared to HIST_H10 and HIST_S10 ensemble simulations. However, when we fix the mass of sulfur injected and compare sulfur-only and co-emission scenarios, we find that transport has a second-order effect. The faster removal of sulfate aerosol in HIST_H10 and HIST_H56 ensemble simulations leads to smaller-sized aerosol due to reduced opportunity for aerosol growth compared with HIST_S10 and HIST_S56, respectively.

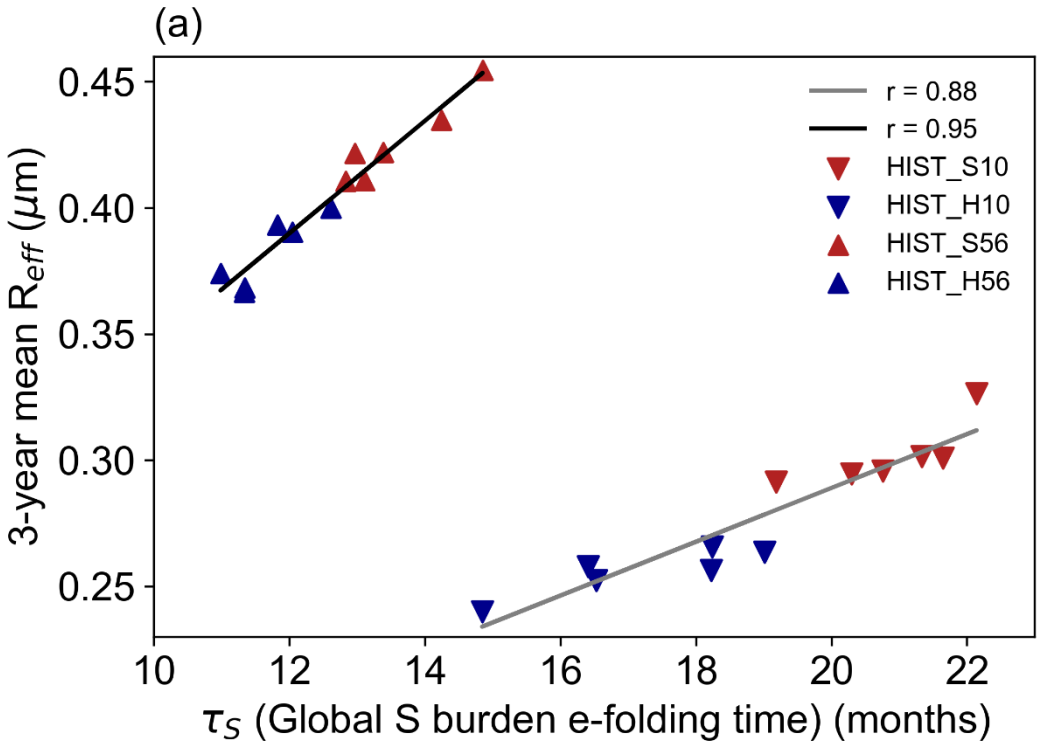

Figure 3.3 Global mean aerosol effective radius over the first 3 post-eruption years as a function of the global total sulfur e-folding time. Both plots have regression lines fitted with correlation coefficient (*r*) showing strong positive correlation.

The radiative impact of sulfate aerosols depends on the particle size (Timmreck et al., 2010). Using Mie scattering theory, Lacis (2015) found that the scattering cross section per unit mass is largest for sulfate aerosol with an effective radius of ~0.20 μm. The smaller aerosol R_{eff} in HIST_H10 and HIST_H56, compared to HIST_S10 and HIST_S56, is closer to 0.20 μm and results in more efficient scattering of SW radiation per unit mass (Timmreck et al., 2010). Therefore, we simulate 11% and 22% higher peak global mean SAOD anomalies at 550 nm in HIST_H10 and HIST_H56 than their equivalent sulfur-only simulations (Figure 3.4), despite having a 14% and 9% smaller peak aerosol burden. Correspondingly, we simulate an 8% and 6% increase in the peak global mean ERF_{ari} in HIST_H10 and HIST_H56 compared to HIST_S10 and HIST_S56 (Figure 3.4), driven by a 14% and 11% increase in peak global mean SW forcing (Figure A4). The SAOD and ERF_{ari} anomalies are a balance between the offsetting effects of smaller aerosol and shorter lifetime which result in a net-zero impact on cumulative ERF_{ari} despite a significant increase in the peak global mean ERF_{ari} (Figure A5).

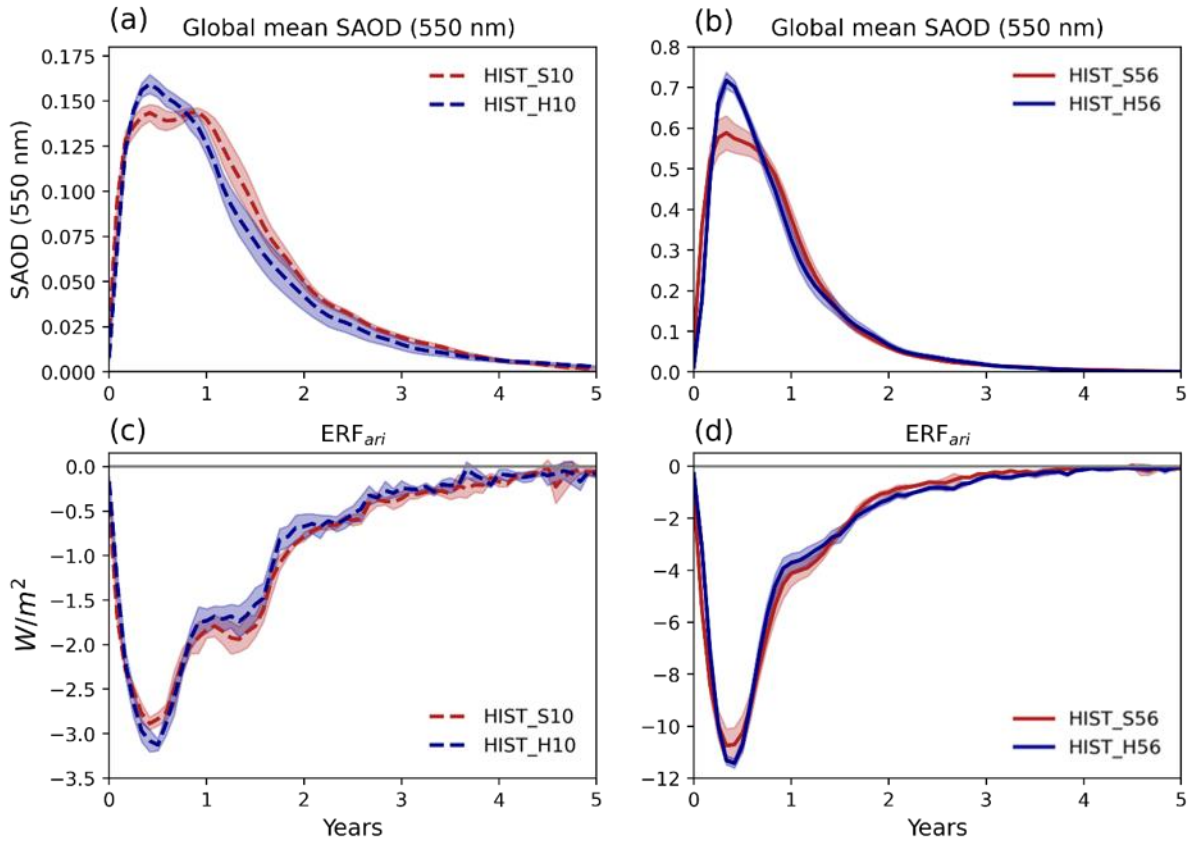

Figure 3.4 Global mean evolution of the stratospheric aerosol optical depth anomaly at 550nm, (a) HIST_S10 and HIST_H10, (b) HIST_S56 and HIST_H56. Global mean evolution of top-of-atmosphere global mean $ERF_{ari,}$ (c) HIST_S10 and HIST_H10, (d) HIST_S56 and HIST_H56. Shading represents the ensemble range.

3.3.2 Composition Changes and Resulting $ERF_{clear,clean}$

Co-emission of volcanic sulfur and halogens causes significant perturbations to the chemistry of the stratosphere beyond the depletion of OH in HIST_H10 and HIST_H56 mentioned in section 3.1. Stratospheric methane, stratospheric water vapour (SWV), and, in particular, stratospheric ozone are all impacted.

In sulfur-only simulations, we simulate a modest reduction in global mean ozone column, -9 DU (-3.9%) in HIST_S10 and -15 DU (-6.6%) in HIST_S56 (Figure 3.5a,c). This ozone depletion is catalysed by halogen radicals activated from background halogens on the surface of volcanic aerosol. We also simulate a redistribution of tropical ozone, with decreases of <0.5 and <2 ppmv between 23 and 28 km and a symmetrical increase in zonal mean tropical ozone above in HIST_S10 and HIST_S56 respectively (Figure 3.6a,c). This tropical ozone dipole pattern is mostly attributed to volcanic heating. Volcanic heating by the aerosol increases the vertical ascent and brings ozone up from below enhancing the local mixing ratio. In simulations with co-emitted halogens we simulate more dramatic ozone depletions; HIST_H10 resulted in a peak global mean ozone reduction of 65 DU (-22%) 1-2 years after the eruption followed by a gradual recovery over the next 3-4 years (Figure 3.5d). HIST_H56 resulted in a peak global mean ozone reduction of 175 DU (-57%) 1-2 years after the eruption followed by a gradual

recovery the remainder of the 10-year simulation, with an average reduction of 82 DU (-27%) over the 10-year simulation (Figure 3.5b).

Volcanic halogen-catalysed ozone depletion is simulated across all latitudes, but the largest magnitude changes in HIST_H10 (-40%) and HIST_H56 (-80%) were found within the aerosol cloud and the polar regions, where the co-emitted halogens are activated on aerosol surfaces and PSCs respectively (Figure 3.5). Ozone depletion predominantly occurs in the tropics between 25 and 30 km in the first post-eruption year, with depletion maxima of -3.5 ppmv and -6 ppmv in HIST_H10 and HIST_H56 respectively (Figure 3.6). By year three, the ozone depletion shows a similar bimodal altitude distribution in the stratosphere similar to that found in Brenna et al. (2020), with depletion maxima both in the lower (20 km) and upper (40km) stratosphere. As the volcanic SO_2 and halogens were introduced into the stratosphere just south of the Equator, they are predominantly dispersed into the southern hemisphere (Figure A6), leading to larger ozone depletions compared with the northern hemisphere. In both HIST_H10 and HIST_H56 tropical ozone was found to recover first with significant depletions recurring during the winter in the polar regions for the remainder of the simulation.

The simulated changes in stratospheric heating following sulfur-only and co-emission eruption scenarios affect the dynamical response of the upper atmosphere, for example, the strength of the Arctic and Antarctic polar vortices (see Figure A7) (Robock, 2000; Toohey et al., 2014). In HIST_S10 and HIST_S56, the positive stratospheric temperature anomalies in the tropics lead to an increased meridional temperature gradient. As a result, we simulate a strengthening of the polar vortex (defined as the mean zonal wind speed at the vortex edge, between 55º - 65º latitude and 1 to 30 hPa) in both the Arctic and Antarctic in the first post-eruption winter. In contrast, the negative stratospheric temperature anomalies in HIST_H10 and HIST_H56, lead to a decreased meridional temperature gradient and a weakening of the polar vortex. In HIST_H10 we simulate significant weakening of the polar vortex in the first two post-eruption winters in the Arctic, and the first and third post-eruption winter at the Antarctic. In HIST_H56, we simulate significant weakening of the polar vortex for 3-4 years at both poles. Polar vortex strength is an important driver of ozone depletion, with stronger polar vortexes leading to enhanced ozone depletion (Solomon, 1999; Zuev and Savelieva, 2019). Lawrence et al. (2020) linked an unusually strong Arctic polar vortex with the record-breaking ozone loss observed in the 2019/2020 Arctic winter. As such, the strengthening of the polar vortices simulated in sulfur-only simulations may intensify ozone depletion in the first post-eruption winters in both the Arctic and Antarctic. Furthermore, the weakening of the polar vortices simulated in co-emission scenarios may dampen the ozone response in both the Arctic and Antarctic. In addition, the simulated changes in polar vortex strength may have important consequences for the North Atlantic Oscillation and Southern Annular Mode (Driscoll et al., 2012; Kwon et al., 2020).

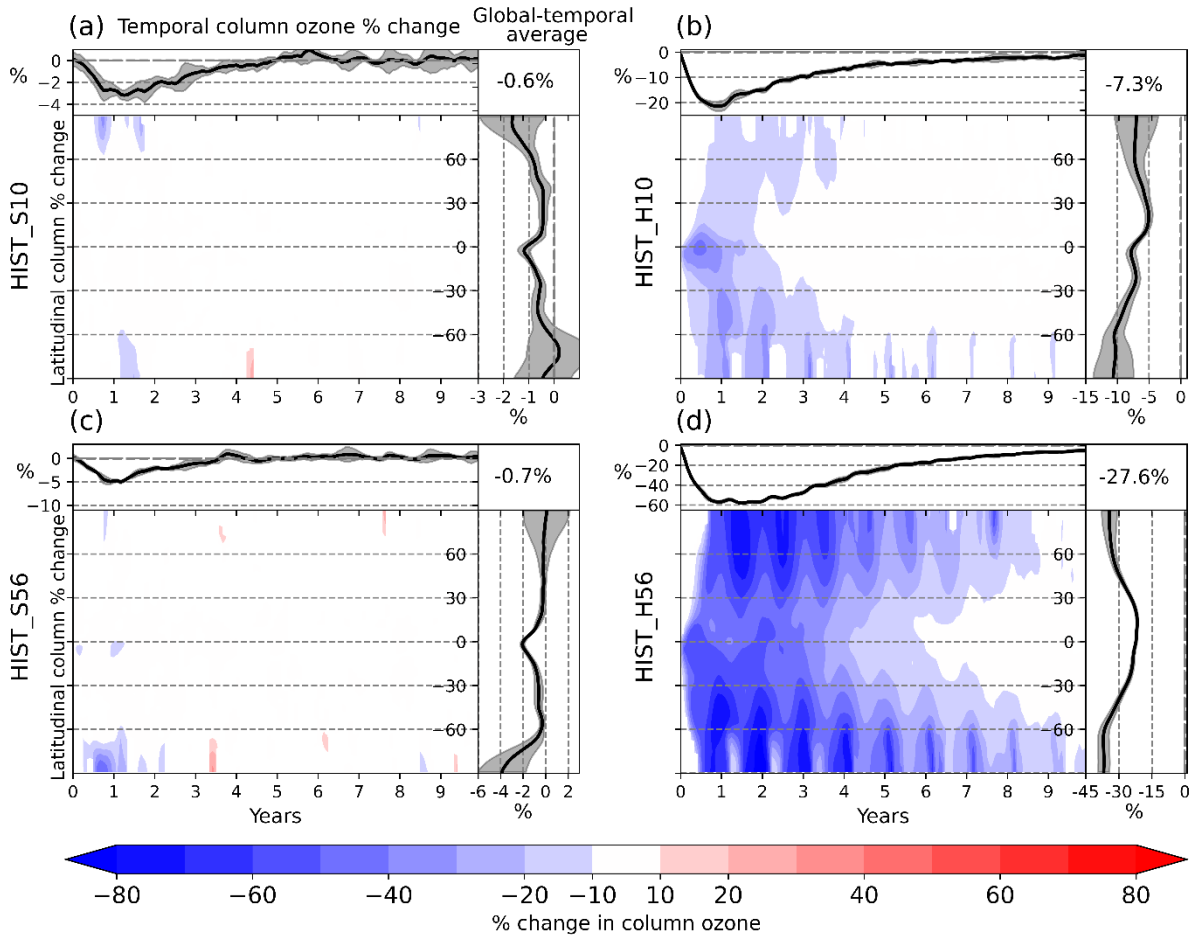

Figure 3.5 Ozone percentage difference in (a) HIST_S10, (b) HIST_H10, (c) HIST_S56, and (d) HIST_H56. Global mean total column ozone anomalies are traced as a function of time at the top of each panel. Temporal-mean ozone anomalies are traced on the right; note the different scales. Global-temporal mean anomalies are enumerated in the top right. Red colours indicate total column ozone enhancement, and blue colours indicate total column ozone depletion. Grey shaded areas represent the ensemble range.

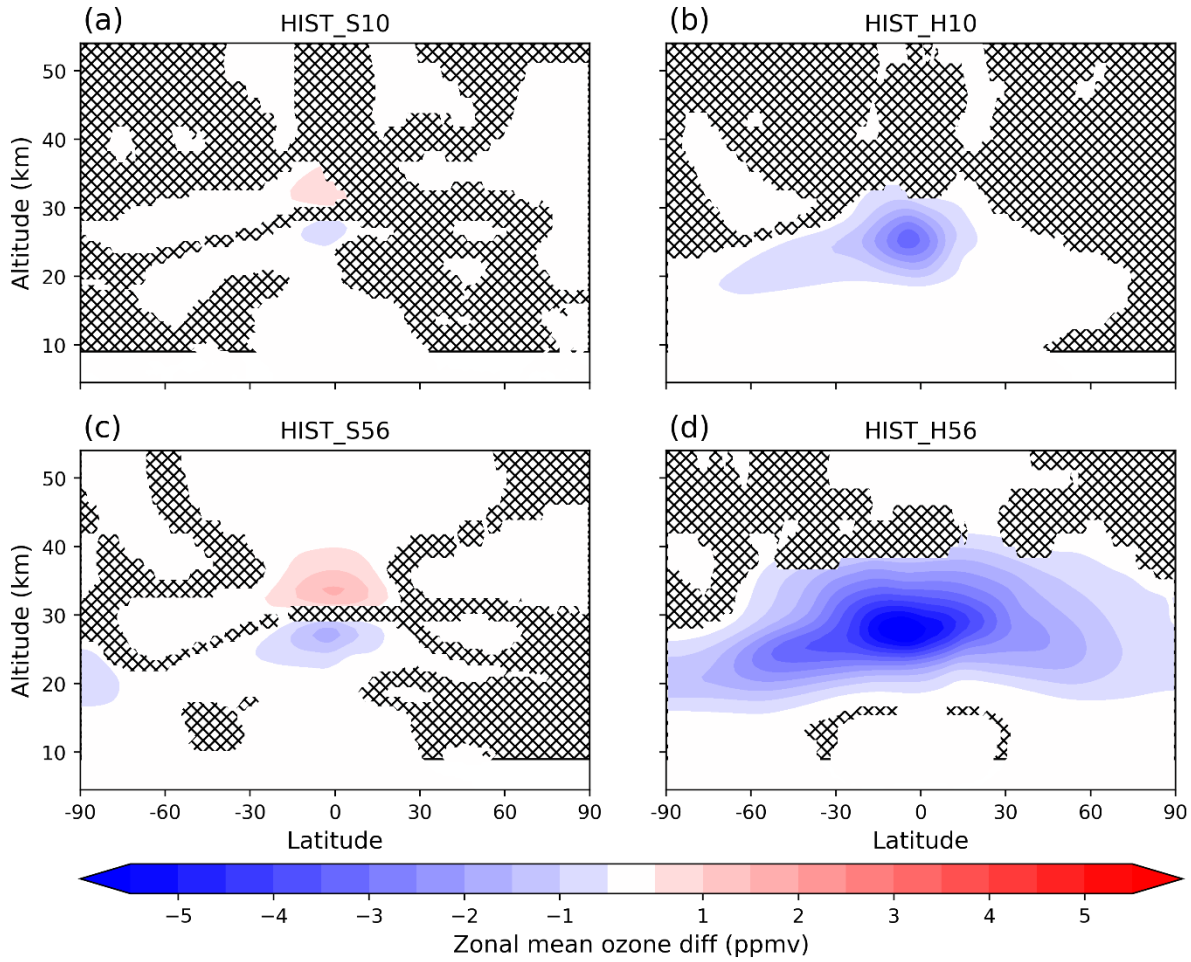

Figure 3.6 Zonal mean ozone anomaly (ppmv) averaged over the first post-eruption year relative to the control climatology, (a) HIST_S10, (b) HIST_H10, (c) HIST_S56, and (d) HIST_H56. Red colours indicate ozone enhancement, and blue colours indicate ozone depletion. Anomalies that are not significant at the 95% confidence interval according to a Mann–Whitney U test are indicated with hatches.

Stratospheric water vapour (SWV) and stratospheric methane are linked. SWV has two main sources: transport from the troposphere and chemical production from methane (Löffler et al., 2016). By contrast, stratospheric methane's only source is transport from the tropics, and it is destroyed by OH (forming SWV) and reaction with halogens via equation 3.5.

$$Cl + CH_4 \rightarrow HCl + CH_3 \qquad \text{(Eq. 3.5)}$$

Following sulfur-only eruptions we simulate small enhancements in SWV and stratospheric methane (Figure 3.8). HIST_S10 and HIST_S56 result in a peak global stratospheric mean increase in SWV of 0.4 ppmv (+7%) and 1.1 ppmv (+17%) and a 10 ppbv (0.6%) and 30 ppbv (1.8%) increase in stratospheric methane, respectively. Perturbations to SWV and stratospheric methane peak 2-3 years after the eruption and recover within 7 years. The increase in stratospheric methane following sulfur-only eruptions is in broad agreement with both Loffler (2015), who showed stratospheric methane mixing ratios increased by ~5% following simulations of El Chichón and 15-20% following the larger Mt Pinatubo eruption, and Kilian et al. (2020) who reported a 10% increase in CH_4

between 40 and 10 hPa, also following simulations of Pinatubo. Kilian et al. (2020) suggested that this was due to enhanced vertical ascent as a result of aerosol heating, lifting relatively methane-rich air from the lower stratosphere into the upper levels. As Kilian et al. (2020) simulated an increase in stratospheric CH_4 burden, they suggested that the lofting of methane must also coincide with an increase in the stratospheric methane lifetime but did not calculate this. In HIST_S10 and HIST_S56 of this work, we simulate an increase in tropical vertical ascent (shown at 50 hPa in Figure A2), however, we simulate a coinciding reduction in the stratospheric methane lifetime, driven by an increase in methane oxidation by OH and Cl. (Figure A8). This suggests that the increased stratospheric methane burden following sulfur-only eruptions HIST_S10 and HIST_S56 is not due to a lengthening of the stratospheric methane lifetime and, instead, is likely due to increased transport of methane across the tropopause from the methane-rich troposphere as a result of increased vertical ascent in the stratosphere (Figure A2). Due to the model set-up employed in this study we were unable to diagnose this any further.

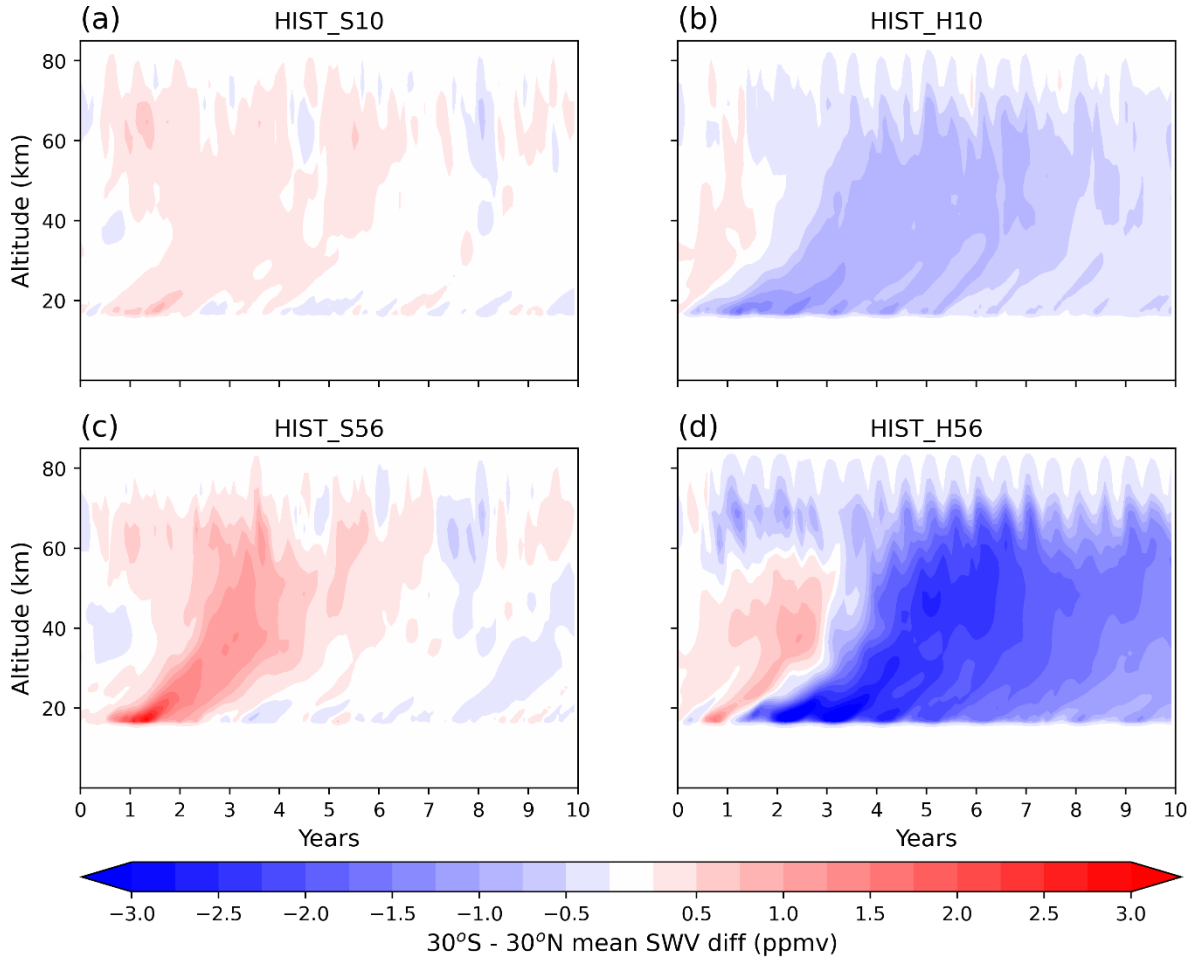

Figure 3.7 The 30°S - 30°N mean stratospheric water vapour anomalies (ppmv) relative to the control climatology as a function of altitude and time, (a) HIST_S10, (b) HIST_H10, (c) HIST_S56, and (d) HIST_H56. Red colours indicate SWV enhancement, and blue colours indicate column SWV depletion.

The simulated changes in methane are small in comparison to the SWV changes across all simulations and can only account for a fraction of the SWV change. The dominant driver of SWV change is the amount of water vapour entering the stratosphere through the tropical tropopause cold point (Löffler et al., 2016). Following both

HIST_S10 and HIST_S56, volcanic aerosol results in warming of the tropical tropopause cold point leading to an increase in vertical ascent (Figure A2) and a weakening of the tropical tropopause cold trap dehydration effect, increasing the transport of water vapour into the stratosphere (Figure 3.8) (Loffler et al., 2016). Elevated SWV is seen to initiate at the tropical troposphere before propagating higher into the stratosphere (Figure 3.7a,c).

Unlike in sulfur-only eruptions, following eruptions with co-emitted halogens we simulate a reduction in SWV and stratospheric methane (Figure 3.8). HIST_H10 and HIST_H56 result in peak global stratospheric mean stratospheric methane reductions of 37 ppbv (-3%) and 214 ppbv (-18%) respectively 2 years after the eruption. In HIST_H10 the stratospheric methane perturbation returns to the background levels by the fourth year whereas in HIST_H56 the perturbation remains below zero for between 7 and 8 years. Co-emission of halogens results in enhanced destruction of methane by chlorine via Eq. 3.5 resulting in the significant decrease in the HIST_H10 and HIST_H56 stratospheric methane levels.

HIST_H10 and HIST_H56 result in peak SWV reductions of 1.0 ppmv (-16%) and 2.3 ppmv (-36%), respectively, 3-4 years after the eruption followed by a gradual recovery. In HIST_H10 SWV perturbation levels return to the background levels within 7 years whereas in HIST_H56 the perturbation does not fully recover within the 10-year duration of the simulation. Just as was the case following sulfur-only eruptions, the dominant driver of SWV changes is the amount of water vapour entering the stratosphere via the tropical tropopause cold point. In HIST_H10 and HIST_H56, the process is the same but in the opposite sense. Cooling in the tropical tropopause vicinity increases the efficiency of the tropical cold trap dehydration effect and reduces the amount of water vapour being brought up from the troposphere (Figure 3.8) (Löffler et al., 2016). The negative SWV anomalies can be seen to initiate at the troposphere before propagating higher into the stratosphere (Figure 3.7b,d)

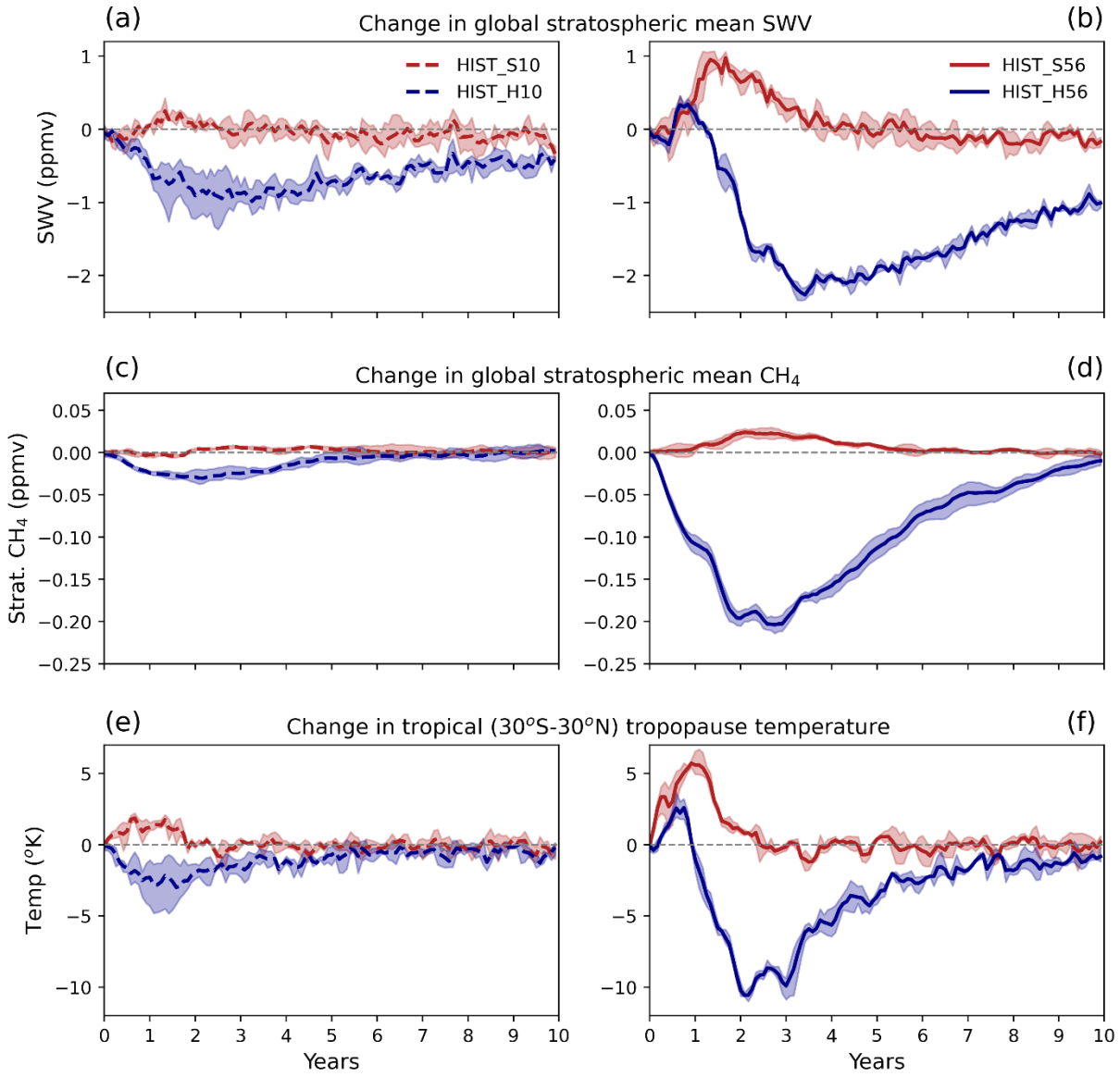

Figure 3.8 Evolution of global stratospheric mean water vapour anomalies (ppmv) in HIST_S10 and HIST_H10 (a), and HIST_S56 and HIST_H56 (b). Evolution of global stratospheric methane anomalies (ppmv) in HIST_S10 and HIST_H10 (c), and HIST_S56 and HIST_H56 (d). Evolution of tropical tropopause cold trap temperature anomaly averaged over 30°S–30°N and 15-20 km in HIST_S10 and HIST_H10 (e), and HIST_S56 and HIST_H56 (f). Shading represents the ensemble range.

Using the forcing diagnosis outlined in Schmidt et al. (2018) and Ghan (2013), we can isolate the radiative forcing due to atmospheric composition and surface albedo changes, $ERF_{clear,clean}$. As surface temperature and sea ice were prescribed, surface albedo changes were small, meaning that $ERF_{clear,clean}$ predominantly represents the forcing from atmospheric composition changes (Figure 3.9 c, d). HIST_H10 results in a peak global mean $ERF_{clear,clean}$ of -1.3 Wm^{-2} one year after the eruption, which is more than double the $ERF_{clear,clean}$ of HIST_S10. The forcing recovers gradually over the next 6-7 years and results in a cumulative $ERF_{clear,clean}$ that is 5 times greater than HIST_S10 (Figure A2d). Similarly, HIST_H56 results in a peak global mean $ERF_{clear,clean}$ of -2.1 Wm^{-2} 1-2 years after the eruption, which is double the peak global mean forcing of HIST_S56. The $ERF_{clear,clean}$ anomaly in

HIST_H56 is more persistent and remains -0.5 Wm^{-2} below zero at the end of the simulation, resulting in a cumulative $ERF_{clear,clean}$ that is 10 times greater than HIST_S56 (Figure A2c).

To calculate the resulting radiative forcing from the ozone changes simulated in this work, we use the ozone radiative kernel (O_3 RK) technique based on Rap et al. (2015) and updated for the whole atmosphere as outlined in Iglesias-Suarez et al. (2018) (Figure A9), see Section 2.4. Using the O_3 RK, we are able to show that the stratospheric ozone change is the dominant driver of the $ERF_{clear,clean}$ accounting for ~75% of the $ERF_{clear,clean}$ (Figure 3.9a,b). The remainder is likely predominantly due to SWV changes with a small contribution from stratospheric methane changes. The latitudinal pattern of ozone radiative forcing reflects the locations of the ozone change, with largest the forcing at the poles, as shown in Figure A10 and A11.

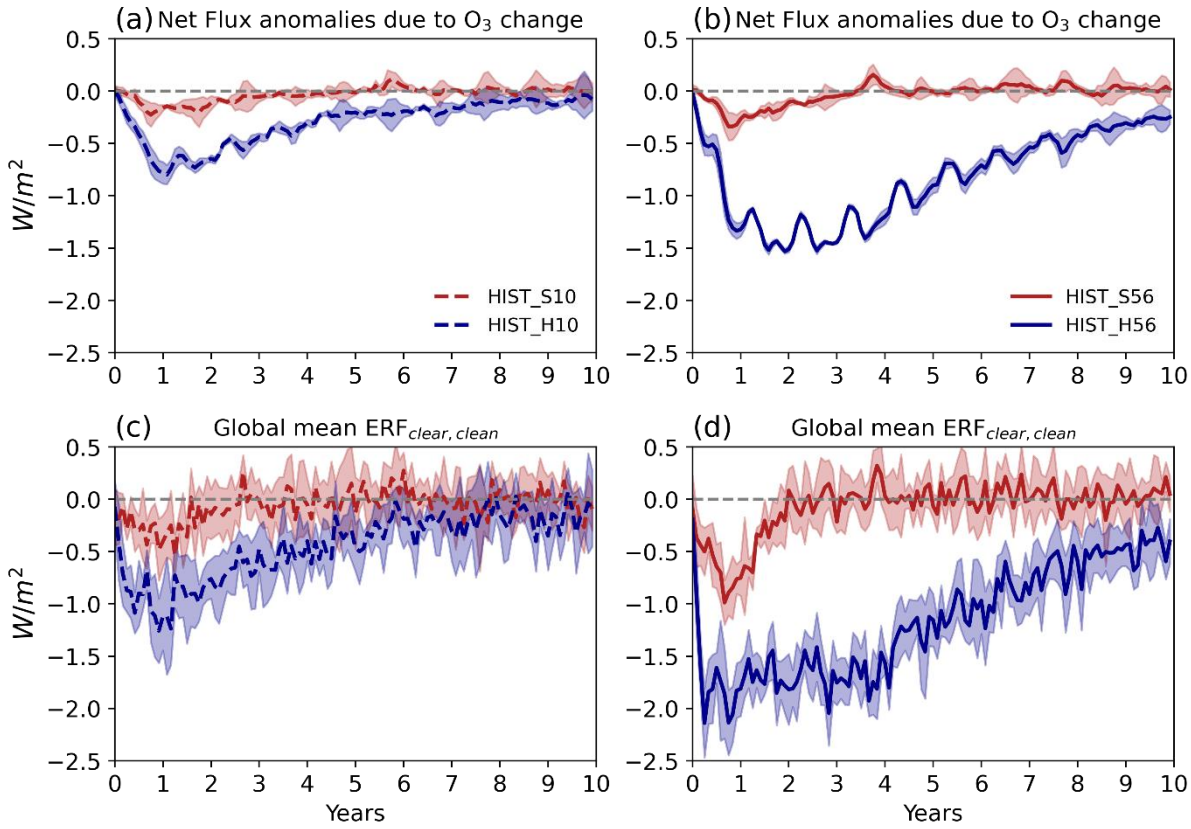

Figure 3.9 Evolution of global mean top-of-atmosphere net flux anomalies due to stratospheric O_3 change estimated from the ozone radiative kernel from Rap et al. (2015) in HIST_S10 and HIST_H10 (a), HIST_S56 and HIST_H56 (b). Evolution of the global mean top-of-atmosphere compositional forcing ($ERF_{clear,clean}$) in HIST_S10 and HIST_H10 (c), HIST_S56 and HIST_H56 (d). Ozone changes make up ~75% of the $ERF_{clear,clean}$. Shading represents the ensemble range.

3.4 Discussion

Using the Ghan (2013) method for diagnosing forcing, we have shown that the co-emission of volcanic halogens results in larger peak global mean ERF_{ari} and $ERF_{clear,clean}$. Taking these in combination, the co-emission of halogens results in substantial increases in the peak global mean volcanic ERF to -4.1 Wm^{-2} (+30%) in HIST_H10,

and -14.1 Wm^{-2} (+24%) in HIST_H56 (Figure 3.10a,b), as well as increases in the total cumulative forcing to -1.37 $x10^{23}$ J (+60%) in HIST_H10 and -3.86$x10^{23}$ J (+100%) in HIST_H56 compared to HIST_S10 and HIST_S56 (Figure A5e,f). In both HIST_H10 and HIST_H56, ~25% of the additional peak global mean volcanic ERF simulated compared to HIST_S10 and HIST_S56 respectively comes from the changes to the ERF_{ari}, with the remainder coming from changes to $ERF_{clear,clean}$.

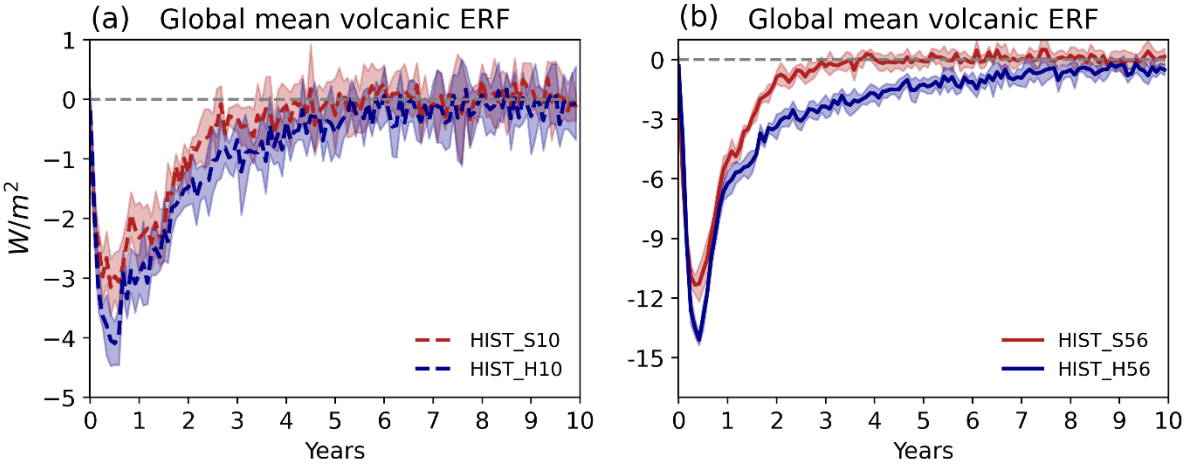

Figure 3.10 Evolution of the global mean top-of-atmosphere total volcanic forcing (ERF*)* relative to the control climatology in HIST_S10 and HIST_H10 (a), HIST_S56 and HIST_H56 (b). Volcanic ERF is the sum of ERF_{ari}, ERF_{acii} and $ERF_{clear,clean}$. Shading represents the ensemble range.

Comparing the perturbations in HIST_H56 to HIST_H10, we find that increasing the volcanic halogen flux by 10 times only results in a ~2.5 times-larger global ozone response and, as $ERF_{clear,clean}$ is dominated by changes in stratospheric ozone, only a ~2 times-larger $ERF_{clear,clean}$. This suggests that there is a saturation in the ozone-depleting potential of co-emitted volcanic halogens. Plotting the total column ozone percentage change against the magnitude of injected halogens expressed as equivalent effective stratospheric chlorine (EESC is a measure of the ozone destruction potential; $EESC=[Cl]_{added\ to\ stratosphere} + 60 \times [Br]_{added\ to\ stratosphere}$;(Cadoux et al., 2015; Montzka et al., 2011; Sinnhuber et al., 2009)) from this study and a number of previous studies, we find an exponential decay curve describes this relationship: as the EESC increases the efficiency of volcanic halogen ozone depletion decreases (Figure 3.11). This relationship suggests that total column ozone is most sensitive to volcanic halogens when the additional EESC is < 20 Tg, and that increasing the volcanic EESC flux beyond 60 Tg has little impact on total column ozone change. This analysis spans simulations with very different background EESC and total column ozone values. Wade et al. (2020), Brenna et al. (2019), and Brenna et al. (2020) simulations are all in a pre-industrial atmosphere background states with low background chlorine levels, whereas, the background chlorine levels in HIST_H10 and HIST_H56 are significantly higher and with lower initial ozone columns. This relationship suggests that the peak global mean ozone loss (%) is dependent more on the volcanically injected EESC than the background chlorine and initial ozone columns. In other words, this relationship is time-independent and this exponential decay curve can be used to estimate the peak global mean ozone loss for an eruption in any climate state, including future eruptions where the background EESC will have

decayed back to pre-1980s levels. This will be especially useful for rapid estimates of ozone change as new or better-constrained volcanic halogen data becomes available.

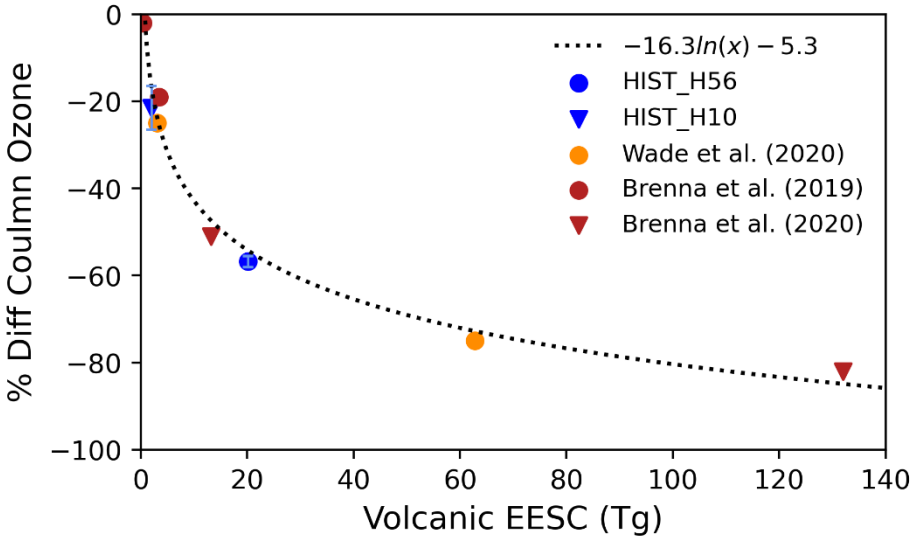

Figure 3.11 Relationship between volcanically emitted equivalent effective stratospheric chlorine (Tg) and peak global mean % difference in total column ozone. Blue: HIST_H10 and HIST_H56 ensemble mean and range. Orange: Wade et al. (2020) ensemble mean. Red: Brenna et al. (2019) and Brenna et al. (2020) ensemble mean.

The implications of ozone depletion in HIST_H10 and HIST_H56 go further than enhancing the $ERF_{clear,clean}$. High anthropogenic fluxes of halocarbons into the atmosphere during the 1980s caused background chlorine levels to be elevated during the 1990s and an ozone hole is simulated to develop in the control simulation over the southern hemisphere polar regions (Figure A12). Using the definition for ozone hole conditions as <220 DU, we simulate enhanced ozone hole conditions following both HIST_H10 and HIST_H56 eruptions (Figure 3.12). In HIST_H10, ozone hole conditions are simulated in the tropics for one year after the eruption, and a deepening of ozone hole conditions is seen in northern hemisphere polar regions for two winters and in the southern hemisphere polar regions for four winters. In HIST_H56, we simulate ozone hole conditions globally for 5 years, continuing for a further three winters in the northern hemisphere polar regions and six winters in the southern hemisphere polar regions

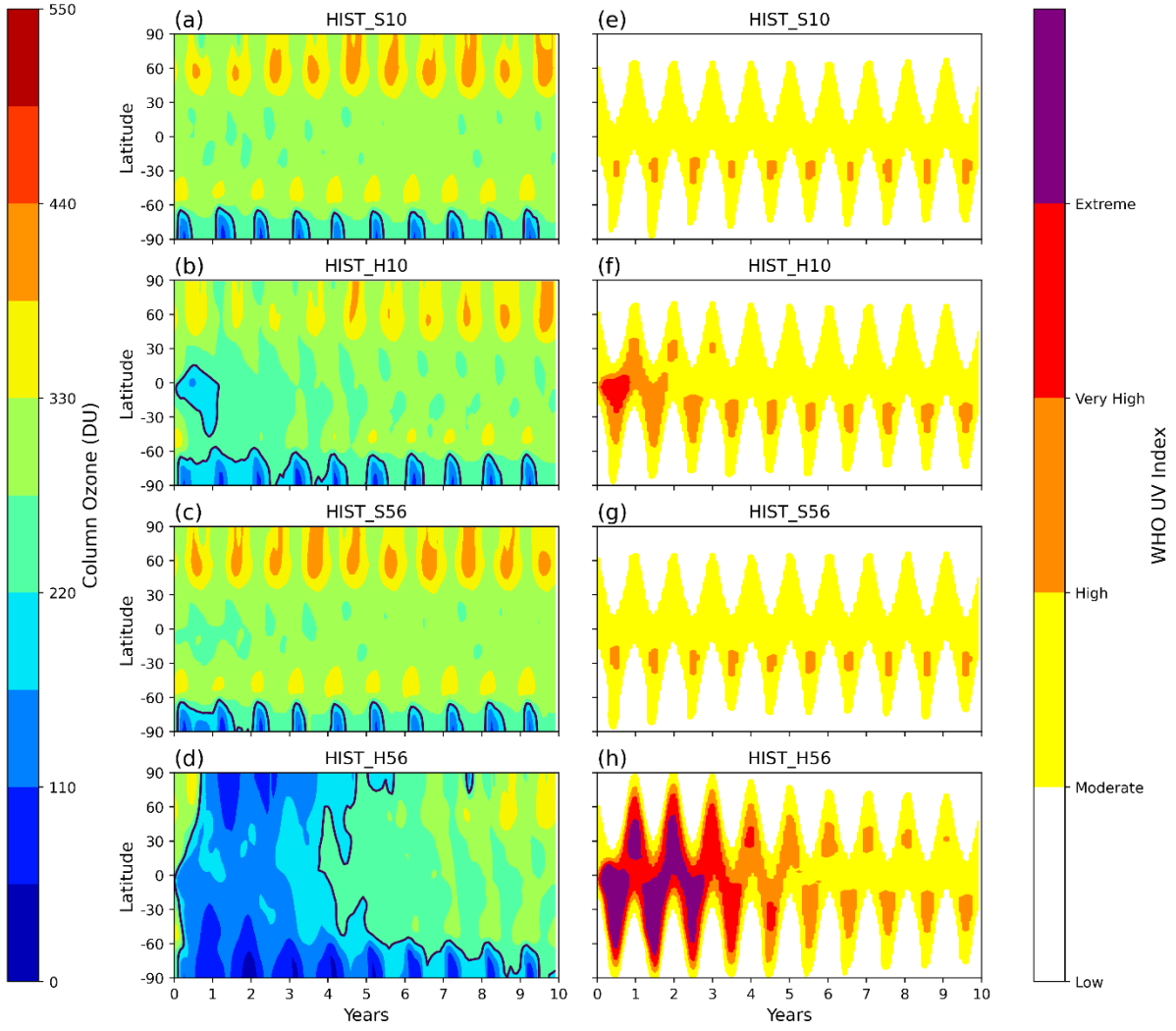

Figure 3.12 Zonal mean total column ozone (a) HIST_S10, (b) HIST_H10, (c) HIST_S56, (d) HIST_H56. Ozone hole conditions are simulated when the total column ozone <220 DU (black solid line). Zonal mean surface UV exposure due to total column ozone changes (WHO UV Index) (e) HIST_S10, (f) HIST_H10, (g) HIST_S56, (h) HIST_H56.

Total column ozone depletion on this scale would dramatically increase the flux of harmful UV to the surface, which could cause DNA damage to animals and plants, and increase the occurrences of skin cancers, eye damage and immune system deficiencies among the population (WHO, 1994). Climate modelling and environmental proxies showed that ozone depletion as a result of halogen degassing during the emplacement of Siberian Traps flood basalts led to ozone depletion that stressed ecosystems and caused DNA mutations which may have contributed to the end-Permian mass extinction (Black et al., 2014). A simple heuristic relating total column ozone to clear-sky surface UV index is given by:

$$UV\ Index\ =\ 12.5\mu_o^{2.42}(\Omega/300)^{-1.23} \qquad \text{(Eq. 3.6)}$$

as defined in (Madronich, 2007), where μ_o is the cosine of the solar zenith angle and Ω is the total vertical ozone column in Dobson units. The monthly mean average UV index coloured by World Health Organization categories (Low [0 to 2], Medium [3 to 5], High [6 to 7], Very High [8 to 10], and Extreme [11+]) is shown in Figure 3.12. This shows that in the HIST_H56 scenario, on average 'Very High' or 'Extreme' UV levels would be expected all day for much of the globe in the three to four summers after the eruption, with noon values being even higher. The change in surface UV levels are shown in Figure A13. Living under such a high UV exposure would cause immediate immunosuppression, epidemic outbreaks, increases in the occurrences of eye damage and, in the longer term, skin cancers among the population living between the Equator and the mid-latitudes, which equates to >95% of the global population. The assessment of surface UV changes is made more challenging by the presence of volcanic aerosols, which also scatter UV radiation. However, damaging UVB and UVC radiation will not be scattered effectively by larger aerosol size distributions and volcanic aerosol levels reduce rapidly after peaking in the first post-eruption year.

Whilst we have been able to calculate the composition and climate impacts of the co-emission of halogens and SO_2 from volcanic eruptions, these calculations are not without some uncertainty. Recent studies carried out as part of the Volcanic Forcings Model Intercomparison Project (VolMIP) showed large model response disparities in simulations of SO_2-only volcanic eruptions (Clyne et al., 2020), but models have been shown to capture the effects of ozone-depleting substances on stratospheric ozone well (WMO (World Meteorological Organization), 2014). As outlined in the introduction, the major uncertainty in this work is the stratospheric injection of HCl and HBr from explosive volcanic eruptions, which is highly variable and depends on both the geochemistry of the volcano and the degree of scavenging determined by the prevailing atmospheric conditions during the eruption. It is clear, however, that significant stratospheric halogen fluxes occur after some explosive volcanic eruptions.

Although this work has focused on simulations of explosive volcanic eruptions in a background climate representative of the 1990s, Figure 3.11 demonstrates the simulated ozone depletion predominantly depends on the volcanic halogen injection size and not the background atmospheric state. Using the relationship outlined in Figure 3.11, we can estimate the peak global mean ozone percentage loss for any size of volcanic halogen injection, past or present. We are currently investigating the impacts that plausible future background atmospheric states (such as different greenhouse gas concentrations, background halogen levels and stratospheric temperatures) may have on the simulated ozone response and volcanic ERF due to co-emitted sulfur and halogen volcanic emissions.

In addition to the co-emission of volcanic halogens, there is also scope to model the co-emission of volcanic water vapour and ash directly into the stratosphere. Legrande et al. (2016) provide a mechanism explaining how SWV originating from volcanic eruptions may alter the chemistry of the stratosphere and the nucleation rate of sulfate aerosol and suggest that this may severely alter the climate impacts. In addition, SWV proved to be an amplifying feedback in simulations in this work and it would be interesting to see how co-emission of water vapour, halogens and sulfur would further alter the volcanic forcing in simulations of explosive volcanic eruptions. Zhu et al. (2020) showed the importance of including volcanic ash injections in climate simulations. When heterogeneous chemistry on ash particles was included, they found that 43% more volcanic sulfur was removed from the stratosphere in

the first 2 months. Volcanic ash is also likely to alter the lifetime, activation, and impact of co-emitted volcanic halogens in climate simulations.

3.5 Conclusions

In this study we utilised UKESM-AMIP simulations of volcanic eruptions to investigate how the co-emission of volcanic halogens and sulfur alters the effective radiative forcing (ERF) of explosive volcanic eruptions under atmospheric conditions representative of the mid-1990s. As the volcanic flux of HCl and HBr into the stratosphere remains uncertain, a range of plausible explosive volcanic emissions scenarios based on petrological degassing estimates, satellite observations and volcanic plume modelling were simulated. The four sets of experiments included one large SO_2 (10 Tg), and one very-large SO_2 (56Tg) emission scenario, both with (HIST_H10 and HIST_H56) and without halogens (HIST_S10 and HIST_S56), each with an ensemble size of 6 sampling different QBO states. These eruption sizes (10 and 56 Tg SO_2) are hypothetical, but they are comparable to a VEI 6 (e.g. 1991 Mt. Pinatubo) and a VEI 7 (e.g. 1257 Mt. Samalas) eruption, representing 1-in-50-100-year and 1-in-500-1000-year events respectively. HIST_H56 utilises the 1257 Mt. Samalas HCl and HBr emission estimates from Vidal et al. (2016) and assumes a conservative ~5% stratospheric halogen injection efficiency. HIST_H10 has a SO_2 injection similar to that found to reproduce the spatial and temporal evolution of SAOD following 1991 Pinatubo (Mills et al., 2016) and a 10-times-smaller HCl and HBr flux than HIST_H56.

We have shown that the co-emission of halogens and sulfur in simulations of explosive volcanic eruptions significantly increases the peak and cumulative volcanic ERF. This is due to a combination of increased forcing from i) volcanic aerosol-radiation interactions (ERF_{ari}) and ii) composition of the stratosphere ($ERF_{clear,clean}$).

Co-emitting halogens results in a larger global mean ERF_{ari} in both HIST_H10 (+8%) and HIST_H56 (+6%). Ozone depletion catalysed by volcanic halogens leads to stratospheric cooling which offsets the volcanic aerosol heating (HIST_S10 ≃ 1.5 K, HIST_S56 ≃ 3.5 K) and results in a net stratospheric cooling (HIST_H10 ≃ -2 K, HIST_H56 ≃ -3.5 K). The ozone-induced stratospheric cooling prevents aerosol self-lofting and keeps the volcanic aerosol lower in the stratosphere with a shorter lifetime, resulting in reduced growth via condensation and coagulation and smaller peak global mean effective radius compared to sulfur-only simulations. The peak global mean effective radii of the HIST_H10 and HIST_H56 sulfate aerosols are found to be 15% and 10% smaller than HIST_S10 and HIST_S56 sulfate aerosols, closer to the most efficient radii for scattering shortwave radiation per unit mass, ~0.20 μm. Subsequently, we find HIST_H10 and HIST_H56 have higher peak global mean SAOD anomalies (+11%, +22%) and ERF_{ari} (+8% + 6%).

Co-emission of halogens also results in significant perturbations to the stratospheric chemistry and compositional-driven forcing. Stratospheric methane was found to decrease by 3% and 18% and stratospheric water vapour (SWV) was found to reduce by 16% and 36% in HIST_H10 and HIST_H56, respectively. The methane reductions were driven by the enhanced destruction flux by volcanic Cl radicals and the SWV changes were attributed to the same stratospheric temperature reductions mentioned previously. Cooling in the tropical tropopause vicinity increased the efficiency of the tropical cold trap dehydration effect, reducing the flux of water vapour from the

troposphere to the stratosphere. The most dramatic change in chemistry was found to be in stratospheric ozone. Significant ozone depletions were simulated globally in both HIST_H10 (22%) and HIST_H56 (57%) with prolonged depletion in both NH and SH winter polar regions. In HIST_H10, ozone hole conditions (<220 DU) were simulated globally for the first post-eruption year and then for 3-5 years at the poles during the winter. In HIST_H56, we simulate an ozone hole globally for 5 years followed by a gradual recovery over the following 5 years until only the polar winters exhibit ozone hole conditions. Stratospheric chemistry changes resulting from the co-emission of halogens increased the peak global mean $ERF_{clear,clean}$ by ~100% to -2.1 Wm^{-2} in HIST_H56 and -1.3 Wm^{-2} in HIST_H10. Stratospheric ozone depletion is the dominant driver of $ERF_{clear,clean}$ accounting for ~75% of the total $ERF_{clear,clean}$.

The combined effect of increased ERF_{ari} and $ERF_{clear,clean}$ is that co-emitting halogens increases the peak global mean volcanic ERF by 30% and 24% and cumulative ERF by 60% and 100% in HIST_H10 and HIST_H56 respectively. Ozone hole conditions exhibited by both HIST_H10 and HIST_H56 would result in dramatic increases in the surface UV flux with 'Extreme' UV levels being experienced over most of the globe for 4 years following HIST_H56 eruptions. UV exposure on this scale would lead to devastating negative consequences for society and the biosphere, including increases in the occurrences of skin cancer, eye damage and immune system deficiencies (WHO, 2002). This work shows for the first time that co-emission of plausible amounts of halogens can amplify the effective radiative forcing in simulations of explosive volcanic eruptions. This highlights the necessity to include volcanic halogens emissions when simulating the climate impacts of past or future eruptions, as well as the critical need to maintain space-borne observations of stratospheric compounds to better constrain the stratospheric injection estimates of volcanic eruptions.

Chapter 4

Climate change amplifies the radiative forcing of large magnitude explosive volcanic eruptions

Abstract

Sulfur gases emitted into the atmosphere by explosive volcanic eruptions are strong drivers of climate variability, but the extent to which climate change may, in turn, alter the volcanic sulfur life cycle and radiative forcing remains largely unexplored. This work investigates the radiative forcing due to volcanic sulfate aerosol (ERF_{ari}) following future explosive tropical volcanic eruptions emitting sulfur (sulfur-only) or sulfur with co-emitted halogens (halogen co-emission). We perform climate model simulations of large (10 Tg SO_2) and very-large (56 Tg SO_2) magnitude sulfur-only eruption scenarios and corresponding large (10 Tg SO_2 & 1.5 Tg HCl & 0.0086 Tg HBr) and very-large (56 Tg SO_2 & 15 Tg HCl & 0.086 Tg HBr) magnitude co-emission eruption scenarios in a historical climate state representative of the 1990s as well as a moderate and high warming future climate state representative of the 2050s. We show that climate change amplifies the peak global mean ERF_{ari} of large (+3-5%) and very-large (+7-11%) sulfur-only and halogen co-emission eruption scenarios. This is due to a reduction in aerosol size, mainly driven by the acceleration of the Brewer-Dobson circulation. Furthermore, we show that the co-emission of halogens amplifies the peak global mean ERF_{ari} by 3% and 6% in future climate states, as was found by Staunton Sykes et al. (2021) in a HIST climate state. Statistical models developed using the simulations in this work show that climate change and the co-emission of halogens significantly amplify ERF_{ari} independently and additively. Climate change was found to amplify the global mean ERF_{ari} twice as much in the very-large eruption scenarios compared with the large eruption scenarios. Tentative use of these statistical models outside the parameter range of the simulations in this work enables us to estimate that climate change between the pre-industrial and the 1990s may have already led to a 1-3% amplification of global mean peak ERF_{ari} and projected climate change between the 1990s and the 2090s may lead to a further 9-11% and 24-28% amplification of the global mean ERF_{ari} following large and very-large eruptions. ERF_{ari} may be further amplified by feedbacks related to plume dynamics and ocean-atmosphere coupling not accounted for in this study. This work identifies a negative climate-volcano feedback loop, which could modulate the climate variability caused by explosive volcanic eruptions and challenges the suitability of the constant volcanic forcing typically used in future climate projections.

4.1 Introduction

Explosive volcanic eruptions are one of the most important drivers of year-to year climate variability (Hegerl et al., 2003; Sigl et al., 2015). Volcanic eruptions inject sulfur gases directly into the atmosphere and have a strong direct climate impact through the formation of sulfuric acid aerosols, which reflect incoming sunlight and cool the Earth's surface (Robock, 2000). Understanding how volcanic eruptions can alter the climate has been a topic of study for over a century (e.g. Humphreys, 1913). In contrast, understanding how climate change may in turn

impact volcanic processes and their climate impact has received less attention. We are living through an era of rapid global climate change driven by anthropogenic greenhouse gas emissions, and it is therefore vital to identify climate-volcano feedbacks and quantify the effect these feedbacks may have on climate variability. Here, we explore climate-volcano feedbacks using results from climate model simulations of large (10 Tg SO_2) and very-large (56 Tg SO_2) sulfur-only eruption scenarios and corresponding large (10 Tg SO_2 & 1.5 Tg HCl & 0.0086 Tg HBr) and very-large (56 Tg SO_2 & 15 Tg HCl & 0.086 Tg HBr) halogen co-emission eruption scenarios in a historical climate state representative of the 1990s (HIST) and two future climate states representative of the 2050s. The two future climate states utilised are moderate and high-end warming climate states respectively, defined by the Shared Socio-economic Pathway (SSP) emissions projections of greenhouse gases and halocarbons for SSP2 4.5 and SSP5 8.5 (hereafter SSP2 and SSP5) (O'Neill et al., 2016).

Climate change may alter the climate effects of volcanic eruptions in several ways, including:

1) By altering the distribution of volcanic eruptions in terms of magnitude, location, and frequency e.g. as a consequence of glaciation-deglaciation cycles (Jellinek et al., 2004; Swindles et al., 2018; Watt et al., 2013).
2) By altering background climatic conditions into which the volcanic eruption takes place, e.g more stratified ocean (Fasullo et al., 2017) and atmosphere (Aubry et al., 2016, 2019).
3) By directly altering the processes that govern the volcanic sulfur cycle and, in turn, the associated aerosol optical properties and radiative forcing. For example, climate change is expected to result in a cooler stratosphere and slower stratospheric reaction kinetics, but also greater stratospheric water vapour concentration which will lead to higher OH concentrations and faster oxidation of SO_2 (Collins et al., 2013). Furthermore, climate change will lead to an acceleration of the Brewer-Dobson circulation which can be expected to reduce the lifetime of stratospheric sulfate aerosol (Butchart, 2014; Collins et al., 2013; Griffiths et al., 2021).

There is substantial evidence linking the frequency, location and magnitude of volcanic eruptions to the deglaciation of ice-covered volcanoes (e.g. Jellinek et al., 2004). However, as the time-lag between ice retreat and volcanic response has been constrained to between 500 and 2000 years (Jellinek et al., 2004; Watt et al., 2013), it is unlikely such impacts are relevant on the timescale of climate projections (up to 2100 and occasionally 2300) (Swindles et al., 2018). Fasullo et al. (2017) reported that, as the Earth warms and the ocean becomes increasingly stratified in the future, the surface temperature response to volcanic eruptions may penetrate less deep into the ocean, resulting in enhanced cooling of the surface ocean and air. However, Hopcroft et al. (2018) used simulations of a Mt. Tambora sized eruption in 2040 RCP6.0 conditions to show that future volcanic eruptions would result in reduced surface cooling. Aubry et al. (2016) and Aubry et al. (2019) reported that the volcanic plume height and the fraction of volcanic sulfur that is injected into the stratosphere is sensitive to climate change due to the increased atmospheric stratification and tropopause height. However, they stopped short of quantifying the effects these changes may have on the volcanic sulfur life cycle or volcanic radiative forcing.

Aubry et al. (under review) is the only study to explore the impacts of climate change on the processes that directly govern the stratospheric volcano sulfur cycle. To achieve this, they utilised an eruptive column model in series

with a global climate model to explicitly simulate how moderate (1 Tg SO_2) and large-magnitude (10 Tg SO_2) tropical eruptions would impact climate in a year 2095 high-end future climate projection (SSP5-8.5) compared to a year 1995 historical climate. Aubry et al. (under review) calculated injection heights for the eruptions in each climate state using an eruptive column model and then utilised these in a global climate model coupled with an interactive stratospheric aerosol module (Mulcahy et al., 2020). In the case of the moderate sized eruption, they reported a significantly muted radiative perturbation in the future SSP5 simulations compared to the historical period, mainly because the tropopause height increase in SSP5 led to a smaller fraction of the degassed sulfur being injected into the stratosphere. In contrast, in simulations of large-magnitude eruptions the warmer climate led to an amplified climate impact. They reported that top-of-atmosphere (TOA) effective radiative forcing (ERF), stratospheric warming, tropospheric cooling and surface cooling increased by 30%, 52%, 55% and 15% with respect to the historical period, primarily due to a decrease in aerosol size driven by the acceleration of the Brewer-Dobson circulation and further modulated by a higher SO_2 injection height. Aubry et al. (under review) did not, however, explore how climate change would impact volcanic radiative forcing in very large-magnitude eruptions (>10 Tg SO_2), with co-emitted volcanic halogens, which were shown to significantly amplify volcanic forcing in Staunton Sykes et al. (2021) and Chapter 3, or in a less extreme future climate scenario and at a time closer to the present day.

Petrological data suggest that volcanic eruptions in some geological settings often release substantial amounts of halogen gases into the atmosphere alongside SO_2 (hereafter halogen co-emission) (Krüger et al., 2015; Kutterolf et al., 2013, 2015). Although co-emitted volcanic halogens are efficiently scavenged by hydrometeors in the plume, direct stratospheric injection of volcanic halogens is predicted theoretically (Textor et al., 2003) and has been observed following eruptions in the satellite era (Carn et al., 2016; Hunton et al., 2005; Prata et al., 2007; Read et al., 2009; Rose et al., 2006). Overall, current datasets show that the stratospheric injection of volcanic halogens is highly variable and depends on both the total mass of halogens released at the vent and the degree of scavenging, determined by the geochemistry of the volcano and the prevailing atmospheric conditions during the eruption, particularly the humidity. It is clear, however, that volcanic halogens are injected into the stratosphere after some volcanic eruptions and research into how these volcanic halogens may alter the volcanic aerosol microphysics, stratospheric chemistry, and the volcanic forcing is still limited.

Staunton Sykes et al. (2021) (Chapter 1) used the same UKESM-AMIP model set-up employed in this work to show, for the first time, that co-emission of volcanic halogens amplifies the volcanic radiative forcing (ERF) of large- and very-large-magnitude volcanic eruptions compared to sulfur-only eruptions. They simulated a large- (10 Tg SO_2) and very-large-magnitude (56 Tg) tropical eruption, both with and without co-emitted halogens in a historical climate representative of the 1990s and reported a ~25% amplification in the peak global mean ERF in co-emission scenarios compared with sulfur-only scenarios. Roughly a third of the additional volcanic ERF was attributed to an enhanced ERF_{ari} with the remainder due to changes in stratospheric ozone. The amplification of ERF_{ari} was caused by a shortening of the aerosol lifetime, which reduced the aerosol growth and led to smaller more numerous aerosol closer to the most efficient aerosol extinction per unit mass. The shortening of the aerosol lifetime resulted from the absence of aerosol self-lofting following co-emission scenarios. Typically, following eruptions, volcanic aerosol absorb radiation leading to stratospheric heating, which lofts the aerosol higher into

the stratosphere. However, in co-emission scenarios, ozone depletion results in a net loss of radiation absorbed in the low-mid stratosphere, resulting in stratospheric cooling and preventing aerosol self-lofting. In simulations of co-emission eruption scenarios, volcanic aerosol remained lower in the stratosphere and was removed faster than in sulfur-only simulations, leading to smaller aerosol and larger TOA ERF. Staunton Sykes et al. (2021) did not, however, explore the role that climate change may have on the climate effects of co-emission volcanic eruptions.

In this study we use UKESM-AMIP model simulations to investigate the role of climate change in determining the peak global mean ERF_{ari} following large explosive sulfur-only and halogen co-emission volcanic eruptions. We report that climate change amplifies the peak global mean ERF_{ari} of explosive sulfur-only and halogen co-emission eruption scenarios. This is driven by a shorter total sulfur (defined as the sum of SO_2 + SO_4) anomaly e-folding time, reduced aerosol growth and larger aerosol extinction per unit mass. Even though the faster removal results in a shorter lifetime, this effect is dominated by a decrease in the aerosol size resulting in larger peak global mean ERF_{ari}. Furthermore, we show that the co-emission of halogens amplifies the peak global mean ERF_{ari} compared to sulfur-only eruption scenarios in future climate states, as was found by Staunton Sykes et al. (2021) in a HIST climate state. We utilise these results to develop statistical models that generalise the effect of climate change and co-emission of halogens on peak global mean ERF_{ari}. Climate change and the co-emission of halogens are shown to significantly amplify ERF_{ari} independently and additively. Finally, we tentatively utilise our statistical models to estimate the amplification of ERF_{ari} that has already taken place since the pre-industrial period and the expected additional amplification of ERF_{ari} by 2090.

4.2 Methods

4.2.1 Experimental Design

Our study utilises the HIST, SSP2 and SSP5 UKESM-AMIP time-slice experiments as described in Chapter 2. The HIST control simulation was run using the January 1995 initialisation file and climatologies calculated using data from the fully coupled UKESM1.0 historical runs produced for CMIP6 (Eyring et al., 2016) and averaged over the years 1990 to 2000. SSP2 and SSP5 control simulations were run using the January 2055 initialisation file and climatologies calculated using data from the fully coupled UKESM1.0 ScenarioMIP runs produced for CMIP6 (Eyring et al., 2016) and averaged over the years 2050 to 2060. By averaging over a decade, the atmosphere-only simulations are forced with boundary conditions typical of the period but not a specific date within that decade. The model was allowed to spin up for 15 years and the control was run for a further 20 years. In this work, climate change is inferred from the difference between the future (SSP2 and SSP5) and HIST control climatologies, and key differences between the control climatologies are highlighted in Table 4.1. The effect of explosive volcanic eruptions was investigated by running three 10-year volcanic perturbation simulations initialised from three different years in the control run to sample the variability in QBO states. Changes are plotted as the difference between the average of the ensemble members and a climatology derived from the 20-year control run.

Volcanic effective radiative forcings are calculated as differences (Δ) in the net (SW+LW) top-of-atmosphere (TOA) radiative fluxes (F) between perturbed and control climatologies (see section 2.2). Extra calls to the

radiation scheme enable the forcing from aerosol-radiation interactions to be isolated (ERF_{ari}), as described in Schmidt et al. (2018) and Ghan (2013).

$$ERF_{ari} = \Delta(F - F_{clean}) \qquad \text{(Eq. 4.1)}$$

Where F_{clean} denotes a radiation flux diagnostic calculation without aerosol-radiation interactions but including aerosol-cloud interactions through microphysics. Thus, $F - F_{clean}$, determines the impact of all aerosol and $\Delta(F - F_{clean})$ is an estimate of the forcing from volcanic aerosol-radiation interactions (ERF_{ari}). Cumulative forcing is calculated as the time-integrated forcing across the Earth's surface and represents the total energy loss (J) as a result of the volcanic eruption.

	HIST (1990s)	**SSP2 4.5** (2050s)	**SSP5 8.5** (2050s)
CO_2 (ppbv)	360	522 (+45%)	601(+67%)
Methane (ppbv)	695	819 (+18%)	1064 (+53%)
SWV (ppbv)	6.8	9.0 (+32%)	10.1 (+49%)
OH (pptv)	0.21	0.24 (+32%)	0.27 (+28%)
EESC (ppbv)	4.5	2.7 (-39%)	2.6 (-41%)
Ozone Column (DU)	306	328 (+7%)	333 (+9%)
Age of Air at 10-50 hPa (Years)	4.5	4.1 (-9%)	3.9 (-13%)
Stratospheric Temp at 10-50 hPa (K)	211	209 (-1%)	208 (-1.5%)

Table 4.1 Overview of the HIST, SSP2 and SSP5 control simulations. Showing the key differences between the HIST, SSP2 and SSP5 control climatologies. SWV, OH, and EESC are calculated as global stratospheric means, whereas methane is calculated as a whole-atmosphere mean, Age of Air and Stratospheric temperature are calculated as mid-stratosphere means (10-50 hPa). Control run values are in the absence of any volcanic eruptions.

The volcanic emissions are prescribed by direct injection of SO_2, HCl and HBr into the stratosphere with a Gaussian plume vertical distribution centred on 21 km and with a width of 2.1 km (10% of the height) (Aubry et al., 2019), lasting for 24 hours on July 1st. An injection altitude of 21 km was chosen as, allowing for lofting, this results in a volcanic sulfate plume altitude consistent with the 1991 eruption of Mt Pinatubo (Guo et al., 2004). The gases were injected in the tropics (5°S latitude and 0° longitude) to represent a typical tropical explosive eruption (Newhall et al., 2018).

Since historical stratospheric volcanic SO_2 fluxes are variable and the volcanic flux of HCl and HBr into the stratosphere remains uncertain, we developed a simulation matrix that spans a range of plausible explosive volcanic emissions, as outlined in Chapter 2. The four sets of experiments have one large-magnitude SO_2 (10 Tg), and one very-large-magnitude SO_2 (56 Tg) emission scenario both with (H10 and H56) and without halogens (S10 and S56), as shown in Table 4.2. These eruptions (10 and 56 Tg SO_2) are hypothetical, but their magnitudes are comparable to a VEI 6 (e.g. 1991 Mt. Pinatubo) and VEI 7 (e.g. 1257 Mt. Samalas) eruption, representing 1-in-

50-100-year and 1 in 500–1000 year events respectively (Newhall et al., 2018). Experiment identifiers used in this work are formed by combining the background climate and eruption scenario identifiers, as shown in Table 4.3.

Scenario	SO_2 (Tg)	HCl (Tg)	HBr (Tg)	HCl:SO_2
S10	10	-	-	-
H10	10	1.5	0.0086	0.26
S56	56	-	-	-
H56	56	15	0.086	0.47

Table 4.2 Showing the eruption masses of SO_2, HCl and HBr in Tg and HCl:SO_2 (relative mixing ratio) for the four sets of experiments.

Experiment Identifier Key	Climate Scenario		
Eruption Scenario	**HIST**	**SSP2**	**SSP5**
S10	HIST_S10	SSP2_S10	SSP5_S10
H10	HIST_H10	SSP2_H10	SSP5_H10
S56	HIST_S56	SSP2_S56	SSP5_S56
H56	HIST_H56	SSP2_H56	SSP5_H56

Table 4.3 Showing the full simulation matrix utilised in this study. Experiment identifiers are formed by combining the climate scenarios (column headings) and emission scenarios (rows).

4.2.2 Isolating the impact of climate change and co-emission of halogens on volcanic forcing

Simulating identical sulfur-only and co-emission eruption scenarios in historical and future climate states allows us to explore and to isolate the impacts of halogen co-emission and climate change on volcanic forcing. The impacts of climate change in sulfur-only (Δ_{CC_SULF}) and halogen co-emission (Δ_{CC_HAL}) eruption scenarios and the impact of halogen co-emission in HIST (Δ_{HAL_1990s}) and future climate states (Δ_{HAL_2050s}) can be calculated by taking the differences between volcanic perturbation experiments as shown in (Figure 4.1).

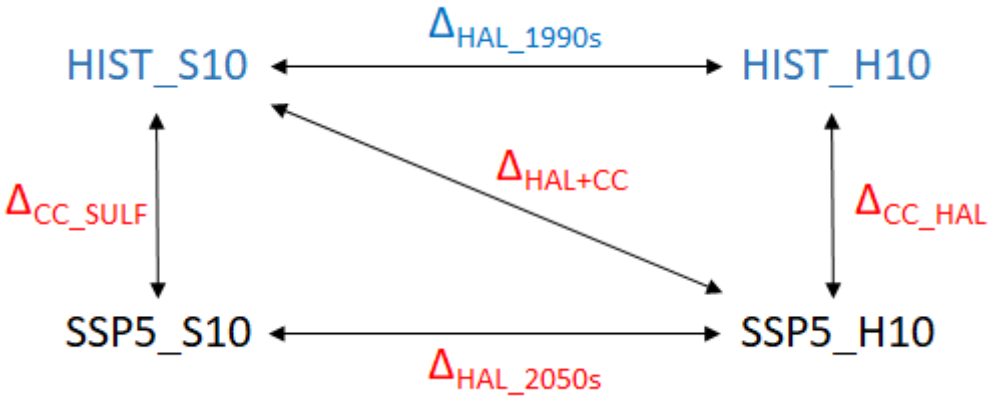

Figure 4.1 Schematic indicating how the impacts of co-emission and climate change on volcanic forcing are isolated. Where '1990s', and '2050s' are used to indicate the historical and future periods, and 'SULF' and 'HAL' are used to indicate sulfur and co-emission of halogens, respectively.

4.3 Results

4.3.1 UKESM-AMIP Simulations

We simulated an amplification of peak global mean ERF_{ari} in future climate states in both sulfur-only (Δ_{CC_SULF}), and halogen co-emission (Δ_{CC_HAL}) eruption scenarios. Table 4.4 shows the details of the changes in SO_2 anomaly e-folding time, total sulfur (defined as the sum of SO_2 + SO_4) anomaly e-folding time, peak global mean aerosol effective radius (R_{eff}) and peak global mean ERF_{ari} due to climate change and halogen co-emission following large and very-large eruption scenarios. In future climate states, climate change results in a +5% and +10% larger peak global mean ERF_{ari} in large and very-large sulfur-only simulations (Δ_{CC_SULF}), and a slightly smaller +3% and +7% larger peak global mean ERF_{ari} in halogen co-emission scenarios (Δ_{CC_HAL}) (Figure 4.2). Climate change results in an amplification of peak global mean ERF_{ari} whilst also resulting in the 8% and 10% faster oxidation of SO_2 in both sulfur-only and halogen co-emission scenarios, and the 4% and 7% faster removal of total sulfur from the atmosphere in sulfur-only simulations and 20% and 9% faster removal of total sulfur from the atmosphere in co-emission scenarios (Figure 4.3).

	SO_2 e-folding time (months)		S e-folding time (months)		Peak Global mean R_{eff} (μm)		Peak Global mean ERF_{ari} (Wm^{-2})	
Size ⇒ Effect ⇓	**10 (large)**	**56 (v. large)**	**10 (large)**	**56 (v. large)**	**10 (large)**	**56 (v. large)**	**10 (large)**	**56 (v. large)**
Δ_{CC_SULF}	-0.13 **(-8%)**	-0.13 **(-10%)**	-1.23 **(-4%)**	-0.17 **(-7%)**	-0.034 **(-9%)**	-0.027 **(-5%)**	-0.15 **(+5%)**	-1.12 **(+10%)**
Δ_{CC_HAL}	-0.13 **(-8%)**	-0.13 **(-10%)**	-3.28 **(-20%)**	-0.96 **(-9%)**	-0.01 **(-3%)**	-0.01 **(-2%)**	-0.08 **(+3%)**	-0.77 **(+7%)**
Δ_{HAL_1990s}	+0.23 **(+23%)**	+0.59 **(+44%)**	-3.89 **(-30%)**	-1.91 **(-20%)**	-0.05 **(-13%)**	-0.06 **(-10%)**	-0.24 **(+8%)**	-0.68 **(+6%)**
Δ_{HAL_2050s}	+0.23 **(+23%)**	+0.59 **(+44%)**	-5.98 **(-30%)**	-2.71 **(-20%)**	-0.022 **(-7%)**	-0.042 **(-8%)**	-0.17 **(+6%)**	-0.34 **(+3%)**
Δ_{CC+HAL}	+0.1 **(+9%)**	+0.46 **(+32%)**	-7.17 **(-33%)**	-2.87 **(-21%)**	-0.056 **(-14%)**	-0.069 **(+12%)**	-0.32 **(+3%)**	-1.46 **(+3%)**
$\Delta_{CC}+\Delta_{HAL}$	+0.1 **(+9%)**	+0.46 **(+32%)**	-5.15 **(-24%)**	-2.08 **(-15%)**	-0.06 **(+15%)**	0.07 **(+12%)**	-0.39 **(+3%)**	-1.80 **(+3%)**

Table 4.4 Summary of the effects of climate change in sulfur-only (Δ_{CC_SULF}) and co-emission (Δ_{CC_HAL}) eruption scenarios, and the effects of co-emission in HIST (Δ_{HAL_1990s}) and SSP5 (Δ_{HAL_2050s}) climate states (as outlined in Figure 4.1) on SO_2 e-folding anomaly lifetime, total sulfur anomaly e-folding lifetime, peak global mean R_{eff}, and peak global mean ERF_{ari}. Note that the negative change in ERF_{ari} reflect larger, more negative values. Pink cells are results taken from Staunton Sykes et al. (2021) and Chapter 3.

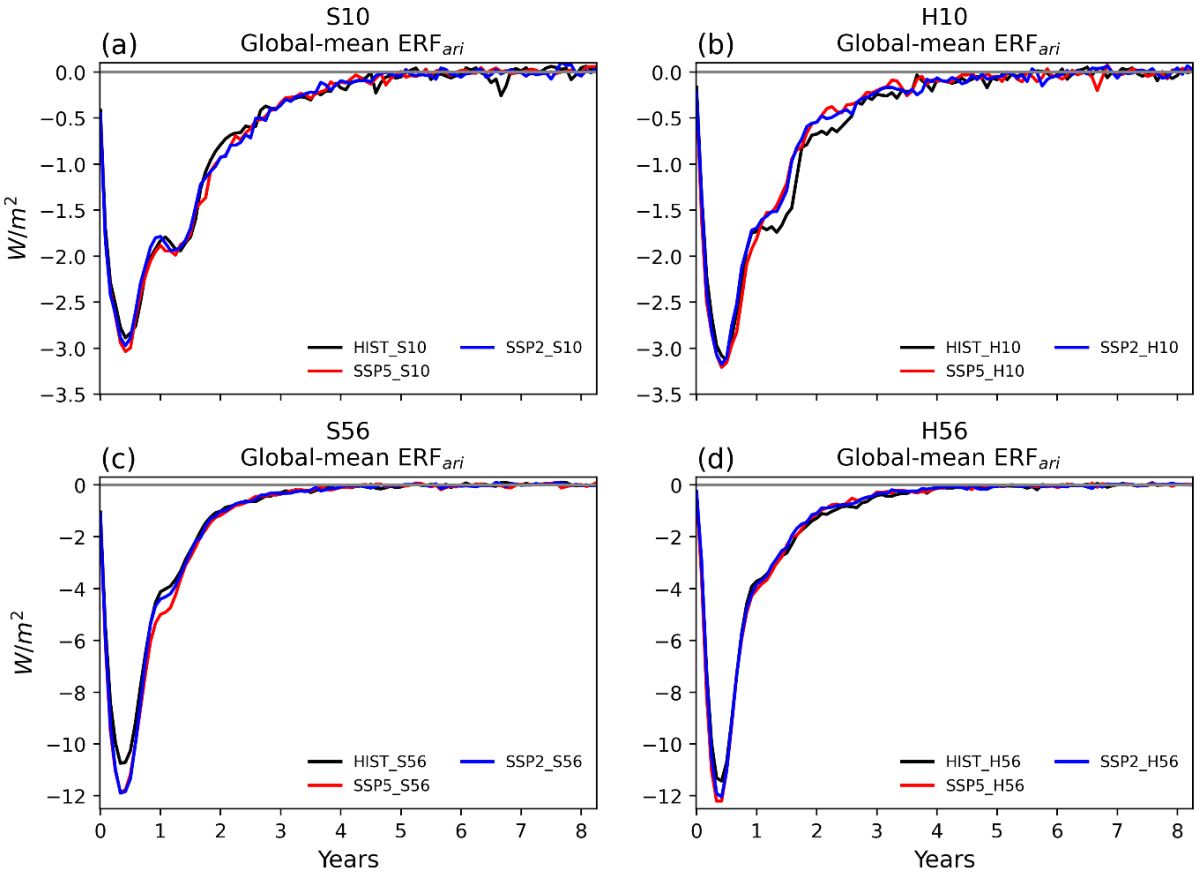

Figure 4.2 Evolution of global mean ERF_{ari} in S10 (a), H10 (b), S56 (c), and H56 (d) eruption scenarios relative to the control climatologies. The difference between red or blue and black lines represents the amplification due to climate change.

In the stratosphere, the volcanic SO_2 e-folding lifetime is determined by the rate of oxidation via OH (Eq 1.1), and thus, the OH concentration. This shortening of the SO_2 e-folding lifetime due to climate change reflects the initial background OH concentration, which is significantly higher in the future due to the higher concentration of stratospheric water vapour, as shown in Table 4.1 and Figure B1. Whereas the amplification of peak global mean ERF_{ari} due to climate change is driven by changes in the volcanic sulfate aerosol microphysics, and specifically the aerosol R_{eff}. The size of volcanic sulfate aerosols alters their SW scattering efficiency and radiative effect. Lacis (2015) used Mie scattering theory to determine that the volcanic sulfate aerosol radius with maximum aerosol extinction per unit mass at 550 nm has a radius of ~0.20 µm, with a substantial drop off for aerosols both larger and smaller. In other words, for a given aerosol burden, radiation is more efficiently scattered when the aerosols have an R_{eff} closer to ~0.20 µm. Volcanic eruptions in future climate states result in smaller aerosol that are closer to this optimal value. Climate change results in a 9% and 5% smaller peak global mean aerosol R_{eff} in SSP5_S10 and SSP5_S56 compared with HIST_S10 and HIST_S56, and a 2% smaller maximum global mean R_{eff} in SSP5_H10 and SSP_H56 compared with HIST_H10 and HIST_H56 (Figure 4.3e,f). This translates into a 5% and 10% larger SAOD.

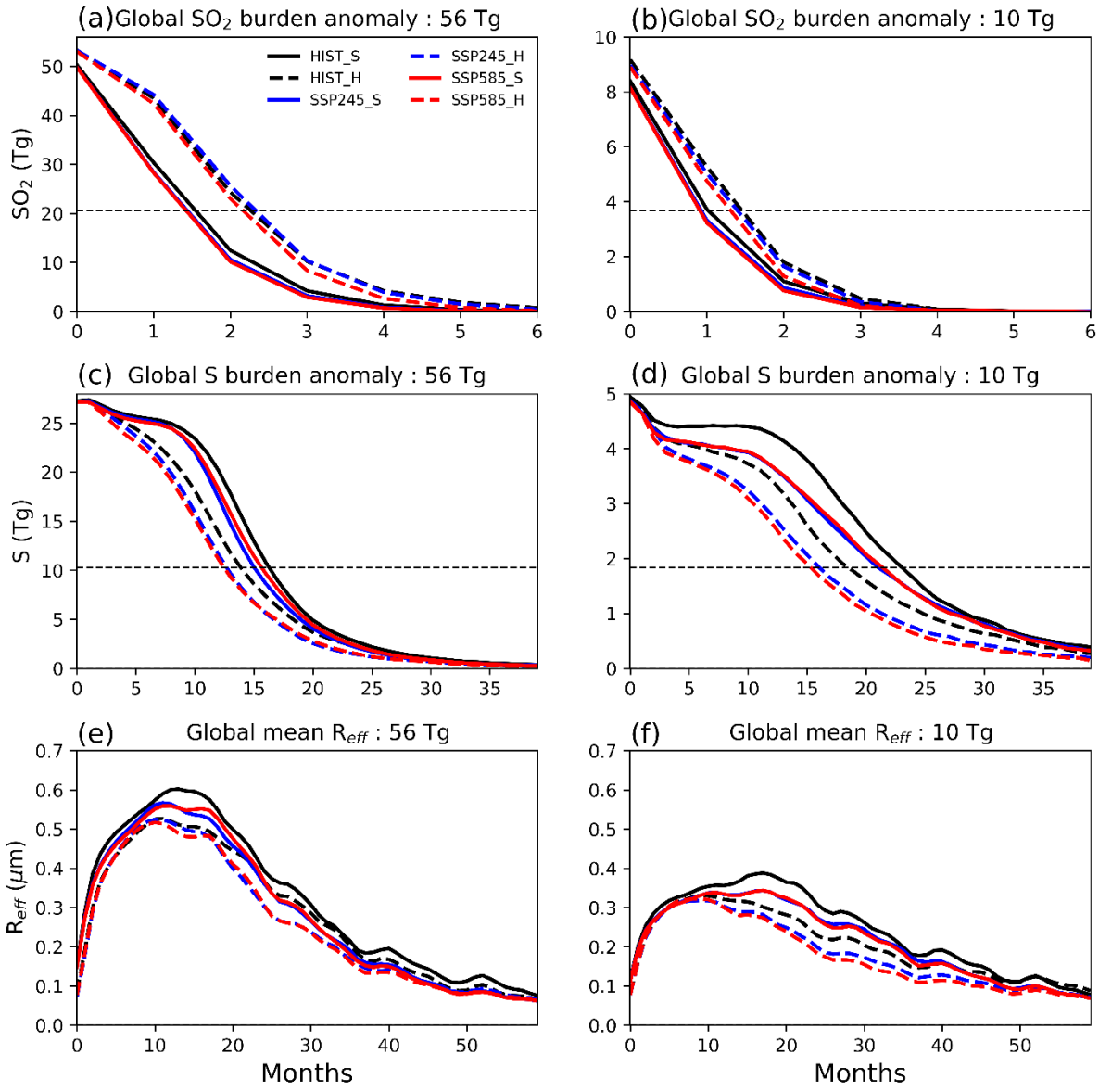

Figure 4.3 Global evolution of SO_2 burden anomaly (top) and total (SO_2+H_2SO_4) total sulfur anomaly burden anomaly (middle) and R_{eff} (bottom) in HIST_S56 and HIST_H56 (left) and HIST_S10 HIST_H10 (right) relative to the control climatologies.

To a first order, the magnitude of the volcanic SO_2 injection determines the aerosol R_{eff} and the total sulfur anomaly e-folding time (Marshall et al., 2019). For example, the aerosol R_{eff} was simulated to be 35% smaller in HIST_S10 (0.38 um) compared with HIST_S56 (0.59 um) and resulted in a 50% longer total sulfur anomaly e-folding lifetime (Figure 4.3e,f). The theory behind this is well understood, larger SO_2 injections result in higher H_2SO_4 concentrations, more aerosol growth, forming larger aerosol, which settle out of the stratosphere faster resulting in a shorter total sulfur anomaly lifetime compared with smaller eruptions (e.g., Timmreck et al., 2010). However, when we fix the magnitude of SO_2 injection and compare across eruption scenarios, we resolve a second-order effect whereby R_{eff} decreases with decreasing total sulfur anomaly e-folding time (Figure 4.4).

By plotting the 3-year averaged global mean aerosol R_{eff} as a function of the total sulfur anomaly e-folding time for each simulation ensemble member across climate states we can clearly resolve this effect (Figure 4.4). Regression analysis reveals a significant strong positive correlation between the total sulfur anomaly e-folding time and R_{eff} within both 10 Tg (r=0.93) and 56 Tg (r=0.9) eruption ensembles. To a first order, the aerosol R_{eff} is determined by the magnitude of the volcanic sulfur injection. In the same transport conditions, the larger SO_2 injection in the 56 Tg ensemble simulations (closed markers) leads to larger-sized sulfate aerosols, faster sedimentation and shorter e-folding lifetime compared to 10 Tg ensemble simulations (open markers). However, when we fix the SO_2 emission size and compare the different climate scenarios (red, blue, and black markers), we find that the transport change is having a second-order effect. The faster removal of sulfate aerosol in future climate ensemble simulations (red and blue) leads to smaller-sized aerosol compared to present day (black). The slope of the line of best fit is significantly larger in 56 Tg simulations compared to 10 Tg simulations, meaning the effect of climate change has a larger impact on aerosol R_{eff} as the magnitude of the SO_2 injection increases.

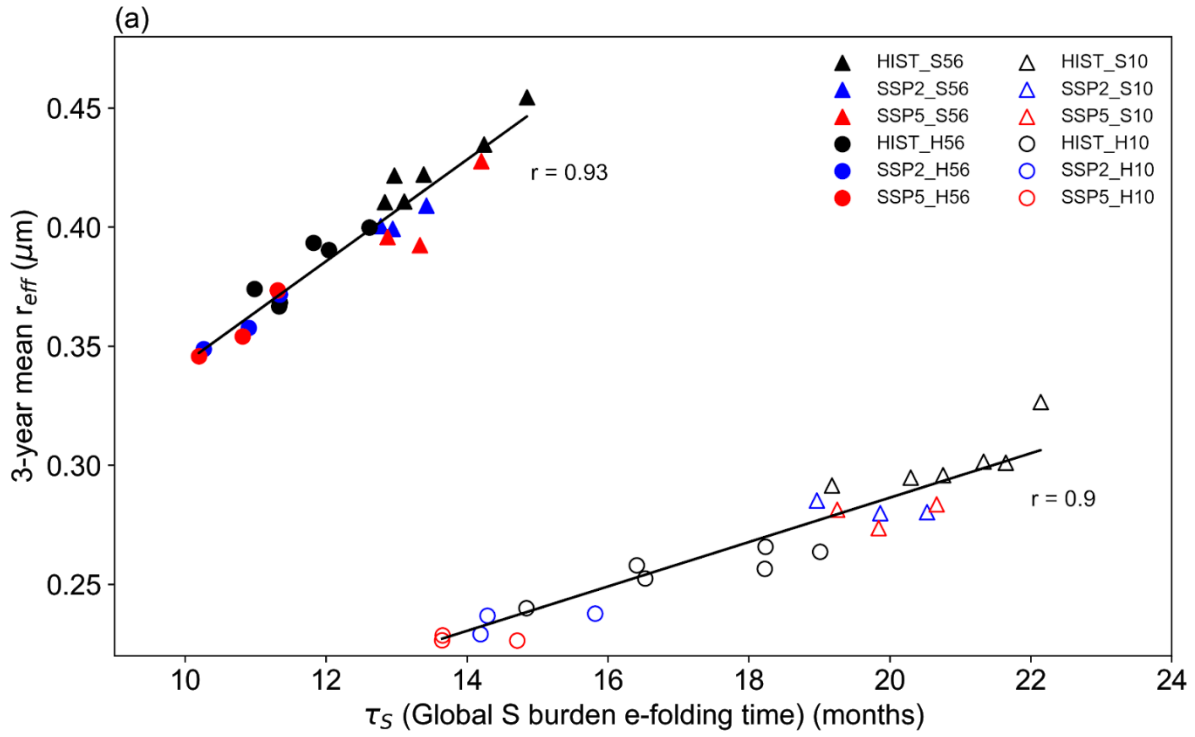

Figure 4.4 3-year averaged global mean aerosol effective radius as a function of the global total sulfur anomaly e-folding lifetime, in S10 and H10 (open markers) and S56 and H56 (closed). Each marker represents an individual ensemble member. Regression lines fitted with correlation coefficient (r) showing strong positive correlation.

Volcanic sulfate aerosols grow through microphysical processes of condensation and coagulation (Kremser et al., 2016). Faster removal from the atmosphere (Figure 4.3c,d) results in reduced opportunity for aerosol growth and results in a larger number of smaller aerosol particles and a reduction in the peak global mean R_{eff}. The reduction in total sulfur anomaly e-folding time in future climates is driven by the faster transport of aerosol to high latitudes by a Brewer-Dobson circulation accelerated by climate change. The effect of climate change on Brewer-Dobson circulation can be clearly seen in the stratospheric age of air (a model-derived estimate of duration since the air was last inside the troposphere) in the control climatologies (Figure B3). The global mean stratospheric age of air

between 10 hPa and 50 hPa is 13% younger in the 2050s under SSP5 compared with the 1990s. The accelerated Brewer-Dobson circulation in the 2050s under SSP5 results in accelerated transport to and removal at high latitudes, resulting in the shorter total sulfur anomaly e-folding lifetime. The acceleration of the Brewer-Dobson circulation due to climate change is a robust result of climate model projections, even though the exact magnitude of this acceleration is model-dependent (Butchart, 2014; Griffiths et al., 2021). The effect of sulfur aerosol e-folding lifetime on R_{eff} is expected to be modulated by the aerosol nucleation rate. The nucleation rate of sulfate aerosol is faster in a colder stratosphere, resulting in smaller but more numerous aerosols (Mann et al., 2010; Timmreck, 2012). At 25 km, the global mean temperature is ~3-4K lower in SSP5 conditions than in HIST (Figure B2), resulting in enhanced nucleation and exacerbating the effects of climate change on reduced aerosol growth on aerosol R_{eff}.

The shorter total sulfur anomaly e-folding lifetime caused by an accelerated Brewer-Dobson circulation due to climate change also results in a faster recovery of global mean ERF_{ari}, however, this does not fully offset the increase in peak global mean ERF_{ari} in sulfur-only eruption scenarios. As such, the cumulative ERF_{ari} (time-integrated energy lost from the Earth system) is 3% and 11% larger in SSP5_S10 (-7.73×10^{22} J) and SSP5_S56 (-1.96×10^{23} J) than in HIST_S10 (-7.52×10^{22} J) and HIST_S56 (-1.76×10^{23} J). Accordingly, climate change not only amplifies the peak global mean ERF_{ari} but also the total loss of energy lost due to the eruption (Figure B4).

Co-emission of halogens resulted in an 8% and 6% increase in peak global mean ERF_{ari} in HIST climate state (Δ_{HAL_1990s}), whilst also resulting in a 23% and 44% longer SO_2 e-folding time and a 30% and 20% shorter total sulfur anomaly e-folding lifetime (Table 4.4, Figure 4.5) (Staunton Sykes et al. 2021; Chapter 1). In future climate states, we also simulate an amplification of peak global mean ERF_{ari} due to the co-emission of halogens, albeit slightly smaller at 6% and 3% (Δ_{HAL_2050s}), driven by a 6% and 8% smaller aerosol R_{eff} (Figure 4.3e,f). Notably, the amplification due to co-emission of halogens in future climate states (Δ_{HAL_2050s}) is in addition to amplification due to climate change (Δ_{CC_SULF}) (Figure 4.5, Table 4.4).

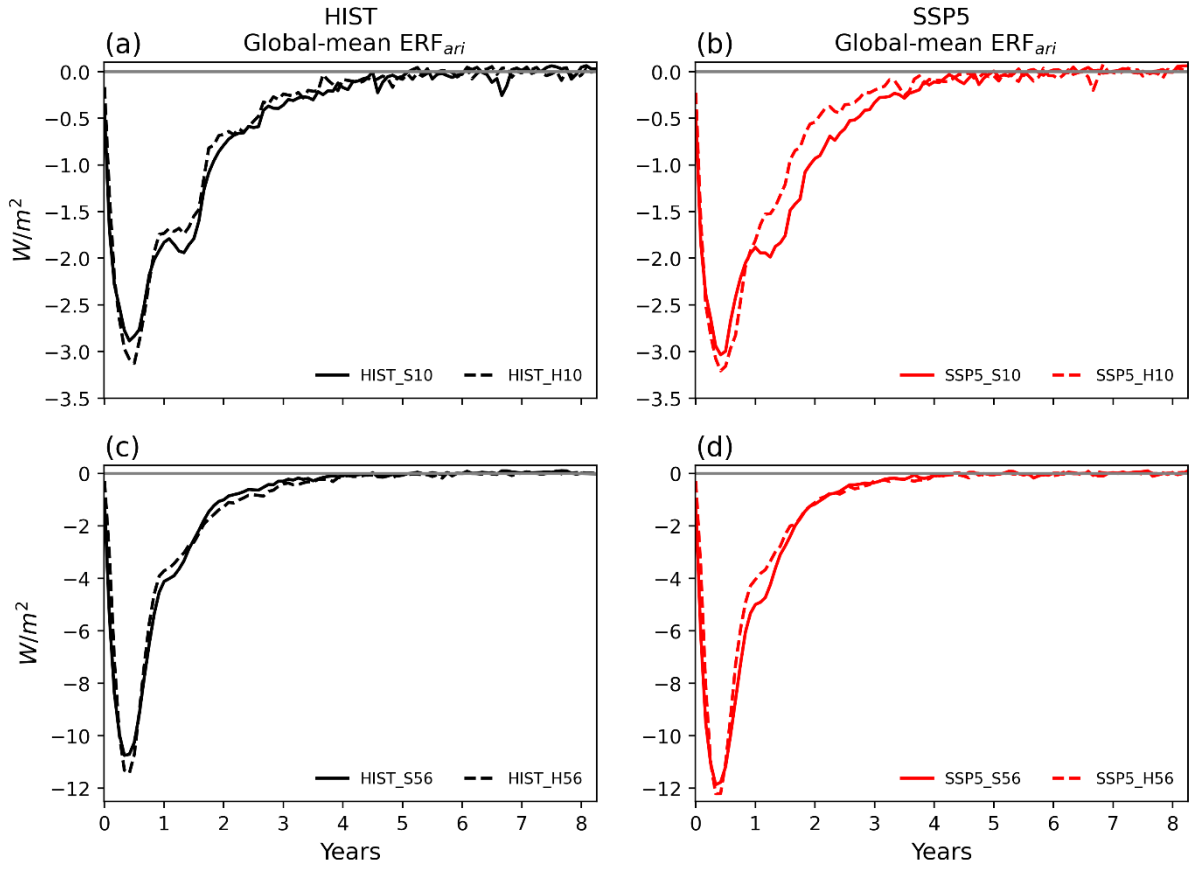

Figure 4.5 Evolution of peak global mean ERF_{ari} in HIST_S10 and HIST_H10 (a), SSP5 _S10 and SSP5 _H10 (b), HIST_S56 and HIST_H56 (c), and SSP5 _S56 and SSP5 _H56 (d) eruption scenarios relative to the control climatologies. The difference between dashed and solid lines represents the amplification due to the co-emission of halogens.

The lengthening of the SO_2 e-folding lifetime due to the co-emission of halogens reflects the further depletion of stratospheric OH compared to sulfur-only eruption scenarios. The main cause of this is reaction between OH and the co-emitted volcanic halogens, via Eq. 4.2, and is approximately the same in both HIST and future climate states.

$$HCl + OH \rightarrow Cl + H_2O \qquad \text{(Eq. 4.2)}$$

As was the case with climate change above, the driver of this amplification is that the total sulfur anomaly has a shorter e-folding time, reducing the opportunity for aerosol growth, and resulting in smaller, more numerous aerosol with a larger aerosol extinction per unit mass. However, the cause of the shorter total sulfur anomaly e-folding time in halogen co-emission scenarios is not the same. Volcanic sulfate aerosol remains at significantly lower altitudes in halogen co-emission scenarios (~21-22 km) compared with sulfur-only (~24-25 km) which results in faster transport to high latitudes and removal from the stratosphere as the speed of the Brewer-Dobson circulation decreases with altitude (Staunton Sykes et al., 2021). The altitude differences are driven by the stratospheric temperature change and dynamical response to the eruption themselves rather than the background climate. Sulfur-only simulations resulted in strong positive temperature anomalies due to aerosol heating in the

tropical stratosphere, increasing tropical vertical ascent and lofting volcanic aerosol to altitudes higher than the initial injection height in the model. By contrast, co-emission of volcanic halogens results in significant stratospheric ozone depletion. Ozone generates heat in the stratosphere by absorbing both incoming shortwave (SW) radiation from the Sun and by absorbing upwelling longwave (LW) radiation from the troposphere. Thus, decreasing stratospheric ozone results in stratospheric cooling, offsetting the volcanic aerosol heating, and resulting in net negative temperature in the tropical stratosphere. This stratospheric cooling decreases the vertical ascent in the tropics and prevents volcanic sulfate aerosol being self-lofted. This behaviour is simulated across both HIST and future climate states, with insignificant differences.

4.3.2 Statistical models generalising the relationship between climate change, halogen co-emission and ERF_{ari}

The results from UKESM-AMIP simulations explored in section 3.1 enable us to develop statistical models to generalise the impact of three predictor variables (atmospheric CO_2, eruption size, and eruption composition) on peak global mean ERF_{ari} using three-way ANOVA (analysis of variance), as described in Section 2.5. Atmospheric CO_2 is used here as a proxy for climate change. We assessed three atmospheric CO_2 values (i.e. the background values in HIST, 2050s under SSP2, and 2050s under SSP5), two SO_2 emission magnitudes (10 Tg or 56 Tg of SO_2) and two eruption compositions (sulfur-only or halogen co-emission). The adjusted equations of the full linear models with three predictor variables are shown in Figure 4.5 (solid lines) and included in full below:

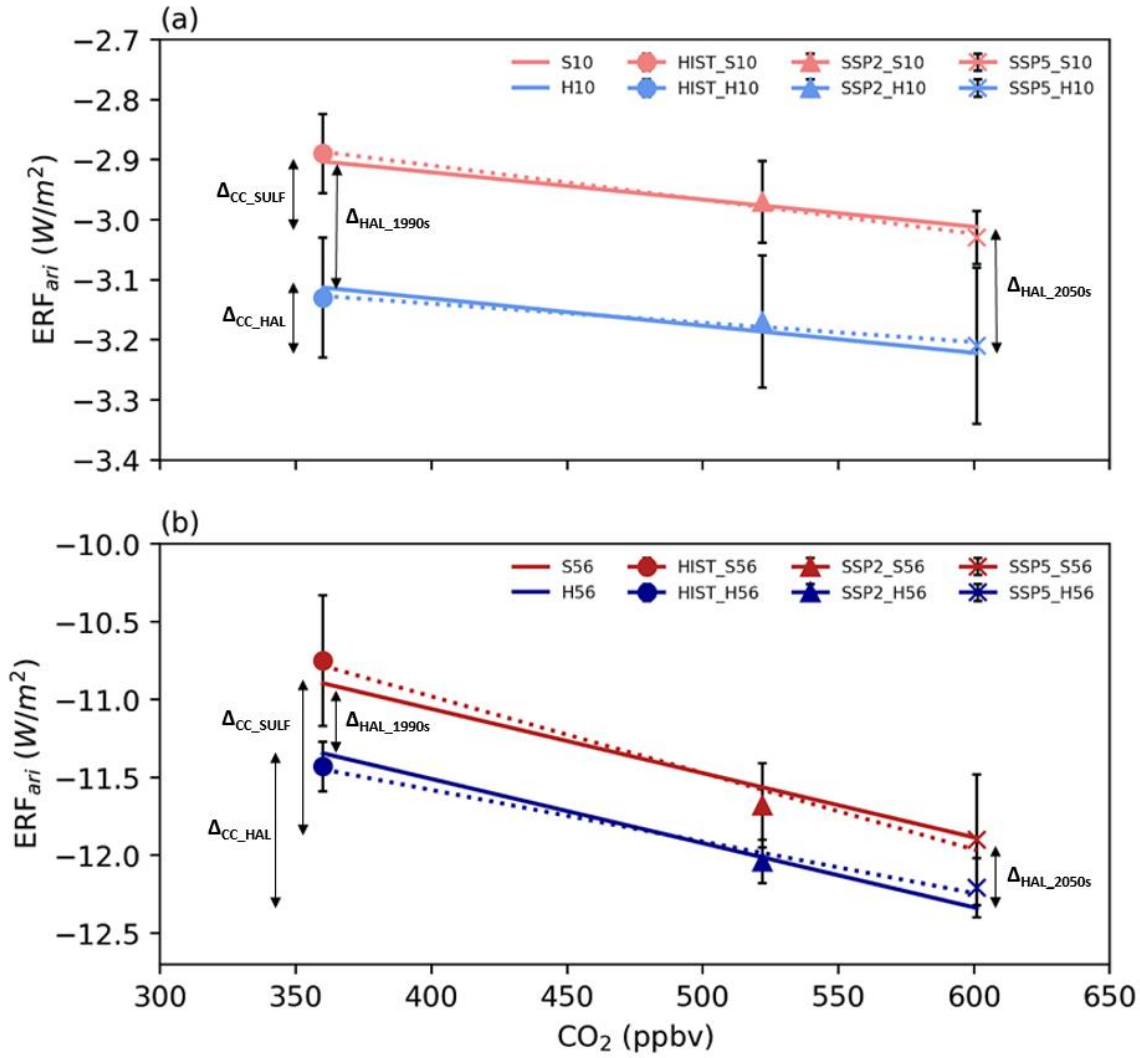

Figure 4.6 Showing the statistical models to estimate the peak global mean ERF_{ari} across atmospheric CO_2, eruption size, and eruption composition predictor variables. (a) S10 (light coral), H10 (light blue). (b) S56 (dark red), H56 (dark blue). Dotted lines show the lines of best fit calculated using ANOVA (analysis of variance) individual predictor variables. Solid lines show the adjusted lines of best fit calculated using ANOVA using the full 3 predictor variables. The effect of climate change in sulfur-only (Δ_{CC_SULF}) and halogen co-emission (Δ_{CC_HAL}) eruption scenarios and the effect of halogen co-emission in HIST (Δ_{HAL_1990s}) and future climate states (Δ_{HAL_2050s}) are indicated with double headed black arrows.

S10	$ERF_{ari} = -0.00045*CO_2 - 2.74$	(Eq. 4.3)
H10	$ERF_{ari} = -0.00045*CO_2 - 2.95$	(Eq. 4.4)
S56	$ERF_{ari} = -0.00413*CO_2 - 9.41$	(Eq. 4.5)
H56	$ERF_{ari} = -0.00413*CO_2 - 9.86$	(Eq. 4.6)

where the units of peak global mean ERF_{ari} are Wm^{-2} and CO_2 are ppbv.

These statistical models show that increasing CO_2 ($p=3.4x10^{-4}$), the magnitude of SO_2 injection ($p=6.6x10^{-13}$), and halogen co-emission ($p=2.3x10^{-3}$) significantly ($p<0.05$) amplify the peak global mean ERF_{ari}. Furthermore, a significant (<0.05) interaction was found only between CO_2 and Eruption Size ($p=1.2x10^{-3}$).

The statistical models give a good fit with the simulated results. For example, in section 3.1, we showed that climate change between HIST and SSP5 conditions amplified the peak global mean ERF_{ari} by 0.14 Wm^{-2} (+5%) in simulations in S10 and 0.08 Wm^{-2} (+3%) in H10 eruption scenarios, which compares well to the 0.11 Wm^{-2} (+4%) amplification estimated using Eq. 4.3 and 4.4 for S10 and H10 under atmospheric CO_2 concentrations representative of the 1990s (~360 ppbv) and the 2050s under SSP5 (~601 ppbv).

CO_2 works well as a continuous predictor variable in these linear statistical models as it is a good proxy for the level of anthropogenic climate change, and specifically, it is a good proxy for the acceleration of the Brewer-Dobson circulation and enhanced nucleation rate, which are the main underlying drivers of the amplification of peak global mean ERF_{ari} due to climate change. This is because both the Brewer-Dobson circulation and nucleation rate are driven by temperature. The fact that CO_2 and eruption composition show no statistically significant interaction (meaning there is not a significant difference in the slope between S10 and H10 or S56 and H56) means that the effects of climate change and halogen composition on peak global mean ERF_{ari} are not dependent processes and can be considered separately and additively. Halogens result in a constant additional peak global mean ERF_{ari} of 0.21 and 0.45 Wm^{-2} in H10 and H56 compared with S10 and S56 simulations, regardless of the CO_2 concentration. This can also be clearly shown in our UKESM-AMIP simulated results, where the amplification of peak global mean ERF_{ari} due to climate change and the co-emission of halogens (ΔCC+HAL) (e.g. SSP5_H10 - HIST_S10) is approximately equal to the sum of the individual amplification of peak global mean ERF_{ari} due to climate change and co-emission separately (ΔCC +ΔHAL) (Table 4.4). This is also reflected in the microphysical mechanism underpinning the amplification of peak global mean ERF_{ari}. In Figure 4.4, which shows the 3-year averaged global mean aerosol R_{eff} as a function of the global sulfur burden anomaly e-folding time, we find that a single linear relationship describes the effect of climate change on aerosol R_{eff} across both sulfur-only and halogen co-emission eruption scenarios. In general, future climate states (shown in red and blue) have a shorter total sulfur anomaly lifetime and smaller R_{eff} compared to HIST (black), but the co-emission of halogens (circles) results in an additional offset towards smaller aerosol R_{eff} in all climate scenarios compared to sulfur-only (triangles).

On the other hand, we find a statistically significant interaction between CO_2 and Eruption Size. This means there is a significant difference in the slope between S10 and S56 or H10 and H56 and CO_2 and Eruption Size must be considered together. A change in CO_2 was associated with a much larger change in peak global mean ERF_{ari} in S56 and H56 (-0.0041 Wm^{-2} per ppbv change in CO_2) compared S10 and H10 (-0.00045 Wm^{-2} per ppbv change in CO_2), working out to be twice as large an effect in relative terms. This can also be seen in Figure 4.4 where the slope of the line of best fit is significantly larger in 56 Tg simulations compared to 10 Tg simulations, meaning the effect of climate change has a larger impact on aerosol R_{eff} as the magnitude of the SO_2 injection increases.

4.4 Discussion

In this work we have used UKESM-AMIP simulations to report that climate change amplifies the global mean peak ERF_{ari} of explosive sulfur-only (Δ_{CC_SULF}) and halogen co-emission (Δ_{CC_HAL}) eruption scenarios, forming a

negative climate-volcano feedback loop. This is predominantly driven by faster removal of volcanic sulfur from the stratosphere and exacerbated by an increase in nucleation rate, resulting in smaller, more numerous aerosol particles that are more efficient at scattering SW radiation, consistent with Aubry et al., (under review). Furthermore, we have shown that the co-emission of halogens amplifies peak global mean ERF_{ari} in future climate states (Δ_{HAL_2050s}), as was found by Staunton Sykes et al. (2021) in a HIST climate state (Δ_{HAL_1990s}). Statistical models developed using the simulations in this work show that climate change and co-emission of halogens both significantly amplify the peak global mean ERF_{ari} of explosive volcanic eruption and with no significant interaction, suggesting the amplification effects of climate change and halogen co-emission are independent of each other and linearly additive. However, the effect of climate change on peak global mean ERF_{ari} was shown to be dependent on the magnitude of the volcanic SO_2 injection, whereby climate change amplifies the peak global mean ERF_{ari} twice as much in the very-large eruption scenarios compared with the large eruption scenarios.

The statistical models (Eq. 4.3, 4.4, 4.5, and 4.6) result in a good fit with the UKESM-AMIP simulations and allow the peak global mean ERF_{ari} to be estimated for any atmospheric CO_2 concentrations within our parameter ranges. We can also utilise these statistical models to tentatively estimate the amplification of the peak global mean ERF_{ari} in the S10, H10, S56 and H56 eruption scenarios under a range of past and future atmospheric CO_2 concentrations, shown in Table 4.5. Extrapolating outside the parameter range explored in our UKESM-AMIP simulations may lead to large errors but it remains an interesting thought experiment. Firstly, we estimate that the increase in peak global mean ERF_{ari} due to the increase in CO_2 between the pre-industrial (PI) (~280 ppbv) and the 1990s under HIST (~360 ppbv) to be 1-4%, a small but significant amplification. In other words, in our present-day atmosphere, climate change may have already amplified the cooling effect of volcanic aerosols following volcanic eruptions.

	Pre-Industrial (CO_2=280 ppmv)	**HIST Yr1990s (CO_2=360 ppmv)**	**SSP2 45 Yr 2050s (CO_2 = 522 ppmv)**	**SSP5 85 Yr 2050s (CO_2= 601 ppmv)**	**SSP2 45 Yr 2090s (CO_2 = 575 ppmv)**	**SSP5 85 Yr 2090s (CO_2= 1060 ppmv)**
S10	-2.85 **(-1%)**	-2.89	-2.97 **(+3%)**	-3.03 **(+5%)**	-3.0 **(+4%)**	-3.2 **(+11%)**
H10	-3.06 **(-2%)**	-3.13	-3.17 **(+1%)**	-3.21 **(+3%)**	-3.2 **(+3%)**	-3.4 **(+9%)**
S56	-10.56 **(-2%)**	-10.75	-11.68 **(+9%)**	-11.9 **(+11%)**	-11.8 **(+10%)**	-13.8 **(+28%)**
H56	-11.01 **(-4%)**	-11.43	-12.04 **(+5%)**	-12.21 **(+7%)**	-12.2 **(+7%)**	-14.2 **(+24%)**

Table 4.5 A table showing the peak global mean ERF_{ari} (Wm^{-2}) under different atmospheric CO_2 concentrations. The climate scenario, year and CO_2 loading are contained in the column headings and the emission scenarios are contained in the row headings. Red shading indicates where the statistical models have been used to estimate the maximum ERF_{ari}, % changes relative to the 1990s Historical values are given in brackets.

Secondly, we can estimate the amplification in peak global mean ERF_{ari} due to the increase in CO_2 between the 1990s under HIST (360 ppbv) and the 2090s under SSP5 (~1060 ppbv) to be 11% and 28% in S10 and S56 simulations. This gives good agreement with the 30% amplification of peak global mean total ERF simulated in the comparable 10 Tg SO_2 eruption scenario (SSP5_HIH) carried out in 2095 by Aubry et al. (under review). The

2 to 3 times-larger amplification of peak global mean ERF_{ari} in the 2090s than in the 2050s (5% and 11%) under SSP5 is due to the greatly enhanced CO_2 and the associated acceleration of the Brewer-Dobson circulation in the 2090s compared with the 2050s. The atmospheric CO_2 concentration is ~601 ppm in the 2050s under SSP5 and ~1060 ppm in 2090s under SSP5, an increase of 241 (+67%) and 700 (+194%) compared to the 1990s under HIST. As the acceleration of the Brewer-Dobson circulation is driven predominantly by increasing CO_2 concentration, this acceleration is significantly smaller between HIST and the 2050s than between HIST and the 2090s. This is reflected in the mean stratospheric age of air between 10-50 hPa, which is 13% younger than HIST in the 2050s under SSP5 conditions compared with 25% younger in the 2090s under SSP5 conditions (Aubry et al., under review).

The amplification of peak global mean ERF_{ari} due to climate change is only slightly larger in SSP5 compared to SSP2 at the 2050s time horizon. This is due to the relatively small difference in atmospheric CO_2 concentration in SSP2 (~522 ppbv) compared to SSP5 (~601 ppbv) and thus a small difference in the acceleration of the Brewer-Dobson circulation (Figure B3). This is reflected in the stratospheric (10-50 hPa) age of air which is 13% younger than HIST under SSP5 conditions compared to 9% younger than HIST in the 2050s under SSP2 conditions. However, larger differences in atmospheric CO_2 between SSP2 (~575 ppbv) and SSP5 (~1060 ppbv) at the 2090s time horizon lead to a 3 times-larger amplification of ERF_{ari} under SSP5 (+11% and +28%) compared with under SSP2 (+4% and +10%). These findings challenge the use of constant volcanic forcing in future climate projection experiments such as ScenarioMIP (O'Neill et al., 2016). This oversimplified approach cannot account for the negative climate-volcano feedback identified in this work.

The main finding of our work is that a reduction in volcanic sulfate aerosol lifetime due to an accelerated Brewer-Dobson circulation in the future leads to a significant increase in the peak global mean ERF_{ari} for a fixed mass of injected SO_2. Although this work only utilised simulations carried out in UKESM-AMIP, the acceleration of the Brewer-Dobson circulation due to climate change is a consistent feature of climate model projections, even though the exact magnitude of this acceleration is model-specific (Butchart, 2014; Griffiths et al., 2021). In this study volcanic gases were injected into the tropical stratosphere at a fixed height of 21 km to represent a typical tropical explosive eruption, in doing so we do not account for the changes in atmospheric plume height due to climate change shown by Aubry et al. (under review) to amplify the volcanic forcing. Furthermore, this study utilised an atmosphere-only model set-up and so does not include ocean-feedbacks which have previously been shown to amplify the surface temperature response following volcanic eruptions (Fasullo et al., 2017). As such our work is likely underestimating the full extent of the amplification effect due to climate change. Experiments combining eruptive column modelling, interactive stratospheric aerosol modelling and coupled ocean-atmosphere models would be required to fully quantify the combined effect of these climate-volcano feedbacks.

4.5 Conclusions

Sulfur gases emitted into the atmosphere by explosive volcanic eruptions are strong drivers of climate variability, but the extent to which climate change may, in turn, alter the volcanic sulfur life cycle and radiative forcing remains largely unexplored. This work investigates the radiative forcing due to volcanic sulfate aerosol (ERF_{ari})

following future tropical explosive volcanic eruptions emitting sulfur (sulfur-only) or sulfur with co-emitted halogens (halogen co-emission). We perform climate model simulations of a large- (10 Tg SO_2) and very-large-magnitude (56 Tg SO_2) sulfur-only eruption scenario and a corresponding large- (10 Tg SO_2 & 1.5 Tg HCl & 0.0086 Tg HBr) and very-large-magnitude (56 Tg SO_2 & 15 Tg HCl & 0.086 Tg HBr) co-emission eruption scenario in a historical climate state representative of the 1990s as well as a moderate and high-end future climate state representative of the 2050s. We show that climate change amplifies the peak global mean ERF_{ari} of large (+3-5%) and very-large (+7-11%) sulfur-only and halogen co-emission eruption scenarios. This is due to a reduction in aerosol size, mainly driven by a reduction in the total sulfur anomaly lifetime and associated aerosol growth, due to an acceleration of the Brewer-Dobson circulation. Furthermore, we show that the co-emission of halogens amplifies the peak global mean ERF_{ari} by 3% and 6% in future climate states, as was found by Staunton Sykes et al. (2021) in a HIST climate state.

We developed statistical models to generalise the impact of climate change on the peak global mean ERF_{ari} of eruption scenarios simulated in this work. The statistical models were shown to give a good fit with the UKESM-AMIP simulated results. The statistical models highlighted that climate change and co-emission of halogens both significantly amplified the peak global mean ERF_{ari} of explosive volcanic eruptions and with no significant interaction. In other words, the amplification effects of climate change and halogen co-emission are not dependent on each other and can be considered separately and additively. However, the effect of climate change on peak global mean ERF_{ari} was shown to be dependent on the magnitude of the volcanic SO_2 injection, whereby climate change amplifies the peak global mean ERF_{ari} twice as much in the very-large eruption scenarios compared with the large eruption scenarios. Tentative use of these statistical models outside the parameter range of the simulations in this work enables us to estimate that climate change between the pre-industrial and the 1990s may have already led to a 1-3% amplification of peak global mean ERF_{ari} and climate change between the 1990s and the 2090s may lead to a further 9-11% and 24-28% amplification of the peak global mean ERF_{ari}.

The amplification of ERF_{ari} due to climate change estimated in this study may be an underestimate as it does not account for feedbacks related to plume height and ocean-atmosphere coupling which have previously been shown to amplify volcanic forcing. This work identifies a negative climate-volcano feedback loop which may modulate climate variability driven by explosive eruptions and challenges the validity of using constant volcanic forcing in future climate projections.

Chapter 5

On the vulnerability and sensitivity of total column ozone to sulfur-only and halogen co-emission volcanic eruptions in future climate states

Abstract

Sulfur species released during explosive volcanic eruptions perturb the total ozone column (TCO), causing a net decrease under present day conditions but a net increase in future climate states. The timing of this transition is, however, poorly constrained and is dependent on the equivalent effective stratospheric chlorine (EESC) concentration. This issue is further complicated by the fact that the co-emission of volcanic halogens into the stratosphere alongside sulfur would result in TCO depletion regardless of the background climate state or EESC concentration. This work investigates the TCO response to future sulfur-only and halogen co-emission volcanic eruptions under different background climate states. We perform climate model simulations of a large (10 Tg SO_2) and very-large (56 Tg SO_2) sulfur-only eruption scenario and a corresponding large (10 Tg SO_2 & 1.5 Tg HCl & 0.0086 Tg HBr) and very-large (56 Tg SO_2 & 15 Tg HCl & 0.086 Tg HBr) co-emission eruption scenario in a historical climate state representative of the 1990s as well as a moderate and high-end future climate state representative of the 2050s. We show that TCO remains vulnerable to large and very-large sulfur-only volcanic eruption scenarios to at least the 2050s. The magnitude of TCO depletion is significantly smaller in the future reflecting the projected decline in EESC concentration but, in contrast to a previous study, we find a very similar TCO response under both the moderate and high-end warming climate futures. We also show that the ozone column is more sensitive to large and very-large volcanic halogen co-emission scenarios in the 2050s compared to the recent historical period, driven by stratospheric ozone recovery. Across both sulfur-only and halogen co-emission eruption scenarios, global mean TCO depletions are found to recover significantly faster in the future due to a faster Brewer-Dobson circulation accelerated by anthropogenic greenhouse gas emissions. This work demonstrates how the global mean TCO response to future sulfur-only and halogen co-emission volcanic eruptions is climate state dependent, with important implications for the magnitude and duration of surface UV exposure, especially in the tropics. The opposing sensitivity of future TCO to sulfur-only and halogen co-emission volcanic eruptions is in stark contrast with the large uncertainty in the flux of volcanic halogens to the stratosphere, clearly highlighting a research priority.

5.1 Introduction

The stratospheric ozone layer absorbs a large fraction of the biologically harmful ultraviolet (UV) radiation from the sun. In doing so, it protects life on Earth from DNA damage and reduces the occurrences of skin cancers, eye damage and immune system deficiencies (World Health Organization, 1994). Explosive volcanic eruptions can strongly perturb stratospheric ozone through both dynamical and chemical effects with significant implications for life on Earth (Solomon, 1999). Climate change has previously been shown to significantly amplify the

simulated radiative forcing following explosive tropical volcanic eruptions (Aubry et al. (under review) and Chapter 4), but how the total column ozone (TCO) response resulting from volcanic eruptions will be altered in future climate remains underexplored, particularly from eruptions that emit halogens alongside sulfur species into the stratosphere. Projected anthropogenic emissions during this century are expected to result in a warmer troposphere, a cooler stratosphere, an accelerated Brewer-Dobson circulation, and lower stratospheric halogen concentrations (Butchart, 2014; Dhomse et al., 2018; Oberländer et al., 2013), all of which will modify the stratospheric ozone response to volcanic eruptions. To explore the vulnerability and sensitivity of TCO in future climate states, including for the first-time halogen co-emission eruption scenarios, we present the results from climate model simulations of a large (10 Tg SO_2) and very-large (56 Tg SO_2) sulfur-only eruption scenario and a corresponding large (10 Tg SO2 & 1.5 Tg HCl & 0.0086 Tg HBr) and very-large (56 Tg SO2 & 15 Tg HCl & 0.086 Tg HBr) co-emission eruption scenario. These eruption scenarios are simulated in a historical climate state representative of the 1990s (HIST) and two future climate states representative of the 2050s. The two future climate states under investigation are moderate and high-end warming climate states respectively, defined by the Shared Socio-economic Pathway (SSP) emissions projections of greenhouse gases and halocarbons for SSP2 4.5 and SSP5 8.5 (hereafter SSP2 and SSP5).

Stratospheric ozone concentrations are determined by a combination of chemical and dynamical processes. Stratospheric ozone is produced photochemically from oxygen by UV primarily in the tropical stratosphere (Chapman, 1930) and is transported from the tropics to higher latitudes by the stratospheric Brewer-Dobson circulation (BDC) (Butchart, 2014). Stratospheric ozone production is balanced by chemical destruction via UV photolysis and catalytic loss cycles involving reactive chlorine, bromine, hydrogen, and nitrogen compounds. The source gases of chlorine and bromine radicals are emitted at the Earth's surface by natural and anthropogenic processes. Increasing consumption of industrially manufactured chlorofluorocarbons (CFCs) from the 1970s led to an accumulation of halogens in the stratosphere and the decline of stratospheric ozone globally (e.g. World Meteorological Organization, 2014). When EESC (equivalent effective stratospheric chlorine, a measure of the ozone destruction potential which includes weighted chlorine and bromine contributions; (Cadoux et al., 2015; Montzka et al., 2011; Sinnhuber et al., 2009)) concentrations peaked in the 1990s, satellites recorded a 7% per decade decline in stratospheric ozone over the northern hemisphere mid-latitudes, and a 5% reduction in global mean TCO compared to the 1964-1980 average (World Meteorological Organization, 2014). The unique and specific meteorological and chemical conditions over Antarctica increased the effectiveness of ozone destruction via reactive halogens, making the Antarctic particularly sensitive to the increases in EESC (Langematz, 2019). Persistent cold temperatures in the isolated polar vortex over Antarctica enable the formation of Polar Stratospheric Clouds (PSCs), creating surface area on which heterogeneous reactions can take place (Crutzen and Arnold, 1986; Solomon, 1999). Heterogeneous reactions in the stratosphere drive changes in the partitioning of NOx, ClO_x, BrO_x and HO_x species between reservoir and active forms. Heterogeneous reactions on the surfaces of the PSCs convert nearly all the available chlorine and bromine into reactive forms (e.g. Molina and Molina, 1987; Solomon et al., 1986) leading to severe ozone depletion annually in the late winter and early spring at southern polar latitudes, commonly referred to as the Antarctic ozone hole (Farman et al., 1985).

Scientists, politicians, and key industry members quickly recognized the threat posed by declining TCO, and in 1987 the Montreal Protocol was ratified by the United Nations member states. The Montreal protocol set out regulations to phase out the production of numerous substances that are responsible for stratospheric ozone depletion. The protocol, and subsequent amendments, has been very successful, and it is seen as a decisive turning point. A slow recovery in stratospheric ozone has been observed since the 2000s (World Meteorological Organization, 2014). The global mean TCO will return to its 1980 benchmark at about the same time as the EESC concentration reaches its 1980 benchmark. This is projected by climate models with interactive chemistry to be roughly the 2050s globally and 2060s over Antarctica (Dhomse et al., 2018). As the EESC concentrations decline over coming decades, ozone will become increasingly affected by climate change. Rising greenhouse gas (GHG) concentrations will cool the stratosphere and strengthen the stratospheric BDC (e.g. Oberlander et al., 2013), reducing the chemical gas-phase depletion of ozone and enhancing the poleward transport of ozone. This will lead to an acceleration of stratospheric ozone recovery to its 1980 benchmark and beyond, especially at the poles (Meul et al., 2016).

Sulfur gases emitted into the stratosphere by explosive volcanic eruptions have a strong direct climate impact through the formation of sulfate aerosol, which reflect incoming radiation from the sun and cool the Earth's surface (Robock, 2000). Volcanic aerosols also have the potential to perturb TCO. The particularly large (5%) reduction in global mean TCO in 1991 was caused by the effects of the Mt. Pinatubo volcanic eruption in the Philippines. The addition of large amounts of volcanic aerosols into the stratosphere increases the surface area on which heterogeneous reactions can take place (Solomon, 1999). Unlike polar stratospheric clouds (PSCs), which only occur in the extremely cold temperatures inside the winter polar vortex, volcanic aerosols provide surfaces for heterogeneous reactions at all latitudes and at all times of the year. N_2O_5 (a reactive nitrogen intermediate) reacts with water vapour on the surfaces of these volcanic aerosols to form HNO_3. This sequesters reactive NO_x species into a long-lived reservoir and limits the availability of NO_x radicals to take part in the catalytic loss reactions which deplete stratospheric ozone, reducing the chemical destruction of ozone (Crutzen, 1970; Johnston, 1971). However heterogenous reactions also liberate reactive ClO_x and BrO_x species from their long-lived reservoirs, increasing the chemical destruction of ozone (Aquila et al., 2013; Solomon, 1999; Solomon et al., 1996). The net chemical impact of stratospheric volcanic aerosol loading on TCO is dependent on the EESC concentration, stratospheric temperature and the concentration of halogen sinks such as methane. The present-day atmosphere remains in a window of elevated EESC caused by the anthropogenic release of halogens into the atmosphere during the second half of the twentieth century. During this window, large explosive eruptions that inject sulfur into the stratosphere (hereafter sulfur-only) result in TCO depletion, but in the future, when EESC concentrations have recovered, sulfur-only explosive volcanic eruptions will have the opposite effect and result in an increase in TCO. However, the timing of this transition is poorly constrained, with previous estimates ranging from 2015 to beyond 2040 (Naik et al., 2017; Rosenfield, 2003; Tie and Brasseur, 1995). Pitari et al. (2014) suggested that the transition may occur after 2050, although this was deduced from a model intercomparison study of sulfur geo-engineering scenarios rather than volcanic emission. Klobas et al. (2017) used a 2D chemical transport model (CTM) to explore the sensitivity of the volcanic TCO response to climate change in future background climate states as defined by Representative Concentration Pathways (RCPs). Klobas et al. (2017) simulated hypothetical 1991 Pinatubo-sized sulfur-only eruptions in four different climate futures and

showed that optimistic climate scenarios with lower greenhouse gas emissions yielded larger TCO losses compared to scenarios with more greenhouse gases. This was due to slower reaction kinetics driven by a decrease in stratospheric temperature and a reduction in active chlorine resulting from enhanced stratospheric methane concentrations. Klobas et al. (2017) ran their simulations using historically averaged climatological transport fields and, as a result, did not include any changes in stratospheric circulation due to climate change or volcanic aerosol heating. Accounting for such feedbacks may be important because of the role dynamics play in the distribution of ozone and the lifetime of volcanic species in the stratosphere.

Petrological data suggest that volcanic eruptions in some geological settings often release substantial amounts of halogen gases into the atmosphere alongside SO_2 (hereafter halogen co-emission) (Krüger et al., 2015; Kutterolf et al., 2013, 2015). Although co-emitted volcanic halogens are efficiently scavenged by hydrometeors in the plume, direct stratospheric injection of volcanic halogens is predicted theoretically (Textor et al., 2003) and has been observed following eruptions in the satellite era (Carn et al., 2016; Hunton et al., 2005; Prata et al., 2007; Read et al., 2009; Rose et al., 2006). Overall, current datasets show that the stratospheric injection of volcanic halogens is highly variable and depends on both the total mass of halogens released at the vent and the degree of scavenging, determined by the geochemistry of the volcano and the prevailing atmospheric conditions during the eruption, particularly the humidity. It is clear, however, that volcanic halogens are injected into the stratosphere after some volcanic eruptions and research into how these volcanic halogens may alter the TCO is still limited, especially following future eruptions. See Chapter 2 for a more detailed discussion of volcanic halogen emissions.

Numerous studies have assessed the role of co-emitted halogens on TCO in pre-industrial climate states (e.g. Brenna et al., 2019; Cadoux et al., 2015; Ming et al., 2020), but only Klobas et al. (2017) has investigated the response in future climate states. They simulated hypothetical 1991 Pinatubo-sized volcanic eruptions with co-emitted stratospheric halogens ($HCl:SO_2$ of ~0.14) in a range of future background climate states defined by the RCPs. However, they only reported the fact that significant reductions in global mean TCO would result regardless of the year or the particular future climate.

In this study we explore the vulnerability and sensitivity of TCO to volcanic eruptions in future climate states, including for the first-time halogen co-emission eruption scenarios. We report that TCO remains vulnerable to large- and very-large-magnitude sulfur-only volcanic eruption scenarios to at least the 2050s under SSP2 and SSP5, although the sensitivity is significantly reduced compared to HIST due to the decline of atmospheric EESC concentrations. Conversely, we show that the ozone column is more sensitive to volcanic halogen emissions in both SSP2 and SSP5 future climate states compared to HIST, due to stratospheric ozone recovery. In both sulfur-only and halogen co-emission simulations, the TCO anomalies recover faster in SSP2 and SSP5 future climates compared to HIST. This is due to the faster removal of the volcanic sulfur, and halogens driven by a faster BDC accelerated by global warming.

5.2 Methods

5.2.1 Experimental Design

Our study utilises the HIST, SSP2 and SSP5 UKESM-AMIP time-slice experiments as described in Chapter 2. The HIST control simulation was run using the January 1995 initialisation file and climatologies calculated using data from the fully coupled UKESM1.0 historical runs produced for CMIP6 (Eyring et al., 2016) and averaged over the years 1990 to 2000. SSP2 and SSP5 control simulations were run using the January 2055 initialisation file and climatologies calculated using data from the fully coupled UKESM1.0 ScenarioMIP runs produced for CMIP6 (Eyring et al., 2016) and averaged over the years 2050 to 2060. By averaging over a decade, the atmosphere-only simulations are forced with boundary conditions typical of the period but not a specific date within that decade. In each case, the model was allowed to spin up for 15 years and the control was run for a further 20 years. In this work, climate change is inferred from the difference between the future (SSP2 and SSP5) and HIST control climatologies. Differences in the background column ozone between the control climatologies are shown in Figure 5.1, and other key differences are highlighted in Table 5.1. The effect of explosive volcanic eruptions was investigated by running three 10-year volcanic perturbation simulations spun off from three different years in the control run to sample the variability in QBO states. Changes are plotted as the difference between the average of the ensemble members and a climatology derived from the 20-year control run. Ensemble ranges are included as envelopes where appropriate.

The volcanic emissions are prescribed by direct injection of SO_2, HCl and HBr into the stratosphere with a Gaussian plume vertical distribution centred on 21 km and a width of 2.1 km (10% of the height) (Aubry et al., 2019), lasting for 24 hours on July 1st. An injection altitude of 21 km was chosen as, allowing for radiative lofting of the sulfate aerosol particles, this results in a volcanic sulfate plume altitude consistent with the 1991 eruption of Mt. Pinatubo (Guo et al., 2004). The gases were injected in the tropics (5^{o}S latitude and 0^o longitude) to represent a typical tropical explosive eruption (Newhall et al., 2018). The impacts of very-short-lived Bromine species are accounted for by adding a fixed contribution of 5 pptv into the CH_3Br surface concentration.

	HIST (1990s)	**SSP2 4.5** (2050s)	**SSP5 8.5** (2050s)
CO_2 (ppbv)	360	522 (+45%)	601(+67%)
Methane (ppbv)	695	819 (+18%)	1064 (+53%)
SWV (ppbv)	6.8	9.0 (+32%)	10.1 (+49%)
OH (pptv)	0.21	0.24 (+14%)	0.27 (+28%)
EESC (ppbv)	4.5	2.7 (-39%)	2.6 (-41%)
Ozone Column (DU)	306	328 (+7%)	333 (+9%)
Age of Air @ 10-50 hPa (Years)	4.5	4.1 (-9%)	3.9 (-13%)
Stratospheric Temp @ 10-50 hPa (^{o}K)	211	209 (-1%)	208 (-1.5%)

Table 5.1 Overview of the HIST, SSP2 and SSP5 control simulations. Showing the key differences between the HIST, SSP2 and SSP5 control climatologies. EESC is calculated as a global stratospheric mean, methane SWV and OH are calculated as whole-atmosphere means, Age of Air and Stratospheric temperature are calculated as mid-stratosphere means (10-50 hPa). Control run values are in the absence of any volcanic eruptions.

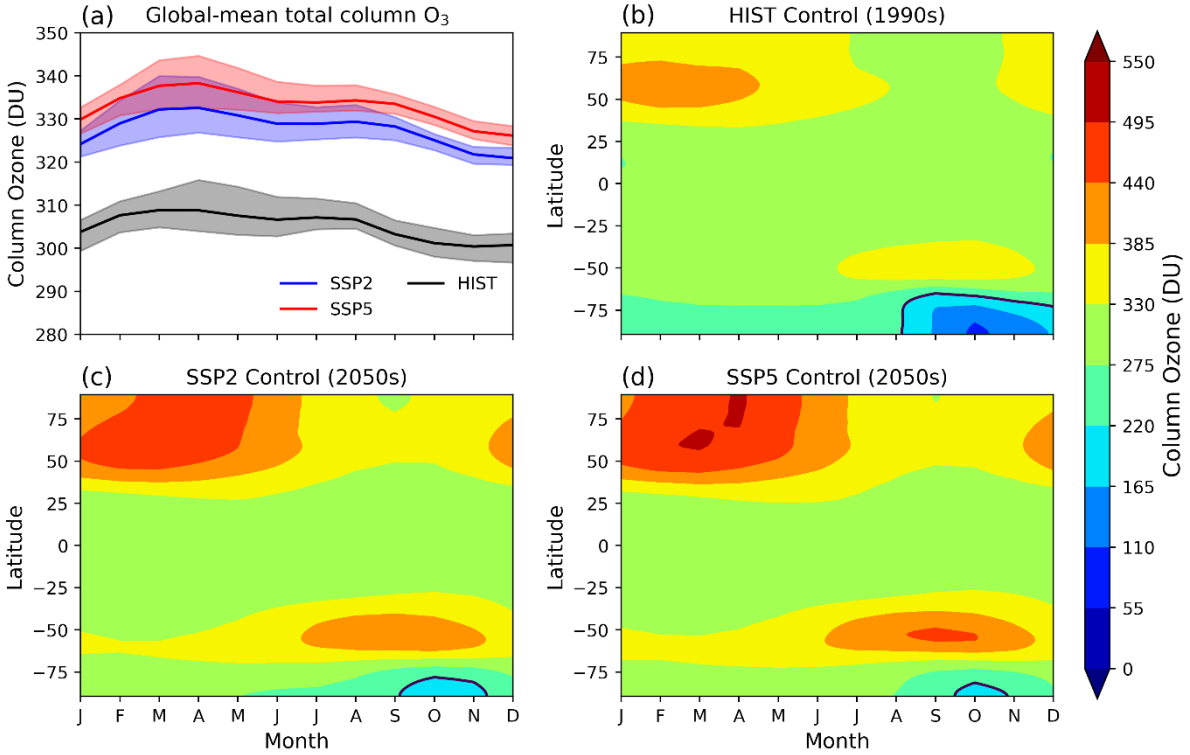

Figure 5.1 Global mean column ozone (a) in HIST control (black), SSP2 control (blue) and SSP5 control (red) climatologies. Shading represents the full range in the control simulations. Zonal mean column ozone in HIST control (b), SSP2 control (c), and SSP5 control (d) climatologies. Ozone hole conditions are simulated when column ozone is <220 DU, indicated by thick black lines. These data highlight the larger global mean TCO levels in the 2050s.

Since historical stratospheric volcanic SO_2 fluxes are variable and the volcanic flux of HCl and HBr into the stratosphere remains uncertain, we developed a simulation matrix that spans a range of plausible explosive volcanic emissions, as outlined in Chapter 2. The four sets of experiments have one large-magnitude SO_2 (10 Tg), and one very-large-magnitude SO_2 (56 Tg) emission scenario both with (H10 and H56) and without halogens (S10 and S56), as shown in Table 5.2. These eruptions (10 and 56 Tg SO_2) are hypothetical, but their magnitudes are comparable to a VEI 6 (e.g. 1991 Mt. Pinatubo) and VEI 7 (e.g. 1257 Mt. Samalas) eruption, representing 1 in 50-100 year and 1-in-500-1000-year events respectively (Newhall et al., 2018). Experiment identifiers used in this work are formed by combining the background climate and eruption scenario identifiers, as shown in Table 5.3.

Scenario	SO_2 (Tg)	HCl (Tg)	HBr (Tg)	HCl:SO_2
S10	10	-	-	-
H10	10	1.5	0.0086	0.26
S56	56	-	-	-
H56	56	15	0.086	0.47

Table 5.2 Showing the eruption masses of SO_2, HCl and HBr in Tg and HCl:SO_2 (relative mixing ratio) for the four sets of experiments.

Experiment identifier Key	**Climate Scenario**		
Eruption Scenario	**HIST**	**SSP2 4.5**	**SSP5 8.5**
S10	HIST_S10	SSP2_S10	SSP5_S10
H10	HIST_H10	SSP2_H10	SSP5_H10
S56	HIST_S56	SSP2_S56	SSP5_S56
H56	HIST_H56	SSP2_H56	SSP5_H56

Table 5.3 Showing the full simulation matrix utilised in our study. Experiment identifiers are formed by combining the climate scenarios (column headings) and emission scenarios (rows)

5.3 Results

5.3.1 Total column ozone changes following future sulfur-only volcanic eruptions

The peak global mean TCO depletion following large- and very-large-magnitude sulfur-only volcanic eruptions is projected to be 30% smaller in SSP2 and SSP5 future climates compared to HIST. We simulated peak global mean TCO depletions of 8 DU (2.5%) in both SSP2_S10 and SSP5_S10 and 13 DU (4.0%) in both SSP2_S56 and SSP5_S56 compared to 11 DU (3.2%) in HIST_S10 and 16 DU HIST_S56 (5.0%), respectively (Figure 5.2). TCO depletion occurs at all latitudes, but with the largest changes in the tropics and the poles (Figure 5.2). The reduction in ozone depletion following future eruptions is largely the result of smaller depletion in the tropics, where depletions of up to 7.5% and 15% were simulated in HIST_S10 and HIST_S56, compared with depletion of up to 5% in SSP2_S10 and SSP5_S10 and 12.5% in SSP2_S56 and SSP5_S56, respectively (Figure 5.2, S15). Large losses of up to 30% were simulated in the Arctic and Antarctic spring but these are insignificantly different across the background climate states (Figure C15). TCO recovers faster in future climate states compared to HIST, with an e-folding recovery time of up to 3 years in future climate states under SSP2 and SSP5 compared to 4 years in HIST (Figure 5.2). The faster recovery in the future is particularly clear in the tropics where the ozone depletion persists for up to 3 years in SSP2_S56 and SSP5_S56 compared to 4 in HIST_S56.

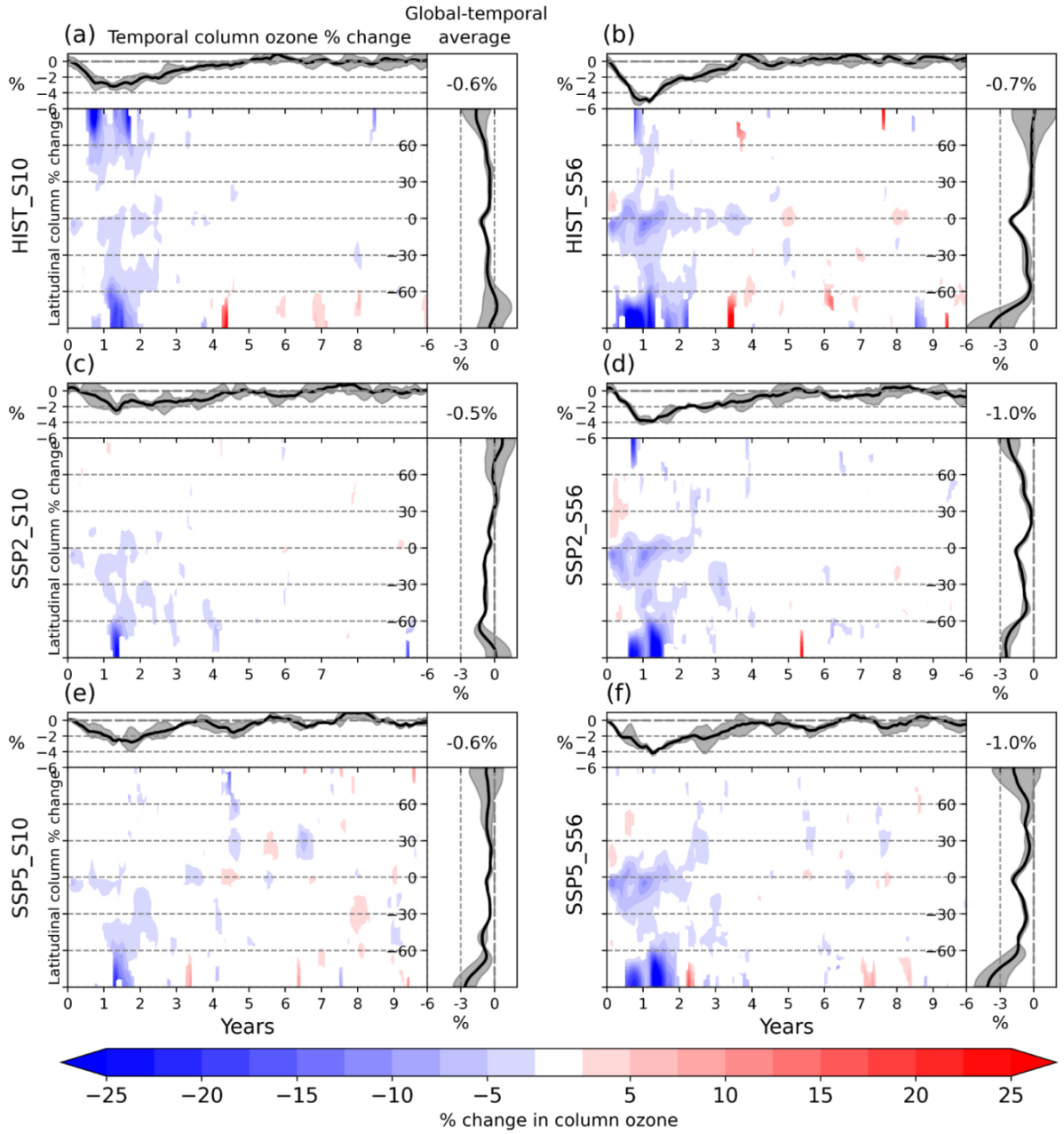

Figure 5.2 Total column ozone % difference in response to the simulated sulfur-only volcanic eruptions relative to the control climatologies, (a) HIST_S10, (b) HIST_S56, (c) SSP2_S10, (d) SSP2_S56, (e) SSP5_S10, (f) SSP5_S56. Global mean total column ozone perturbations are traced atop each panel as a function of time. Temporal average ozone anomalies are traced on the right. Global-temporal averages are enumerated in the top right. Red colours indicate total column ozone enhancement, and blue colours indicate total column ozone depletion relative to the control climatology.

The 30% smaller global mean TCO depletion in the future is predominantly caused by reduced chemical destruction via ClO_x throughout the entire stratosphere (~15 to 50 km) and BrO_x loss cycles in the lower stratosphere (~15 to 20 km) compared to HIST (Figure C14). This is driven by a 40% lower EESC concentration under both SSP2 (2.7ppbv, -38%) and SSP5 (2.6 ppbv, -42%) compared to HIST (4.5 ppbv) (Table 5.1). The lower EESC concentrations in the future mean that up to 50% less ClO_x is liberated from background reservoir species via heterogeneous reactions on the surface of volcanic aerosol (Figure 5.3a,b) resulting in up to 50% less ozone destruction via ClO_x loss cycles compared to in HIST (Figure 5.3c,d).

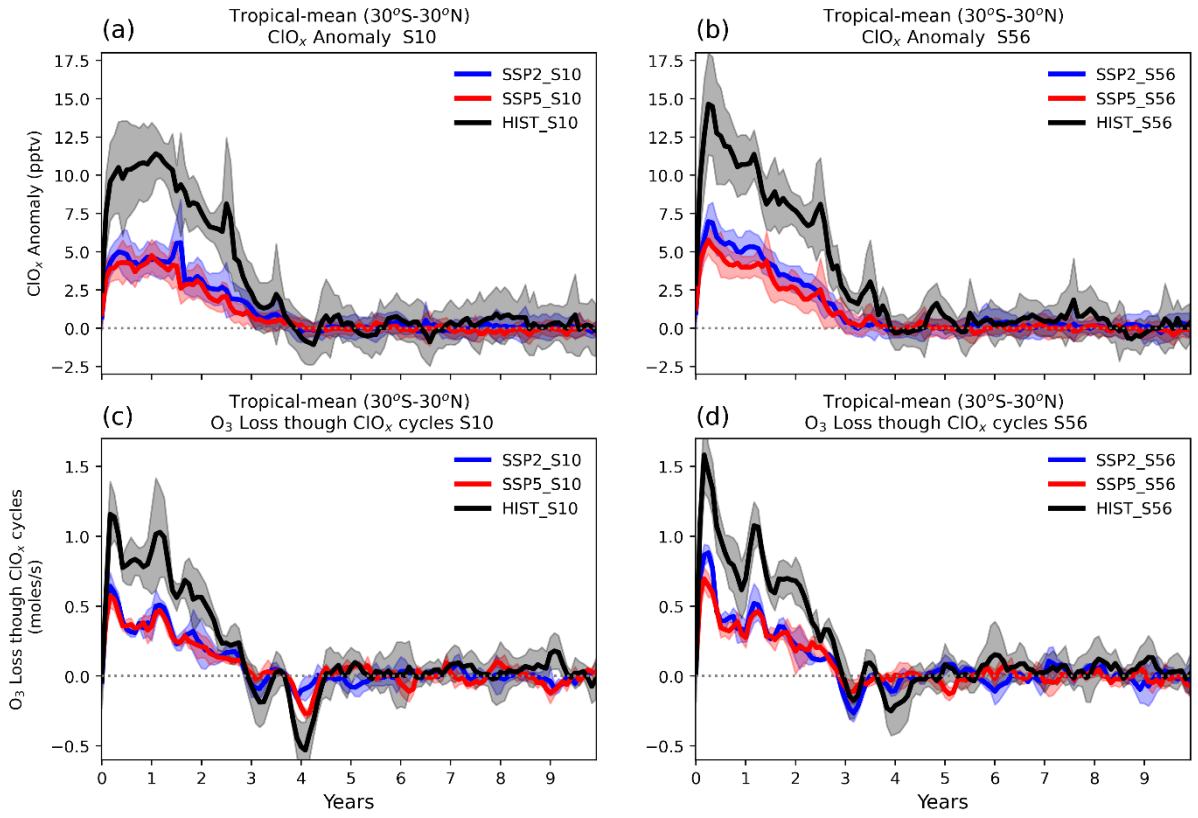

Figure 5.3 Time-series of tropical mean (30°S-30°N) ClO_x anomaly between 20-30 km relative to the control climatologies, a) large- and b) very-large-magnitude sulfur-only eruption scenarios. Time-series of tropical mean (30°S-30°N) ClO_x O_3 loss anomaly at 30 km relative to the control climatology c) large- and d) very-large-magnitude sulfur-only eruption scenarios.

Our model simulations suggest that TCO remains vulnerable to explosive sulfur-only volcanic eruptions to at least the 2050s under SSP2 and SSP5, decades longer than early estimates which ranged from 2015 to beyond 2040 (Naik et al., 2017; Rosenfield, 2003; Tie and Brasseur, 1995) but in agreement with the more recent study by Klobas et al. (2017) which reported ozone vulnerability following a 7 Tg SO_2 eruption to at least 2071 under RCP6.0. Despite still resulting in net ozone depletion, the magnitude of the peak global mean TCO depletion is 30 % smaller in the 2050s under both SSP2 and SSP5 compared to HIST, reflecting the decline in EESC concentrations.

However, unlike Klobas et al. (2017), who simulated stark differences in the ozone response at the 2100 time horizon under different climate futures, namely net ozone loss under RCP4.5 and net ozone gain under RCP8.5, we simulate very little difference between the peak global mean ozone depletion in SSP2 (SSP equivalent of RCP4.5) and SSP5 (SSP equivalent of RCP8.5) at the 2050s time horizon. Klobas et al. (2017) attributed the differences primarily to reduced reaction kinetics due to the lower stratospheric temperature in RCP8.5, with the remainder largely due to the higher methane mixing ratio, as methane reacts with Cl radicals in the stratosphere to terminate the ClO_x ozone loss cycle. At the 2100 time horizon used in Klobas et al. (2017), the stratospheric temperature is 3.4K cooler and the stratospheric methane is 1318 ppbv (+140%) higher under RCP8.5 (230.0 K,

2240 ppbv) compared to under RCP4.5 (234.4K, 922 ppbv). In contrast, at the 2050s time horizon in our study, the differences are much smaller. The stratospheric temperature is only 1K cooler (Figure C6) and the global mean methane concentration is ~250 ppbv (+30%) higher (Figure C3) in SSP5 compared to SSP2 (Table 5.1). Instead, the TCO response at the 2050s time horizon is driven by very similar ClO_x concentration and ClO_x ozone loss flux anomalies (Figure 5.3) (and also BrO_x concentration and BrO_x ozone loss flux anomalies, not shown). While we would expect to simulate the same results as Klobas et al. (2017) at the 2100 time horizon, our results suggest the differences in stratospheric temperature and methane concentrations between SSP2 and SSP5 at the 2050s time horizon are not large enough to cause a significant difference in the ozone response to sulfur-only volcanic eruptions, and instead the response is dominated by the similar EESC concentrations.

5.3.2 Total column ozone changes following future volcanic eruptions with halogen co-emission

Halogen co-emission eruptions result in large global mean TCO depletion regardless of the background climate state; however, the magnitude is larger in SSP2 and SSP5 future climates compared to HIST and the timeline for recovery is shorter (Figure 5.4). The maximum global mean TCO depletion was 15% and 18% larger in SSP5_H10 (-75 DU) and SSP5_H56 (-200 DU) than in HIST_H10 (-65 DU) and HIST_H56 (-170 DU) with a recovery e-folding time of 2.5 years in both SSP5_H10 and SSP5_H56 compared with 3 years and 3.5 years in HIST_H10 and HIST_H56 (Figure 5.5a,b).

TCO depletion peaks and recovers in the tropics (20ºS-20ºN) first, reaching a maximum within the first year followed by a gradual recovery over the course of up to 6 years (Figure 5.4). In both the Arctic and Antarctic, TCO losses were simulated to be significant at all times of the year but overprinted by a strong seasonal cycle with the largest anomalies simulated in the spring. The larger global mean TCO depletions simulated in the future are replicated in the tropics (Figure 5.5b,c), Arctic (Figure 5.5e,f) and particularly in the Antarctic (Figure 5.5g,h) where the peak TCO depletion is more than double in future climate states compared to in HIST.

Compared to HIST, TCO recovers faster at all latitudes, but it is particularly clear in the tropics, where climate change results in a 20-30% faster recovery in both SSP2 and SSP5 future climate states (Figure 5.4,5.5).

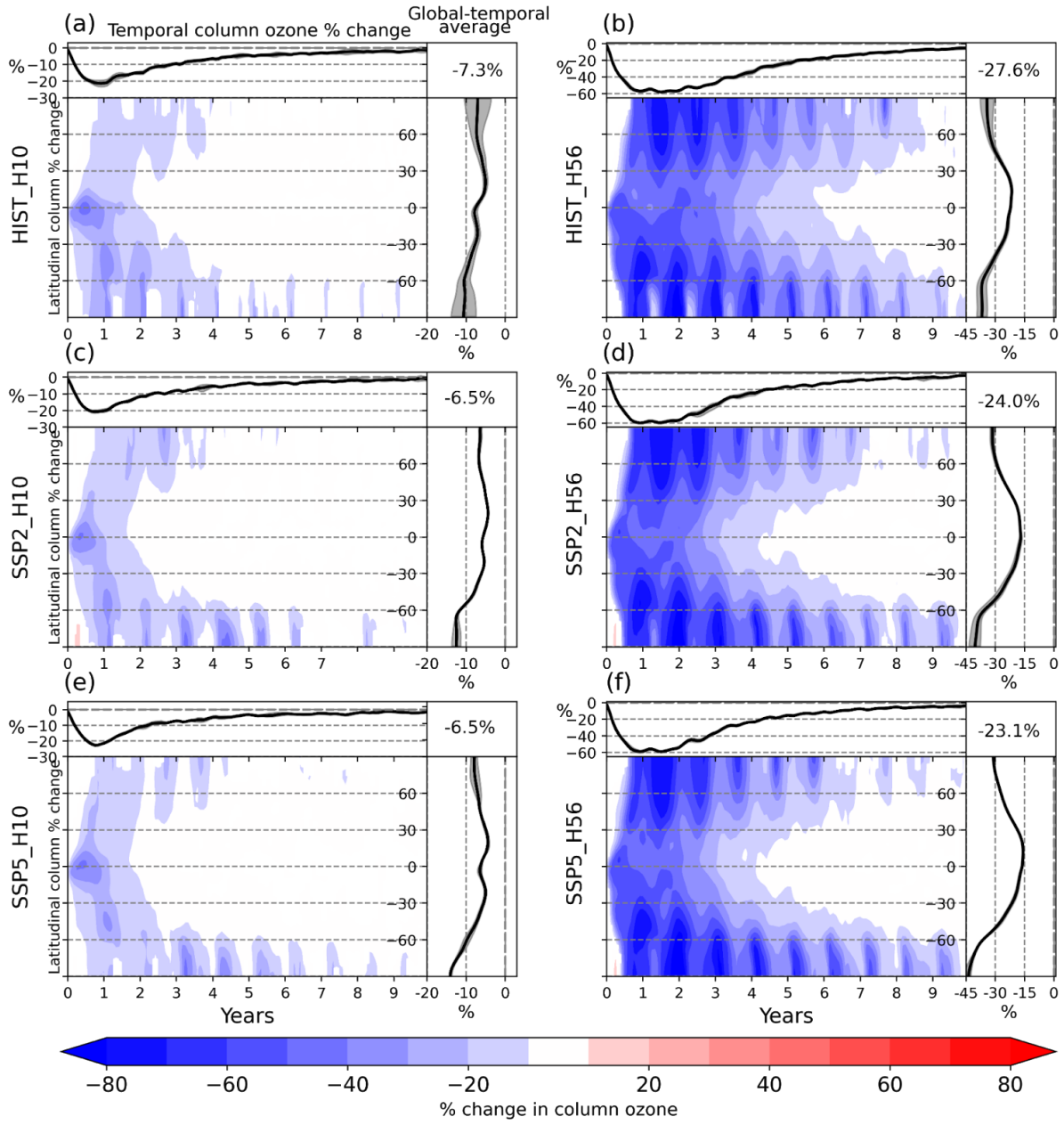

Figure 5.4 Total column ozone % difference in response to the simulated volcanic eruptions relative to the control climatologies, (a) HIST_H10, (b) HIST_H56, (c) SSP2_H10, (d) SSP2_H56, (e) SSP5_H10, (f) SSP5_H56. Global mean total column ozone perturbations are traced atop each panel as a function of time. Temporal average total column ozone anomalies are traced right, note different scales. Global-temporal averages are stated in the top right. Red colours indicate total column ozone enhancement, and blue colours indicate total column ozone depletion relative to the control climatology.

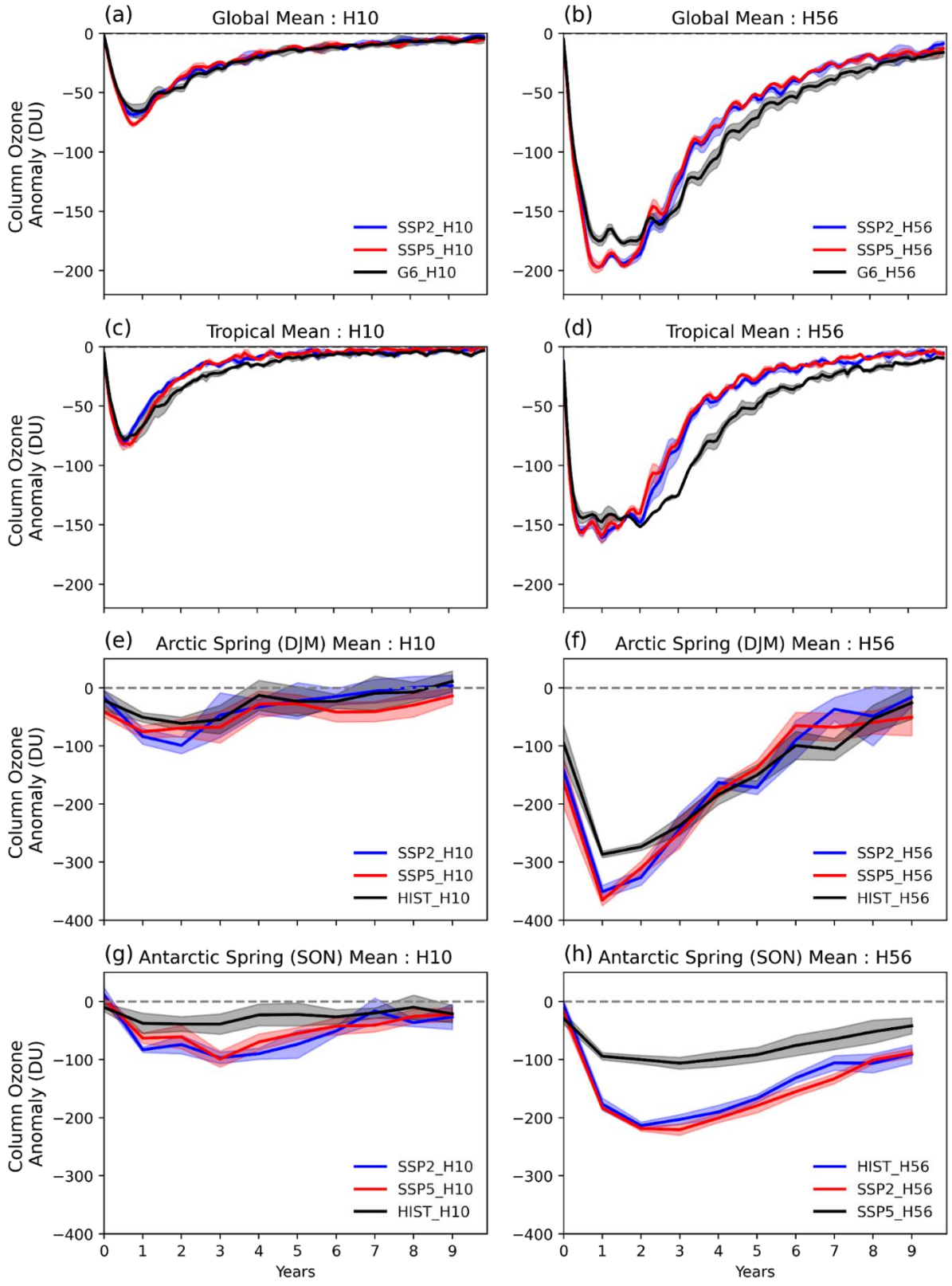

Figure 5.5 Evolution of global mean, tropical-mean (30°S-30°N), Arctic-spring-mean (90°S-60°S), Antarctic-spring-mean (60°N-90°N) total column ozone anomaly in HIST_H10, SSP2_H10 and SSP5_H10 shown in (a,c,f, and g respectively) and HIST_H56, SSP2_H56 and SSP5_H56 shown in (b,d,e, and f respectively) relative to the control climatologies.

Halogen co-emission eruption scenarios dramatically, but temporarily, increase the atmospheric EESC relative to the background EESC in both HIST and future atmospheres. As a result, the decline of background atmospheric EESC plays little direct role in the different TCO response in future climate states. Instead, the increased sensitivity of TCO to halogen co-emission in the future is a product of the future stratospheric ozone recovery which results in background global mean TCO that is 10% and 11% larger in the 2050s under SSP2 (~328 DU) and SSP5 (~333 DU) compared with HIST (~300 DU) (Figure 5.1). The co-emission of volcanic halogens results in near total stratospheric ozone depletion at ~20km in the tropics (Figure C8) and ~15km at the poles (Figure C9 and C10), leading to larger absolute TCO depletion in future reflecting the greater background ozone column. Future stratospheric ozone recovery takes place at all latitudes, but it is most pronounced in the Antarctic polar region where only a small and short-lived ozone hole (<220 DU) remains in the spring (Figure 5.1). As such, although the increased TCO sensitivity is seen in the tropics (Figure C11) and Arctic (Figure C12) it is most extreme and best showcased in the Antarctic (60°S-90°S) spring. Here, the mean TCO anomaly was 2.5 times-larger in SSP5_H56 (-250 DU) compared with HIST_H56 (-100 DU) and 2 times-larger in SSP5_H10 (-100 DU) compared with HIST_H10 (-55 DU) (Figure 5.6).

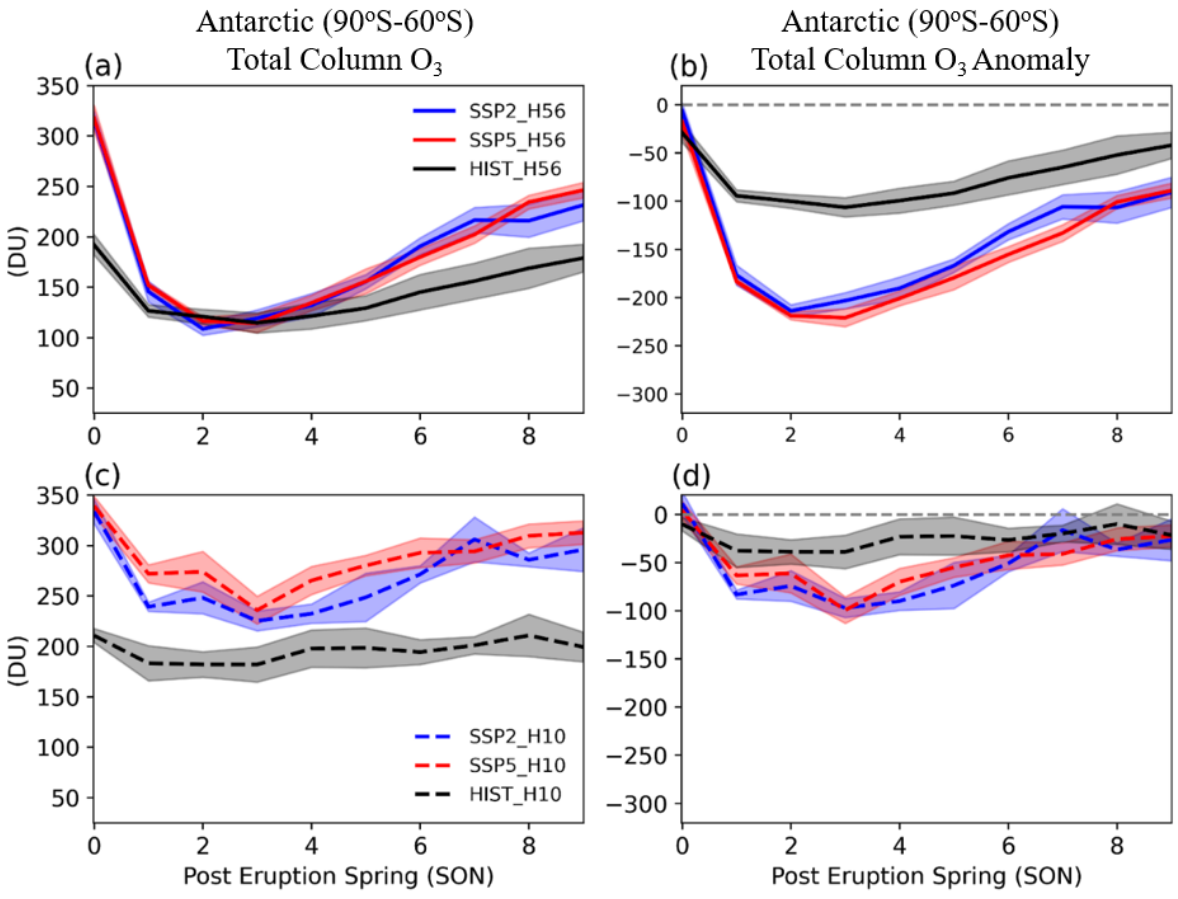

Figure 5.6 Timeseries of Antarctic (90°S-60°S) Spring (SON) mean total column ozone (left) and anomalies relative to the control climatology (right) relative to the control climatologies. Very-large co-emission scenarios (H56) are shown in solid lines, large co-emission scenarios (H10) are shown in dashed lines.

TCO following co-emission scenarios, and the corresponding UV flux incident on the surface of the Earth, is a combination of both the background ozone column and the change in TCO due to the eruption. Thus, the TCO depletion results in a smaller ozone column and deeper, more extensive ozone holes in HIST_H10 compared to SSP5_H10 (Figure 5.7). The very large increase in atmospheric EESC concentrations in HIST_H56 and SSP_H56 simulation causes near total ozone column collapses in some areas, regardless of the initial ozone background column. For example, across HIST_H56, SSP2_H56, and SSP5_H56, TCO bottoms out at ~140 DU in the tropics (Figure C12), ~100 DU in the Arctic (Figure C12), and ~90 DU in Antarctica (Figure 5.6) suggesting that the TCO loss has been saturated in these regions. As a result, we simulated a similar ozone column minimum and global ozone hole conditions in both HIST_H56 and SSP5_H56. The faster recovery of TCO in the future is clearly visible, with shorter-lived ozone holes across both eruption sizes.

TCO depletion on this scale would dramatically increase the flux of harmful UV to the surface, which could cause DNA damage to animals and plants, and increase the occurrences of skin cancers, eye damage and immune system deficiencies among the population (World Health Organization, 1994). Climate modelling and environmental proxies showed that ozone depletion as a result of halogen degassing during the emplacement of Siberian Traps flood basalts led to ozone depletion that stressed ecosystems and caused DNA mutations which may have contributed to the end-Permian mass extinction (Black et al., 2014). A simple heuristic relating TCO to clear-sky surface UV index is given by:

$$\text{UV Index} = 12.5\mu_o^{2.42}\,(\Omega/300)^{-1.23} \qquad \text{(Eq. 5.1)}$$

as defined in (Madronich, 2007), where μ_o is the cosine of the solar zenith angle and Ω is the total vertical ozone column in Dobson units. The monthly mean average UV index coloured by World Health Organization categories (Low [0 to 2], Medium [3 to 5], High [6 to 7], Very High [8 to 10], and Extreme [11+]) is shown in Figure 5.7. This shows that on average 'Very High' or 'Extreme' UV levels would be expected all day for much of the globe in the three to four summers after the eruption in H10 and H56 eruption scenarios respectively, with noon values being even higher. Living with the high levels of UV exposure simulated here would cause immediate immunosuppression, epidemic outbreaks, increases in the occurrences of eye damage and, in the longer term, skin cancers among the population living between the Equator and the mid-latitudes, which equates to >95% of the global population. Although this simple heuristic does not resolve differences in the peak UV exposure, it does clearly track the faster recovery of the UV index in future climate states reflecting the faster recovery of TCO, greatly reducing the duration of elevated surface UV exposure with important consequences for the people living between the impacted latitudes. The assessment of surface UV changes is made more challenging by the presence of volcanic aerosols, which also scatter UV radiation (Banda et al., 2015; Visioni et al., 2017). However, the enhanced aerosol burden is short lived compared to the column ozone anomalies. The volcanic aerosol levels reduce rapidly after peaking in the first post-eruption year whereas the column ozone anomalies take up to 10 years to recover.

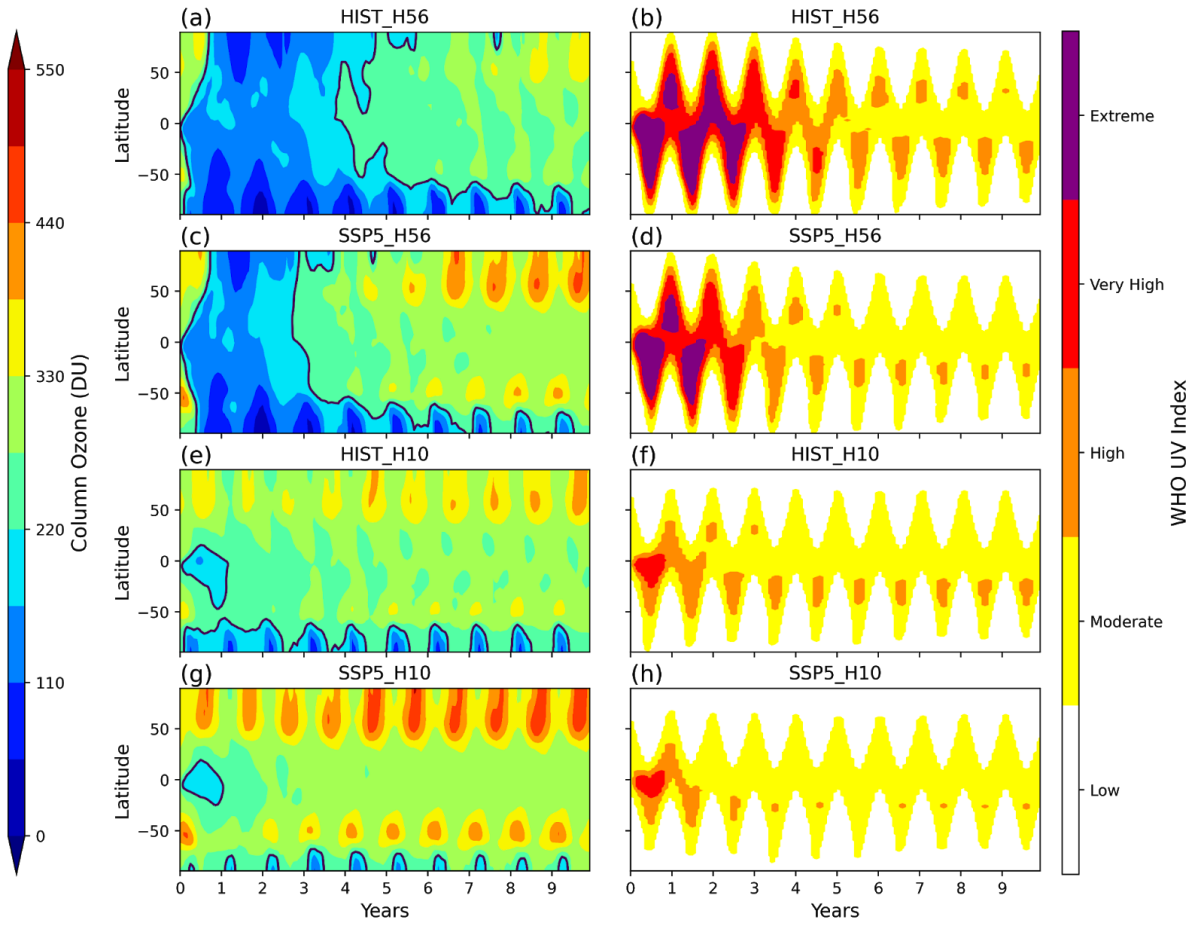

Figure 5.7 Longitudinal mean total column ozone and WHO UV Index in HIST_H56 (a,b), SSP5_H56 (c,d), HIST_H10 (e,f), SSP5_H10 (g,h). Solid lines indicate the location of ozone holes (< 220 DU).

5.4 Discussion

In this study we show how the TCO response to large- and very-large-magnitude volcanic eruption scenarios will be different in moderate (SSP2) and high-end (SSP5) future climate states representative of the 2050s compared to a historical climate state representative of the 1990s (HIST). One constant feature across the results reported in our study is that all the perturbations in stratospheric chemistry recover faster in future climate states. All stratospheric chemistry perturbations are the result of either the volcanic halogens or sulfur or both, as such, the recovery timescale of these perturbations mirrors the recovery timescales of the volcanic sulfate and halogen anomalies (e.g. EESC). The e-folding time of the total sulfur burden anomaly is 5% and 7% shorter in SSP5_S10 and SSP5_S56 compared with HIST_S10 and HIST_S56 (see Chapter 4) and the e-folding time of the EESC concentration anomaly is 30% and 24% shorter in SSP5_H10 and SSP5_H56 respectively (Figure 5.8). The faster removal of volcanic sulfur and halogens from the stratosphere is driven by a faster BDC in the 2050s which has been accelerated by anthropogenic emissions of greenhouse gases (Butchart, 2014). This is clearly shown in the global mean stratospheric age of air, which is 11% younger in future conditions compared with HIST at 25 km (Figure B13). The accelerated BDC in future climates, disperses the volcanic aerosol and halogens to higher latitudes faster, where they descend into the troposphere and are effectively removed.

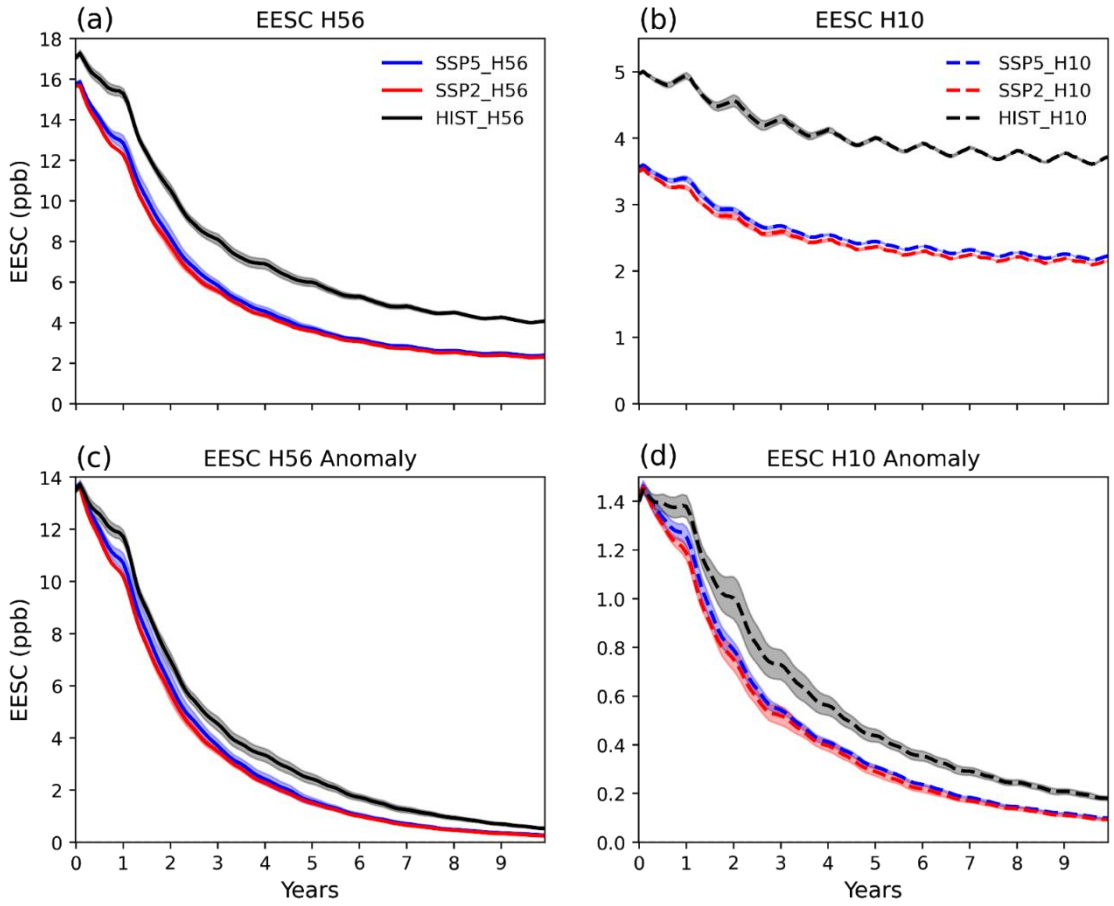

Figure 5.8 Timeseries of equivalent effective stratospheric chlorine (EESC) concentration (ppbv) (solid lines) and change relative to the climatologies (dashed lines). HIST_H56, SSP2_H56 and SSP5_H56 shown in (a and b respectively) and HIST_H10, SSP2_H10 and SSP5_H10 shown in (c and d respectively).

Although we have been able to estimate the TCO impacts of explosive volcanic eruptions, these results are not without uncertainty, particularly with regards to the stratospheric injection of HCl and HBr from explosive volcanic eruptions. As such, we implemented a simulation matrix that spans a range of possible explosive volcanic emission scenarios. However, the opposing sensitivity trend to sulfur-only and halogen co-emission volcanic eruptions in future climate states is in stark contrast with the large uncertainty in the flux of volcanic halogens to the stratosphere, clearly highlighting a research priority. Other drivers that are important to our results are less variable. UKESM has been shown to capture the effects of ozone-depleting substances on stratospheric ozone well (Dhomse et al., 2018; World Meteorological Organization, 2014), and the recovery of stratospheric ozone in the future is widely observed and simulated, assuming the continued compliance with the Montreal Protocol. The interannual variability of global mean TCO is less than 2% in the 20-year HIST, SSP2 and SSP5 control simulations (Figure 5.1), and this is predominantly driven by interannual variability (up to 10%) at the poles, the region with the largest dynamic variability. The acceleration of the Brewer-Dobson circulation due to climate change is a consistent feature of climate model projections, even though the exact magnitude of this acceleration is model-specific (Butchart, 2014; Griffiths et al., 2021). It is acknowledged that the initial conditions in volcanic perturbation simulations will have an impact on the simulated response, particularly the volcanic sulfur and

halogen lifetime. Aubry et al. (under review) showed that the plume height of future large-magnitude tropical eruptions is amplified due to increased atmospheric stratification, prolonging the lifetime of volcanic sulfur. Here, volcanic gases were injected into the tropical stratosphere at a fixed altitude of 21 km across all simulations, representing a typical tropical explosive eruption but, as such, does not include the plume height climate-volcano feedback identified in Aubry et al. (under review). Osipov et al. (2020) used the Goddard Institute for Space Studies (GISS) Earth system model (ModelE) to simulate the Toba super eruption (2000 Tg SO_2) which erupted 74,000 years ago. They reported that the eruption resulted in severe stratospheric ozone loss globally for over a year, caused by the suppression of oxygen photolysis and ozone formation by the volcanic plume. This paper highlights another mechanism by which sulfur-only volcanic eruptions can result in ozone depletion. The coupled aerosol-radiation scheme (Fast-Jx) utilised in this thesis as part of UKESM-AMIP ensures this feedback is also included in the results presented here (Telford et al., 2013). However, we do not expect it to have a large impact on the TCO results in this study due to the comparatively small magnitude of the volcanic SO_2 emission.

Research into the effects of volcanic eruptions on stratospheric composition had typically focussed on ozone because of its role in the flux of harmful UV to the Earth's surface. However, volcanic eruptions can also perturb stratospheric water vapour (SWV) and methane (e.g. Löffler et al., 2016; Kilian et al., 2020). Legrande et al. (2016) provided a mechanism explaining how SWV originating from direct volcanic emission may alter the chemistry of the stratosphere and suggested that this may severely alter the climate impacts. Staunton-Sykes et al. (2021) (Chapter 3) utilised the same model set-up as is implemented in this chapter to simulate the indirect effects of large and very-large sulfur-only and halogen co-emission eruption scenarios on SWV and methane in the HIST climate state. They reported an increase in SWV and a relatively small increase in stratospheric methane burden following sulfur-only simulations caused by warming of the tropical tropopause cold point and enhanced tropical vertical ascent due to aerosol heating, enabling a greater flux of water vapour and methane to be brought up from the troposphere. Conversely, in co-emission scenarios, the process was shown to be the same but in the opposite sense. Staunton-Sykes et al. (2021) reported a decrease in SWV, caused by ozone-loss induced cooling of the tropical tropopause cold point and reduced tropical vertical ascent reducing the flux of water vapour from the troposphere, and stratospheric methane burden caused by enhanced destruction of methane by Cl. Recent work by Alicia Kroll et al. (2021) reported that the additional SWV following sulfur-only volcanic eruptions counterbalances roughly 4% of the negative aerosol forcing from the volcanic aerosols. Results from the simulations outlined in this chapter (not shown), show that SWV anomalies and stratospheric methane anomalies are amplified following eruption scenarios in the future, which is hypothesised to be due to the greater tropospheric concentrations of water vapour and methane resulting from anthropogenic emissions and tropospheric warming. As such, the changes in stratospheric water vapour following future sulfur-only eruptions would be expected to counterbalance a larger fraction of the negative forcing from volcanic aerosols. It is important to explore this new climate-volcano feedback in future work in order to understand the full and wide-reaching consequences of climate change.

The results in this chapter can be used to infer the implications of a future solar radiation management (SRM) by direct injection of sulfur into the stratosphere, as explosive volcanic eruptions are the natural analogues of this process. SRM by direct stratospheric sulfur injection would aim to artificially maintain a layer of sulfate aerosol

in the stratosphere to produce a constant negative radiative forcing and cool the surface (Kravitz et al., 2013). It is often invoked as a mechanism to partially offset global warming, allowing more time to decarbonise the economy. It is perhaps the most discussed SRM mechanism as it would be effective and the impacts are thought to be predictable based on our understanding of explosive volcanic eruptions (Kravitz et al., 2015). The results in this work would suggest that any SRM by direct sulfur injection deployed before the 2050s at the earliest will result in significant global mean TCO depletion which will need to be taken into consideration during future discussions of SRM by direct sulfur injection as a potential mitigation strategy.

5.5 Conclusions

Sulfur species released during explosive volcanic eruptions perturb ozone column. The net chemical impact of volcanic eruptions on TCO is dependent on the EESC concentration. In the present day, high EESC conditions volcanic eruptions result in TCO increase, whereas in the future, when EESC has declined, they will result in an increase. The timing of this transition is, however, poorly constrained, with previous estimates ranging from 2015 to beyond 2040 (Naik et al., 2017; Rosenfield, 2003; Tie and Brasseur, 1995). This issue is further complicated by the fact that the co-emission of volcanic halogens into the stratosphere alongside sulfur results in TCO depletion regardless of the background climate state. This work investigates the vulnerability and sensitivity of TCO to future sulfur-only and, for the first time, halogen co-emission volcanic eruptions. We perform climate model simulations of a large (10 Tg SO_2) and very-large (56 Tg SO_2) sulfur-only eruption scenario and a corresponding large (10 Tg SO_2 & 1.5 Tg HCl & 0.0086 Tg HBr) and very-large (56 Tg SO_2 & 15 Tg HCl & 0.086 Tg HBr) co-emission eruption scenario in a historical climate state representative of the 1990s as well as a moderate and high-end future climate state representative of the 2050s. We show that TCO remains vulnerable to large and very-large sulfur-only volcanic eruption scenarios to at least the year 2050s in both future climates. The magnitude of ozone depletion is significantly smaller in the future reflecting the projected decline in stratospheric halogens concentration. However, in contrast to a previous study we find very similar TCO responses under both the moderate and high-end warming climate futures. This is mainly as a result of the limited difference between the EESC concentration, stratospheric temperature, and methane concentrations in these scenarios at the 2050s time horizon. In contrast, we show that the TCO is more sensitive to large and very-large volcanic halogen co-emission scenarios in the 2050s future climate, especially at the poles. This increased sensitivity is driven by the decline of EESC and stratospheric ozone recovery. Across both sulfur-only and halogen co-emission eruption scenarios global mean TCO anomalies are shown to recover significantly faster in the future, driven by a faster Brewer-Dobson circulation accelerated by anthropogenic greenhouse gas emissions. Stratospheric ozone absorbs a large fraction of the biologically harmful ultraviolet (UV) radiation from the sun. In doing so, it protects life on Earth from DNA damage and reduces the occurrences of skin cancers, eye damage and immune system deficiencies (World Health Organization., 1994). This work demonstrates how the global mean TCO response to future sulfur-only and halogen co-emission volcanic eruptions differs in future climates compared to HIST, with important implications for the magnitude and duration of surface UV exposure, especially in the tropics. The opposing sensitivity trend to sulfur-only and halogen co-emission volcanic eruptions in future climate states is in stark contrast with the large uncertainty in the flux of volcanic halogens to the stratosphere, clearly highlighting a research priority.

Chapter 6

Complex and non-additive climate response to volcanic eruptions during SRM

Abstract

Solar radiation management by direct sulfur injection (hereafter SRM) is a possible mechanism through which the climate could be engineered to mitigate global warming. However, there is limited research into the implications of a concurrent explosive volcanic eruption emitting sulfur dioxide (SO_2) into the stratosphere. Here we show that explosive volcanic eruptions concurrent with SRM result in large additional cumulative radiative forcing, albeit smaller compared to the same eruption occurring without concurrent SRM. This is driven by the formation of larger sulfate aerosol, as found by Laakso et al. (2016), but also due to faster poleward transport and removal of volcanic sulfur due to a faster Brewer-Dobson circulation accelerated by SRM aerosol heating in the tropical stratosphere. We report that the reduction in cumulative radiative forcing lessens as the mass of volcanic SO_2 emitted increases relative to the SRM emission flux. A 10 Tg SO_2 sulfur-only volcanic eruption results in a 38% smaller cumulative forcing compared to the same eruption without SRM. In contrast, a 56 Tg SO_2 sulfur-only volcanic eruption results in an 18% smaller cumulative forcing compared to the same eruption without SRM. The co-emission of volcanic sulfur and halogens results in a further 12% and 21% reduction in the additional cumulative forcing compared to a sulfur-only eruption during SRM. We suggest that this is due to the shorter lifetime of volcanic sulfur following explosive volcanic eruptions that co-emit sulfur and halogens. Furthermore, we report a significant overshoot in the recovery of the total sulfur burden and global mean volcanic forcing beyond the pre-volcanic levels. This is because the additional emission of volcanic sulfur unbalances the previously stable total sulfur burden equilibrium established during SRM. Finally, we report that explosive volcanic eruptions result in broadly the same global mean total column ozone depletion with or without concurrent SRM, but the total column ozone is shown to recover faster following eruptions concurrent with SRM. Our results demonstrate the difficulties associated with maintaining a stable level of radiative forcing in the relatively likely event that a large explosive volcanic eruption takes place during SRM.

6.1 Introduction

Concerns that the decarbonisation of the global economy is progressing too slowly to prevent significant climatic changes has motivated many to explore of the possibilities of direct human intervention (Keith, 2000). Climate engineering is widely expected to be a last resort response to climate change, but the likelihood of needing to resort to these measures is only growing with every year of inaction. However, there is limited research into these intervention mechanisms and their possible side effects (National Research Council, 2015).

Solar radiation management (SRM) has been suggested as one means of engineering the climate and mitigating the worst of global warming, buying time to find a more permanent solution. Several mechanisms for SRM have been proposed including reducing the incoming solar radiation with reflective mirrors in low earth orbit (e.g. Govindasamy and Caldeira, 2000), by increasing the reflectivity of Earth's surface (e.g. Irvine et al., 2011), or by injecting stratospheric aerosol precursors (e.g. Rasch et al., 2008), calcium carbonate particles (Dai et al., 2020; Keith et al., 2016) or titanium oxide crystals (Ferraro et al., 2015) into the stratosphere to increase its albedo. The climate response to different methods of SRM has been studied under the dedicated Geoengineering Model Intercomparison Project (GeoMIP) (Kravitz et al., 2011, 2013, 2015), including SRM via direct sulfur injection. Direct stratospheric injection of sulfate aerosol precursors is the most discussed SRM mechanism as it is thought to be an effective and relatively predictable option based on our understanding of the natural analogue - explosive volcanic eruptions.

Sulfur dioxide (SO_2) emitted into the stratosphere during explosive volcanic eruptions is oxidised by OH to form sulfuric acid vapour (H_2SO_4) which condenses to form sulfate aerosol particles. Sulfate aerosol particles scatter shortwave radiation (SW) and absorb longwave radiation (LW), resulting in net surface and tropospheric cooling and stratospheric heating. Stratospheric sulfate aerosols are advected globally with a lifetime of up to 1 to 2 years before being deposited to the surface (Robock, 2000), although the surface cooling can be prolonged by ocean feedbacks resulting in multi-decadal impacts (e.g. Free and Robock, 1999; Gupta and Marshall, 2018; Stenchikov et al., 2009). Explosive volcanic eruptions can also perturb stratospheric composition. Ozone is impacted dynamically by stratospheric circulation changes induced by sulfate aerosol heating, and chemically by changes to ozone catalytic loss cycles as the aerosol acts as a surface for heterogeneous chemistry. Aerosol heating in the stratosphere increases the vertical ascent in the tropics and enhances the transport of ozone to higher altitudes and latitudes, resulting in an ozone decrease in the tropics and an increase at high latitudes (Kinne et al., 1992). The addition of large amounts of volcanic aerosols increases the surface area of the stratosphere on which heterogeneous reactions, that result in ozone depletion, can take place (Solomon, 1999).

SRM by direct sulfur injection (hereafter SRM) analogizes the temporary radiative effect of explosive volcanic eruptions and aims to continuously maintain a layer of sulfate aerosol in the stratosphere to produce a stable negative radiative forcing that partially offsets global warming and allows more time to decarbonise the economy. While the climate effects of volcanic eruptions and SRM have been well-studied independently, only Laakso et al. (2016) has studied the implications of an explosive volcanic eruption in a SRM climate state. Volcanic eruptions are random events that are impossible to predict, however, they recur with typical frequency. Volcanic Explosivity Index (VEI) 6 (e.g. 1991 Mt. Pinatubo) and VEI 7 (e.g. 1257 Mt. Samalas) eruptions occur approximately every 50-100 and 500-1000 years, respectively (Newhall et al., 2018). To explore the effect of an explosive volcanic eruption in an SRM climate, Laakso et al. (2016) used the of MAECHAM5 climate model (Giorgetta et al., 2006) coupled to the HAM-SALSA (Hamburg Aerosol Model, Sectional Aerosol module for Large Scale Applications) aerosol microphysical module. They simulated an 8.5 Tg S volcanic injection of SO_2 in the tropical stratosphere (24 km altitude) in three experiments, one without SRM, (Volc), one where SRM is ceased immediately after the eruption (SRM Volc), and one where SRM is continued throughout (SRM Cont). The SRM emission was 8 Tg S yr^{-1} of SO_2 injected between 30°N and 30°S and 20 and 25 km altitude. Laakso et

al., (2016) reported that the effects of SRM and volcanic eruptions are not additive; the peak global mean forcing was 21% smaller and recovered faster in SRM Cont compared to Volc. This was because volcanic sulfur not only nucleated new particles but also condensed onto or coagulated with pre-existing particles forming fewer but larger particles compared with the experiment without SRM. Increasing the size of volcanic sulfate aerosols ($r >\sim 0.20$ μm) reduces the scattering cross section per unit mass and reduces the lifetime (Lacis, 2015). Laakso et al. (2016) only explored one eruption magnitude and did not consider volcanic eruption scenarios larger than the annual SRM SO_2 emission (e.g. >10 Tg SO_2) or the co-emission of volcanic halogens, which were shown to significantly amplify volcanic forcing in Staunton Sykes et al. (2021) and Chapter 3. Furthermore, they did not explore the effects of concurrent volcanic eruptions during SRM on total column ozone.

In this study we use UKESM-AMIP model simulations to investigate the radiative forcing and total column ozone response to large explosive sulfur-only and halogen co-emission volcanic eruptions in climate states with and without SRM. SRM emissions are continued unchanged throughout the volcanic eruption simulations. In line with Laakso et al. (2016), we find that the effects of SRM and volcanic eruptions are not additive. Sulfur-only and halogen co-emission volcanic eruptions during SRM result in a smaller volcanic forcing compared to the same eruptions without SRM. However, we find that the magnitude of the reduction is sensitive to both emission magnitude and volcanic halogen co-emission. We report a significant overshoot in the recovery of the total sulfur burden and global mean volcanic forcing beyond the pre-volcanic levels. This is because the additional emission of volcanic sulfur unbalances the previously stable total sulfur burden equilibrium established during SRM. We also report that sulfur-only and halogen co-emission eruptions during SRM result in broadly the same global mean total column ozone depletion, but smaller tropical ozone depletion compared to the same eruptions without SRM. We simulate a faster recovery of the volcanic forcing and ozone depletion in SRM climates due to a faster BDC which has been accelerated by tropical stratospheric heating by SRM aerosols.

6.2 Methods

Our study utilises the SSP2, SSP5 and G6_SRM UKESM-AMIP time-slice experiments as described in Chapter 2. The SSP2 and SSP5 control simulations were run using the January 2055 initialisation file and climatologies calculated using data from the fully coupled UKESM1.0 ScenarioMIP runs produced for CMIP6 (Eyring et al., 2016) and averaged over the years 2050 to 2060. The model set-up used for G6_SRM was identical to that of SSP5, except with an additional emissions file to incorporate the direct emission of SO_2. In G6_SRM continuous direct injections of sulfur into the stratosphere are used to maintain an artificially high sulfate aerosol burden which mitigates the anthropogenic radiative forcing in SSP5 down to the level in SSP2 at the 2050s time horizon. To achieve this, 6.4 Tg of SO_2 is injected annually into the stratosphere between 10^oS-10^oN and 18-20 km altitude (see section 6.3.1 and Figure 6.1). The SRM emission strength required to reduce the SSP5-8.5 forcing down to the levels of SSP2-4.5 is model dependent was found by trial and error as part of Jones et al. (2021). The model was allowed to spin up for 15 years allowing the SRM sulfur burden to stabilise and then a control simulation was run for a further 20 years. In this work, changes due to the SRM are inferred from the difference between the SSP5 and G6_SRM control climatologies. The effect of explosive volcanic eruptions was investigated by running three of 10-year volcanic perturbation simulations initialised from three different years in the control run to sample the

variability in QBO states as described in Chapter 2. Changes are plotted as the difference between the average of the ensemble members and a climatology derived from the 20-year control run. The ensemble range is included as an envelope where appropriate. SRM emissions are continued throughout the volcanic perturbation simulations. Mode merging from the accumulation to coarse modes is turned off above 100 hPa in all control and volcanic perturbation experiments, see Section 2.1 for more details.

Volcanic effective radiative forcings are calculated as differences (Δ) in the net (SW+LW) top-of-atmosphere (TOA) radiative fluxes (F) between perturbed and control climatologies (see Chapter 2, Section 2.2). Extra calls to the radiation scheme enable the forcing from aerosol-radiation interactions to be isolated (ERF_{ari}), as described in Schmidt et al. (2018) and Ghan (2013).

$$ERF_{ari} = \Delta(F - F_{clean}) \qquad \text{(Eq. 6.1)}$$

Where F_{clean} denotes a radiation flux diagnostic calculation without aerosol-radiation interactions but including aerosol-cloud interactions through microphysics. Thus, $F - F_{clean}$, determines the impact of all aerosol and $\Delta(F - F_{clean})$ is an estimate of the forcing from volcanic aerosol-radiation interactions (ERF_{ari}). Cumulative forcing is calculated as the time-integrated forcing across the Earth's surface and represent the total energy loss (J) as a result of the volcanic eruption.

The volcanic emissions are prescribed by direct injection of SO_2, HCl and HBr into the stratosphere with a Gaussian plume vertical distribution centred on 21 km and with a width of 2.1 km (10% of the height) (Aubry et al., 2019), lasting for 24 hours on July 1st. An injection altitude of 21 km was chosen as, allowing for lofting, this results in a volcanic sulfate plume altitude (20-25 km, as shown in Figure 6.5) consistent with recent historical eruptions from the 1991 eruption of Mt. Pinatubo (Guo et al., 2004). The gases were injected in the tropics (5°S latitude and 0° longitude) to represent a typical tropical explosive eruption (Newhall et al., 2018).

Since historical stratospheric volcanic SO_2 fluxes are variable and the volcanic flux of HCl and HBr into the stratosphere remains uncertain, we developed a simulation matrix that spans a range of plausible explosive volcanic emissions, as outlined in Chapter 2. The four sets of experiments have one large-magnitude SO_2 (10 Tg), and one very-large-magnitude SO_2 (56 Tg) emission scenario both with (H10 and H56) and without halogens (S10 and S56) (Table 6.1). These eruptions (10 and 56 Tg SO_2) are hypothetical, but their magnitudes are comparable to a VEI 6 (e.g. 1991 Mt. Pinatubo) and VEI 7 (e.g. 1257 Mt. Samalas) eruption, representing 1-in-50-100-year and 1 in 500–1000 year events respectively (Newhall et al., 2018). Experiment identifiers used in this work are formed by combining the background climate and eruption scenario identifiers, as shown in Table 6.2.

Scenario	SO_2 (Tg)	HCl (Tg)	HBr (Tg)	HCl:SO_2
S10	10	-	-	-
H10	10	1.5	0.0086	0.26
S56	56	-	-	-
H56	56	15	0.086	0.47

Table 6.1 Showing the eruption masses of SO_2, HCl and HBr in Tg and HCl:SO_2 (relative mixing ratio) for the four sets of experiments. See Chapter 2 for more details on the volcanic eruption scenarios used in this work.

Simulation Key	**Climate Scenario**		
Eruption Scenario	**SSP2**	**SSP5**	**G6_SRM**
S10	SSP2_S10	SSP5_S10	G6_S10
H10	SSP2_H10	SSP5_H10	G6_H10
S56	SSP2_S56	SSP5_S56	G6_S56
H56	SSP2_H56	SSP5_H56	G6_H56

Table 6.2 Showing the full simulation matrix utilised in this study. Experiment identifiers are formed by combining the climate scenarios (column headings) and emission scenarios (rows).

6.3 Results

6.3.1 Control Simulations

The SRM emission strength of 6.4 Tg (SO_2) yr^{-1} in G6_SRM results in a stable global mean TOA ERF_{ari} of -2.2 Wm^{-2} compared to SSP5. As desired, this results in the global mean radiative forcing required to mitigate the anthropogenic radiative forcing in SSP5 down to the level in SSP2 at the 2050s time horizon. The total sulfur burden peaks at 16 Gg in the tropics between 15-25 km altitude (Figure 6.1b). The abundant sulfate aerosol particles in G6_SRM causes stratospheric heating of up to 3.5 K at 19-20 km altitude (Figure 6.1d), which increases the tropical vertical ascent, accelerates the BDC, and increases the transport of ozone from the tropics to the poles. Furthermore, the elevated sulfur burden provides the surface area to facilitate heterogeneous reactions which activate atmospheric halogens leading to ozone depletion. Stratospheric warming also accelerates ozone loss cycle kinetics. This net result of SRM in G6_SRM is a 1% smaller global mean total column ozone, a 30% drop in total column ozone in the tropics and a 10-40% increase at high latitudes compared to SSP5 (Figure 6.2). This is in accordance with Tilmes et al. (2008) who reported enhanced stratospheric ozone chemical losses during SRM using the Whole Atmosphere Chemistry Climate Model 3 (WACCM3) and Chapter 5 of this thesis which showed that total column ozone remains vulnerable to the addition of sulfate aerosol into the stratosphere to at least the 2050s.

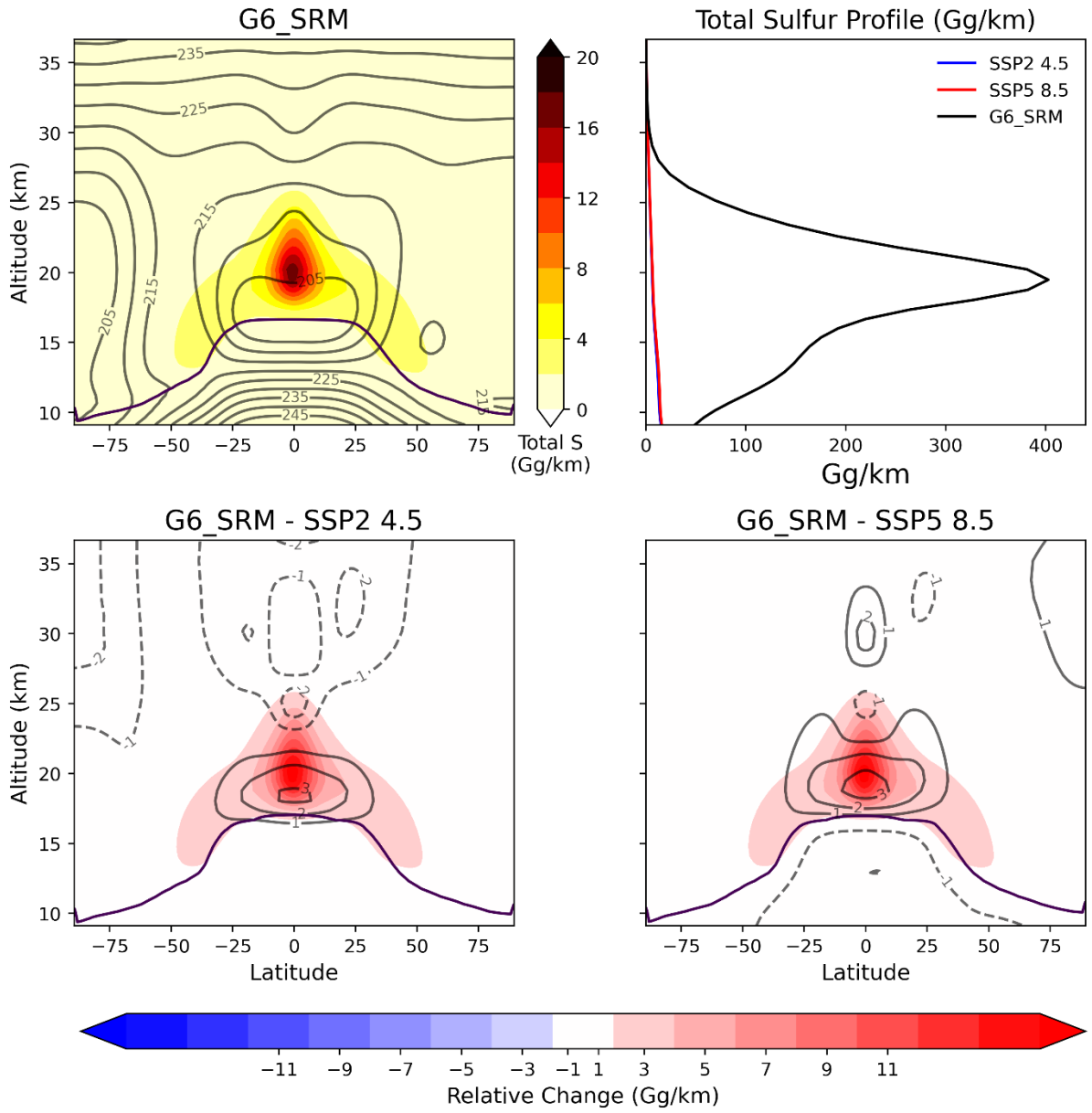

Figure 6.1 (a) Zonal sum total sulfur (Gg/km) profile in G6_SRM with zonal mean temperature (K) contours overplotted in dark grey (b) Global sum total sulfur (Gg/km) profile in G6_SRM (black), SSP5 (red) and SSP2 (blue). Difference in zonal sum total sulfur (Gg/km) between G6_SRM and SSP2 (c) and G6_SRM and SSP5 (d). Difference in zonal sum temperature (K) contours between G6_SRM and SSP2 (c) and G6_SRM and SSP5 (d) are overplotted in dark grey. Solid purple lines indicate the tropopause.

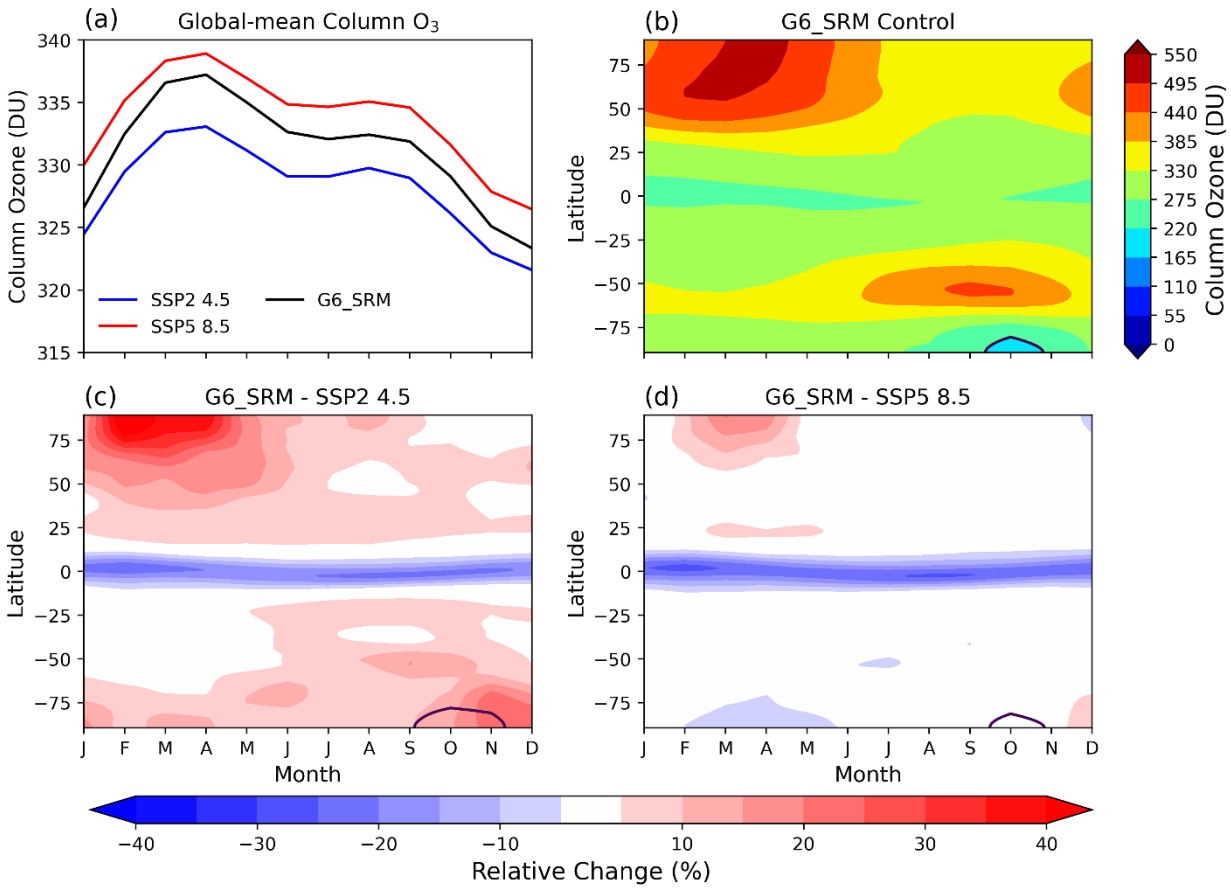

Figure 6.2 (a) Global mean total column ozone in G6_SRM (black), SSP5 (red) and SSP2 (blue). (b) Zonal mean total column ozone in G6_SRM. Difference in zonal mean total column ozone between G6_SRM and SSP2 (c) and G6_SRM and SSP5 (d).

6.3.2 Volcanic perturbation simulations

6.3.2.i Radiative effects of concurrent volcanic eruption and SRM

A sulfur-only volcanic eruption concurrent with SRM results in a smaller peak global mean and cumulative TOA ERF_{ari} compared to an eruption without SRM, in agreement with Laakso et al. (2016). We simulate a 25% and 12% smaller peak global mean TOA ERF_{ari} in G6_S10 (-2.3 Wm^{-2}) and G6_S56 (-10.5 Wm^{-2}) compared to SSP5_S10 (-3.0 Wm^{-2}) and SSP5_S56 (-12.0 Wm^{-2}), respectively (Figure 6.3 a and b). The peak global mean TOA ERF_{ari} was reached approximately within the first 6 months in G6_S10 and G6_S56 and slightly later in SSP5_S10 and SSP5_S56, before recovering back towards pre-eruption background levels. This results in a 38% and 18% smaller cumulative forcing in G6_S10 and G6_S56 compared to SSP5_S10 and SSP5_S56, respectively.

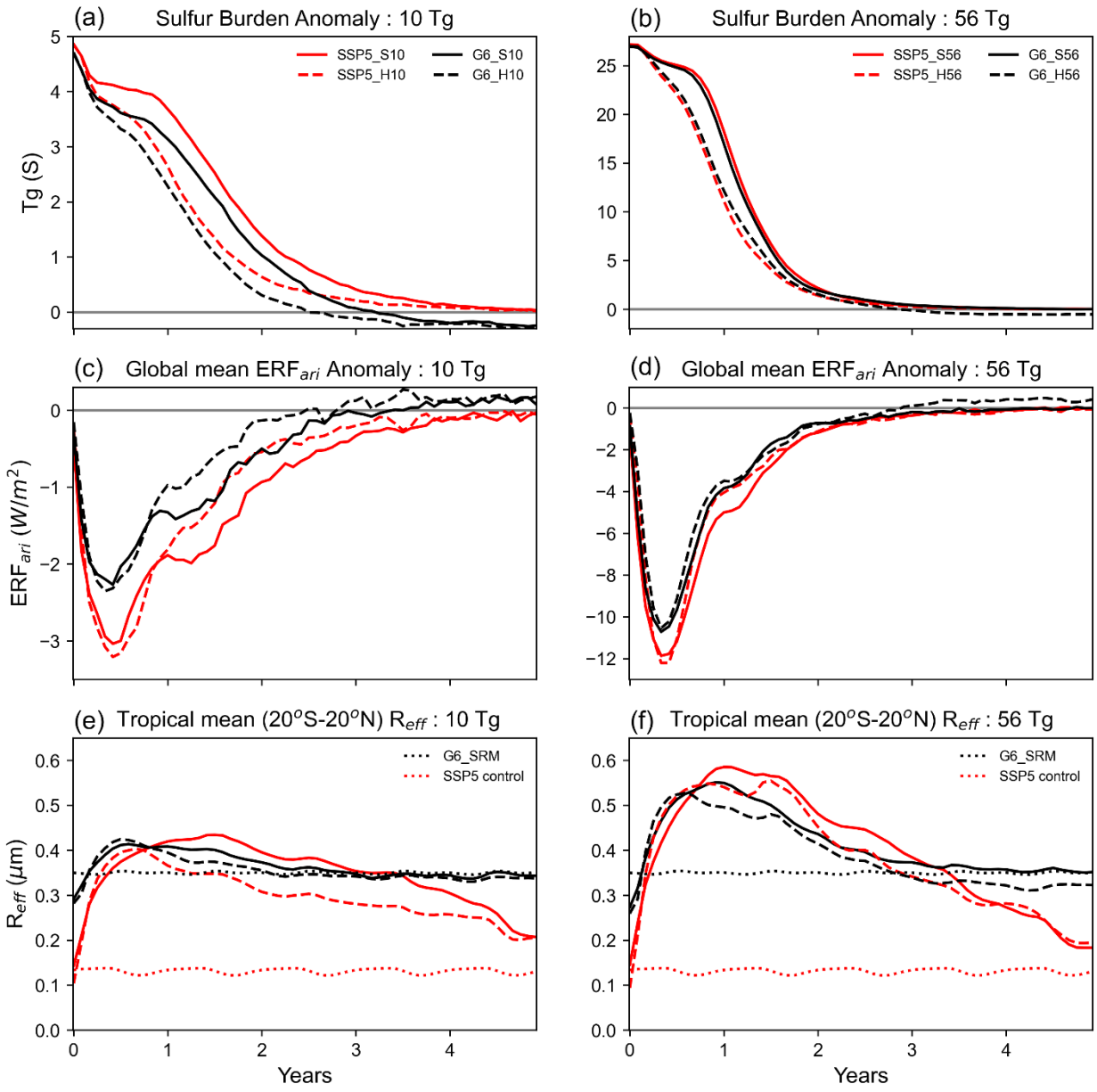

Figure 6.3 Global evolution of total sulfur, ERF_{ari} and aerosol effective radius relative to the control climatologies for post-eruption years 1 to 5. Total sulfur burden anomalies in (a) S10 and H10 and (b) S56 and H56. Global mean TOA ERF_{ari} in (a) S10 and H10 and (b) S56 and H56. Tropical mean aerosol effective radius between 20 km and 25 km in (a) S10 and H10 and (b) S56 and H56. The black and red dotted lines in panels (e) and (f) corresponds to the pre-volcanic aerosol effective radius in G6_SRM and SSP5 control climatologies.

We attribute the smaller peak and cumulative volcanic forcing in G6_S10 and G6_S56 compared to SSP5_S10 and SSP5_S56 (solid black and red lines in Figure 6.3) to be due to a combination of two factors:

i) the formation of fewer (Figure D1) but larger aerosols (Figure 6.3 panels e and f)

ii) faster stratospheric meridional transport to higher latitudes (Figure D2)

Volcanic sulfur in G6_S10 and G6_S56 not only nucleates new particles but also condenses onto, and coalesces with, pre-existing stratospheric sulfate aerosol from SRM. In agreement with Laakso et al. (2016), this results in a smaller number (Figure D1) of larger (Figure 6.3e,f) sulfate aerosols with a lower extinction per unit mass at 550 nm, larger gravitational setting velocity, and shorter total sulfur burden anomaly e-folding time. However, the differences in aerosol R_{eff} are not large enough, nor do they last long enough, to be the only reason the total sulfur burden anomaly e-folding time is smaller in G6_S10 and G6_S56 compared to SSP5_S10 and SSP5_S56. Instead, the faster removal of volcanic sulfur can also be attributed to changes in the stratospheric dynamics resulting from SRM. SRM aerosols heat the tropical low- to mid-stratosphere, increasing the vertical ascent and accelerating the stratospheric BDC (Figure 6.1). The accelerated BDC transports the volcanic aerosol to high latitudes faster where they descend into the troposphere and are effectively removed, leading to a shorter total sulfur burden anomaly e-folding time. This is clearly shown by comparing the age-of-air, which is 25% younger at 25 km in G6_SRM compared to SSP5 (Figure D2).

The reduction in peak global mean and cumulative radiative forcing gets smaller as the magnitude of the volcanic SO_2 emission increases relative to the SRM SO_2 emission magnitude (6.4 Tg yr^{-1} SO_2). The reduction in peak global mean and cumulative ERF_{ari} is roughly twice as big in G6_S10 (10 Tg SO_2) compared to G6_S56 (56 Tg SO_2). This is reflected in the total sulfur burden anomalies (Figure 6.3a,b) and the aerosol R_{eff} (Figure 6.3e,f), where the difference between G6_S10 and SSP5_S10 is much larger than between G6_S56 and SSP5_S56.

The co-emission of volcanic sulfur and halogens results in a slightly larger peak global mean ERF_{ari} but a further 12% and 21% reduction in cumulative forcing in G6_H10 and G6_H56 compared to G6_S10 and G6_S56, respectively. As was reported in Chapter 3, in scenarios with co-emitted volcanic sulfur and halogens the volcanic sulfur is not lofted as high into the stratosphere by volcanic sulfate aerosol heating like it is in sulfur-only simulations due to the stratospheric cooling associated with halogen-induced ozone depletion. This leads to a shorter lifetime, reduced opportunity for aerosol growth and smaller aerosols closer in size to the peak scattering cross section per unit mass (Staunton Sykes et al., 2021). The effect of volcanic halogens does not significantly differ with or without SRM.

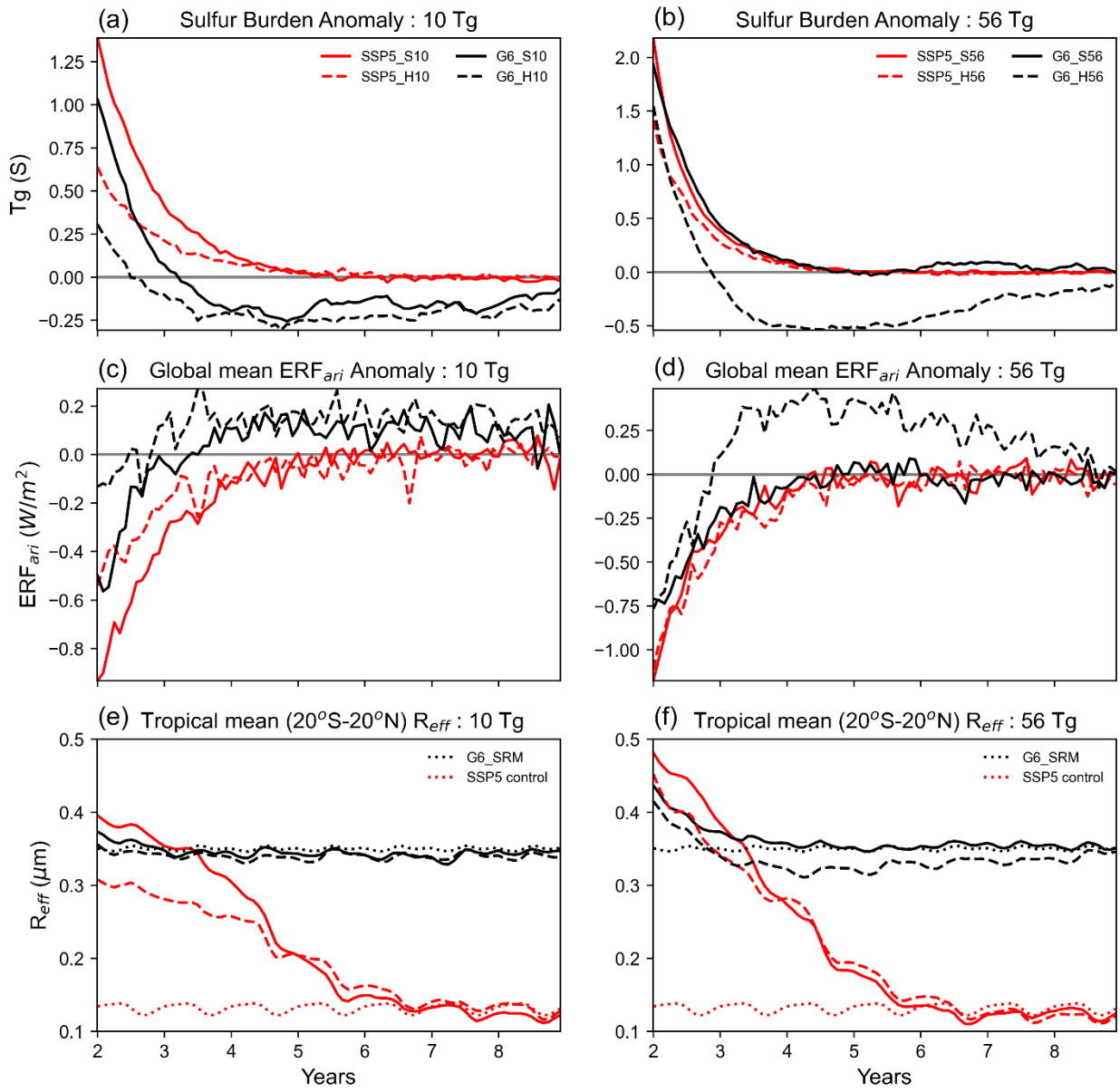

Figure 6.4 As in Figure 6.3 but for post-eruption years 2 to 9. Global evolution of total sulfur, ERF_{ari} and aerosol effective radius relative to the control climatologies. Total sulfur burden anomalies in (a) S10 and H10 and (b) S56 and H56. Global mean TOA ERF_{ari} in (a) S10 and H10 and (b) S56 and H56. Tropical mean aerosol effective radius between 20 and 25km in (a) S10 and H10 and (b) S56 and H56. The black and red dotted lines in panels (e) and (f) corresponds to the pre-volcanic aerosol effective radius in G6_SRM and SSP5 control climatologies.

In all SSP5 and G6_SRM volcanic perturbation experiments the ERF_{ari} perturbation peaks within the first year and recovers back to the pre-eruption levels between years 3 and 5. However, in G6_S10, G6_H10 and G6_H56 we simulate a recovery overshoot in the total sulfur burden, aerosol R_{eff} and global mean ERF_{ari} beyond the pre-volcanic levels (Figure 6.4). In detail, we simulate a 6%, 7% and 13% recovery overshoot in total sulfur burden (Figure 6.4a,b) leading to a 5%, 7% and 18% recovery overshoot in the global mean ERF_{ari} (Figure 6.4c,d) in G6_S10, G6_H10 and G6_H56 compared to the G6_SRM control climatology, respectively. The overshoot gradually recovers back up to the SRM equilibrium over the following 7 years, but it results in a prolonged period

(years 3 to 10) where the total sulfur burden, aerosol R_{eff} and ERF_{ari} are less than the targeted stable pre-volcanic SRM level. We do not simulate an overshoot for the G6_S56 scenario.

The overshoot seen in G6_S10, G6_H10 and G6_H56 can be explained by considering changes in the rate of total sulfur loss from the stratosphere relative to the G6_SRM control climatology. The total sulfur burden is a balance of emissions and loss fluxes from the stratosphere. In G6_SRM the annual SRM emission (6.4 Tg SO_2 yr^{-1}) is in equilibrium with the loss of sulfate aerosol, resulting in a stable total sulfur burden (~4 Tg S). Following the volcanic eruption, volcanic sulfur condenses on and coagulates with SRM aerosols, forming larger aerosols. These larger aerosols have a higher settling velocity than the smaller pre-volcanic aerosol, and thus are removed from the stratosphere faster, temporarily increasing the loss of total sulfur compared to the emissions. This is reflected in Figure D3, which shows that the stratospheric sulfur has been lost from between 10°N and 10°S, coincidental with the largest SRM total sulfur burden and the volcanic emissions.

We do not simulate a recovery overshoot in G6_S56. This is because the volcanic sulfur in G6_S56 is radiatively lofted higher into the atmosphere compared to G6_S10, G6_H10 and G6_H56 (Figure 6.5). The mechanism which explains the overshoot outlined above requires the coexistence of volcanic and SRM sulfur. Due to the large magnitude of the SO_2 emission in G6_S56, we simulate very strong heating in the G6_S56 tropical stratosphere (up to 8K) (Figure D4c) which lofts the aerosols higher into the stratosphere (black dashed line) and away from the majority of the SRM aerosols which are predominantly in the lower stratosphere (solid blue line) (Figure 6.5). The minimal coexistence of volcanic and SRM sulfur at 25 km reduces the growth of aerosol and does not upset the total sulfur burden balance (Figure 6.5). In contrast, the relatively small heating in the tropical stratosphere simulated in G6_S10 (up to 3K) and the tropical stratosphere cooling in G6_H10 (-3K) and G6_H56 (-6K) (Figure D4) results in less aerosol self-lofting and therefore greater overlap of volcanic sulfur with the region of greatest SRM burden (solid blue line).

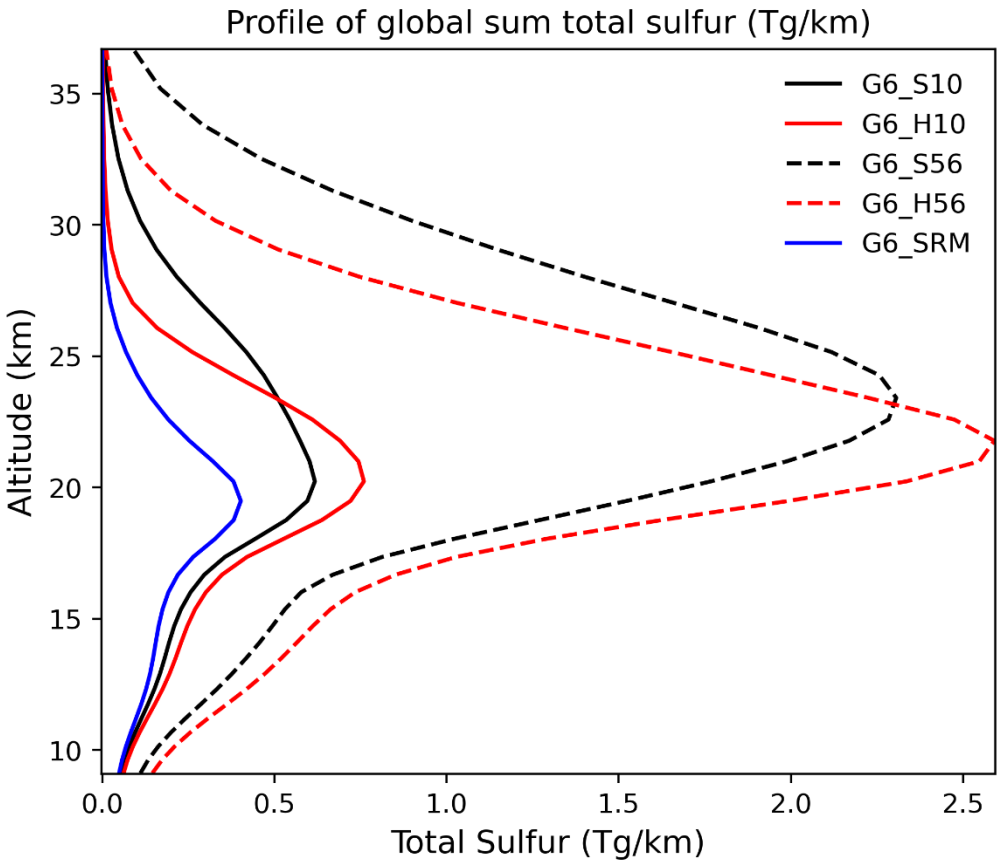

Figure 6.5 Total sulfur profile (Tg/km) in G6_S10 (black solid line), G6_H10 (red solid line), G6_S56 (black dashed line) and G6_H56 (red dashed line), as well as in the G6_SRM control climatology (blue solid line).

6.3.2.ii Effects of concurrent volcanic eruption and SRM on stratospheric ozone

A sulfur only volcanic eruption concurrent with SRM results in a very similar peak global mean ozone depletion but a smaller peak tropical mean ozone depletion compared to an eruption without SRM (Figure 6.6). The peak tropical (30ºS-30ºN) mean ozone depletion was up to 40% smaller in G6_S10 and G6_S56 compared to SSP5_S10 and SSP5_S56. This is predominantly caused by a smaller increase in chemical destruction, driven by a significantly smaller halogen activation anomaly (e.g. ClO_x as shown). Activation of halogens takes places via heterogenous reactions on the surface of sulfate aerosols. In SRM conditions the stratosphere already contains large amounts of sulfate aerosols which enable heterogenous reactions and the activation of halogens. The addition of more sulfate aerosol from a volcanic eruption has a much smaller effect on the surface area of the stratosphere in SRM conditions compared to non-SRM (Figure 6.7a,b), reflected in the change in ClO_x (Figure 6.7c,d). This effect is also exacerbated by the lower total column ozone in the tropical stratosphere during SRM (Figure 6.2).

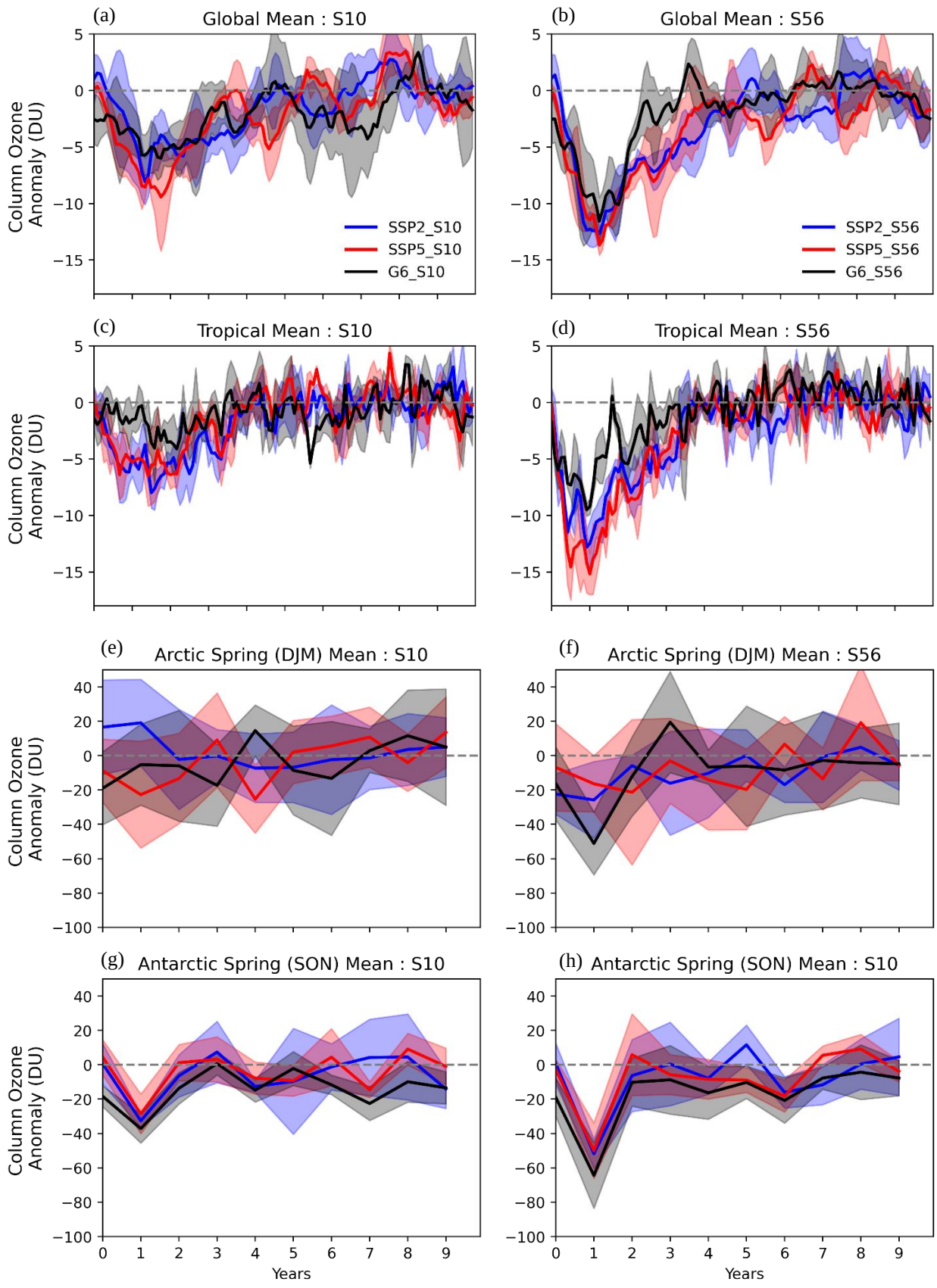

Figure 6.6 Time series of global mean, tropical mean (30ºS-30ºN), Artic (60ºN-90ºN) Spring and Antarctic (90ºS-60ºS) spring total column ozone depletions in (a,c,e,g) S10 and (b,d,f,h) S56 relative to the control climatologies.

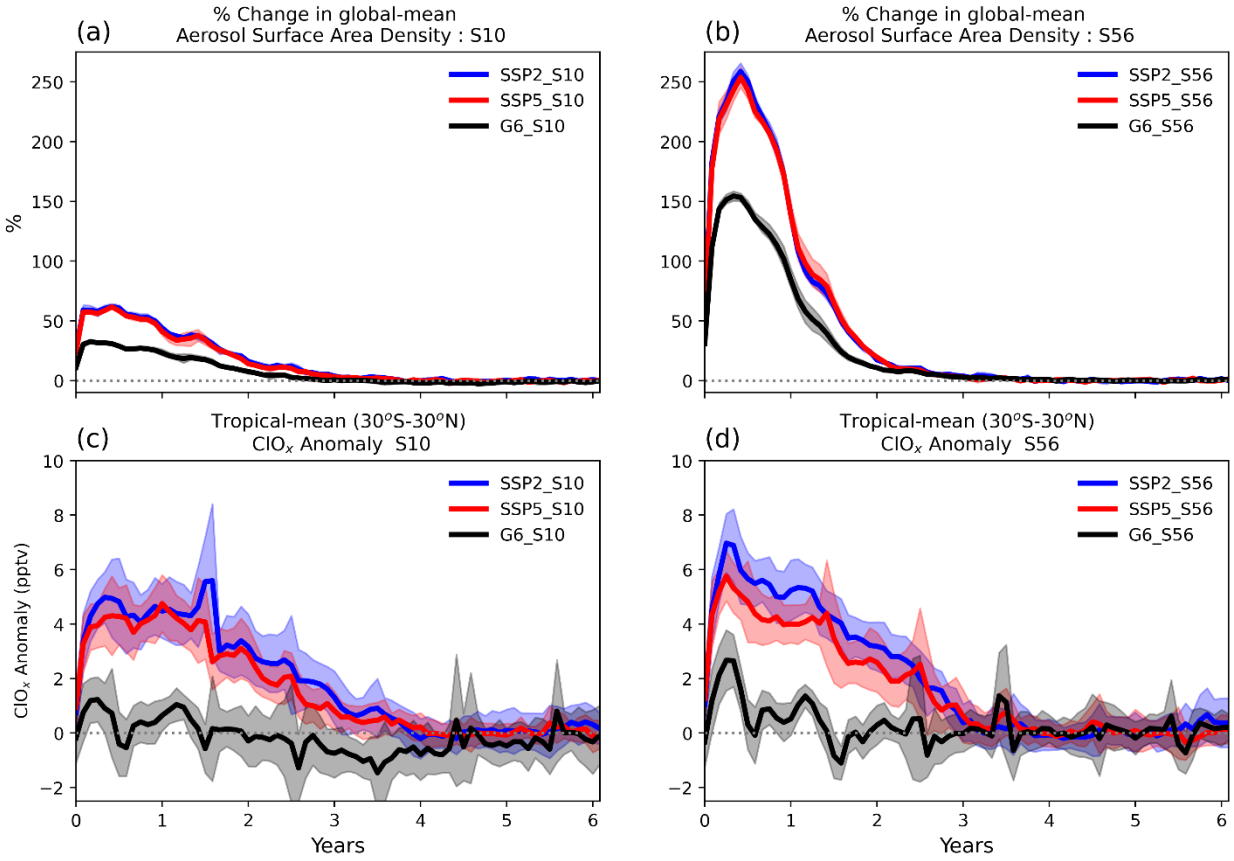

Figure 6.7 Time series of the change in aerosol surface area density in (a) S10 and (b) S56 and the tropical (30°S-30°N) mean ClOx concentration anomaly in (c) S10 and (d) S56 relative to the control climatologies.

Halogen co-emission scenarios result in roughly the same, large global mean ozone depletions both with and without SRM (Figure 6.8). However, the total column ozone depletion was up to 15% smaller in the tropics (30°S-30°N) and 40% larger in the Arctic (60°N-90°N) and Antarctic (90°S-60°S) in G6_H10 and G6_H56 compared to SSP5_H10 and SSP5_H56. Halogen co-emission eruption scenarios dramatically, but temporarily, increase the atmospheric EESC relative to the background EESC in both HIST and future atmospheres. As a result, the halogen activation anomaly is very similar in both SRM and non-SRM climate states. Instead, the reduced sensitivity of column ozone to halogen co-emission in the tropics and enhanced sensitivity to halogen co-emission in the poles reflects the background global mean column ozone. SRM strongly perturbs stratospheric ozone, leading to enhanced total column ozone at the poles and reduced total column ozone in the tropics (Figure 6.2).

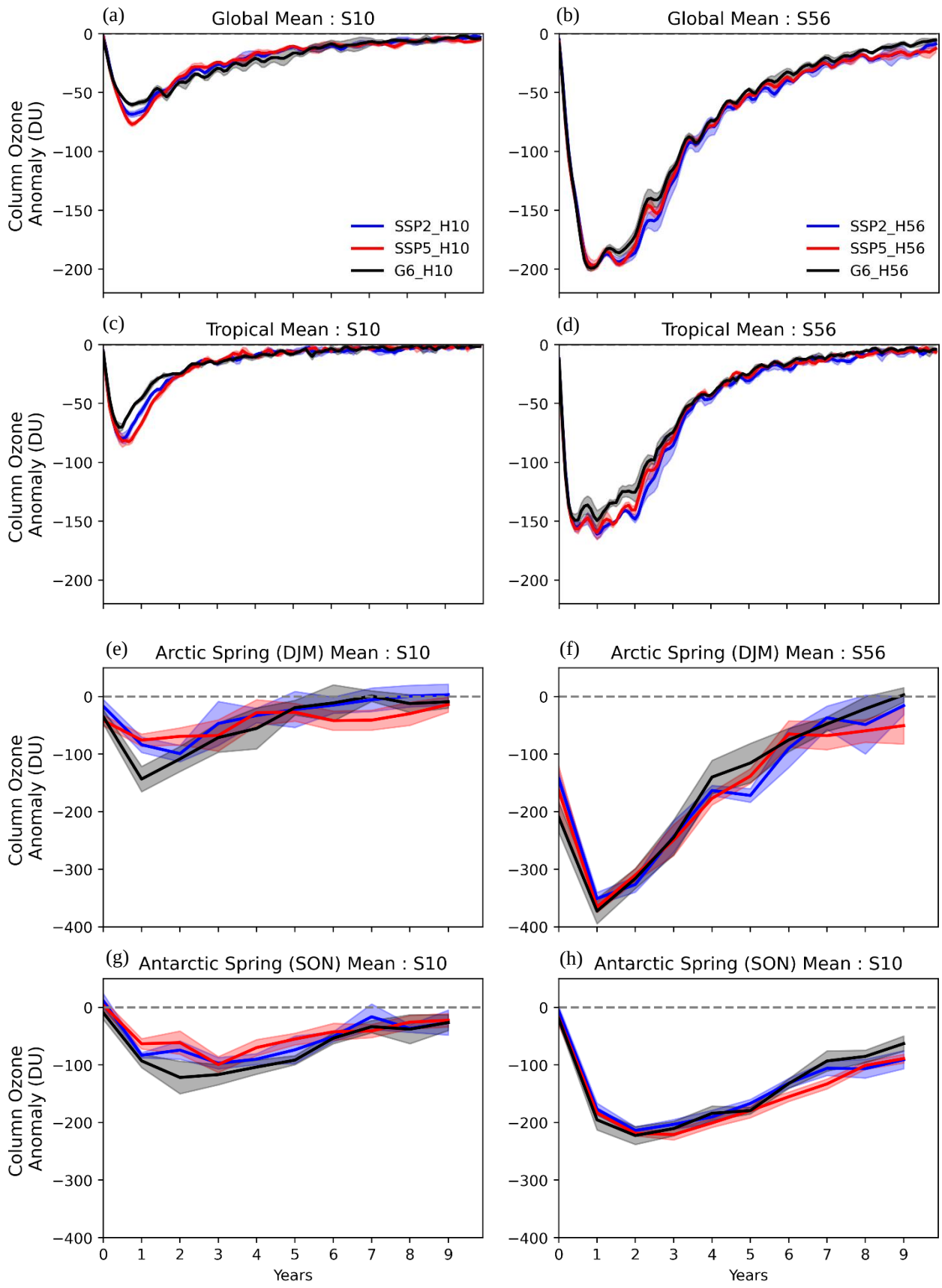

Figure 6.8 Time series of global mean, tropical mean (30ºS-30ºN), Artic (60ºN-90ºN) Spring and Antarctic (90ºS-60ºS) spring total column ozone depletions in (a,c,e,g) H10 and (b,d,f,h) H56 relative to the control climatologies.

6.4 Discussion

The goal of a future SRM project would likely be to utilise SRM to achieve a consistent and predetermined negative radiative forcing that counterbalances all or part of the radiative forcing due to anthropogenic emissions of greenhouse gases. This work shows that it will be extremely difficult to maintain the desired level of forcing in the relatively likely event (Newhall et al., 2018) that a large explosive volcanic eruption (VEI 6+) took place during SRM. Volcanic eruptions concurrent with SRM result in large additional negative radiative forcing which would lead to a further reduction in surface temperature and precipitation (Laakso et al., 2016). Although, the volcanic radiative forcing is significantly muted compared to a volcanic eruption without SRM. The magnitude of the climate impact from an eruption in SRM cannot be estimated based on the climate impact of eruptions during non-SRM conditions as the processes are non-linear, and the effects are not additive. Processes would have to be put in place to either cease or reduce the annual SRM emission flux immediately after an eruption to minimise the additional effects on climate. This is further complicated as the magnitude of the reduction is sensitive to both emission magnitude and volcanic halogen co-emission, suggesting that the size, composition, and plume height of volcanic eruptions would have to be monitored carefully and in near real time to enable a quick consensus of the appropriate action.

The recovery overshoot following a volcanic eruption during SRM highlights a further complexity associated with maintaining the desired SRM negative radiative forcing and has not been reported before. It suggests that the annual SRM emission flux would have to be increased a few years after the eruption to counteract the microphysical processes that drive the overshoot. Determining how the SRM emission magnitude should change in the aftermath of an eruption while the stratosphere is pre-loaded with volcanic sulfur and the aerosol properties are changing significantly on timescales on a few years would require detailed research as well as international agreement.

In the model set-up used in this chapter, mode merging of aerosols from the accumulation to coarse modes is turned off above 100 hPa in all control and volcanic perturbation experiments. This enabled accumulation mode aerosols to grow larger than 1 micron without being transferred into the coarse mode, as described in Dhomse et al. (2014) and in accordance with Kokkola et al. (2009) who showed this improved the aerosol R_{eff} fit compared to a reference sectional scheme in volcanically perturbed simulations. As such we do not expect the recovery overshoots simulated in G6_S10, G6_H10 and G6_S56 to be model artefacts resulting from mode merging (e.g. the resulting sulfate aerosol distribution amongst the accumulation or coarse modes, which have different physical properties and lifetimes) but rather a sulfate aerosol microphysical phenomenon captured by the model. However, Laakso et al. (2016) did not simulate a recovery overshoot in their simulations using a sectional model and it would, therefore, be desirable to repeat the simulations carried out in this chapter in an aerosol-climate model with a sectional aerosol scheme.

The deposition of sulfate (in the form of sulfuric acid) from SRM and volcanic eruptions at the land or ocean surface can be harmful to ecosystems and human health (Kleinschmitt et al., 2018). Kravitz et al. (2009) and

Visioni et al. (2018) reported that the increased sulfate deposition during SRM in the form of sulfuric acid was not large enough to have a significant impact on global ecosystems, and Schmidt et al. (2016) concluded that ecosystems were resilient to sulfate deposition and only very high deposition rates sustained for several centuries would lead to an environmental crisis. Furthermore, Kleinschmitt et al. (2018) reported that SRM could result in a 2% increase in global mean $PM_{2.5}$ compared to the present-day but do not estimate the associated effect on morbidity due to uncertainties in the health effects. In this chapter we showed that an explosive volcanic eruption concurrent with SRM results in fewer but larger sulfate aerosol with a shorter lifetime, and a recovery overshoot due to the temporarily increased loss flux. This could lead to a temporary significantly larger stratospheric sulfur deposition compared to both SRM and volcanic eruption independently. Research should be undertaken to quantify the increase in sulfate deposition of volcanic eruptions during SRM and the associated impact on ecosystems and human morbidity.

The global mean total column ozone anomaly and resulting minimum global mean total column ozone is insignificantly different following a volcanic eruption both with and without SRM. This suggests there would be no significant difference in the globally averaged UV flux to the surface. However, the smaller tropical total column ozone anomalies following sulfur-only and halogen co-emission volcanic eruptions in SRM and faster recovery may have implications for the magnitude and duration of surface UV exposure in the tropics and may also have dynamical feedback effects. Tropical ozone has previously been shown to dynamically couple with stratospheric and tropospheric circulation leading to large changes in regional climate (e.g. Son et al., 2010).

One consistent feature of the ERF_{ari} and total column ozone results reported in this work is that the perturbations recover faster in SRM conditions compared to non-SRM conditions, reflecting the faster recovery timescales of the volcanic sulfate and halogen anomalies in SRM conditions compared to non-SRM conditions. This is due to the acceleration of the BDC driven by aerosol heating in the stratosphere caused by the continued emission of SO_2 into the tropics during SRM. The speed of the BDC is reflected in the stratospheric age of air which is 25% younger at 25 km in G6_SRM compared with SSP5 (Figure D2). This is in agreement with Aquila et al. (2012) who found that stratospheric heating by volcanic sulfate aerosol following the 1991 eruption of Mt. Pinatubo led to greater vertical and meridional transport and Kleinschmitt et al. (2018) who found the same thing in SRM simulations with radiatively interactive aerosols but contrary to Niemeier and Schmidt (2017) also showed that radiative heating from SRM slows down the QBO resulting in a stronger subtropical transport barrier reducing the meridional transport, trapping sulfate aerosol at low latitudes, causing the particles to grow larger and removed faster. The dynamical changes caused by SRM limits the magnitude and the duration of the additional ERR_{ari} (as described in Section 6.3.2i) representing a climate-SRM negative feedback loop which threatens the scalability of SRM to larger negative radiative forcing. Not only would increasing the magnitude of SRM SO_2 emissions result in a reduced radiative forcing efficiency per unit mass due to the decreasing efficiency with which sulfate aerosol scatter SW radiation with increasing size (e.g. Lacis, 2015; Niemeier and Timmreck, 2015), but the tropical stratosphere would also be heated more, accelerating the BDC, and reducing the lifetime of the SRM aerosol. This negative feedback (reduction in the efficiency of SRM with increasing SO_2 flux) would suggest that there is a logistical and economical limit to the negative radiative forcing achievable with SRM.

6.5 Summary & Conclusions

Solar radiation management by direct sulfur injection (SRM) is a possible mechanism through which the climate could be engineered to mitigate global warming. However, there is limited research into the effects of a concurrent explosive volcanic eruption. Here we use UKESM-AMIP model simulations to investigate the radiative forcing and total column ozone response to large (10 Tg of SO_2) and very-large (56 Tg of SO_2) sulfur-only eruption scenarios and corresponding large (10 Tg SO_2, 1.5 Tg HCl, 0.0086 Tg HBr) and very-large (56 Tg SO_2, 15 Tg HCl, 0.086 Tg HBr) co-emission eruption scenarios in climate states with and without SRM. Explosive volcanic eruptions concurrent with SRM result in significant additional negative radiative forcing that would lead to a further reduction in surface temperature and precipitation, but, in line with Laakso et al. (2016), we report that the effects of SRM and volcanic eruptions are not additive. We simulated a 25% and 12% smaller peak global mean forcing and a 38% and 18% smaller cumulative global mean forcing following a 10 Tg and 56 Tg sulfur-only volcanic eruption during SRM compared to the same eruptions without SRM. This is driven by the formation of larger aerosol, as found by Laakso et al. (2016), but also due to faster poleward transport and removal of volcanic sulfur due to a faster Brewer-Dobson circulation accelerated by SRM. The magnitude of the reduction is sensitive to both emission magnitude and volcanic halogen co-emission. The reduction in peak global mean and cumulative radiative forcing gets smaller as the magnitude of the volcanic SO_2 emission increases relative to the SRM SO_2 emission magnitude (6.4 Tg yr^{-1} SO_2). The reduction in peak global mean and cumulative ERF_{ari} was found to be roughly twice as big following a 10 Tg sulfur-only eruption during SRM compared to 56 Tg sulfur-only eruption during SRM. The co-emission of volcanic sulfur and halogens results in a further 12% and 21% reduction in the additional cumulative ERF_{ari} compared to a sulfur-only eruption during SRM. This is due to the shorter lifetime of volcanic sulfur following explosive volcanic eruptions that co-emit sulfur and halogens. We also report a significant overshoot in the recovery of the total sulfur burden and global mean ERF_{ari} beyond the pre-volcanic levels. This is because the additional emission of volcanic sulfur unbalances the previously stable total sulfur burden equilibrium established during SRM. Finally, we report that explosive volcanic eruptions result in broadly the same global mean total column ozone depletion with or without concurrent SRM. Although the total column ozone was shown to recover faster following eruptions concurrent with SRM.

Our results demonstrate the difficulties associated with maintaining a stable level of radiative forcing in the relatively likely event that a large explosive volcanic eruption occurs during SRM. The size, composition, and plume height of volcanic eruptions, as well as the evolving sulfur burden and aerosol size distribution would have to be monitored carefully and in near real time to enable the appropriate action to be resolved and enacted.

Chapter 7

Summary & Future Directions

7.1 Summary of key results

This chapter details the conclusions of this thesis in context with the aims and research questions outlined in Section 1.8.

1. In Chapter 3 we addressed the following research question:

How is the volcanic radiative forcing and stratospheric composition altered by the co-emission of volcanic halogens and sulfur from large explosive volcanic eruptions?

To do this we carried out four sets of UKESM-AMIP volcanic perturbation experiments under atmospheric conditions representative of the mid-1990s. The four sets of experiments included one large SO_2 (10 Tg), and one very-large SO_2 (56 Tg) emission scenario, both with (HIST_H10 and HIST_H56) and without halogens (HIST_S10 and HIST_S56), each with an ensemble size of six sampling different QBO states. We found that the co-emission of volcanic sulfur and halogens significantly amplified the peak and cumulative global mean ERF due to halogen-induced modifications to the volcanic sulfur life cycle and stratospheric composition, explained in more detail in the following subsections.

a) How does the co-emission of volcanic halogens modify the volcanic sulfur life cycle?

Co-emitting halogens resulted in a larger peak global mean radiative forcing due to volcanic aerosol-radiation interactions (ERF_{ari}) in both HIST_H10 (+8%) and HIST_H56 (+6%). Ozone depletion catalysed by volcanic halogens led to stratospheric cooling which is roughly twice as large as the volcanic aerosol heating found in sulfur-only eruption scenarios (HIST_S10 ≃ +1.5 K, HIST_S56 ≃ +3.5 K) and resulted in a net stratospheric cooling in halogen co-emission scenarios (HIST_H10 ≃ -2 K, HIST_H56 ≃ -3.5 K). The ozone-induced stratospheric cooling prevented aerosol self-lofting and kept the volcanic aerosol lower in the stratosphere with a shorter lifetime, resulting in reduced growth via condensation and coagulation and smaller peak global mean effective radius compared to sulfur-only simulations. The peak global mean effective radii of the HIST_H10 and HIST_H56 sulfate aerosols was found to be 15% and 10% smaller than HIST_S10 and HIST_S56 sulfate aerosols, closer to the most efficient radii (~0.20 μm) for scattering shortwave radiation per unit mass. Subsequently, we found that HIST_H10 and HIST_H56 have higher peak global mean SAOD anomalies (+11%, +22%) and ERF_{ari} (+8% + 6%).

b) How does the co-emission of volcanic halogens affect stratospheric composition and compositional forcing?

Co-emission of halogens also resulted in significant perturbations to the stratospheric chemistry and compositional-driven radiative forcing ($ERF_{clear,clean}$). Stratospheric methane was found to decrease by 3% and 18% and stratospheric water vapour (SWV) was found to reduce by 16% and 36% in HIST_H10 and HIST_H56, respectively. The methane reductions were driven by the enhanced destruction flux by volcanic Cl radicals and the SWV changes were attributed to the same stratospheric temperature reductions discussed in 1.(a). Cooling in the tropical tropopause vicinity increased the efficiency of the tropical cold trap dehydration effect, reducing the flux of water vapour from the troposphere to the stratosphere. The most dramatic change in chemistry was found to be in stratospheric ozone. We simulated significant ozone depletions globally in both HIST_H10 (22%) and HIST_H56 (57%) with prolonged depletion in both NH and SH winter polar regions. In HIST_H10, we simulate ozone hole conditions (<220 DU) globally for the first post-eruption year and then for 3-5 years at the poles during the winter. In HIST_H56, we simulated an ozone hole globally for 5 years followed by a gradual recovery over the following 5 years until only the polar winters exhibit ozone hole conditions. Stratospheric chemistry changes resulting from the co-emission of halogens increased the peak global mean $ERF_{clear,clean}$ by ~100% to - 2.1 Wm^{-2} in HIST_H56 and -1.3 Wm^{-2} in HIST_H10. Stratospheric ozone depletion was the dominant driver of $ERF_{clear,clean}$ accounting for ~75% of the total $ERF_{clear,clean}$.

c) How does the co-emission of volcanic halogens alter the volcanic effective radiative forcing?

The combined effect of the increased peak global mean ERF_{ari} and $ERF_{clear,clean}$ (discussed in 1.(a) and 1.(b), respectively) was that co-emitting halogens increased the peak global mean volcanic ERF by 30% and 24% and cumulative ERF by 60% and 100% in HIST_H10 and HIST_H56, respectively. This work showed for the first time that co-emission of plausible amounts of halogens can amplify the effective radiative forcing in simulations of explosive volcanic eruptions.

In conclusion, the work presented in Chapter 3 highlighted the necessity to include volcanic halogens emissions when simulating the climate impacts of past or future eruptions, and the critical need to maintain space-borne observations of stratospheric compounds to better constrain the stratospheric injection estimates of volcanic eruptions.

2. In Chapters 4 and 5 we addressed the following research question:

How will climate change alter the effects of tropical explosive sulfur-only and halogen co-emission volcanic eruptions?

To do this we carried out the same four sets of eruption scenario experiments as in Chapter 3 but this time in a historical climate state representative of the 1990s as well as a moderate (SSP2) and high-end (SSP5) future climate state representative of the 2050s. We found that climate change significantly amplified the peak global mean ERF_{ari} predominantly due to the acceleration of the Brewer-Dobson circulation (BDC). We also reported that the total column ozone (TCO) is less vulnerable to sulfur-only explosive volcanic eruptions but more sensitive

to halogen co-emission explosive volcanic eruptions, driven by the decline of equivalent effective stratospheric chlorine (EESC) and stratospheric ozone recovery. This is explained in more detail in the following subsections.

a) How will climate change impact the volcanic sulfur life cycle and forcing of future tropical explosive volcanic eruptions?

Climate change was found to amplify the peak global mean ERF_{ari} of large (+3-5%) and very-large (+7-11%) sulfur-only and halogen co-emission eruption scenarios. This was due to a reduction in aerosol size, mainly driven by a reduction in the total sulfur anomaly lifetime and associated aerosol growth, due to an acceleration of the BDC. Furthermore, we showed that the co-emission of halogens amplifies the peak global mean ERF_{ari} by 3% and 6% in future climate states, the same magnitude as was found by Staunton Sykes et al. (2021) in a HIST climate state.

b) Can statistical models be developed to generalise the change in volcanic forcing under a wide range of CO_2 concentrations?

Statistical models were successfully developed to generalise the impact of climate change on the effects of eruptions simulated in Chapter 4, using atmospheric CO_2 concentrations as a proxy. The statistical models highlighted that climate change and co-emission of halogens both significantly amplify the peak global mean ERF_{ari} of explosive volcanic eruptions and with no significant interaction. In other words, the amplification effects of climate change and halogen co-emission are not dependent on each other and can be considered separately and additively. However, the effect of climate change on peak global mean ERF_{ari} was shown to be dependent on the magnitude of the volcanic SO_2 injection, whereby climate change amplifies the peak global mean ERF_{ari} twice as much in the very-large eruption scenarios compared with the large eruption scenarios. Tentative use of these statistical models outside the parameter range of the simulations in this work enabled us to estimate that climate change between the pre-industrial and the 1990s may have already led to a 1-3% amplification of peak global mean ERF_{ari} and climate change between the 1990s and the 2090s may lead to a further 9-11% and 24-28% amplification of the peak global mean ERF_{ari}.

c) How sensitive and vulnerable is total column ozone to explosive volcanic eruptions in future climate states?

We showed that TCO remains vulnerable to large- and very-large-magnitude sulfur-only volcanic eruption scenarios to at least the 2050s in both future climates. The magnitude of ozone depletion was significantly smaller in the future reflecting the projected decline in stratospheric halogens concentration. However, in contrast to a previous study we find very similar TCO responses under both the moderate and high-end warming climate futures. This was mainly due to the limited difference between the EESC concentration, stratospheric temperature, and methane concentrations in these scenarios at the 2050s time horizon. In contrast, we showed that TCO is more sensitive to large and very-large volcanic halogen co-emission scenarios in the 2050s future climate, especially at the poles. This increased sensitivity is driven by the decline of EESC and stratospheric ozone recovery. Across both sulfur-only and halogen co-emission eruption scenarios global mean TCO anomalies were shown to recover significantly faster in the future, driven by a faster BDC accelerated by anthropogenic greenhouse gas emissions.

In conclusion, the work presented in Chapter 4 identified a negative climate-volcano feedback loop (described in 2.(a) and 2.(b)), which could modulate the climate variability caused by explosive volcanic eruptions and challenge the suitability of the constant volcanic forcing typically used in future climate projections. Furthermore, work presented in Chapter 5 demonstrated how the global mean TCO response to future sulfur-only and halogen co-emission volcanic eruptions is expected to differ in future climates compared to HIST (described in 2.(c)), with important implications for the magnitude and duration of surface UV exposure, especially in the tropics. The opposing sensitivity trend to sulfur-only and halogen co-emission volcanic eruptions in future climate states is in stark contrast with the large uncertainty in the flux of volcanic halogens to the stratosphere, clearly highlighting a research priority.

3. In Chapter 6 we addressed the following research question:

How will sulfate aerosol geo-engineering alter the atmospheric effects of explosive sulfur-only and halogen co-emission volcanic eruptions?

To do this we carried out the same four sets of eruption scenario experiments as in Chapters 3, 4, and 5 but this time in a moderate (SSP2) and high-end (SSP5) future climate state representative of the 2050s and a geo-engineering climate state, which employs solar radiation management by direct stratospheric sulfur injection (SRM). We found that a volcanic eruption during SRM led to additional negative radiative forcing and TCO depletion, but the response was complex and non-additive, explained in more detail in the following subsections.

a. How are the volcanic sulfur life cycle and radiative forcing effects of explosive tropical volcanic eruptions altered in a climate state which has been geo-engineered by direct stratospheric SO_2?

Tropical explosive volcanic eruptions concurrent with SRM resulted in significant additional negative radiative forcing that would lead to a further reduction in surface temperature and precipitation, but, in line with Laakso et al. (2016), we reported that the effects of SRM and volcanic eruptions are not additive. We simulated a 25% and 12% smaller peak global mean forcing and a 38% and 18% smaller cumulative global mean forcing following a 10 Tg and 56 Tg sulfur-only volcanic eruption during SRM compared to the same eruptions without SRM. This was driven by the formation of larger aerosol, as found by Laakso et al. (2016), but also due to faster poleward transport and removal of volcanic sulfur due to a faster BDC accelerated by SRM. The magnitude of the reduction was sensitive to both emission magnitude and volcanic halogen co-emission. The reduction in peak global mean and cumulative radiative forcing was found to get smaller as the magnitude of the volcanic SO_2 emission increased relative to the SRM SO_2 emission magnitude (6.4 Tg yr^{-1} SO_2). The reduction in peak global mean and cumulative ERF_{ari} was found to be roughly twice as big following a 10 Tg sulfur-only eruption during SRM compared to 56 Tg sulfur-only eruption during SRM. The co-emission of volcanic sulfur and halogens resulted in a further 12% and 21% reduction in the additional cumulative ERF_{ari} compared to a sulfur-only eruption during SRM. This was due to the shorter lifetime of volcanic sulfur following explosive volcanic eruptions that co-emit sulfur and halogens. We also reported a significant overshoot in the recovery of the total sulfur burden and global mean ERF_{ari} beyond the pre-volcanic

levels. This was because the additional emission of volcanic sulfur unbalances the previously stable total sulfur burden equilibrium established during SRM.

b. How is the sensitivity and vulnerability of total column ozone to explosive volcanic eruptions altered by concurrent SRM?

We reported that explosive volcanic eruptions result in broadly the same global mean TCO depletion and resulting TCO with or without concurrent SRM. Although the TCO anomaly was found to be smaller in the tropics and recover faster following eruptions concurrent with SRM, which may have implications for the magnitude and duration of surface UV exposure in the tropics and may also lead to dynamical feedback effects.

In conclusion, the work presented in Chapter 6 demonstrated the difficulties associated with maintaining a stable level of radiative forcing in the relatively likely event that a large explosive volcanic eruption took place during SRM. The size, composition, and plume height of volcanic eruptions, as well as the evolving sulfur burden and aerosol size distribution would have to be monitored carefully and in near real time to enable the appropriate action to be resolved and enacted.

7.2 Future Directions

7.2.1 Eruption composition

Chapter 3 showed for the first time how the co-emission of plausible amounts of volcanic halogens can amplify the volcanic ERF in simulations of large tropical explosive eruptions. It emphasised the need to include volcanic halogen emissions when simulating the climate impacts of past or future eruptions, and the necessity to maintain space-borne observations of stratospheric compounds to better constrain the stratospheric injection estimates of future volcanic eruptions. It also highlighted several further research priorities including, exploring the effect of co-emitted volcanic halogens from smaller eruptions, the sensitivity to the form of volcanic halogen injection (e.g. HCl vs ClO), and the effect of co-emitting volcanic water vapour or ash emissions in addition to halogens.

i) Sensitivity to volcanic halogens from small eruptions

The large eruptions studied in this work are rare, occurring every 50-100 years (Newhall et al., 2018). As it stands, no large volcanic eruptions in the satellite era have been observed to emit large amounts of volcanic halogens directly into the stratosphere. However, the global annual mean volcanic chlorine flux has been estimated to be 23 Tg yr^{-1} based of 14 small (VEI $\leq$ 4) eruptions between 2004 and 2016, with bromine fluxes 3 orders of magnitude smaller (Aiuppa et al., 2009; Carn et al., 2016). Furthermore, Microwave Limb Sounder (MLS) observations have indicated detectable stratospheric halogen injection following the same 14 small eruptions with a HCl:SO_2 of between 0.1 and 0.3 and enhancing the local stratospheric HCl concentration by as much as 9 ppbv (Carn et al., 2016). This suggests that small eruptions may be a significant source of halogens into the stratosphere.

Klobas et al. (2017) reported that the primary determinant of the future ozone response to volcanic eruptions within any RCP emission scenario is the emission of very short lived (VSL) bromine from biogenic sources. This sensitivity mainly arose beyond 2050 when the EESC concentration approaches the 1980 benchmark. They simulated five volcanic perturbation experiments in the year 2100 under a RCP6.0 climate state, varying the VSL bromine from 0 to 8 pptv. Using simulations of a Pinatubo-sized sulfur-only volcanic eruption in the year 2100 under RCP6.0, they reported a net enhanced total column ozone when the VSL bromine contribution was kept at 0 ppt, but net total column ozone depletion when they used more realistic VSL bromine values (>2 pptv). This work suggested that including realistic VSL bromine emissions would prolong the vulnerability of ozone to sulfur-only volcanic eruptions through the beginning of the next century and highlights two potential research opportunities regarding halogen fluxes from small volcanic eruptions: 1) what was the stratospheric ozone response to the direct injection of volcanic halogens into the stratosphere from the small but frequent eruptions during the satellite period and how would the response change in future low-EESC climate states, 2) does the flux of volcanic halogens into the stratosphere from small but frequent eruptions contribute to the maintenance of an EESC concentration which could prolong the vulnerability of ozone to large sulfur-only volcanic eruptions.

ii) The sensitivity to reduced vs oxidised volcanic halogen injection

One of the key results of the halogen co-emission eruption experiments is the further depletion of stratospheric OH by reaction with HCl, as outlined in Chapter 3. Lurton et al. (2018) simulated the 2009 Sarychev Peak eruption (0.9 Tg of SO_2) (one of the 14 small eruptions studied in Carn et al. (2016)) in CESM1(WACCM) and showed how inclusion of co-emitted halogens (27 Gg of HCl) resulted in a lengthening of the SO_2 lifetime, due to the further depletion of OH, and a corresponding delay in the formation of aerosols, giving better agreement between modelled and observed SO_2 burden. In both Chapter 3 and Lurton et al. (2018), the volcanic chlorine was injected into the stratosphere in a reduced form (e.g. hydrogen halide, HCl) in agreement with what is commonly detected at the volcanic vent. However, Rüdiger et al. (2021) reported data from ground-based measurements to suggest that a significant fraction of the hydrogen halides initially emitted are rapidly converted into reactive oxidised forms (e.g. ClO and BrO) within the first 11 minutes inside the tropospheric column. Injecting volcanic halogens into the stratosphere in an oxidised form would lead to very different behaviour compared to in a reduced form. For one, we would likely not expect to see the depletion of OH and delay in the formation of aerosol reported by Lurton et al. (2018). Furthermore, the ClO would rapidly deplete ozone without the need for activation on the surface of aerosols first which may lead to larger ozone depletion and stronger stratospheric temperature decrease in the first year. Stratospheric temperature was shown to play an important role in the lifetime and volcanic forcing in halogen co-emission scenarios. This highlights two potential research priorities: 1) what fraction of the volcanic halogens injected into the stratosphere are injected as HCl and HBr compared to other Cl_y and Br_y species, 2) how sensitive are the findings of chapters 3 and 5 to changes to the specific form of volcanic halogens.

iii) Extending the volcanic emissions to water and ash.

In addition to the co-emission of volcanic halogens, there is also scope to model the co-emission of volcanic water vapour and ash directly into the stratosphere or the perturbation in stratospheric water vapour due to the change in stratosphere-troposphere exchange. Legrande et al. (2016) provided a mechanism explaining how co-emitting

volcanic water vapour may increase the nucleation rate of sulfate aerosol, altering the volcanic sulfur life cycle and the associated climate impacts. There is little evidence of direct water vapour emissions during the satellite era, however indirect perturbations in stratospheric water vapour due to an increase in stratosphere-troposphere exchange have been reported by Kilian et al. (2020), Kroll et al. (2021), and Chapter 3 of this thesis. In addition, Zhu et al. (2020) showed the importance of including volcanic ash injections in climate simulations. When heterogeneous chemistry on ash particles was included, they found that 43% more volcanic sulfur was removed from the stratosphere in the first 2 months. Volcanic ash is also likely to alter the lifetime, activation, and impact of co-emitted volcanic halogens in climate simulations. It would be interesting to explore how the inclusion of stratospheric water vapour perturbations and the direct stratospheric injection of ash would further alter the volcanic forcing in simulations of explosive volcanic eruptions.

7.2.2 Model set-up

In Chapter 4, we quantified that the co-emission of halogens and projected climate change results in the significant amplification of ERF_{ari} in simulations of large tropical explosive volcanic eruptions. Experiments run as part of this work were limited to atmosphere-only simulations of large, tropical eruptions in July. This model set-up ensured the experiments were systematic allowing us, in the first instance, to understand the response of the volcanic sulfur cycle and radiative forcing. However, understanding the sensitivities of our results to the volcanic eruption parameters as well as quantifying the full earth system response is an important next step. Running fully coupled transient experiments while covarying input parameters would be associated with significant computational cost and may instead be suitable for statistical emulation.

i) Volcanic eruption source parameters

The amplification of the volcanic forcing described in Chapter 4 was driven by changes in the total volcanic sulfur lifetime. As such, the results are likely to be sensitive to the eruption source parameters, which have previously been shown to alter the total volcanic sulfur lifetime (e.g. Toohey et al 2011, 2013, Metzner et al 2014). Marshall et al. (2019) utilised statistical emulation to explore the radiative impact of eruptions over a wide covarying range of SO_2 emission magnitudes, injection heights, and eruption latitudes. They found that the net radiative forcing is primarily determined by the mass of SO_2 emitted, but with secondary effects due to altitude and latitude driven by changes to the total volcanic sulfur lifetime. Zhuo et al. (2021) simulated longer total volcanic sulfur lifetimes and larger global mean volcanic forcing in simulations of tropical (15^{o}N) eruptions compared to extratropical (64^{o}N) eruptions, but smaller hemispheric mean forcing. They also simulated a larger ozone depletion in tropical eruptions compared to an extratropical eruption. Similar experiments to those carried out in this thesis should be conducted for extra-tropical eruptions, in different QBO phases, and with different plume heights to investigate how sensitive the amplification due to climate change and volcanic halogens are to changes in the eruption parameters and QBO phase.

ii) Model Couplings

Volcanic gases in all volcanic perturbation experiments described in Chapter 4 were injected into the tropical stratosphere at a fixed height of 21 km to represent a typical tropical explosive eruption. In doing so, we did not

account for the changes in atmospheric plume height due to climate change, a climate-volcano feedback shown by Aubry et al. (under review) to increase the total volcanic sulfur lifetime and amplify the volcanic forcing of large volcanic eruptions. Furthermore, all simulations in this thesis were run using an atmosphere-only model set-up and do not include ocean-feedbacks which have previously been shown to amplify the surface temperature response following volcanic eruptions (Fasullo et al., 2017). As a result, it is likely our work is underestimating the full extent of the amplification effect due to climate change. Experiments using an eruptive plume model in series with a fully coupled transient earth system model would enable the full extent of the climate-volcano feedback to be assessed and quantified.

iii) Climate-volcano feedbacks in the context of past climate change

Chapter 4 described a negative climate-volcano feedback where global warming between the present day and the 2050s results in an amplification of peak and cumulative ERF_{ari}, due to the associated acceleration in the stratospheric BDC. Climate models suggest there was a relatively slower BDC in past colder climates (Wang et al., 2020) and vice versa for past warmer climates (Szopa et al., 2019). This suggests that this climate-volcano feedback may have had a large effect on volcanic forcing during periods of high and low global mean temperatures throughout Earth's past, with important implications for climate. For example, in the Middle Eocene Climatic Optimum (MECO) where the atmospheric CO_2 concentration reached at least 4000 ppm (Pearson, 2010), the forcing due to large explosive volcanic eruptions was likely enhanced, whereas in the last glacial maximum where the CO_2 concentration was as low as ~180 ppm (Bouttes et al., 2011)b, the forcing due to large explosive volcanic eruptions would be smaller compared to the present day.

In Chapter 4 we reported statistical models that generalise the impact of climate change on the peak global mean ERF_{ari}. Using these relationships we estimate up to a 10% reduction in peak ERF_{ari} following large tropical explosive volcanic eruptions during the last glacial maximum and an amplification of peak ERF_{ari} of up to 80% during the MECO compared to present day. These atmospheric CO_2 ranges are well outside the parameter range used to build the statistical models (360 ppbv– 601 ppbv) and it is unlikely that a linear relationship between ERF_{ari} and CO_2 concentration would persist over this wide range and as such we appreciate that using these statistical models may result in very large errors. However, this remains an interesting thought experiment and highlights an area that warrants further and targeted research. Previous studies have suggested that volcanic events, such as continental flood basalts, during the Phanerozoic, when the global mean CO_2 concentration may have reached as high as 6000 ppm (Royer, 2006), may have led to major environmental shifts. The climate-volcano feedback identified in Chapter 4 may have exacerbated the climatic effect of these events, leading to even larger surface temperature changes compared to what we might expect based on the emissions magnitude and the behaviour of volcanic sulfur in the recent historical atmosphere.

iv) Using statistical emulation to explore how eruption source parameters, volcanic halogens and climate state impact volcanic radiative forcing and total column ozone

In a typical volcanic perturbation experiment, the range of multidimensional parameter space that can be explored is restricted due the computational expense and the required data storage capacity. For example, sampling

adequate parameter space to investigate how covarying a combination of SO_2 emission magnitude, volcanic halogen emission magnitude, background climate state or eruption source parameters (e.g. plume height, latitude, QBO), as suggested in i), ii) and iii), influences volcanic forcing or ozone depletion in a fully coupled global climate model is not realistic. Statistical emulation, however, may enable this to be done using a fraction of the computing resource, as was shown in Marshall et al. (2019). Emulators are statistical models developed from a limited set of simulations which effectively sample the desired parameter space. The emulator maps the relationship between the simulated model output (such as radiative forcing) and the experiment input parameters (e.g. SO_2 emission magnitude, background climate state, or eruption source parameter) within an uncertainty (compared to the original model) that can be quantified. Once developed the emulator is fast to evaluate and can be used to predict the output quantity for any combination of input parameters. This enables multidimensional response surfaces of output behaviour across the entire parameter space to be generated or the individual response for a unique set of input parameters.

Creating statistical emulators to investigate the sensitivities of volcanic forcing (or even surface cooling) and stratospheric ozone depletion to covarying SO_2 emission magnitudes, halogen co-emission magnitudes, and eruption source parameters would be immensely powerful. It would allow the individual and combined effect of each parameter on the volcanic radiative forcing and ozone depletion to be quantified and assessed. It could also be used by policy makers as a rapid assessment tool to prepare for and respond to future volcanic eruptions, whatever the magnitude of volcanic SO_2 or halogens, climate state, and eruption source parameter.

Furthermore, in Chapter 4, we presented evidence to suggest that climate change would amplify the volcanic forcing of large and very-large-magnitude volcanic eruptions and the magnitude of the amplification was shown to increase with volcanic SO_2 mass. Conversely, Aubry et al. under review, showed that climate change reduces the forcing of moderate magnitude (<1 Tg, intensity of 1.3×10^7 kg/s) sulfur-only volcanic eruptions. This was because climate change results in an elevated tropopause and so a smaller fraction of volcanic sulfur is emitted above the tropopause. This creates an interesting balance, climate change will reduce the volcanic forcing of smaller, more frequent eruptions, but amplify the large, rare eruptions. Clarifying the net effect of these climate-volcano feedbacks, say on the millennial timescale, would require the simulation of statistically realistic eruption distributions in terms of frequency, SO_2 mass, intensity, and location as well as ocean-atmosphere coupled climate modelling to account for the feedbacks relating to ocean stratification. This would require hundreds (if not thousands) of volcanic perturbation experiments. Alternatively, statistical emulators could enable this study with a comparatively low computational cost.

7.2.3 Ozone model bias and looking beyond stratospheric ozone

Research into the effects of volcanic eruptions on stratospheric composition have typically focussed on stratospheric ozone because of its role in the flux of harmful UV-B to the Earth's surface. However, previous studies have shown how sulfur-only volcanic eruptions can increase stratospheric water vapour (SWV) and methane (e.g. Kilian et al., 2020; Löffler et al., 2016), and Chapter 3 showed for the first time how co-emission

of volcanic halogens leads to the reduction of SWV and stratospheric methane. Furthermore, the significant changes to stratospheric ozone are expected to lead to significantly altered tropospheric chemistry.

i) Model Biases

Perturbation experiments, like the ones carried out in this thesis, allow gross biases to be zeroed out. However, it is possible that there are feedbacks emergent in the model and our results are sensitive to these biases. For example, modelled stratospheric ozone was found to be high biased in UKESM1.0 compared to observations and the CMIP6 multi-model mean (Keeble et al., 2021). This was largely caused by the omission of the 0.6 times scaling of NO photolysis typically recommended for Fast-Jx and the omission of the 8 additional heterogenous reactions outlined by Dennison et al. (2019) (N.B. these reactions are included in the model set-up employed in this thesis). In Chapter 5, we reported that the total column ozone in the future is more sensitive to co-emitted volcanic halogens because there was more stratospheric ozone to lose and, as such, it is possible that these results may be impacted by the high bias resulting from the too fast NO photolysis in UKESM1.0. These model biases have largely been fixed in the most recent update of UKESM. We do not expect the results to be altered significantly however, this could be confirmed by re-running the simulations in this work in the updated version of UKESM or another model with a better fit with observations and the CMIP6 multi-model mean.

ii) SWV and CH_4 in the future.

In Chapter 3 of this thesis, an increase in SWV and a relatively small increase in stratospheric methane burden was reported following sulfur-only simulations caused by warming of the tropical tropopause cold point and enhanced tropical vertical ascent due to aerosol heating, enabling a greater flux of water vapour and methane to be brought up from the troposphere. Conversely, in co-emission scenarios, the process was shown to be the same but in the opposite sense. Chapter 3 reported a decrease in SWV, caused by ozone-loss induced cooling of the tropical tropopause cold point and reduced tropical vertical ascent reducing the flux of water vapour from the troposphere, and stratospheric methane burden caused by enhanced destruction of methane by Cl. Recent work by Kroll et al. (2021) reported that the additional SWV following sulfur-only volcanic eruptions counterbalances roughly 4% of the negative aerosol forcing from the volcanic aerosols. Our results using the model set-up outlined in Chapter 5, show that SWV anomalies and stratospheric methane anomalies are amplified following eruption scenarios in the future, which is hypothesised to be due to the greater tropospheric concentrations of water vapour and methane resulting from anthropogenic emissions and tropospheric warming. As such, the changes in stratospheric water vapour following future sulfur-only eruptions would be expected to counterbalance a larger fraction of the negative forcing from volcanic aerosols. It is important to explore this earth system feedback in future work in order to understand the full and wide-reaching consequences of climate change.

iii) Tropospheric chemistry

In Chapter 3 and 5, we reported enhanced UV flux reaching the Earth's surface for up to 5 years in halogen co-emission scenarios due to the reduction in stratospheric ozone. Not only would this have negative implications for society and the biosphere, but it would also significantly impact tropospheric chemistry. For example, we

simulate a reduction in tropospheric and surface ozone, increasing tropospheric OH resulting in a methane lifetime decrease, and significant shift in NO_x partitioning (Figure 7.1, Table 7.1).

The reduction in tropospheric ozone is a combination of reduced flux of ozone transported from the stratosphere and the increase in J(O1D) (the photolysis rate of ozone) due to the enhanced transmission of UV through the stratosphere and into the troposphere. The combined effect of these two factors results in a 15% decrease in tropospheric ozone, as well as a 15% increase in HO_x (HO_2 and OH) concentrations (Table 7.1). The maximum changes in surface ozone (0-100m) (Figure 7.1) mirror the spatial patterns of total column ozone depletion and surface UV exposure shown in Chapter 3, with the largest losses in the mid-latitudes during the northern and southern hemisphere summer.

The 15% increase in OH concentration following H10 simulations due to enhanced production from the photolysis of ozone, results in a 12.5% shorter tropospheric methane lifetime. The change in HO_x also causes a reduction in the tropospheric NO_x (-1%), NOy (-6%) and NOz (-5%) burden which may have significant consequences in remote regions, where a small change in NO_x concentration can have a large impact on local O_3 concentrations.

Tropospheric ozone is a greenhouse gas and a pollutant detrimental to human health and crops and ecosystems productivity (Archibald et al., 2020). A drop in surface ozone would reduce the human exposure to ozone, however, a drop in ozone higher in the troposphere would result a larger flux of UV-B to the surface, increasing the occurrences of eye-damage, skin cancers and immunodeficiencies (World Meteorological Organization, 2014). A reduction in the methane lifetime on this scale would result in significant reduction in the tropospheric methane concentration and would result in a negative radiative effect. If we assume the perturbation persisted until a new tropospheric methane concentration equilibrated, we can use the method outlined in Etminan et al. (2016) to estimate that a -12.5% reduction in methane lifetime would result in a ~340 ppbv (19%) reduction in tropospheric methane concentration and an associated global mean instantaneous radiative forcing of up to -0.175 Wm^{-2}, assuming a N_2O (310 ppbv) and CH_4 (1750 pbbv) concentration typical of the 1990s. This is roughly 25% of the radiative forcing attributed to methane concentration increases between the pre-industrial and the year 2000 (Etminan et al., 2016). However, the tropospheric methane lifetime would be expected to fully recover within 10 years, much shorter than the time required to reach a new equilibrium methane concentration (several times the lifetime e.g. 25 years). As such, the long-term change would be significantly smaller. The sustained changes to stratospheric ozone simulated in geo-engineering studies may lead to more permanent changes in the methane lifetime and radiative forcing, with knock on effects on oxidants and aerosols (O'Connor et al., 2021; Weber et al., 2020).

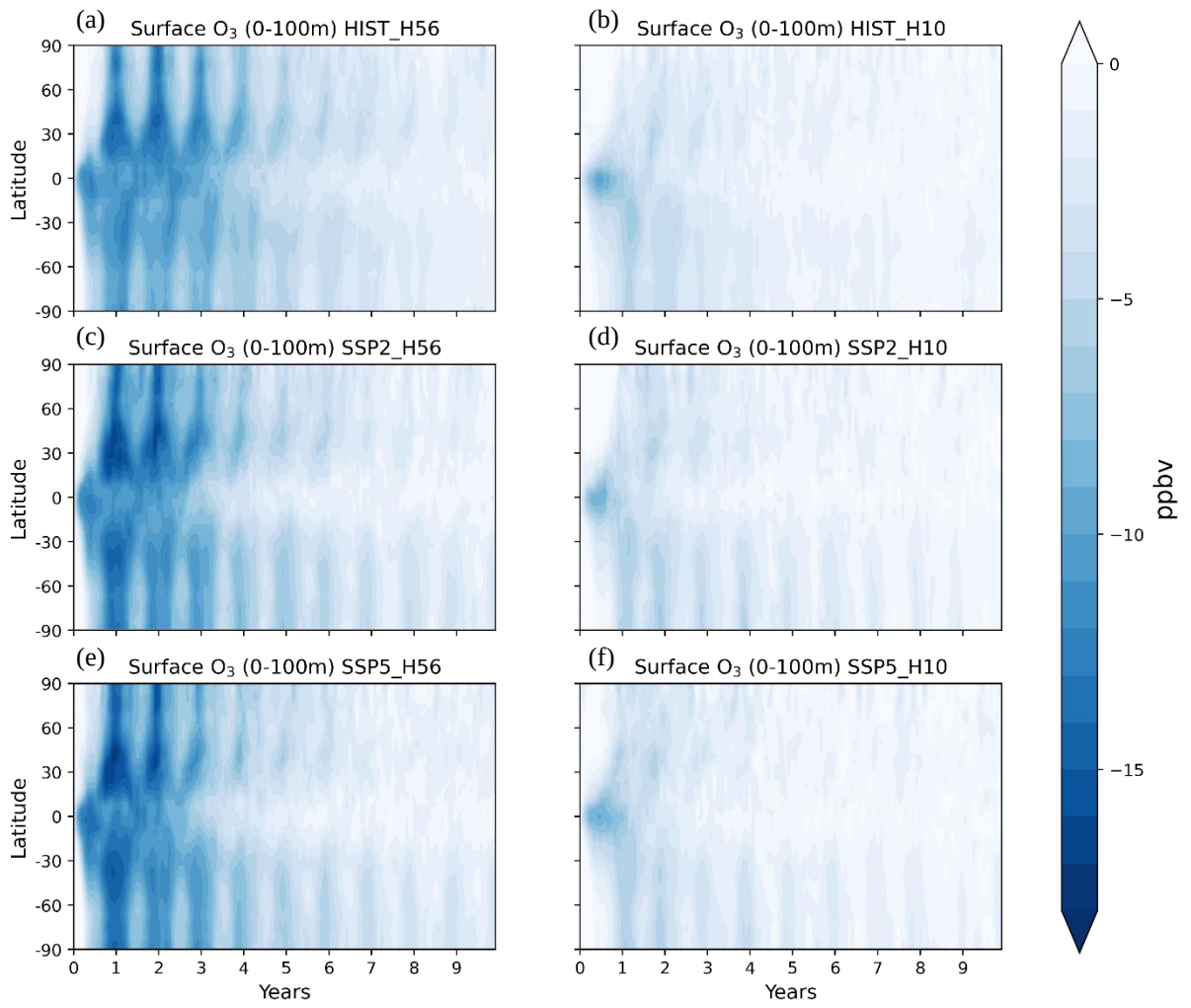

Figure 7.1 - Change in surface ozone (ppbv) relative to control climatologies in HIST_H56 (a), HIST_H10 (b), SSP2_H56 (c), SSP2_H56 (d), SSP5_H56 (e) and SSP5_H10 (f).

	Control	**H10**
Trop. O_3 Burden (Tg)	340	288 (-15%)
NO_2 Column (x10^{15} Molecules/cm^3)	1.18	1.14 (-3%)
OH (x10^6 Molecules/cm3)	1.20	1.38 (+15%)
Methane Lifetime (years)	7.2	6.1 (-12.5%)
Trop. NO_x burden (Tg of N)	0.1543	0.1524 (-1%)
Trop. NO_y burden (Tg of N)	0.9020	0.8512 (-6%)
Trop. NO_z burden (Tg of N)	1.0562	0.8512 (-5%)

Table 7.1 - A non-exhaustive list of perturbations to tropospheric chemistry in the HIST control and the first post eruption year following HIST_H10. NO_2 column, methane lifetime, and [OH] are calculated as a global tropospheric means. O_3, NO_x, NO_y, NO_z are reported as tropospheric burdens.

Appendix A

Supplementary Information for Chapter 3 "Co-emission of volcanic sulfur and halogens amplifies volcanic effective radiative forcing"

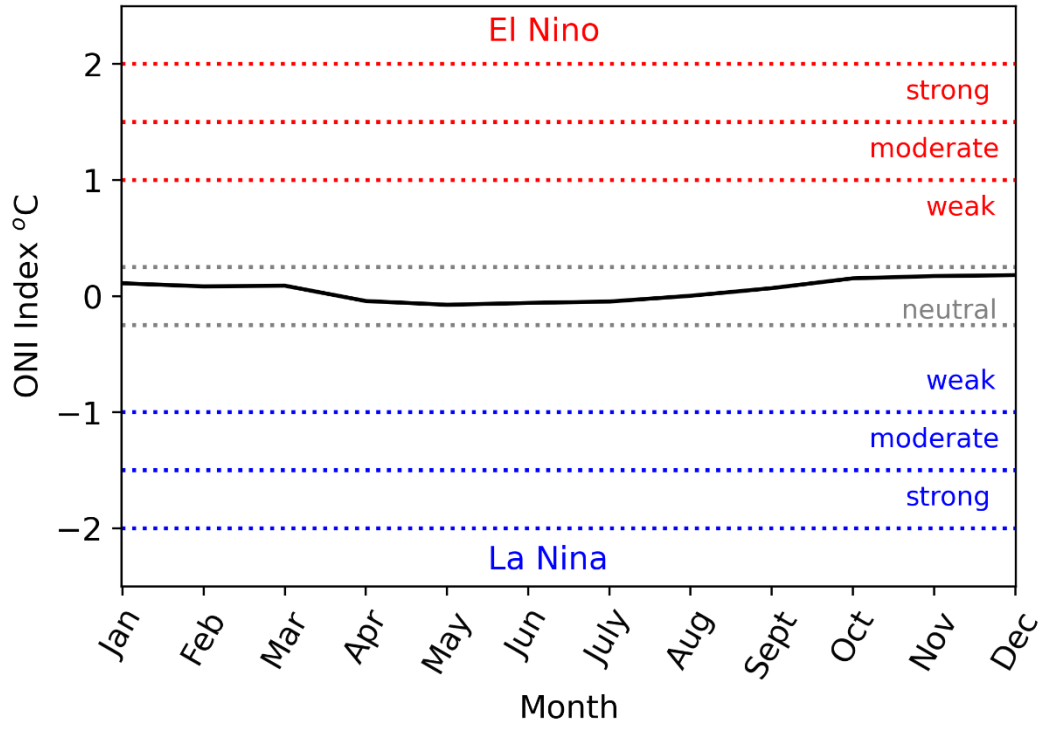

Figure A1 The Oceanic Niño Index (ONI) of the prescribed SST used to force the atmosphere-only simulations. ONI is defined as the 3-month running mean of SST anomalies in the Niño 3.4 region (5ºN-5ºS, 120-170ºW) compared to the 1971- 2000 base period.

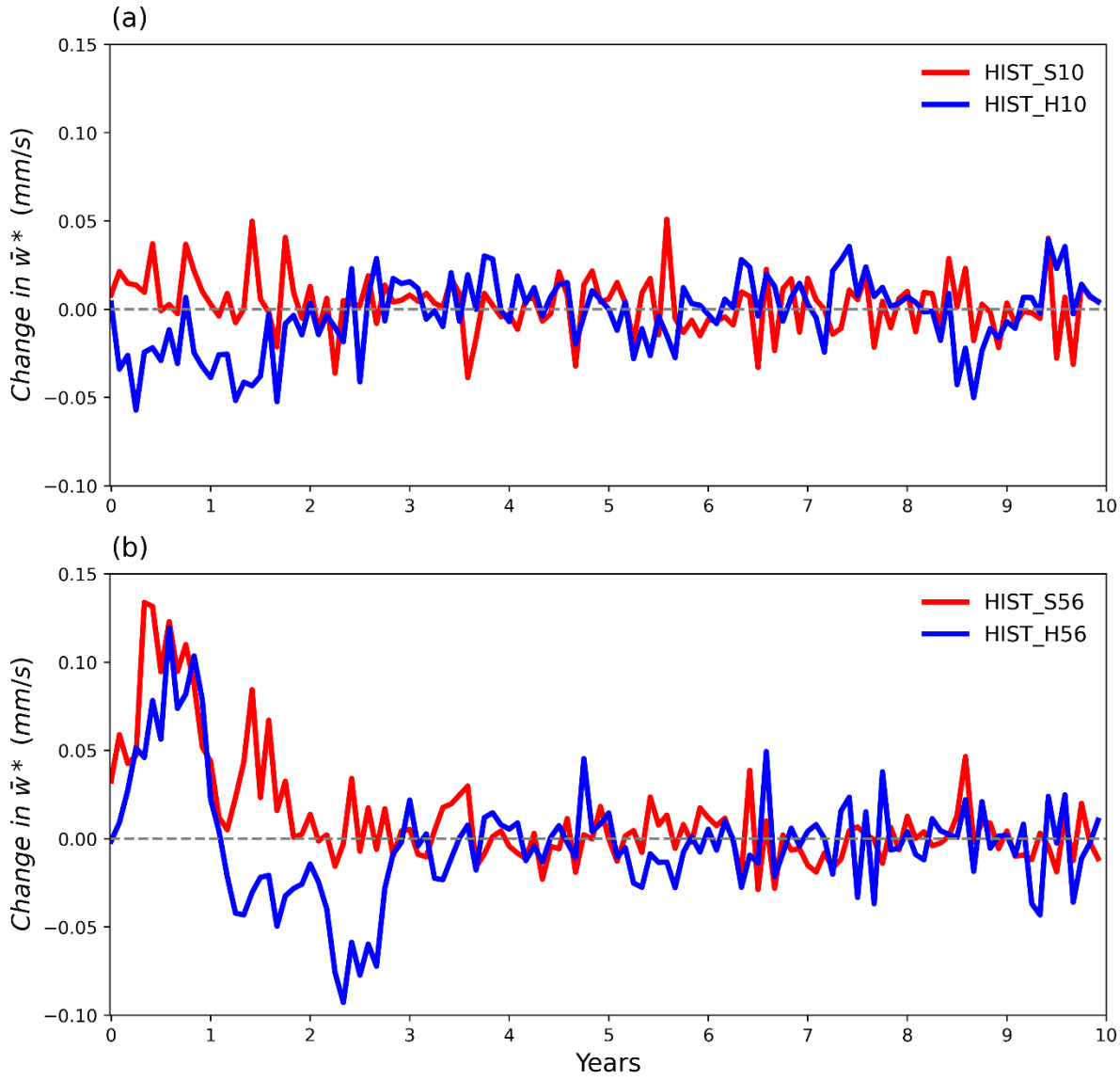

Figure A2 Time series of change in 20ºS – 20ºN mean $\bar{w}^*$ (residual mean vertical velocity) at 50 hPa for (a) HIST_S10 and HIST_H10, (b) HIST_S56 and HIST_H56 compared to the control climatology.

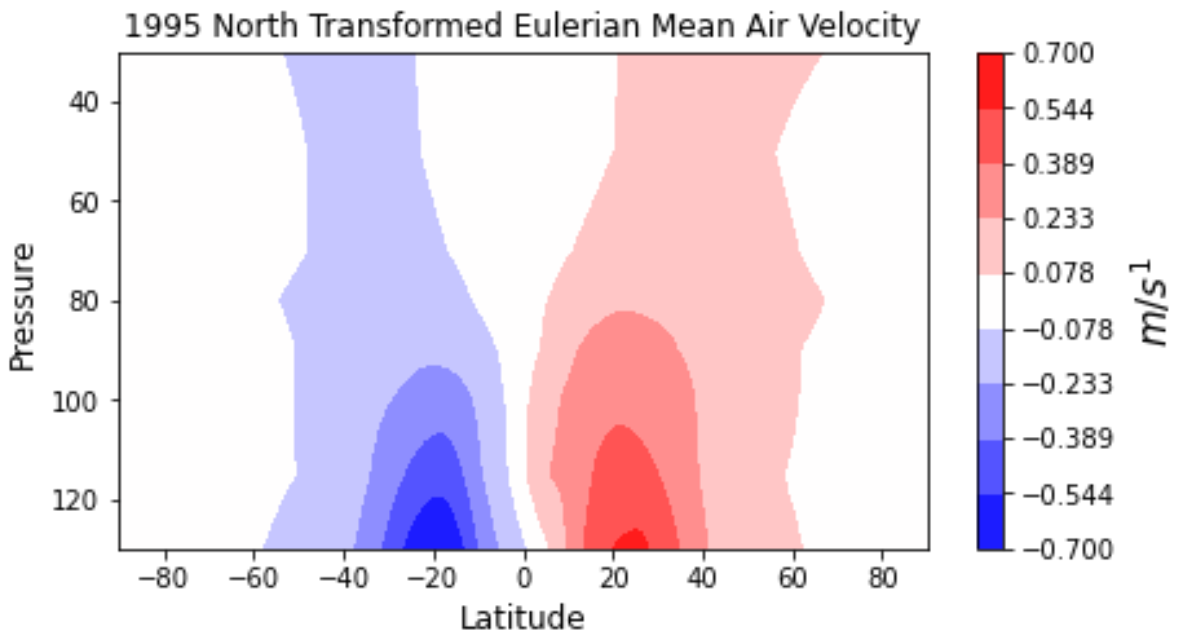

Figure A3 Northward transformed eulerian mean air velocity (ms^{-1}) in the control simulation, averaged over the full 20 years. The poleward velocity reduces with altitude.

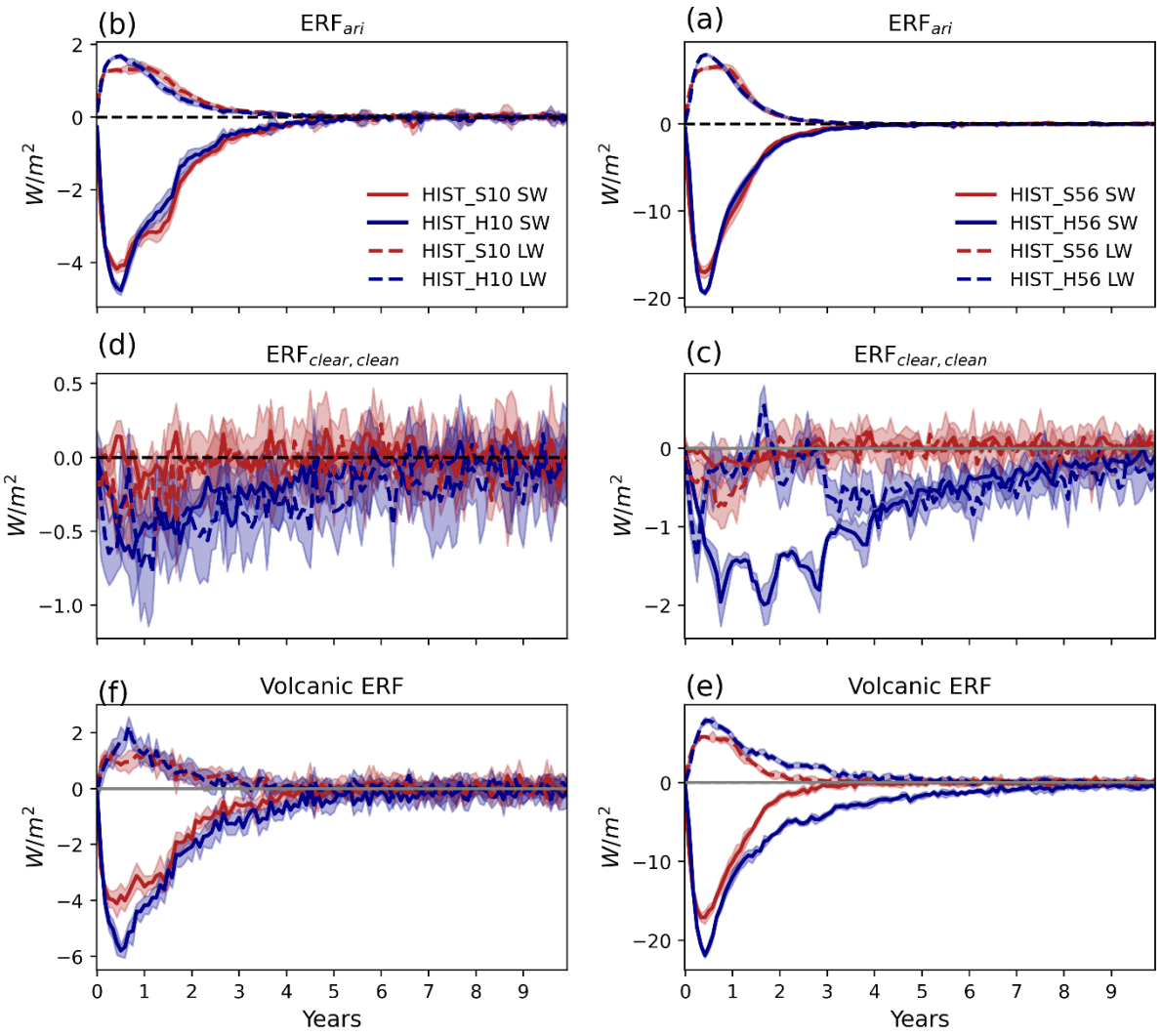

Figure A4 Global mean evolution of TOA ERF_{ari} (top), $ERF_{clear,clean}$ (middle) and volcanic ERF (bottom), in HIST_S10 and HIST_H10 (left) and HIST_S56 and HIST_H56 (right). Sulfur-only (red), co-emission (blue), SW forcing (solid), LW forcing (dashed). Shading represents the ensemble range.

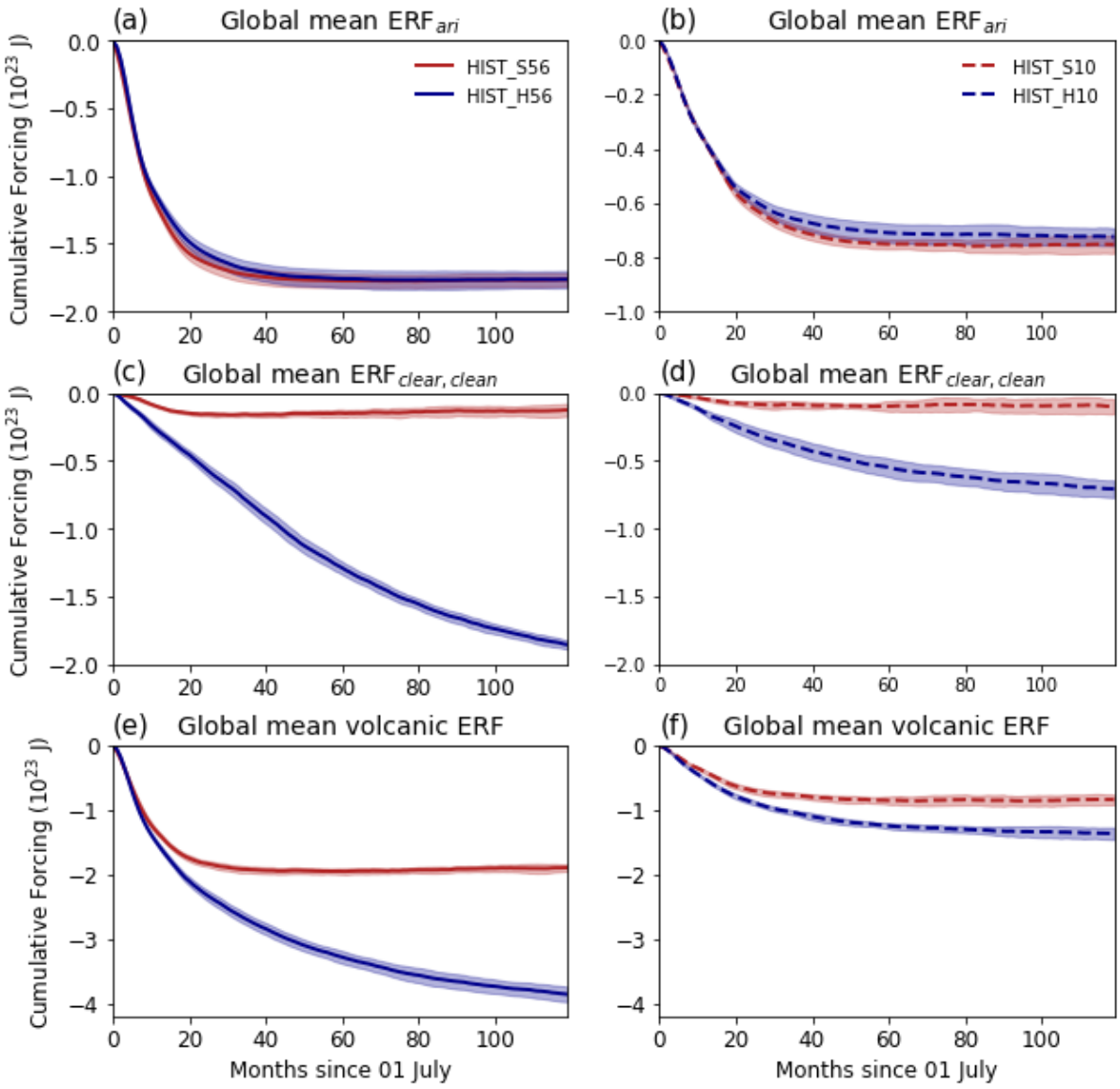

Figure A5 Cumulative global mean TOA ERF_{ari} in HIST_S56 & HIST_H56 (a) and HIST_S10 & HIST_H10 (b), $ERF_{clear,clean}$ in HIST_S56 & HIST_H56 (c) and HIST_S10 & HIST_H10 (d), Volcanic ERF in HIST_S56 & HIST_H56 (e) and HIST_S10 & HIST_H10 (f), Shading represents the ensemble range.

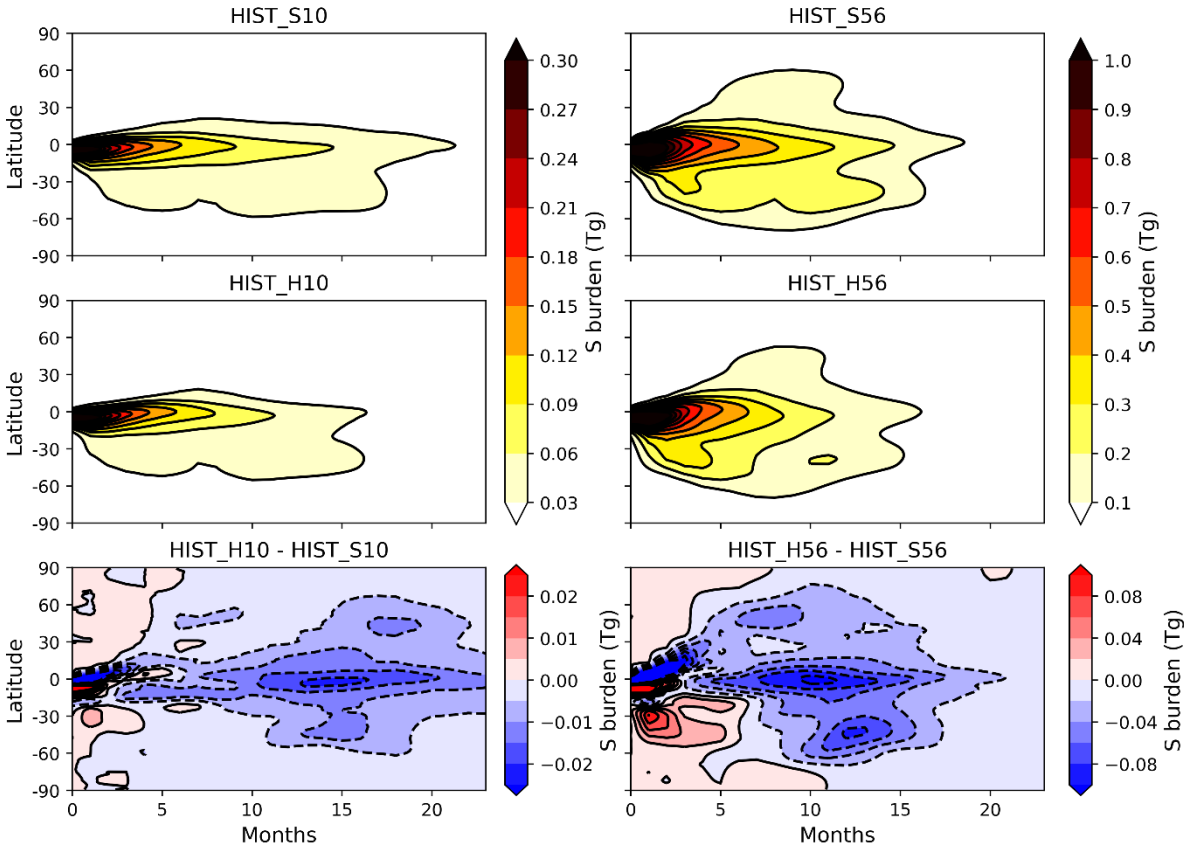

Figure A6 Evolution of total sulfur burden, in HIST_S10 (a), HIST_S56 (b), HIST_H10 (c) and HIST_H56 (d). The HIST_H10 – HIST_S10 difference is shown in (e) and the HIST_H56 - HIST_S56 difference is shown in (f).

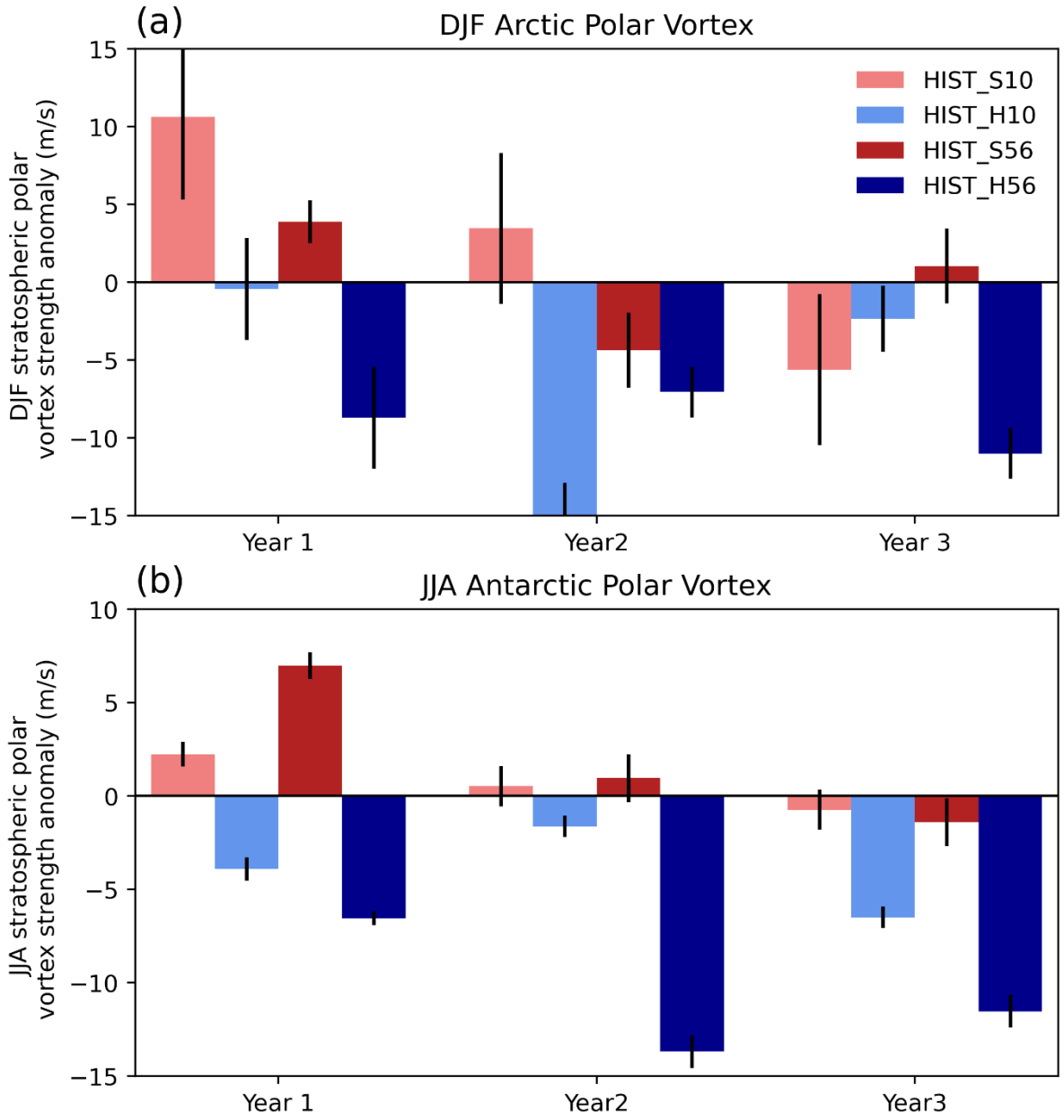

Figure A7 Polar vortex strength in the northern hemisphere winter (DJF) (a) and southern hemisphere winter (JJA) (b) in the first 3 post eruption years. The polar vortex strength was defined as the zonal mean wind speed averaged over 55º-65º and 1-30hPa. Error bars show one standard deviation across the ensemble.

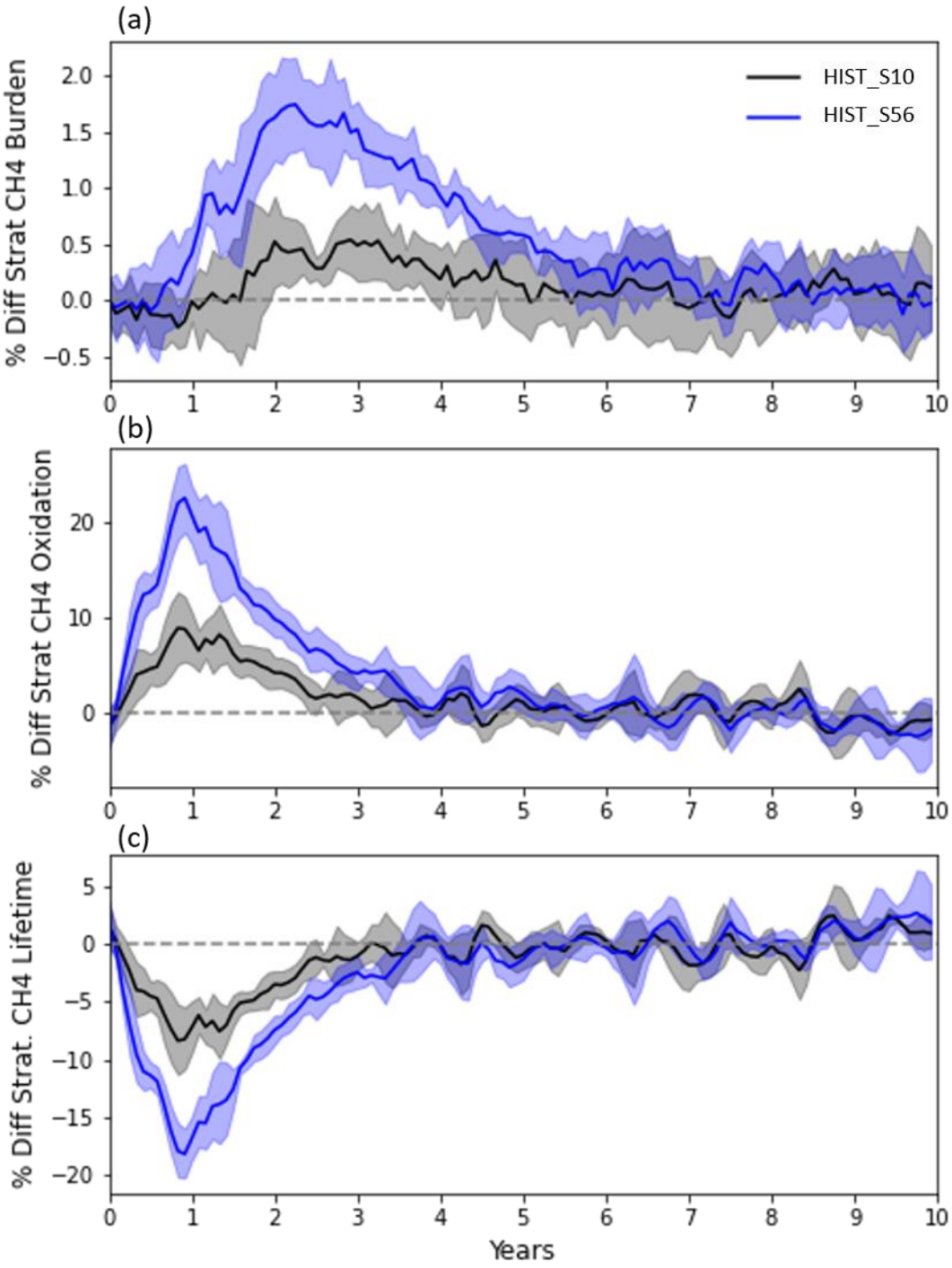

Figure A8 Timeseries of percentage change in stratospheric methane burden (a), stratospheric methane oxidation flux (b) and stratospheric methane lifetime (c). Shading represents the ensemble range.

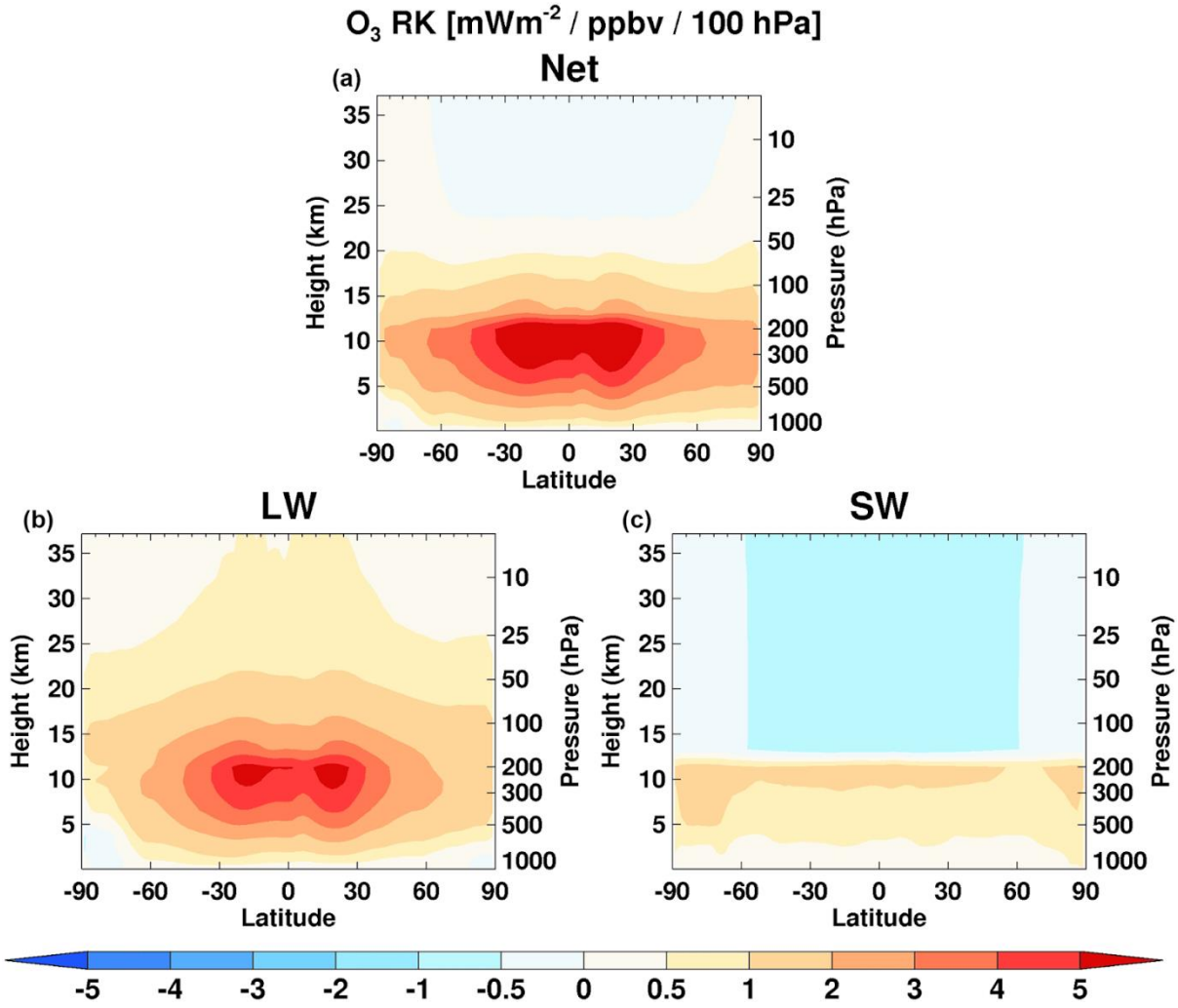

Figure A9 Annual zonal mean whole atmosphere ozone radiative kernel from (Rap et al., 2015) under all-sky conditions for (a) net (LW + SW), (b) LW, and (c) SW components. Figure taken from Iglesias-Suarez et al. (2018).

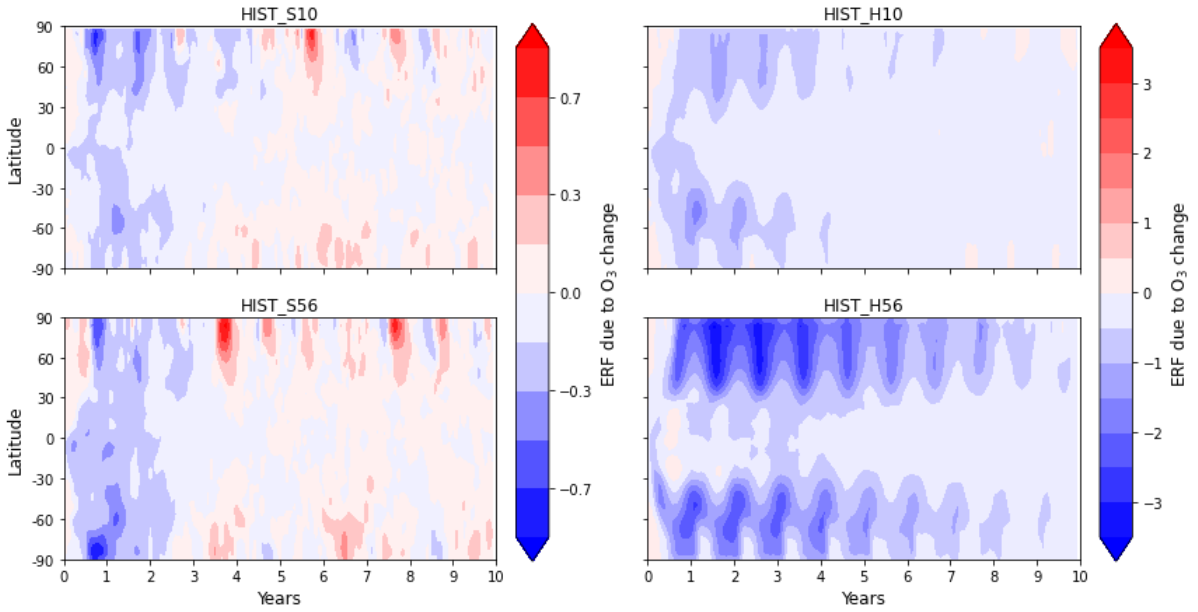

Figure A10 Evolution of the TOA net flux anomalies due to stratospheric ozone change in HIST_S10, HIST_H10, HIST_S56 and HIST_H56 estimated from the ozone radiative kernel from Rap et al. (2015). The increases in TOA net forcing are shown in shades of red, and decreases in shades of blue.

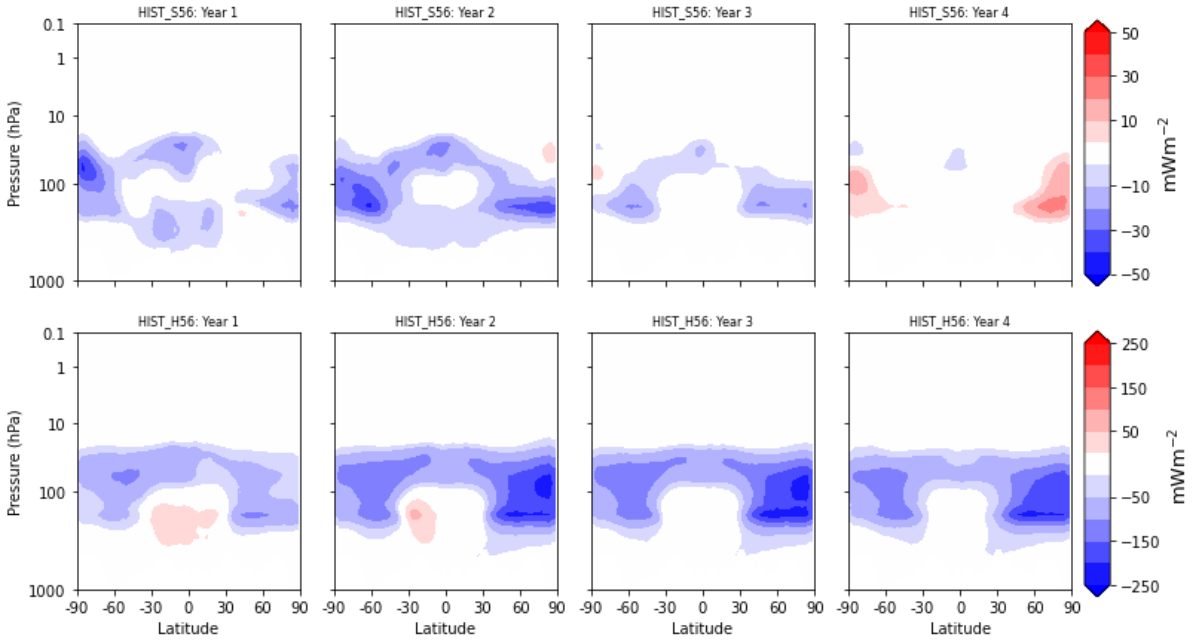

Figure A11 Zonal mean difference in TOA net flux anomalies for the first four post eruption years due to stratospheric ozone change in HIST_S56 (top) and HIST_H56 (bottom) estimated from the ozone radiative kernel from Rap et al. (2015). Increases in net forcing are shown in shades of red and decreases in shades of blue.

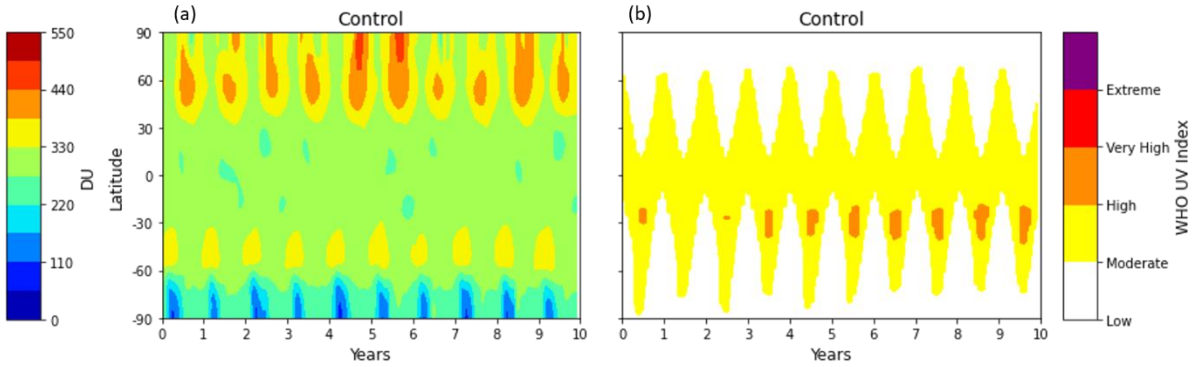

Figure A12 Zonal mean column ozone (a) and zonal mean daily average UV index (b) in the control simulation. Ozone hole conditions are simulated when the column ozone < 220 DU.

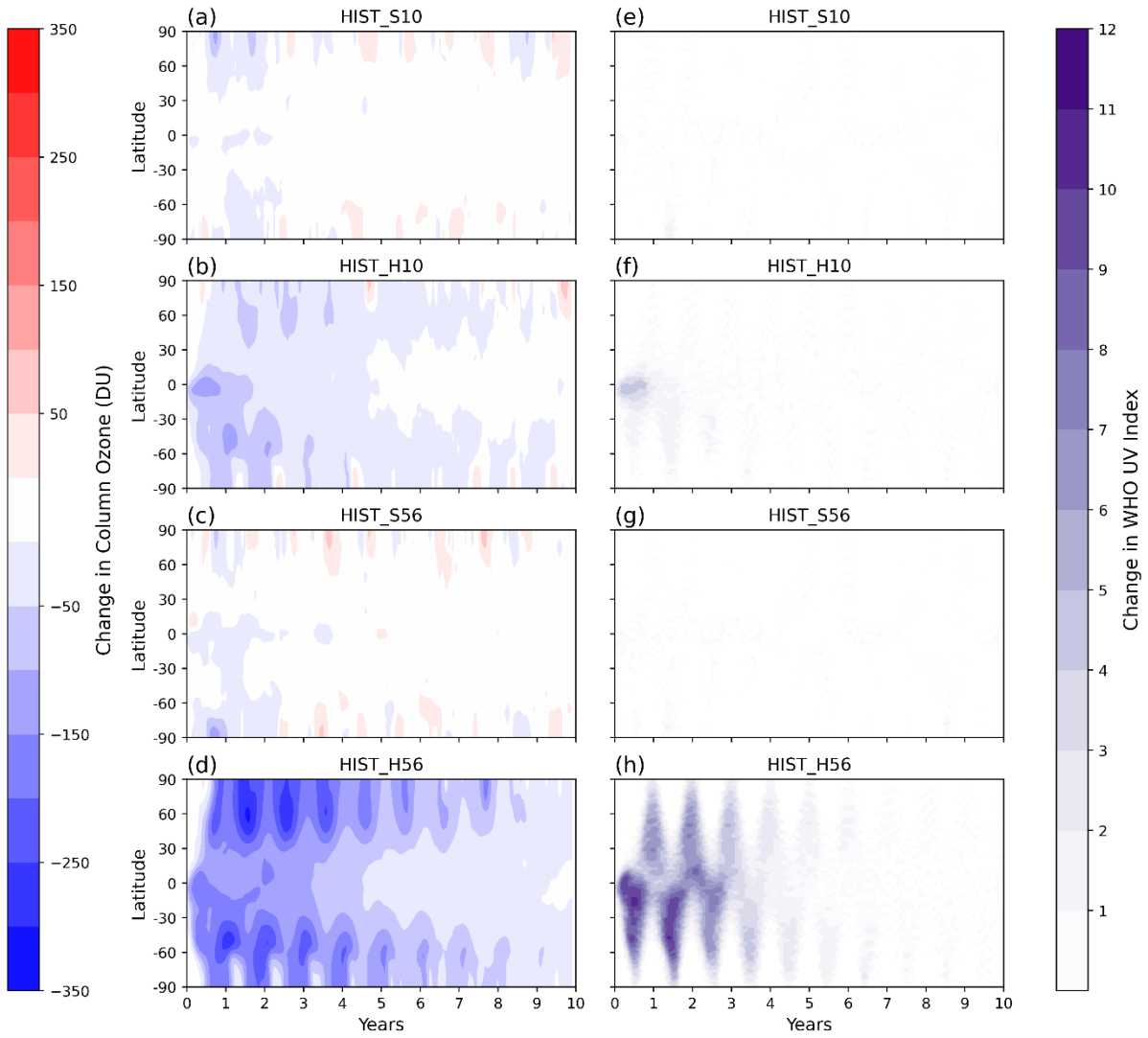

Figure A13 Zonal mean change in column ozone (left) and Zonal mean change in the WHO UV index (right) in the control simulation.

Appendix B

Supplementary Information for Chapter 4 "Climate change amplifies the radiative forcing of large magnitude explosive volcanic eruptions"

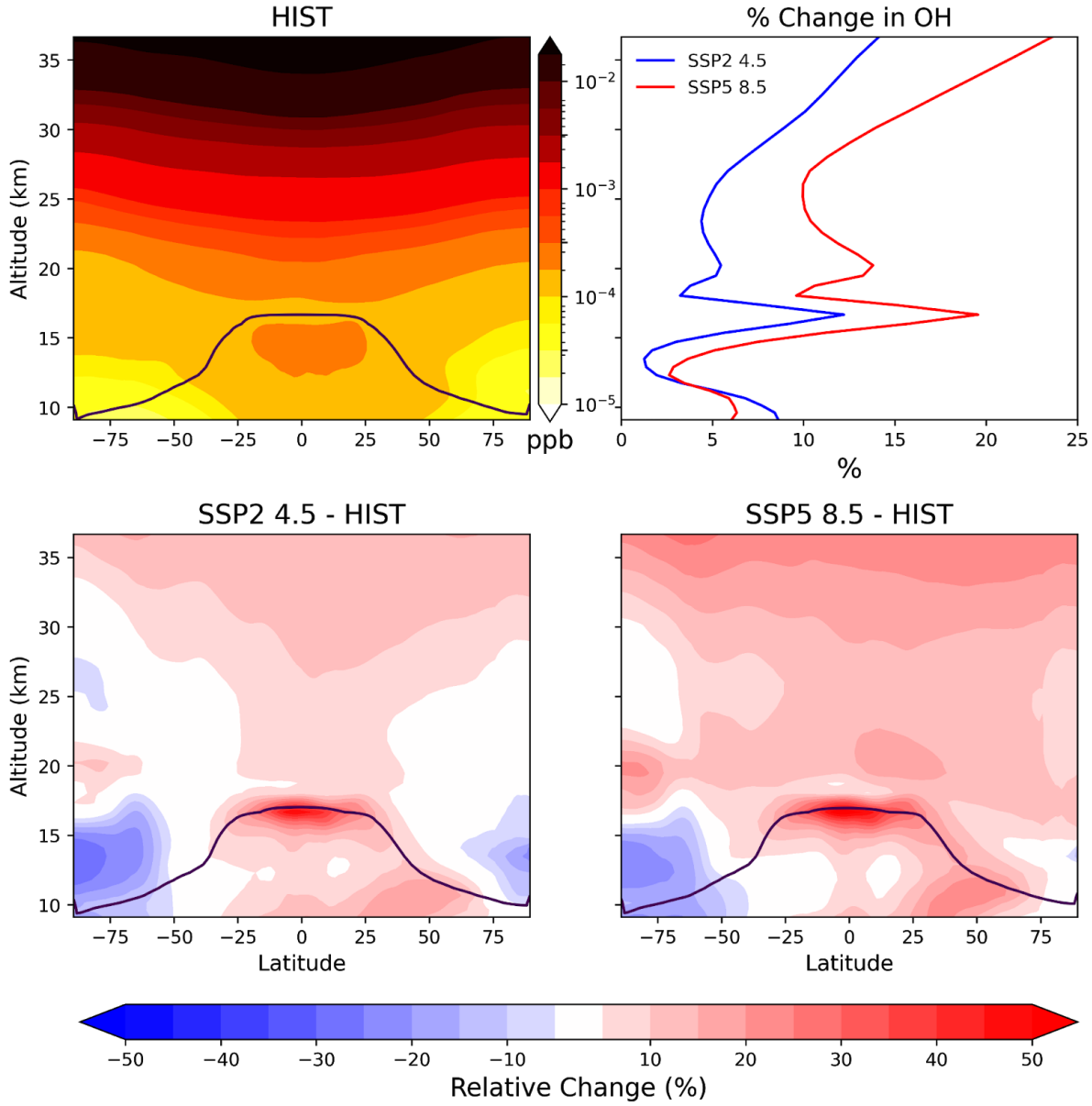

Figure B1 (a) Annual zonal mean OH (ppbv) in HIST control climatology. (b) Profile of % change in annual global mean OH (ppbv) in SSP2 (blue) and SSP5 (red) control climatologies relative to HIST control climatology. % change in annual zonal mean OH (ppbv) in (c) SSP2 and (d) SSP5 relative to HIST control climatology. The zonal mean tropopauses are indicated by the solid lines.

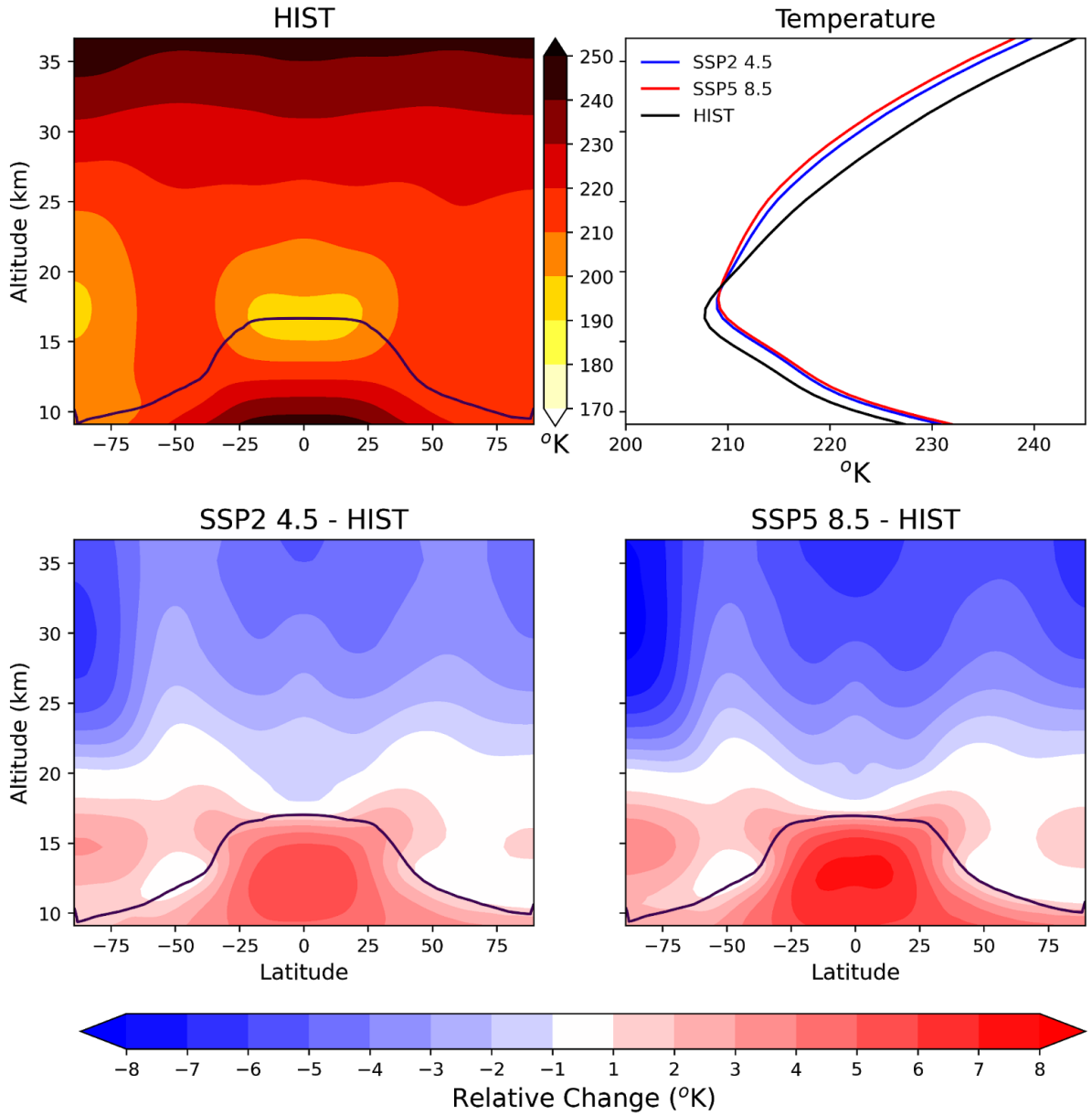

Figure B2 (a) Annual zonal mean temperature in HIST control climatology. (b) Profile of % change in annual global mean temperature in SSP2 (blue) and SSP5 (red) control climatologies relative to HIST control climatology. % change in annual zonal mean temperature in (c) SSP2 and (d) SSP5 relative to HIST control climatology. The zonal mean tropopauses are indicated by the solid lines.

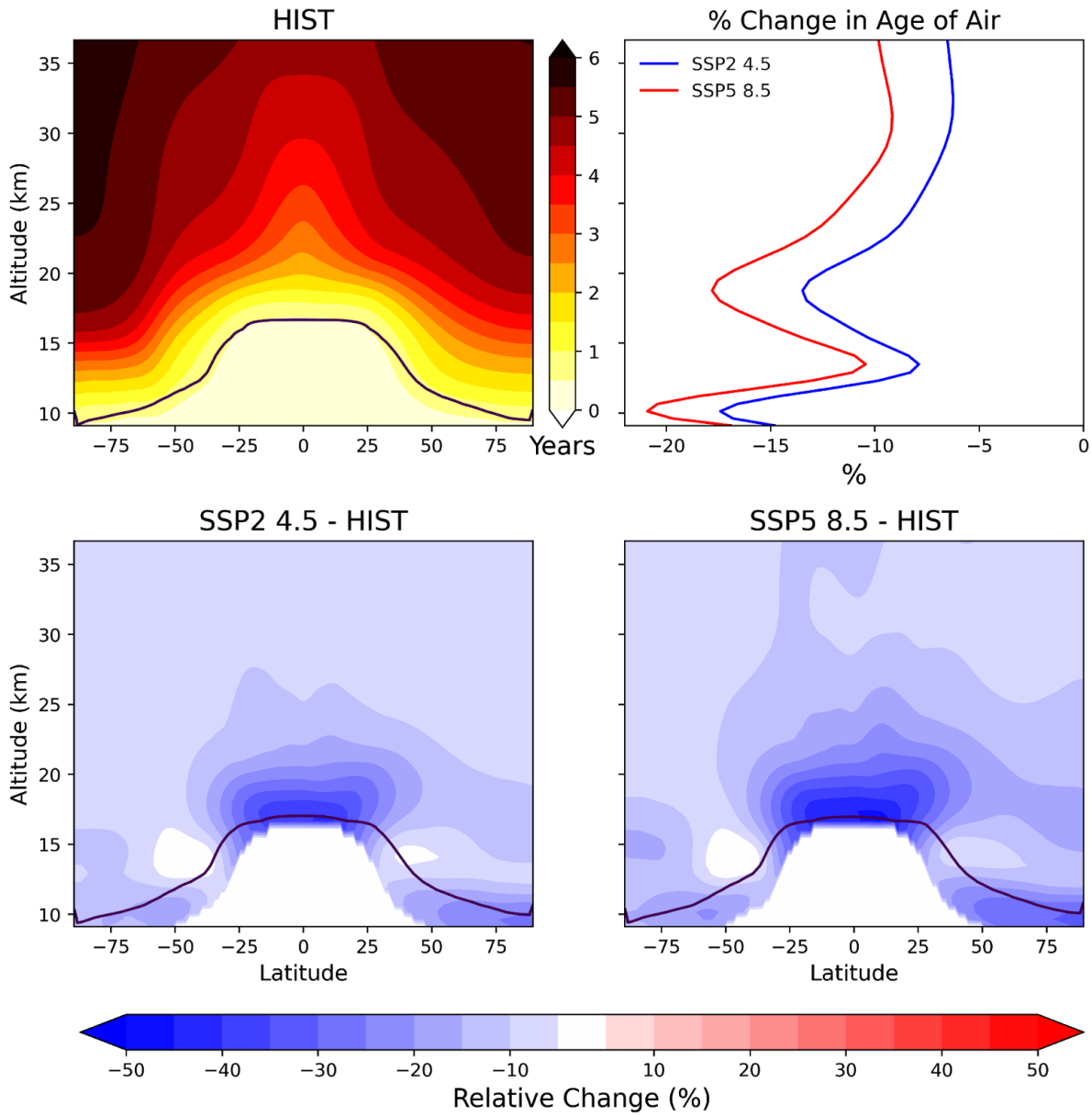

Figure B3 (a) Annual zonal mean stratospheric age of air in HIST control climatology. (b) Profile of % change in annual global mean stratospheric age of air in SSP2 (blue) and SSP5 (red) control climatologies relative to HIST control climatology. % change in annual zonal mean stratospheric age of air in (c) SSP2 and (d) SSP5 relative to HIST control climatology. The zonal mean tropopauses are indicated by the solid lines.

Volcanic SO_2 (months)	**S10**	**H10**	**S56**	**H56**
HIST	1.1	1.3	1.5	2.1
SSP2	1.0	1.3	1.4	2.1
SSP5	1.0	1.2	1.3	1.9

Table B1 Showing the e-folding lifetime of volcanic SO_2 in months.

S (months)	S10	H10	S56	H56
HIST	21.2	17.3	13.6	11.7
SSP2	19.8	14.7	13.1	10.8
SSP5	19.9	14.0	13.5	10.8

Table B2 Showing the e-folding lifetime of total sulfur burden anomaly in months.

Appendix C

Supplementary Information for Chapter 5 "On the vulnerability and sensitivity of total column ozone to sulfur-only and halogen co-emission volcanic eruptions in future climate states"

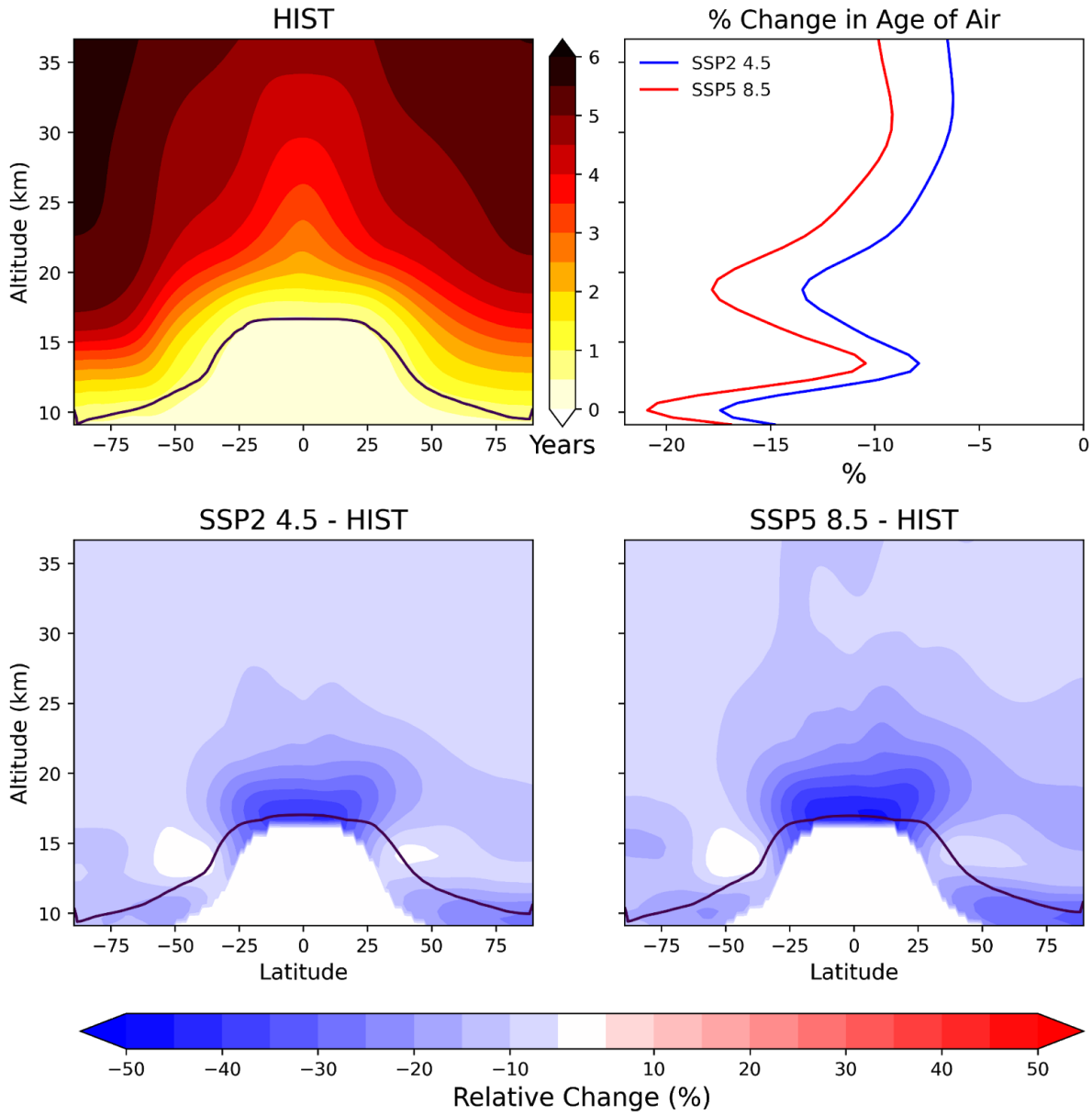

Figure C1 (a) Annual zonal mean stratospheric age of air in HIST control climatology. (b) Profile of % change in annual global mean stratospheric age of air in SSP2 (blue) and SSP5 (red) control climatologies relative to HIST control climatology. % change in annual zonal mean stratospheric age of air in (c) SSP2 and (d) SSP5 relative to HIST control climatology. The zonal mean tropopauses are indicated by the solid lines.

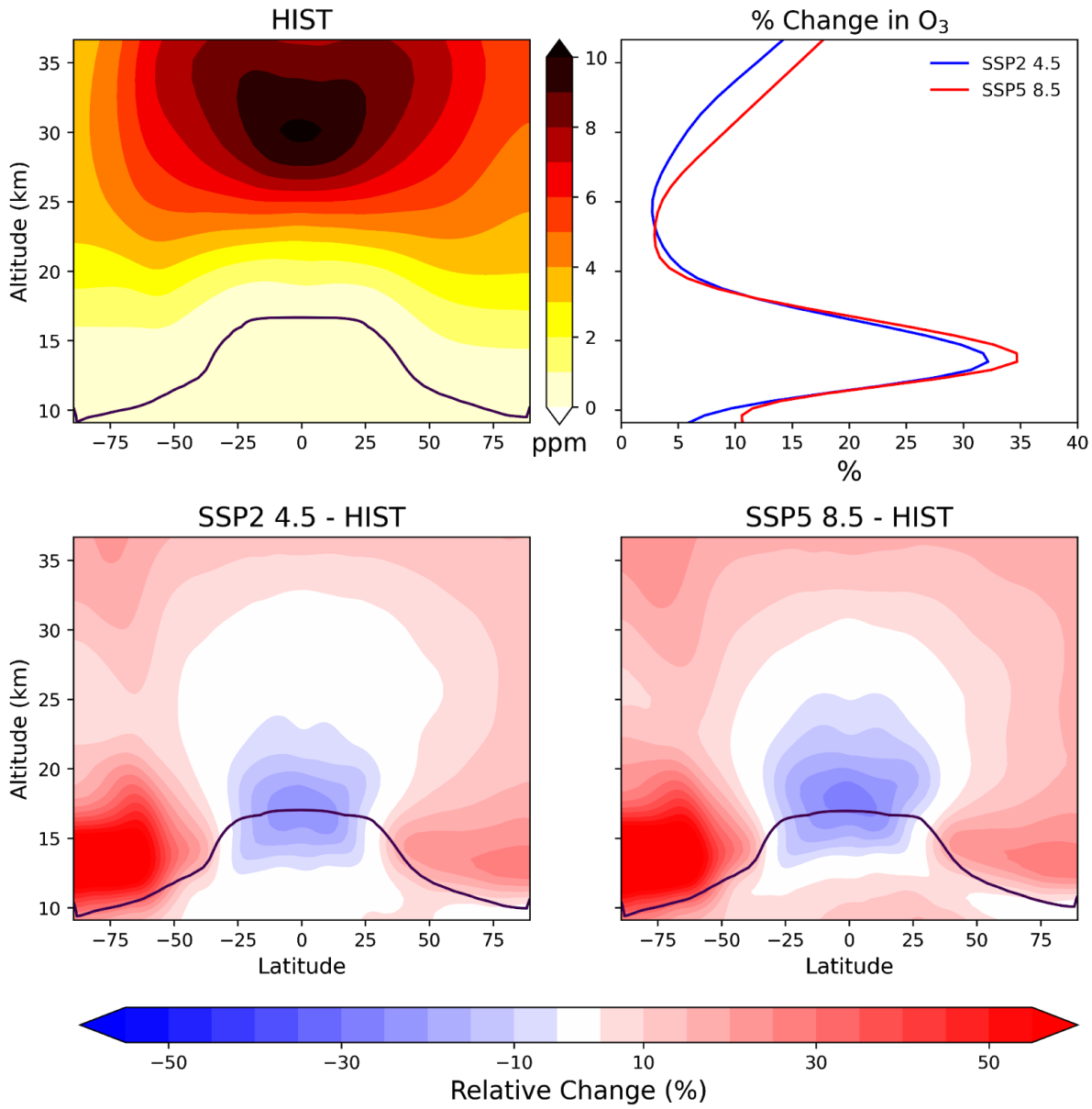

Figure C2 (a) Annual zonal mean O_3 (ppmv) in HIST control climatology. (b) Profile of % change in annual global mean O_3 (ppmv) in SSP2 (blue) and SSP5 (red) control climatologies relative to HIST control climatology. % change in annual zonal mean O3 (ppmv) in (c) SSP2 and (d) SSP5 relative to HIST control climatology. The zonal mean tropopauses are indicated by the solid lines.

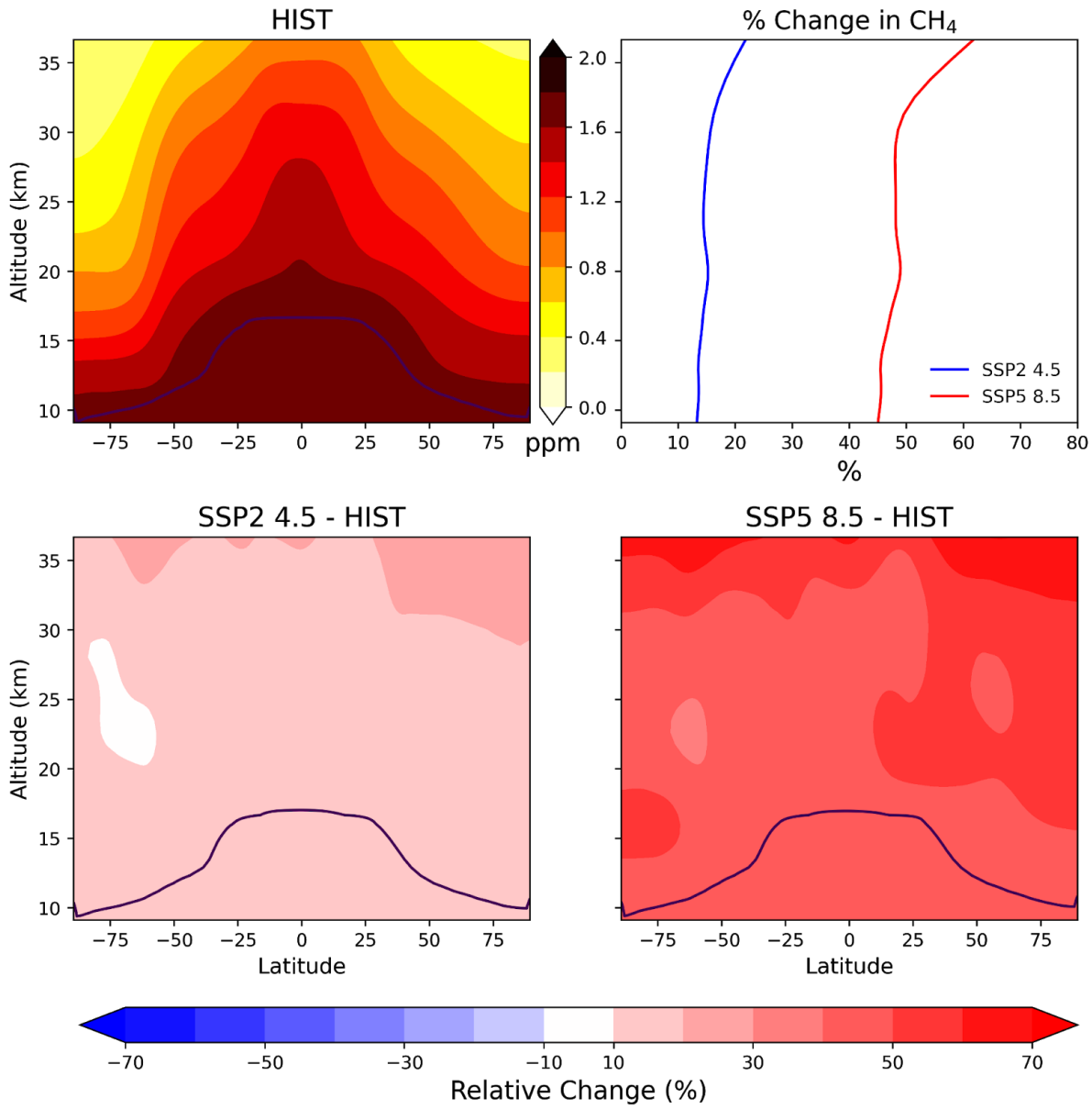

Figure C3 (a) Annual zonal mean CH_4 (ppmv) in HIST control climatology. (b) Profile of % change in annual global mean CH_4 in SSP2 (blue) and SSP5 (red) control climatologies relative to HIST control climatology. % change in annual zonal mean CH4 in (c) SSP2 and (d) SSP5 relative to HIST control climatology. The zonal mean tropopauses are indicated by the solid lines.

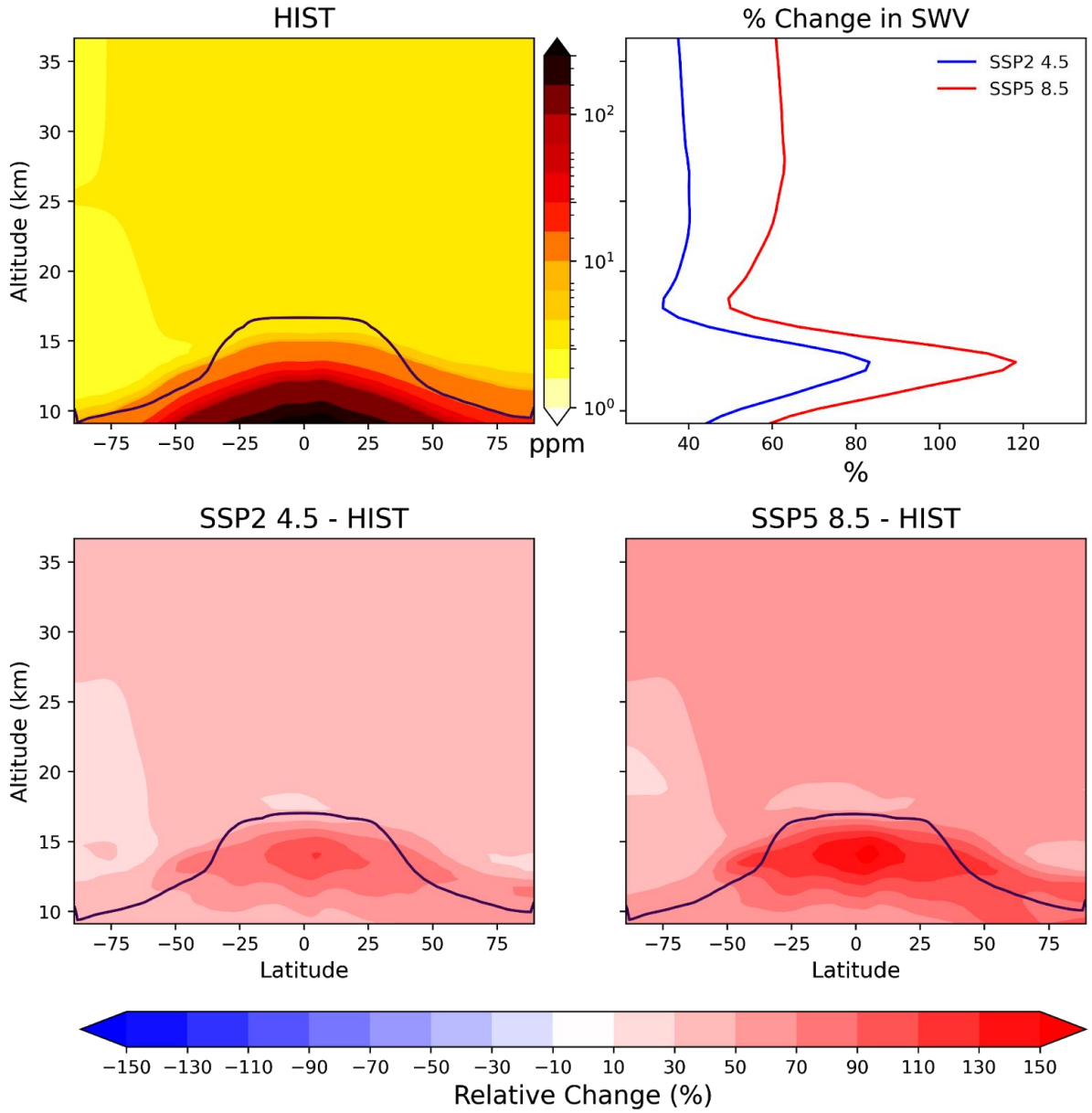

Figure C4 (a) Annual zonal mean SWV (ppmv) in HIST control climatology. (b) Profile of % change in annual global mean SWV (ppmv) in SSP2 (blue) and SSP5 (red) control climatologies relative to HIST control climatology. % change in annual zonal mean SWV (ppmv) in (c) SSP2 and (d) SSP5 relative to HIST control climatology. The zonal mean tropopauses are indicated by the solid lines.

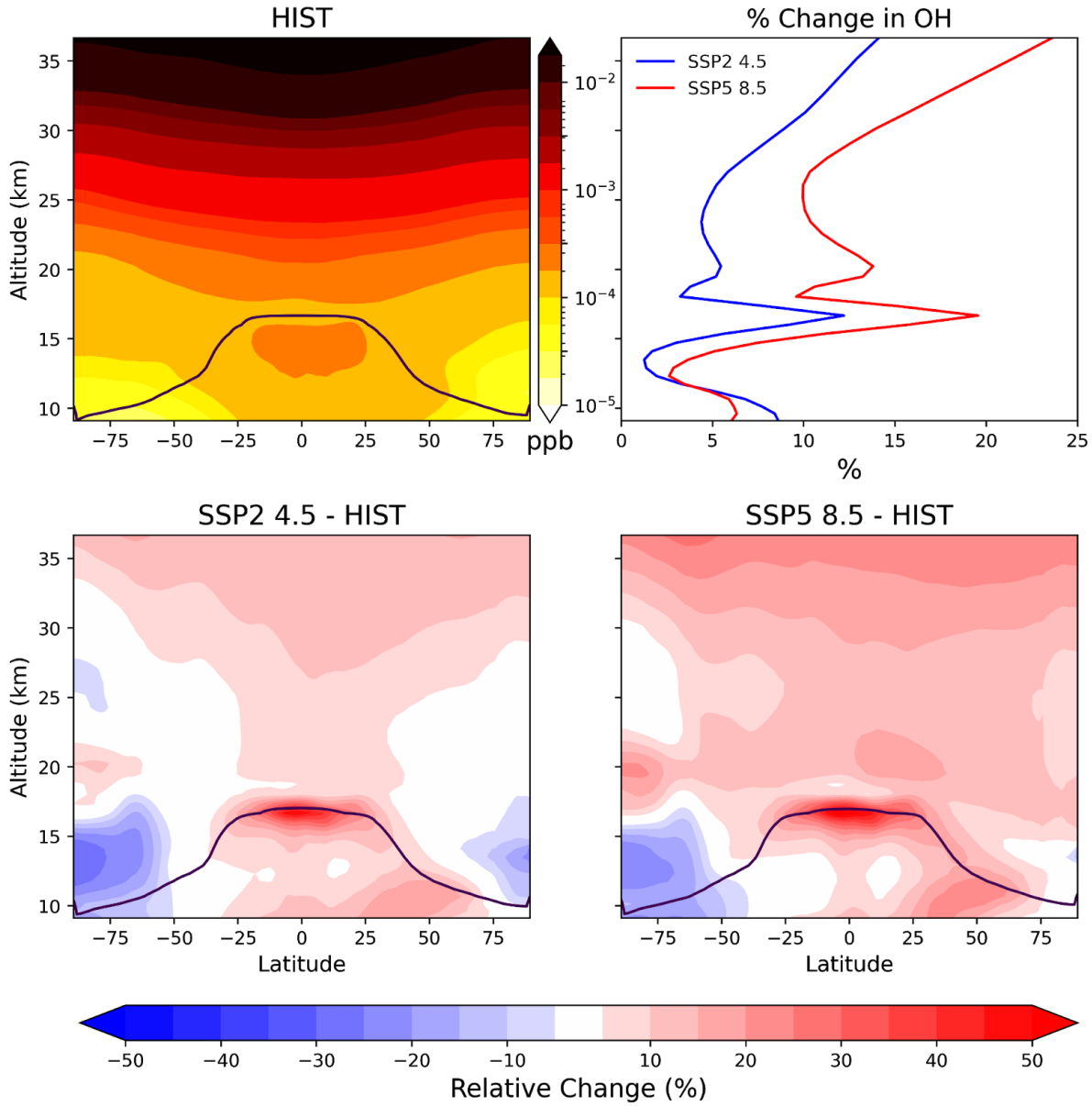

Figure C5 (a) Annual zonal mean OH (ppbv) in HIST control climatology. (b) Profile of % change in annual global mean OH (ppbv) in SSP2 (blue) and SSP5 (red) control climatologies relative to HIST control climatology. % change in annual zonal mean OH (ppbv) in (c) SSP2 and (d) SSP5 relative to HIST control climatology. The zonal mean tropopauses are indicated by the solid lines.

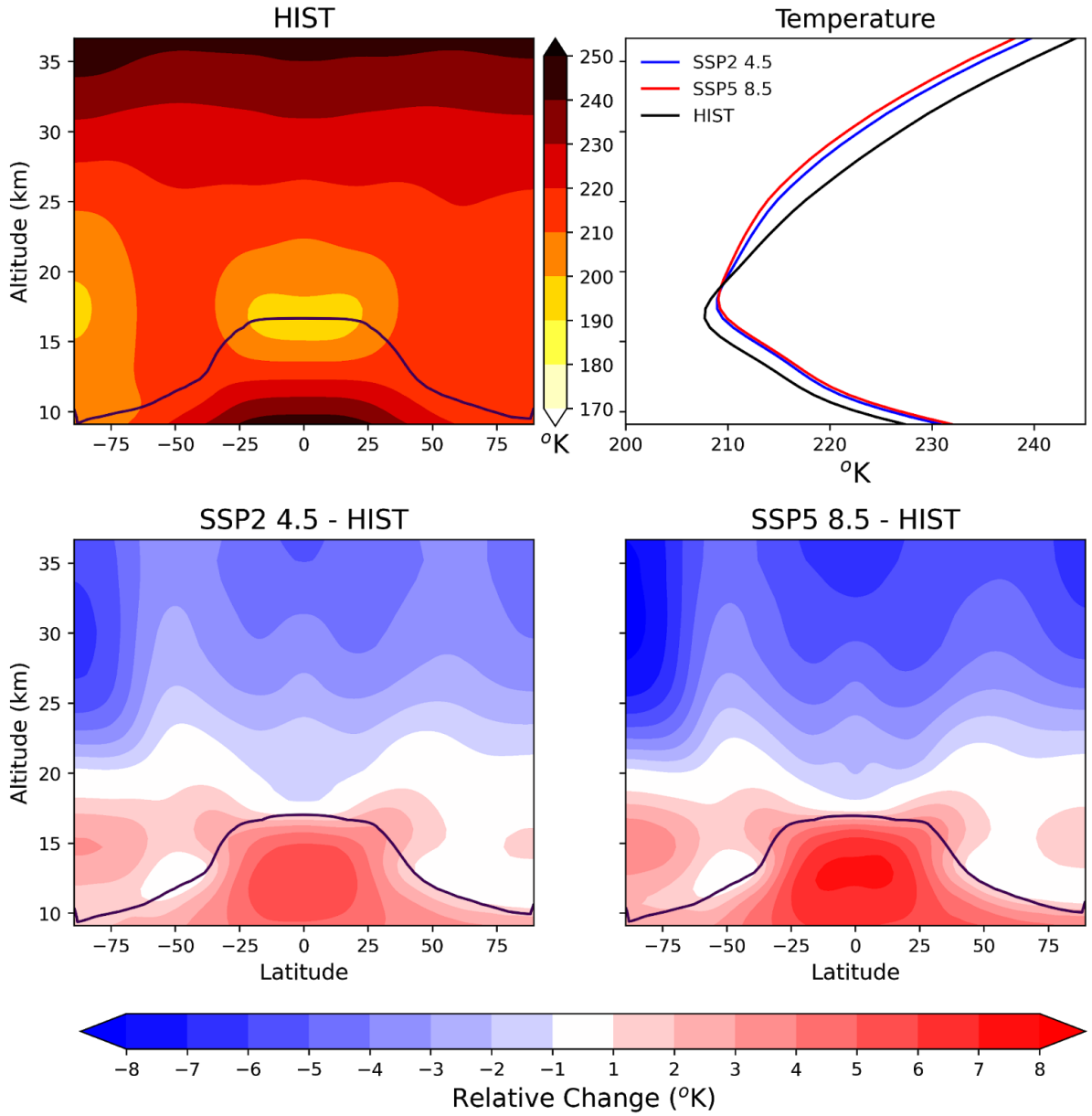

Figure C6 (a) Annual zonal mean temperature in HIST control climatology. (b) Profile of % change in annual global mean temperature in SSP2 (blue) and SSP5 (red) control climatologies relative to HIST control climatology. % change in annual zonal mean temperature in (c) SSP2 and (d) SSP5 relative to HIST control climatology. The zonal mean thermal tropopause is indicated by the solid lines.

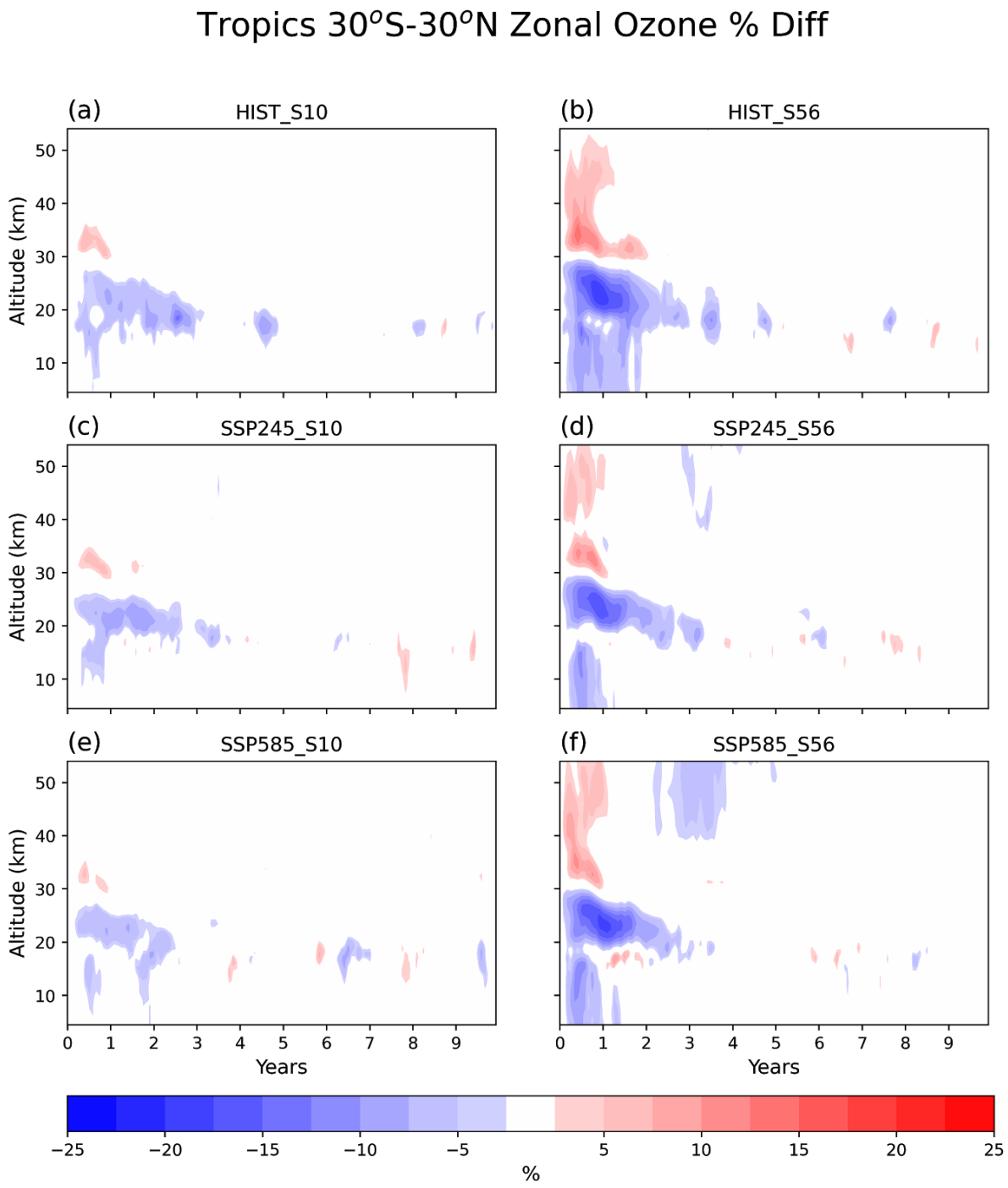

Figure C7 30°S - 30°N mean percentage difference in ozone as a function of altitude and time, (a) HIST_S10, (b) HIST_S56, (c) SSP2_S10, (d) SSP2_S56, (e) SSP5_S10, (f) SSP5_S56. Red colours indicate ozone enhancement, and blue colours indicate ozone depletion.

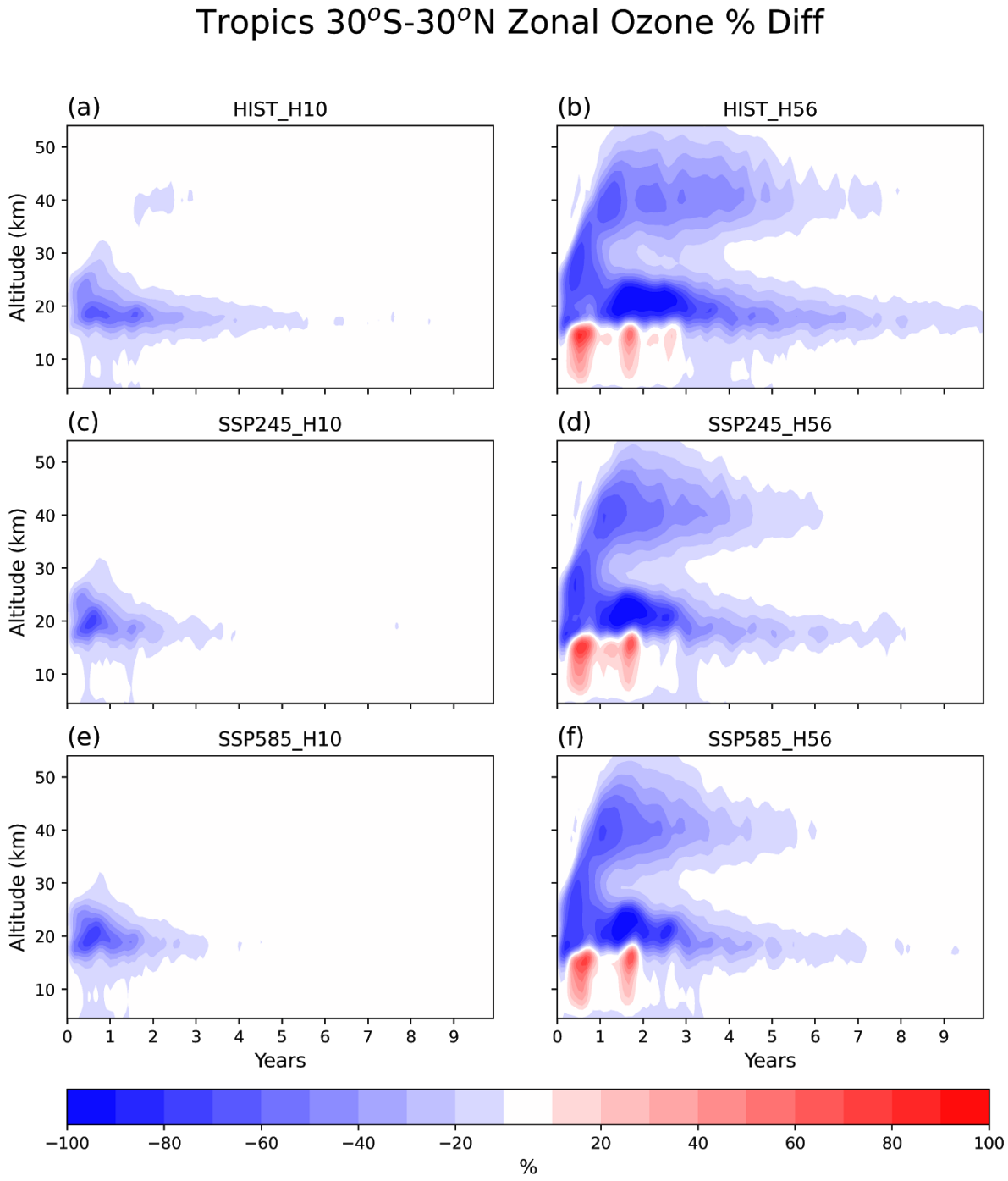

Figure C8 Tropical (30ºN - 30ºS) mean ozone % difference in response to the simulated volcanic eruptions (a) HIST_H10, (b) HIST_H56, (c) SSP2_H10, (d) SSP2_H56, (e) SSP5_H10, (f) SSP5_H56. Red colours indicate ozone enhancement, and blue colours indicate ozone depletion.

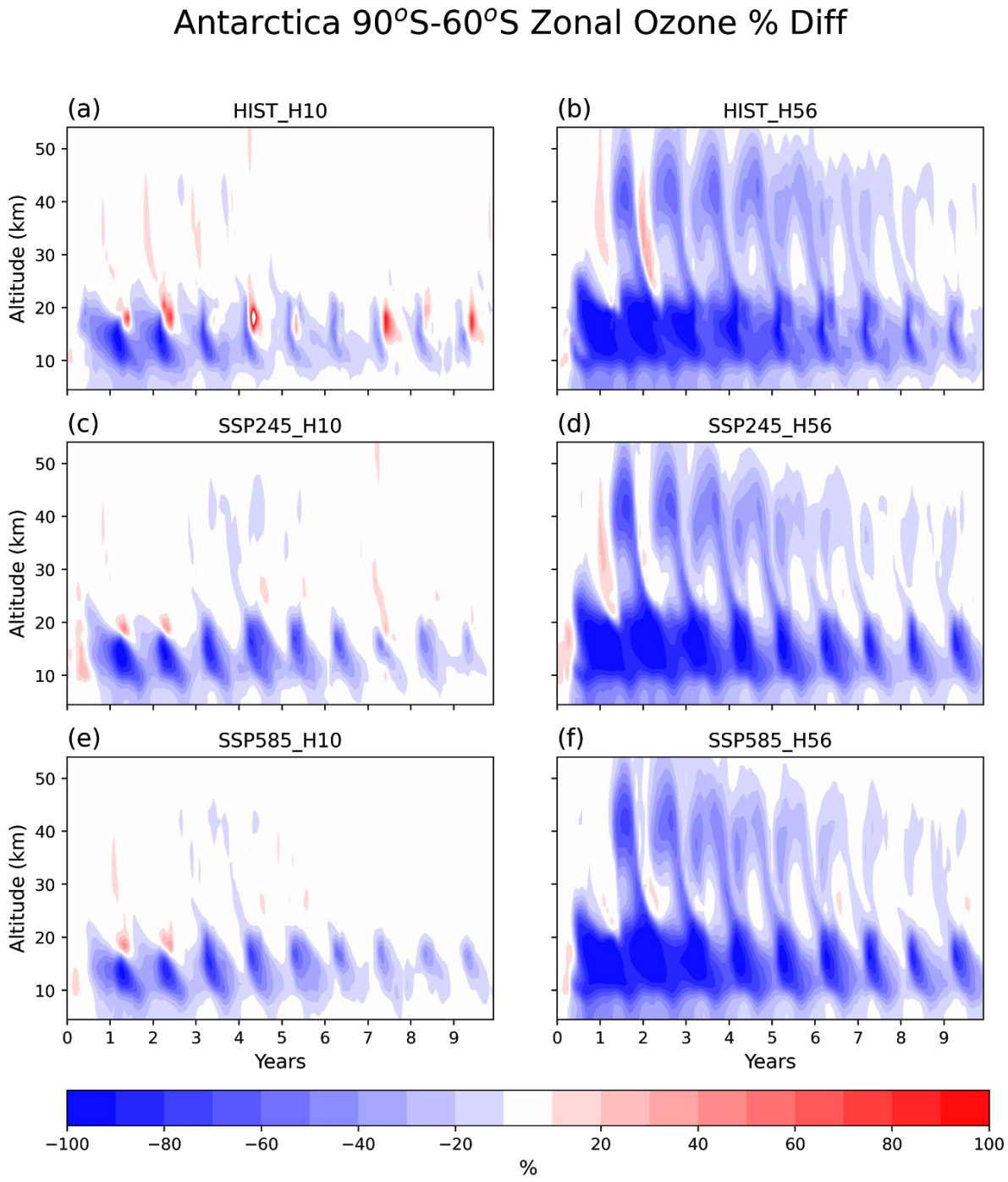

Figure C9 Antarctic (90ºS - 60ºS) mean ozone % difference in response to the simulated volcanic eruptions (a) HIST_H10, (b) HIST_H56, (c) SSP2_H10, (d) SSP2_H56, (e) SSP5_H10, (f) SSP5_H56. Red colours indicate ozone enhancement, and blue colours indicate ozone depletion.

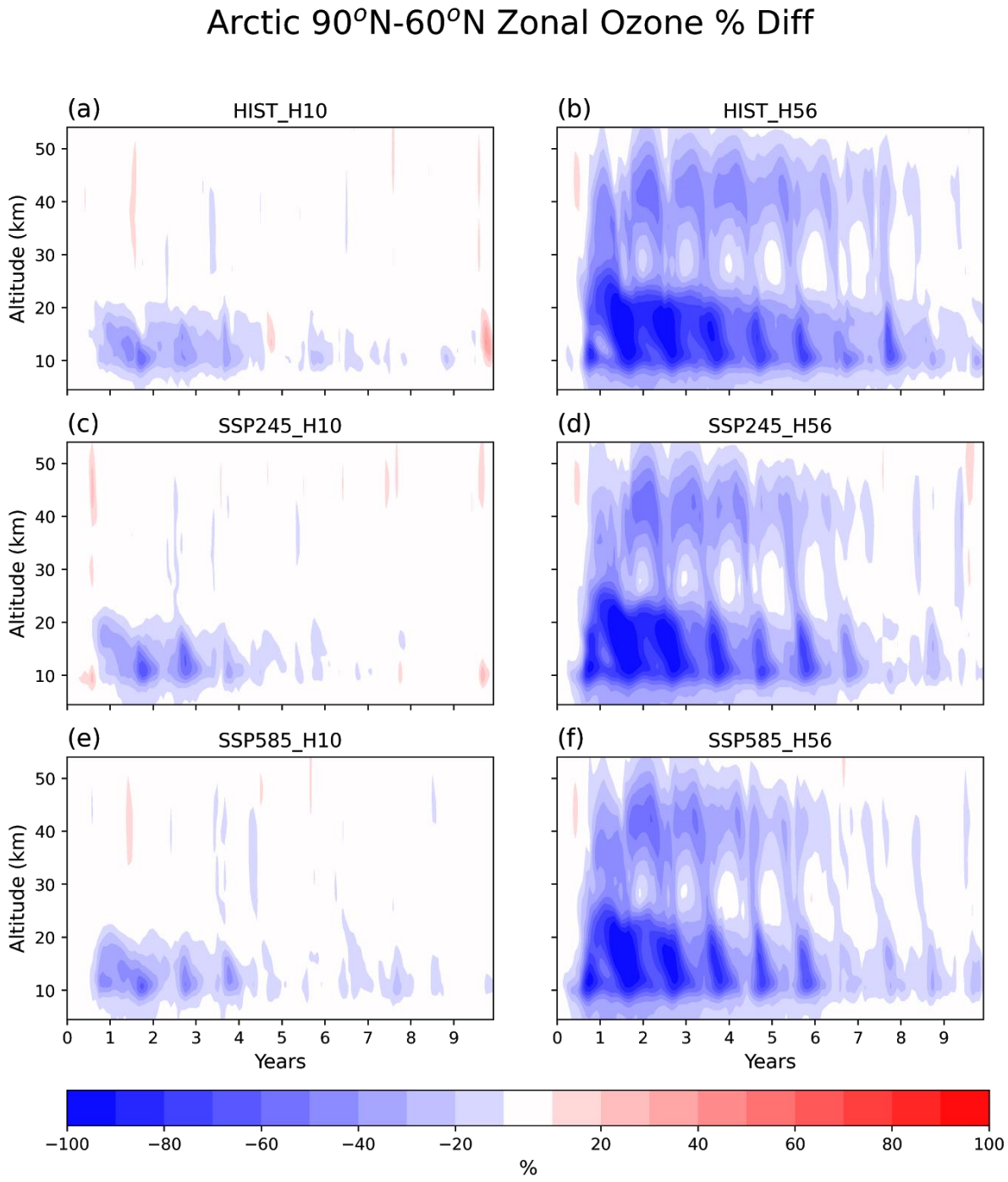

Figure C10 Arctic (90ºN - 60ºN) mean ozone % difference in response to the simulated volcanic eruptions (a) HIST_H10, (b) HIST_H56, (c) SSP2_H10, (d) SSP2_H56, (e) SSP5_H10, (f) SSP5_H56. Red colours indicate ozone enhancement, and blue colours indicate column depletion.

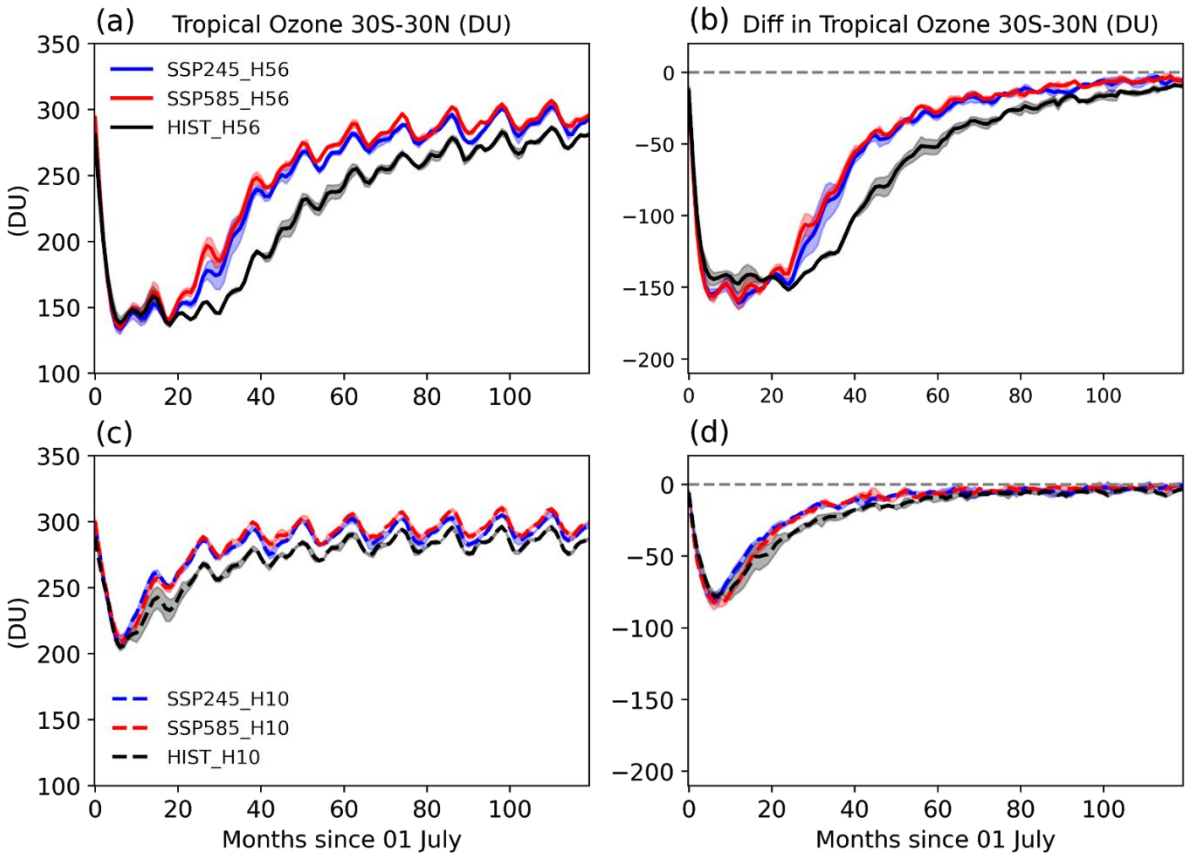

Figure C11 Timeseries of tropical (30ºS - 30ºN) mean column ozone (left) and anomalies (right). Very-large co-emission scenarios (H56) are shown in solid lines, large co-emission scenarios (H10) are shown in dashed lines.

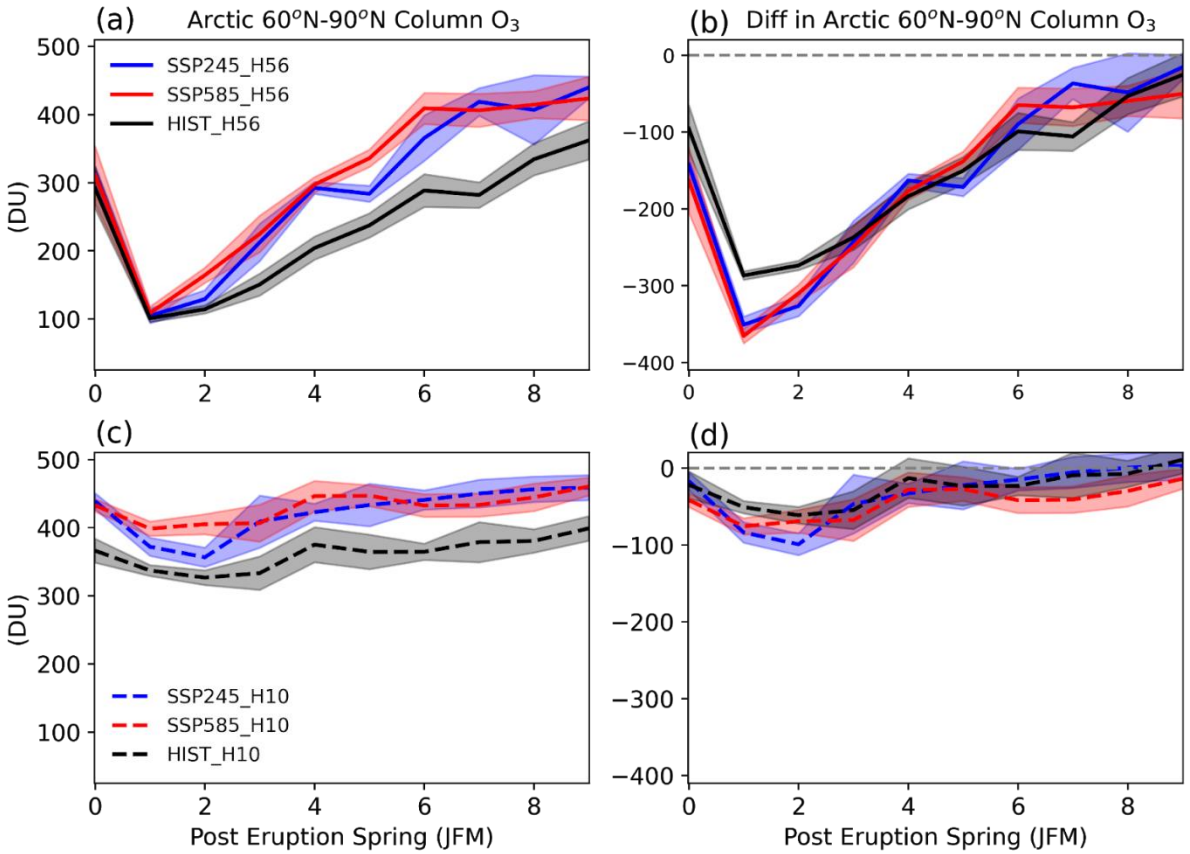

Figure C12 Timeseries of Arctic (60ºN-90ºN) Spring (JFM) mean column ozone (left) and anomalies (right). Very-large co-emission scenarios (H56) are shown in solid lines, large co-emission scenarios (H10) are shown in dashed lines.

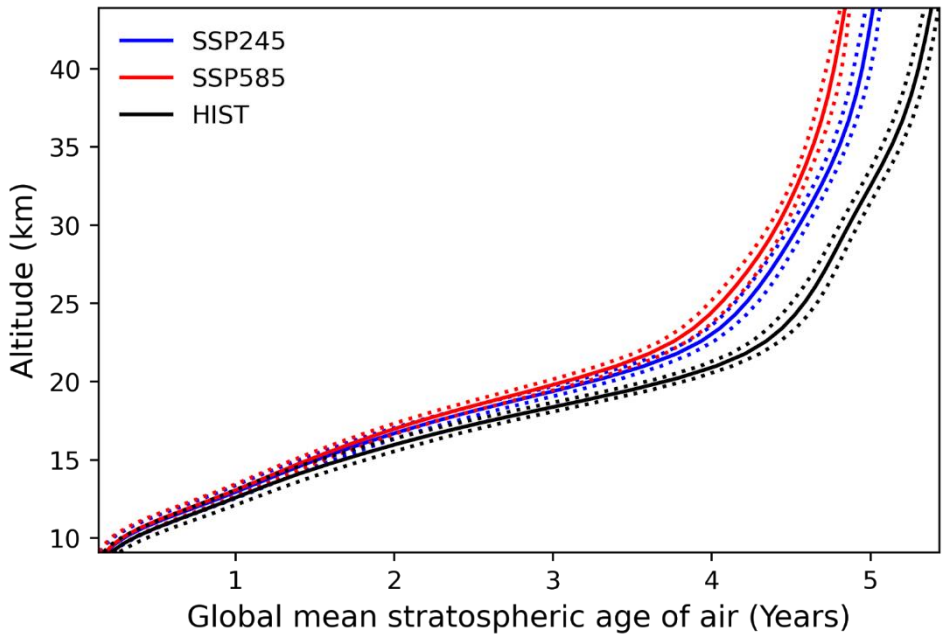

Figure C13 Global mean stratospheric age of air profile in HIST (black), SSP2 (blue), SSP5 (red) control climatologies. Dotted lines show the interannual range within the 20-year control simulations.

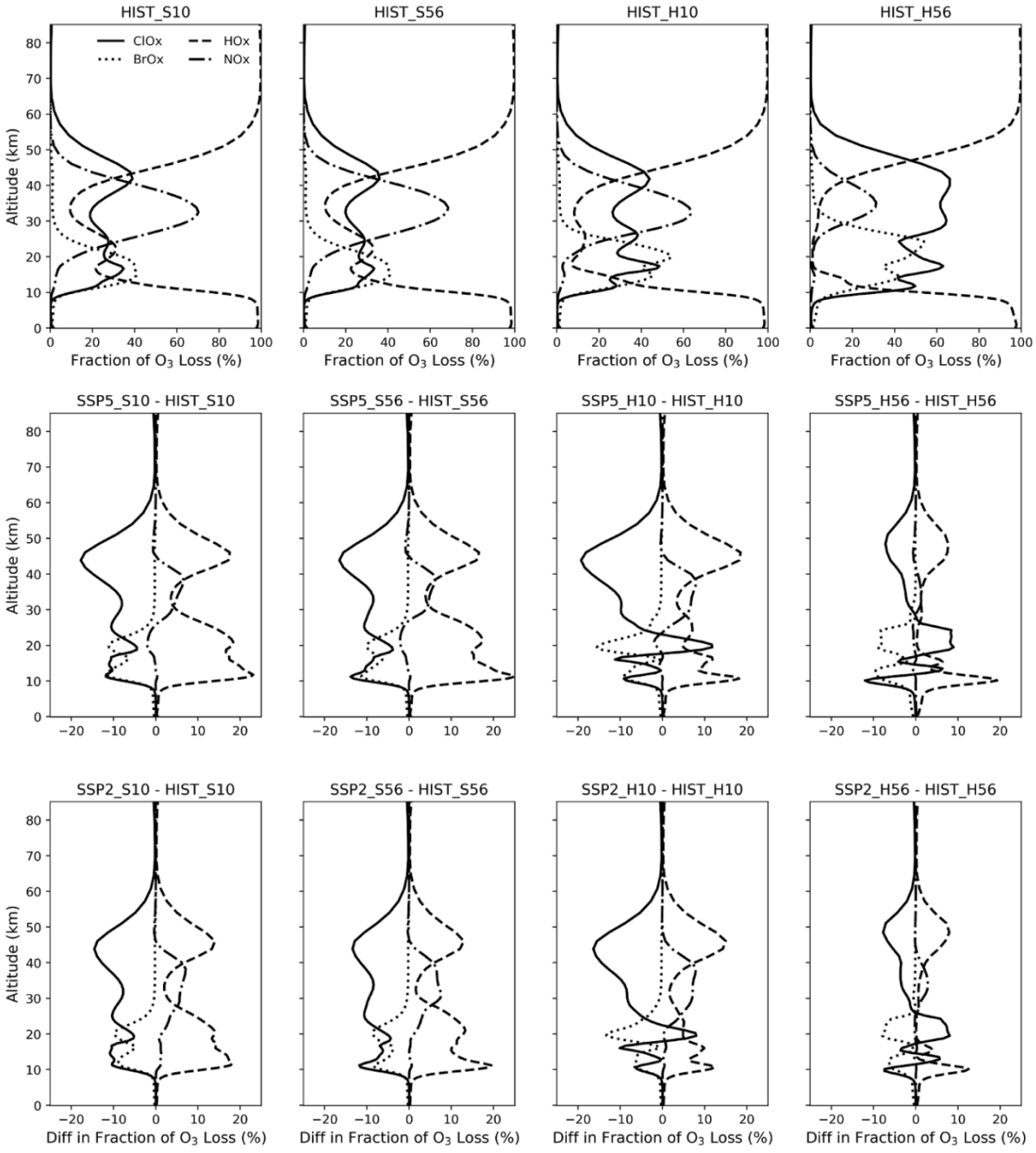

Figure C14 Figure shows the fractional contributions of ClO_x, BrO_x, NO_x, and HO_x, loss cycles to the net loss of O_3, in the first post eruption year.

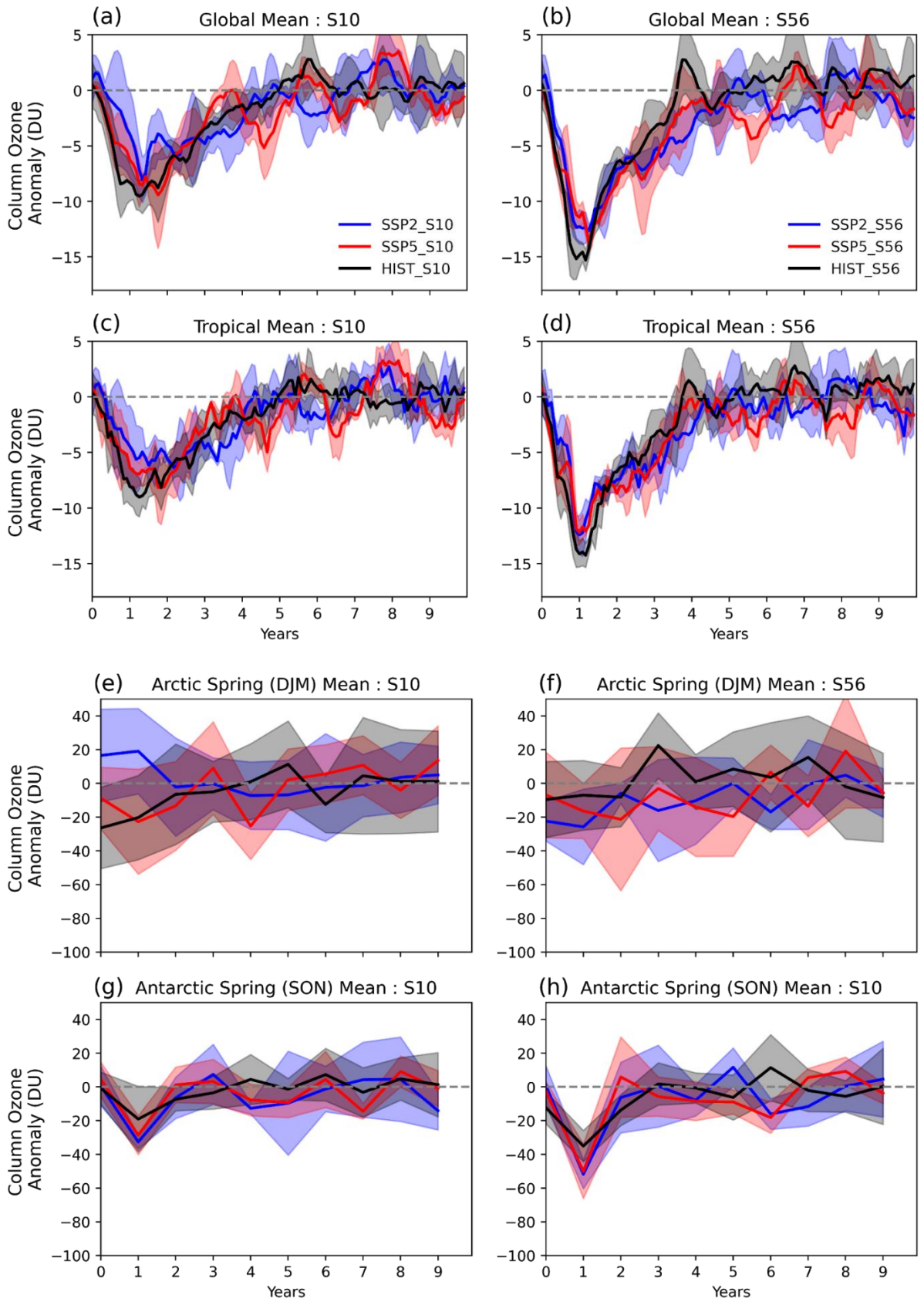

Figure C15 Evolution of global mean, tropical-mean (30ºS-30ºN), Arctic-spring-mean (90ºS-60ºS), Antarctic-spring-mean (60ºN-90ºN) column ozone anomaly in HIST_S10, SSP2_S10 and SSP5_S10 shown in (a,c,f, and g respectively) and HIST_S56, SSP2_S56 and SSP5_S56 shown in (b,d,e, and f respectively).

Appendix D

Supplementary Information for Chapter 6 "Complex and non-additive climate response to volcanic eruptions during SRM"

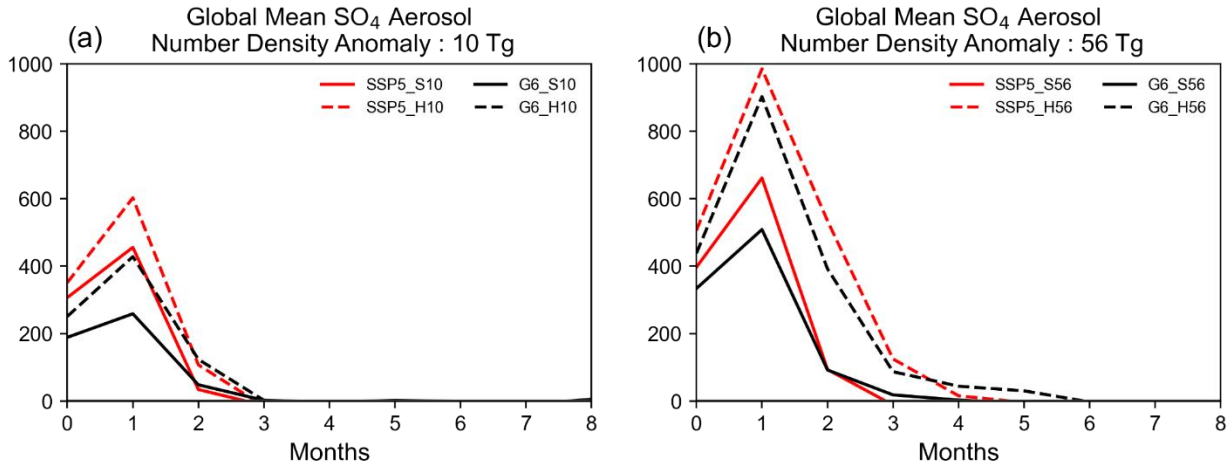

Figure D1 Global mean aerosol number density anomaly in (a) SSP5_S10 (red solid), SSP5_H10 (red dashed), G6_S10 (black solid), G6_S10 (black dashed), and (b) SSP5_S56 (red solid), SSP5_H56 (red dashed), G6_S56 (black solid), G6_S56 (black dashed).

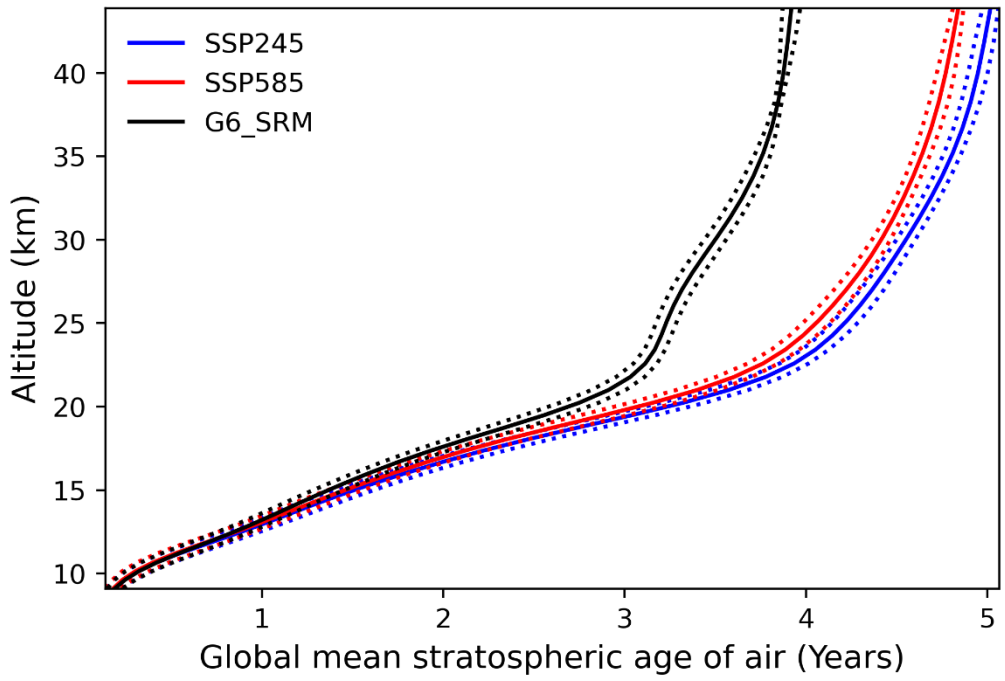

Figure D2 Annual zonal mean stratospheric age of air in G6_SRM (black), SSP245 (blue), and SSP585 (red) control climatologies.

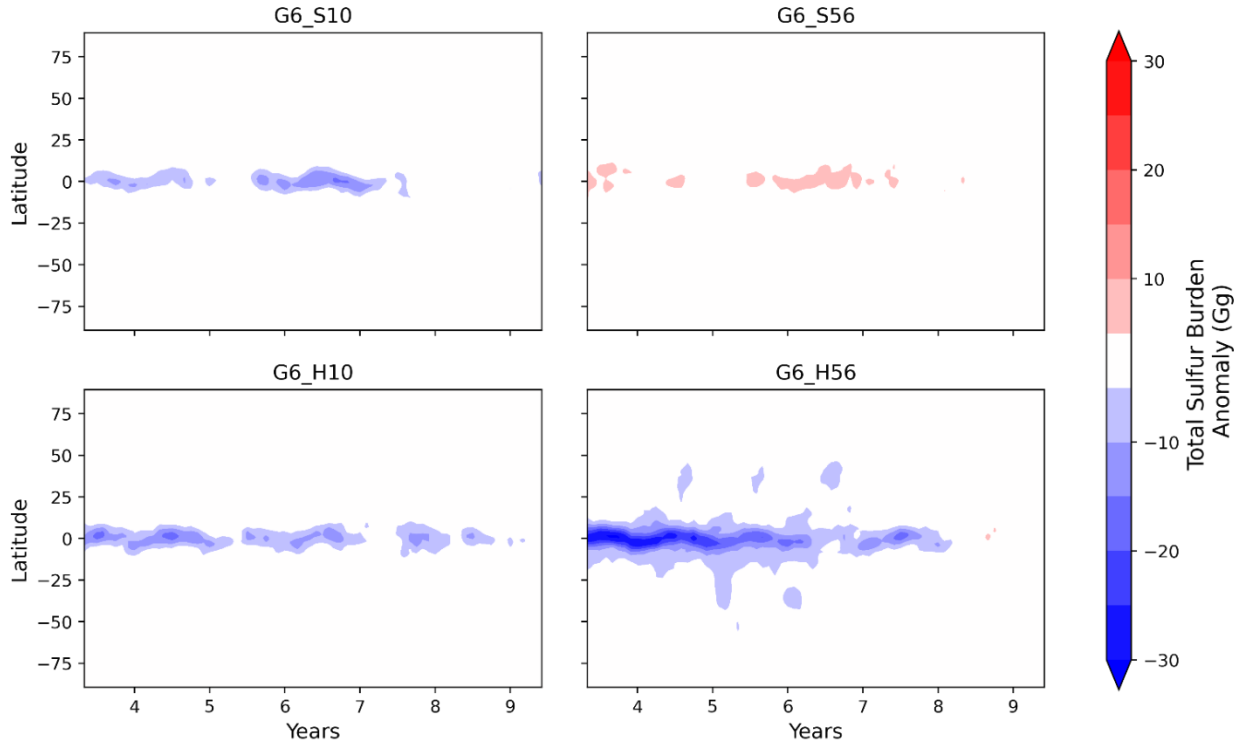

Figure D3 Total sulfur burden anomaly hovmoller plot for post-eruption years 3 to 9 in (a) G6_S10, (b) G6_S56, (c) G6_H10, (d) G6_H56. Red colours indicate total sulfur burden enhancement, and blue colours indicate total sulfur burden loss.

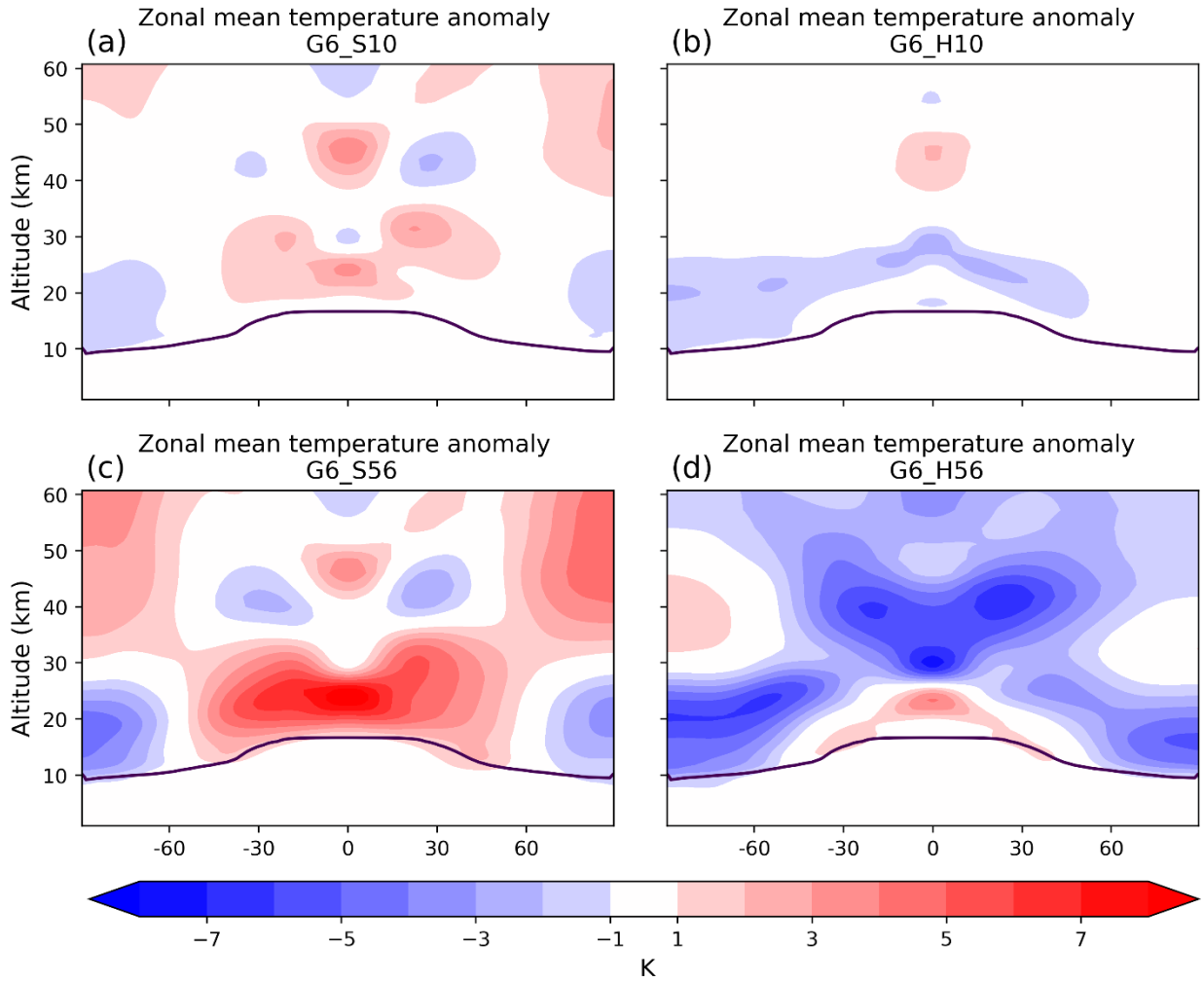

Figure D4 Zonal mean temperature anomaly (K) averaged over the first post-eruption year relative to the control climatology (a) G6_S10, (b) G6_H10, (c) G6_S56, and (d) G6_H56. Red colours indicate temperature enhancement, and blue colours indicate temperature depletion.

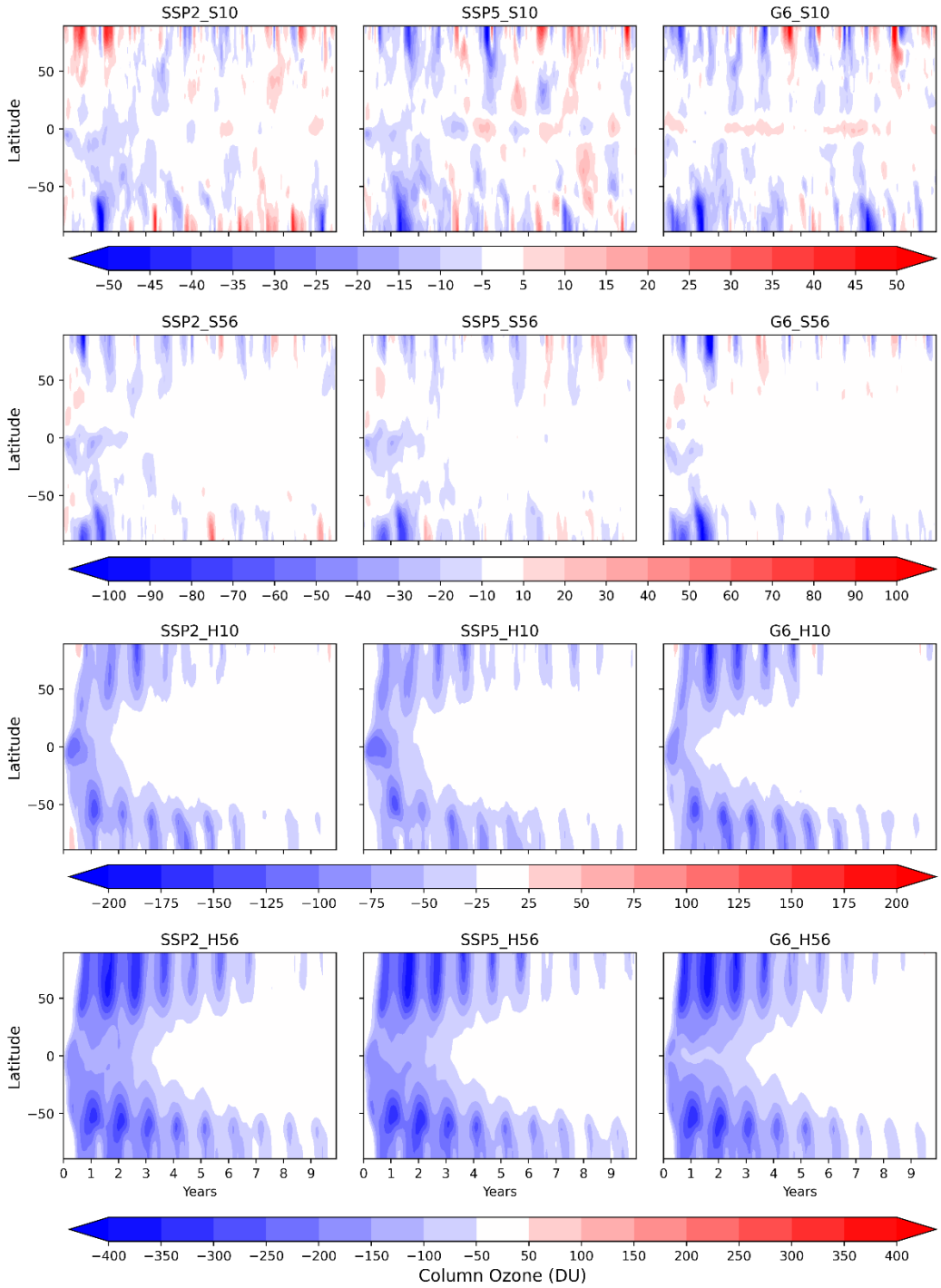

Figure D5 Total column ozone % difference in response to the simulated volcanic eruptions relative to the control climatology. Red colours indicate ozone enhancement, and blue colours indicate column depletion.

References

Aiuppa, A., Baker, D. R. and Webster, J. D.: Halogens in volcanic systems, Chem. Geol., 263(1–4), 1–18, doi:10.1016/j.chemgeo.2008.10.005, 2009.

Antonopoulos, J.: The great Minoan eruption of Thera volcano and the ensuing tsunami in the Greek Archipelago, Nat. Hazards, 5(2), 153–168, doi:10.1007/BF00127003, 1992.

Aquila, V., Oman, L. D., Stolarski, R. S., Colarco, P. R. and Newman, P. A.: Dispersion of the volcanic sulfate cloud from a Mount Pinatubo-like eruption, J. Geophys. Res. Atmos., 117(6), n/a-n/a, doi:10.1029/2011JD016968, 2012.

Aquila, V., Oman, L. D., Stolarski, R., Douglass, A. R. and Newman, P. A.: The response of ozone and nitrogen dioxide to the eruption of mt. pinatubo at southern and northern midlatitudes, J. Atmos. Sci., 70(3), 894–900, doi:10.1175/JAS-D-12-0143.1, 2013.

Archibald, A., M O'Connor, F., Luke Abraham, N., Archer-Nicholls, S., P Chipperfield, M., Dalvi, M., A Folberth, G., Dennison, F., S Dhomse, S., T Griffiths, P., Hardacre, C., J Hewitt, A., S Hill, R., E Johnson, C., Keeble, J., O Köhler, M., Morgenstern, O., P Mulcahy, J., Ordóñez, C., J Pope, R., T Rumbold, S., R Russo, M., H Savage, N., Sellar, A., Stringer, M., T Turnock, S., Wild, O. and Zeng, G.: Description and evaluation of the UKCA stratosphere-troposphere chemistry scheme (StratTrop vn 1.0) implemented in UKESM1, Geosci. Model Dev., 13(3), 1223–1266, doi:10.5194/gmd-13-1223-2020, 2020.

Aubry, T. J., Jellinek, A. M., Degruyter, W., Bonadonna, C., Radíc, V., Clyne, M. and Quainoo, A.: Impact of global warming on the rise of volcanic plumes and implications for future volcanic aerosol forcing, J. Geophys. Res., 121(22), 13,326-13,351, doi:10.1002/2016JD025405, 2016.

Aubry, T. J., Cerminara, M. and Jellinek, A. M.: Impacts of Climate Change on Volcanic Stratospheric Injections: Comparison of 1-D and 3-D Plume Model Projections, Geophys. Res. Lett., 46(17–18), 10609–10618, doi:10.1029/2019GL083975, 2019.

Bacon, C. R., Newman, S. and Stolper, E.: Water, CO2, Cl, and F in melt inclusions in phenocrysts from three Holocene explosive eruptions, Crater Lake, Oregon, Am. Mineral., 77(9–10), 1021–1030, 1992.

Banda, N., Krol, M., van Weele, M., van Noije, T., Le Sager, P. and Röckmann, T.: Can we explain the observed methane variability after the Mount Pinatubo eruption?, Atmos. Chem. Phys. Discuss., 15(13), 19111–214, doi:10.5194/acp-16-195-2016, 2015.

Bates, D. R. and Nicolet, M.: Atmospheric Hydrogen, Publ. Astron. Soc. Pacific, 62, 106, doi:10.1086/126244, 1950.

Bekki, S.: Oxidation of volcanic SO2: A sink for stratospheric OH and H2O, Geophys. Res. Lett., 22(8), 913–916, doi:10.1029/95GL00534, 1995.

Black, B. A., Lamarque, J. F., Shields, C. A., Elkins-Tanton, L. T. and Kiehl, J. T.: Acid rain and ozone depletion from pulsed siberian traps magmatism, Geology, 42(1), 67–70, doi:10.1130/G34875.1, 2014.

Bluth, G. J. S., Doiron, S. D., Schnetzler, C. C., Krueger, A. J. and Walter, L. S.: Global tracking of the SO2

clouds from the June, 1991 Mount Pinatubo eruptions, Geophys. Res. Lett., 19(2), 151–154, doi:10.1029/91GL02792, 1992.

Bönisch, H., Engel, A., Birner, T., Hoor, P., Tarasick, D. W. and Ray, E. A.: On the structural changes in the Brewer-Dobson circulation after 2000, Atmos. Chem. Phys., 11(8), 3937–3948, doi:10.5194/acp-11-3937-2011, 2011.

Bouttes, N., Paillard, D., Roche, D. M., Brovkin, V. and Bopp, L.: Last glacial maximum CO2 and δ13C successfully reconciled, Geophys. Res. Lett., 38(2), n/a-n/a, doi:10.1029/2010GL044499, 2011.

Braesicke, P., Keeble, J., Yang, X., Stiller, G., Kellmann, S., Abraham, N. L., Archibald, A. T., Telford, P. and Pyle, J. A.: Consistent circulation differences in the Southern Hemisphere caused by ozone changes: a chemistry-climate model and observational study, Atmos. Chem. Phys. Discuss., 13(3), 8455–8487, doi:10.5194/acpd-13-8455-2013, 2013.

Brenna, H., Kutterolf, S. and Krüger, K.: Global ozone depletion and increase of UV radiation caused by pre-industrial tropical volcanic eruptions, Sci. Rep., 9(1), 9435, doi:10.1038/s41598-019-45630-0, 2019.

Brenna, H., Kutterolf, S., Mills, M. J. and Krüger, K.: The potential impacts of a sulfur- And halogen-rich supereruption such as Los Chocoyos on the atmosphere and climate, Atmos. Chem. Phys., 20(11), 6521–6539, doi:10.5194/acp-20-6521-2020, 2020.

Butchart, N.: The Brewer-Dobson circulation, Rev. Geophys., 52(2), 157–184, doi:10.1002/2013RG000448, 2014.

Cadoux, A., Scaillet, B., Bekki, S., Oppenheimer, C. and Druitt, T. H.: Stratospheric Ozone destruction by the Bronze-Age Minoan eruption (Santorini Volcano, Greece), Sci. Rep., 5(1), 12243, doi:10.1038/srep12243, 2015.

Carn, S. A., Clarisse, L. and Prata, A. J.: Multi-decadal satellite measurements of global volcanic degassing, J. Volcanol. Geotherm. Res., 311, 99–134, doi:10.1016/j.jvolgeores.2016.01.002, 2016.

Chapman, S.: A theory of upper-atmospheric ozone, Edward Stanford, London., 1930.

Clyne, M., Lamarque, J.-F., Mills, M., Khodri, M., Ball, W., Bekki, S., Dhomse, S., Lebas, N., Mann, G., Marshall, L., Niemeier, U., Poulain, V., Robock, A., Rozanov, E., Schmidt, A., Stenke, A., Sukhodolov, T., Timmreck, C., Toohey, M., Tummon, F., Zanchettin, D., Zhu, Y. and Toon, O.: Model physics and chemistry causing intermodel disagreement within the VolMIP-Tambora Interactive Stratospheric Aerosol ensemble, Atmos. Chem. Phys., 1–43, doi:10.5194/acp-2020-883, 2020.

Collins, M., Knutti, R., Gutowski, W. J., Brooks, H. E., Shindell, D., Webb, R. and Et Al: Long-term climate change: Projections, commitments and irreversibility, in Climate Change 2013 the Physical Science Basis: Working Group I Contribution to the Fifth Assessment Report of the Intergovernmental Panel on Climate Change, vol. 9781107057, pp. 1029–1136., 2013.

Crutzen, P. J.: The influence of nitrogen oxides on the atmospheric ozone content, Q. J. R. Meteorol. Soc., 96(408), 320–325, doi:10.1002/qj.49709640815, 1970.

Crutzen, P. J. and Arnold, F.: Nitric acid cloud formation in the cold Antarctic stratosphere: A major cause for the springtime “ozone hole,” Nature, 324(6098), 651–655, doi:10.1038/324651a0, 1986.

Dai, Z., Weisenstein, D., Keutsch, F. and Keith, D.: Experimental reaction rates constrain estimates of ozone response to calcium carbonate geoengineering, Commun Earth Environ., 1(63) [online] Available from: https://doi.org/10.1038/s43247-020-00058-7, 2020.

Dennison, F., Keeble, J., Morgenstern, O., Zeng, G., Luke Abraham, N. and Yang, X.: Improvements to stratospheric chemistry scheme in the UM-UKCA (v10.7) model: Solar cycle and heterogeneous reactions, Geosci. Model Dev., 12(3), 1227–1239, doi:10.5194/gmd-12-1227-2019, 2019.

Deshler, T., Liley, J. Ben, Bodeker, G., Matthews, W. A. and Hoffmann, D. J.: Stratospheric aerosol following Pinatubo, comparison of the north and south mid latitudes using in situ measurements, Adv. Sp. Res., 20(11), 2089–2095, doi:10.1016/S0273-1177(97)00600-5, 1997.

Dhomse, S. S., Emmerson, K. M., Mann, G. W., Bellouin, N., Carslaw, K. S., Chipperfield, M. P., Hommel, R., Abraham, N. L., Telford, P., Braesicke, P., Dalvi, M., Johnson, C. E., O'Connor, F., Morgenstern, O., Pyle, J. A., Deshler, T., Zawodny, J. M. and Thomason, L. W.: Aerosol microphysics simulations of the Mt.∼Pinatubo eruption with the UM-UKCA composition-climate model, Atmos. Chem. Phys., 14(20), 11221–11246, doi:10.5194/acp-14-11221-2014, 2014.

Dhomse, S. S., Kinnison, D., Chipperfield, M. P., Salawitch, R. J., Cionni, I., Hegglin, M. I., Abraham, N. L., Akiyoshi, H., Archibald, A. T., Bednarz, E. M., Bekki, S., Braesicke, P., Butchart, N., Dameris, M., Deushi, M., Frith, S., Hardiman, S. C., Hassler, B., Horowitz, L. W., Hu, R.-M., Jöckel, P., Josse, B., Kirner, O., Kremser, S., Langematz, U., Lewis, J., Marchand, M., Lin, M., Mancini, E., Marécal, V., Michou, M., Morgenstern, O., O'Connor, F. M., Oman, L., Pitari, G., Plummer, D. A., Pyle, J. A., Revell, L. E., Rozanov, E., Schofield, R., Stenke, A., Stone, K., Sudo, K., Tilmes, S., Visioni, D., Yamashita, Y. and Zeng, G.: Estimates of ozone return dates from Chemistry-Climate Model Initiative simulations, Atmos. Chem. Phys., 18(11), 8409, doi:10.5194/acp-18-8409-2018, 2018.

Dhomse, S. S., Mann, G. W., Juan-Carlos, A. M., Shallcross, S. E., Chipperfield, M. P., Carslaw, K. S., Marshall, L., Luke Abraham, N. and Johnson, C. E.: Evaluating the simulated radiative forcings, aerosol properties, and stratospheric warmings from the 1963 Mt Agung, 1982 El Chichón, and 1991 Mt Pinatubo volcanic aerosol clouds, Atmos. Chem. Phys., 20(21), 13627–13654, doi:10.5194/acp-20-13627-2020, 2020.

Driscoll, S., Bozzo, A., Gray, L. J., Robock, A. and Stenchikov, G.: Coupled Model Intercomparison Project 5 (CMIP5) simulations of climate following volcanic eruptions, J. Geophys. Res. Atmos., 117(17), 105, doi:10.1029/2012JD017607, 2012.

Edwards, J. M. and Slingo, A.: Studies with a flexible new radiation code. I: Choosing a configuration for a large-scale model, Q. J. R. Meteorol. Soc., 122(531), 689–719, doi:10.1002/qj.49712253107, 1996.

Etminan, M., Myhre, G., Highwood, E. J. and Shine, K. P.: Radiative forcing of carbon dioxide, methane, and nitrous oxide: A significant revision of the methane radiative forcing, Geophys. Res. Lett., 43(24), 12,614-12,623, doi:10.1002/2016GL071930, 2016.

Eyring, V., Bony, S., Meehl, G. A., Senior, C. A., Stevens, B., Stouffer, R. J. and Taylor, K. E.: Overview of the Coupled Model Intercomparison Project Phase 6 (CMIP6) experimental design and organization, Geosci. Model Dev., 9(5), 1937–1958, doi:10.5194/gmd-9-1937-2016, 2016.

Farman, J. C., Gardiner, B. G. and Shanklin, J. D.: Large losses of total ozone in Antarctica reveal seasonal ClO x/NOx interaction, Nature, 315(6016), 207–210, doi:10.1038/315207a0, 1985.

Fasullo, J. T., Tomas, R., Stevenson, S., Otto-Bliesner, B., Brady, E. and Wahl, E.: The amplifying influence of increased ocean stratification on a future year without a summer, Nat. Commun., 8(1), 1236–1236, doi:10.1038/s41467-017-01302-z, 2017.

Ferraro, A. J., Charlton-Perez, A. J. and Highwood, E. J.: Stratospheric dynamics andmidlatitude jets under geoengineering with space mirrors and sulfate and titania aerosols, J. Geophys. Res., 120(2), 414–429, doi:10.1002/2014JD022734, 2015.

Free, M. and Robock, A.: Global warming in the context of the Little Ice Age, J. Geophys. Res. Atmos., 104(D16), 19057–19070, doi:10.1029/1999JD900233, 1999.

Gerlach, T. M., Westrich, H. R. and Symonds, R. B.: Preeruption Vapor in Magma of the Climactic Mount Pinatubo Eruption: Source of the Giant Stratospheric Sulfur Dioxide Cloud, Fire Mud Eruptions lahars Mt. Pinatubo, Philipp., 415–433, 1996.

Ghan, S. J.: Technical note: Estimating aerosol effects on cloud radiative forcing, Atmos. Chem. Phys., 13(19), 9971–9974, doi:10.5194/acp-13-9971-2013, 2013.

Giorgetta, M. A., Manzini, E., Roeckner, E., Esch, M. and Bengtsson, L.: Climatology and forcing of the quasi-biennial oscillation in the MAECHAM5 model, J. Clim., 19(16), 3882–3901, doi:10.1175/JCLI3830.1, 2006.

Govindasamy, B. and Caldeira, K.: Geoengineering Earth's radiation balance to mitigate CO2-induced climate change, Geophys. Res. Lett., 27(14), 2141–2144, doi:10.1029/1999GL006086, 2000.

Griffiths, P. T., Murray, L. T., Zeng, G., Shin, Y. M., Abraham, N. L., Archibald, A. T., Deushi, M., Emmons, L. K., Galbally, I. E., Hassler, B., Horowitz, L. W., Keeble, J., Liu, J., Moeini, O., Naik, V., O'Connor, F. M., Oshima, N., Tarasick, D., Tilmes, S., Turnock, S. T., Wild, O., Young, P. J. and Zanis, P.: Tropospheric ozone in CMIP6 simulations, Atmos. Chem. Phys., 21(5), 4187–4218, doi:10.5194/acp-21-4187-2021, 2021.

Guillet, S., Corona, C., Stoffel, M., Khodri, M., Lavigne, F., Ortega, P., Eckert, N., Sielenou, P. D., Daux, V., Churakova Sidorova, O. V., Davi, N., Edouard, J. L., Zhang, Y., Luckman, B. H., Myglan, V. S., Guiot, J., Beniston, M., Masson-Delmotte, V. and Oppenheimer, C.: Climate response to the Samalas volcanic eruption in 1257 revealed by proxy records, Nat. Geosci., 10(2), 123–128, doi:10.1038/ngeo2875, 2017.

Guo, S., Bluth, G. J. S., Rose, W. I., Watson, I. M. and Prata, A. J.: Re-evaluation of SO2 release of the 15 June 1991 Pinatubo eruption using ultraviolet and infrared satellite sensors, Geochemistry, Geophys. Geosystems, 5(4), doi:10.1029/2003GC000654, 2004.

Gupta, M. and Marshall, J.: The climate response to multiple volcanic eruptions mediated by ocean heat uptake: Damping processes and accumulation potential, J. Clim., 31(21), 8669–8687, doi:10.1175/JCLI-D-17-0703.1, 2018.

Halmer, M. M., Schmincke, H. U. and Graf, H. F.: The annual volcanic gas input into the atmosphere, in particular into the stratosphere: A global data set for the past 100 years, J. Volcanol. Geotherm. Res., 115(3–4), 511–528, doi:10.1016/S0377-0273(01)00318-3, 2002.

Hegerl, G. C., Crowley, T. J., Baum, S. K., Kim, K. and Hyde, W. T.: Detection of volcanic, solar and greenhouse gas signals in paleo-reconstructions of Northern Hemispheric temperature, Geophys. Res. Lett., 30(5), n/a-n/a, doi:10.1029/2002GL016635, 2003.

Hitchman, M. H., McKay, M. and Trepte, C. R.: A climatology of stratospheric aerosol, J. Geophys. Res., 99(D10), doi:10.1029/94jd01525, 1994.

Holton, J. R., Haynes, P. H., McIntyre, M. E., Douglass, A. R., Rood, R. B. and Pfister, L.: Stratosphere-troposphere exchange, Rev. Geophys., 33(4), 403–439, doi:10.1029/95RG02097, 1995.

Hopcroft, P. O., Kandlbauer, J., Valdes, P. J. and Sparks, R. S. J.: Reduced cooling following future volcanic eruptions, Clim. Dyn., 51(4), 1449–1463, doi:10.1007/s00382-017-3964-7, 2018.

Houghton, J. T., Jenkins, G. J. and Ephraums, J. J.: Climate change: the IPCC scientific assessment, Cambridge University Press, Cambridge., 1990.

Humphreys, W. J.: Volcanic dust and other factors in the production of climatic changes, and their possible relation to ice ages, J. Franklin Inst., 176(2), 131–160, doi:10.1016/S0016-0032(13)91294-1, 1913.

Hunton, D. E., Viggiano, A. A., Miller, T. M., Ballenthin, J. O., Reeves, J. M., Wilson, J. C., Lee, S. H., Anderson, B. E., Brune, W. H., Harder, H., Simpas, J. B. and Oskarsson, N.: In-situ aircraft observations of the 2000 Mt. Hekla volcanic cloud: Composition and chemical evolution in the Arctic lower stratosphere, J. Volcanol. Geotherm. Res., 145(1–2), 23–34, doi:10.1016/j.jvolgeores.2005.01.005, 2005.

Iglesias-Suarez, F., Kinnison, D. E., Rap, A., Maycock, A. C., Wild, O. and Young, P. J.: Key drivers of ozone change and its radiative forcing over the 21st century, Atmos. Chem. Phys., 18(9), 6121–6139, doi:10.5194/acp-18-6121-2018, 2018.

IPCC: IPCC Special Report on the impacts of global warming of 1.5°C, Ipcc - Sr15, 144(4), 32 [online] Available from: https://report.ipcc.ch/sr15/pdf/sr15_spm_final.pdf%0Ahttp://www.ipcc.ch/report/sr15/, 2018.

IPCC, P. I. sobre M. C.: Special Report on climate change, desertification, land degradation, sustainable land management, food security, and greenhouse gas fluxes in terrestrial ecosystems (SR2), edited by Engineering & Physical Science Research Council (EPSRC) and Natural Environment Research Council (NERC), book. [online] Available from: https://www.ipcc.ch/site/assets/uploads/2018/07/sr2_background_report_final.pdf, 2019.

Irvine, P. J., Ridgwell, A. and Lunt, D. J.: Climatic effects of surface albedo geoengineering, J. Geophys. Res. Atmos., 116(24), n/a-n/a, doi:10.1029/2011JD016281, 2011.

Jellinek, A. M., Manga, M. and Saar, M. O.: Did melting glaciers cause volcanic eruptions in eastern California? Probing the mechanics of dike formation, J. Geophys. Res. Solid Earth, 109(9), n/a-n/a, doi:10.1029/2004JB002978, 2004.

Johnston, H.: Reduction of stratospheric ozone by nitrogen oxide catalysts from supersonic transport exhaust, Science (80-.)., 173(3996), 517–522, doi:10.1126/science.173.3996.517, 1971.

Jones, A., Haywood, J. M., Jones, A. C., Tilmes, S., Kravitz, B. and Robock, A.: North Atlantic Oscillation response in GeoMIP experiments G6solar and G6sulfur: Why detailed modelling is needed for understanding regional implications of solar radiation management, Atmos. Chem. Phys., 21(2), 1287–1304, doi:10.5194/acp-

21-1287-2021, 2021.

Junge, C.E., Chagnon, C.W. and Manson, J. E.: Stratospheric aerosol studies, J. Geophys. Res., 66(7), 2163–2182, doi:10.1029/jz066i007p02163, 1961.

Keeble, J., Hassler, B., Banerjee, A., Checa-Garcia, R., Chiodo, G., Davis, S., Eyring, V., Griffiths, P. T., Morgenstern, O., Nowack, P., Zeng, G., Zhang, J., Bodeker, G., Burrows, S., Cameron-Smith, P., Cugnet, D., Danek, C., Deushi, M., Horowitz, L. W., Kubin, A., Li, L., Lohmann, G., Michou, M., Mills, M. J., Nabat, P., Olivié, D., Park, S., Seland, Ø., Stoll, J., Wieners, K. H. and Wu, T.: Evaluating stratospheric ozone and water vapour changes in CMIP6 models from 1850 to 2100, Atmos. Chem. Phys., 21(6), 5015–5061, doi:10.5194/acp-21-5015-2021, 2021.

Keith, D. W.: Geoengineering the climate: History and prospect, Annu. Rev. Energy Environ., 25(1), 245–284, doi:10.1146/annurev.energy.25.1.245, 2000.

Keith, D. W., Weisenstein, D. K., Dykema, J. A. and Keutsch, F. N.: Stratospheric solar geoengineering without ozone loss, Proc. Natl. Acad. Sci. U. S. A., 113(52), 14910–14914, doi:10.1073/pnas.1615572113, 2016.

Kilian, M., Brinkop, S. and Jöckel, P.: Impact of the eruption of Mt Pinatubo on the chemical composition of the stratosphere, Atmos. Chem. Phys., 20(20), 11697–11715, doi:10.5194/acp-20-11697-2020, 2020.

Kinne, S., Toon, O. B. and Prather, M. J.: Buffering of stratospheric circulation by changing amounts of tropical ozone a Pinatubo Case Study, Geophys. Res. Lett., 19(19), 1927–1930, doi:10.1029/92GL01937, 1992.

Kleinschmitt, C., Boucher, O. and Platt, U.: Sensitivity of the radiative forcing by stratospheric sulfur geoengineering to the amount and strategy of the SO2injection studied with the LMDZ-S3A model, Atmos. Chem. Phys., 18(4), 2769–2786, doi:10.5194/acp-18-2769-2018, 2018.

Klobas, E. J., Wilmouth, D. M., Weisenstein, D. K., Anderson, J. G. and Salawitch, R. J.: Ozone depletion following future volcanic eruptions, Geophys. Res. Lett., 44(14), 7490–7499, doi:10.1002/2017GL073972, 2017.

Kokkola, H., Hommel, R., Kazil, J., Niemeier, U., Partanen, A.-I., Feichter, J. and Timmreck, C.: Aerosol microphysics modules in the framework of the ECHAM5 climate model – intercomparison under stratospheric conditions, Geosci. Model Dev., 2(2), 97–112, doi:10.5194/gmd-2-97-2009, 2009.

Kravitz, B., Robock, A., Oman, L., Stenchikov, G. and Marquardt, A. B.: Sulfuric acid deposition from stratospheric geoengineering with sulfate aerosols, J. Geophys. Res. Atmos., 114(14), doi:10.1029/2009JD011918, 2009.

Kravitz, B., Robock, A., Boucher, O., Schmidt, H., Taylor, K. E., Stenchikov, G. and Schulz, M.: The Geoengineering Model Intercomparison Project (GeoMIP), Atmos. Sci. Lett., 12(2), 162–167, doi:10.1002/asl.316, 2011.

Kravitz, B., Caldeira, K., Boucher, O., Robock, A., Rasch, P. J., Alterskjær, K., Karam, D. B., Cole, J. N. S., Curry, C. L., Haywood, J. M., Irvine, P. J., Ji, D., Jones, A., Kristjánsson, J. E., Lunt, D. J., Moore, J. C., Niemeier, U., Schmidt, H., Schulz, M., Singh, B., Tilmes, S., Watanabe, S., Yang, S. and Yoon, J. H.: Climate model response from the Geoengineering Model Intercomparison Project (GeoMIP), J. Geophys. Res. Atmos., 118(15), 8320–8332, doi:10.1002/jgrd.50646, 2013.

Kravitz, B., Robock, A., Tilmes, S., Boucher, O., English, J. M., Irvine, P. J., Jones, A., Lawrence, M. G., MacCracken, M., Muri, H., Moore, J. C., Niemeier, U., Phipps, S. J., Sillmann, J., Storelvmo, T., Wang, H. and Watanabe, S.: The Geoengineering Model Intercomparison Project Phase 6 (GeoMIP6): Simulation design and preliminary results, Geosci. Model Dev., 8(10), 3379–3392, doi:10.5194/gmd-8-3379-2015, 2015.

Kremser, S., Thomason, L. W., von Hobe, M., Hermann, M., Deshler, T., Timmreck, C., Toohey, M., Stenke, A., Schwarz, J. P., Weigel, R., Fueglistaler, S., Prata, F. J., Vernier, J. P., Schlager, H., Barnes, J. E., Antuña-Marrero, J. C., Fairlie, D., Palm, M., Mahieu, E., Notholt, J., Rex, M., Bingen, C., Vanhellemont, F., Bourassa, A., Plane, J. M. C., Klocke, D., Carn, S. A., Clarisse, L., Trickl, T., Neely, R., James, A. D., Rieger, L., Wilson, J. C. and Meland, B.: Stratospheric aerosol—Observations, processes, and impact on climate, Rev. Geophys., 54(2), 278–335, doi:10.1002/2015RG000511, 2016.

Kroll, A. C., Dacie, S., Azoulay, A., Schmidt, H. and Timmreck, C.: The impact of volcanic eruptions of different magnitude on stratospheric water vapor in the tropics, Atmos. Chem. Phys., 21(8), 6565–6591, doi:10.5194/acp-21-6565-2021, 2021.

Krüger, K., Kutterolf, S. and Hansteen, T. H.: Halogen release from Plinian eruptions and depletion of stratospheric ozone, in Volcanism and Global Environmental Change, pp. 244–259., 2015.

Kutterolf, S., Hansteen, T. H., Appel, K., Freundt, A., Krüger, K., Pérez, W. and Wehrmann, H.: Combined bromine and chlorine release from large explosive volcanic eruptions: A threat to stratospheric ozone?, Geology, 41(6), 707–710, doi:10.1130/G34044.1, 2013.

Kutterolf, S., Hansteen, T. H., Freundt, A., Wehrmann, H., Appel, K., Krüger, K. and Pérez, W.: Bromine and chlorine emissions from Plinian eruptions along the Central American Volcanic Arc: From source to atmosphere, Earth Planet. Sci. Lett., 429, 234–246, doi:10.1016/j.epsl.2015.07.064, 2015.

Kwon, H., Choi, H., Kim, B. M., Kim, S. W. and Kim, S. J.: Recent weakening of the southern stratospheric polar vortex and its impact on the surface climate over Antarctica, Environ. Res. Lett., 15(9), 094072, doi:10.1088/1748-9326/ab9d3d, 2020.

Laakso, A., Kokkola, H., Partanen, A. I., Niemeier, U., Timmreck, C., Lehtinen, K. E. J., Hakkarainen, H. and Korhonen, H.: Radiative and climate impacts of a large volcanic eruption during stratospheric sulfur geoengineering, Atmos. Chem. Phys., 16(1), 305–323, doi:10.5194/acp-16-305-2016, 2016.

Labitzke, K. and McCormick, M. P.: Stratospheric temperature increases due to Pinatubo aerosols, Geophys. Res. Lett., 19(2), 207–210, doi:10.1029/91GL02940, 1992.

Lacis, A.: Volcanic aerosol radiative properties, Past Glob. Chang. Mag., 23(2), 50–51, doi:10.22498/pages.23.2.50, 2015.

Langematz, U.: Future ozone in a changing climate, Comptes Rendus - Geosci., 350(7), 403–409, doi:10.1016/j.crte.2018.06.015, 2018.

Langematz, U.: Stratospheric ozone: down and up through the anthropocene, ChemTexts, 5(2), 1–12, doi:10.1007/s40828-019-0082-7, 2019.

Lawrence, Z. D., Perlwitz, J., Butler, A. H., Manney, G. L., Newman, P. A., Lee, S. H. and Nash, E. R.: The

Remarkably Strong Arctic Stratospheric Polar Vortex of Winter 2020: Links to Record-Breaking Arctic Oscillation and Ozone Loss, J. Geophys. Res. Atmos., 125(22), n/a-n/a, doi:10.1029/2020JD033271, 2020.

Legrande, A. N., Tsigaridis, K. and Bauer, S. E.: Role of atmospheric chemistry in the climate impacts of stratospheric volcanic injections, Nat. Geosci., 9(9), 652–655, doi:10.1038/ngeo2771, 2016.

Löffler, M., Brinkop, S. and Jöckel, P.: Impact of major volcanic eruptions on stratospheric water vapour, The Regensburg University of Applied Sciences., 2016.

Lurton, T., Jégou, F., Berthet, G., Renard, J. B., Clarisse, L., Schmidt, A., Brogniez, C. and Roberts, T. J.: Model simulations of the chemical and aerosol microphysical evolution of the Sarychev Peak 2009 eruption cloud compared to in situ and satellite observations, Atmos. Chem. Phys., 18(5), 3223–3247, doi:10.5194/acp-18-3223-2018, 2018.

M. Toohey, K. Krüger, U. Niemeier and C. Timmreck: The influence of eruption season on the global aerosol evolution and radiative impact of tropical volcanic eruptions, Atmos. Chem. Phys., 11(23), 12351–12367, doi:10.5194/acp-11-12351-2011, 2011.

Madronich, S.: Analytic formula for the clear-sky UV index, Photochem. Photobiol., 83(6), 1537–1538, doi:10.1111/j.1751-1097.2007.00200.x, 2007.

Mankin, W. G. and Coffey, M. T.: Increased stratospheric hydrogen chloride in the El Chichon cloud., Science (80-.)., 226(4671), 170–172, doi:10.1126/science.226.4671.170, 1984.

Mankin, W. G., Coffey, M. T. and Goldman, A.: Airborne observations of SO2, HCl, and O3 in the stratospheric plume of the Pinatubo Volcano in July 1991, Geophys. Res. Lett., 19(2), 179–182, doi:10.1029/91GL02942, 1992.

Mann, G. W., Carslaw, K. S., Spracklen, D. V., Ridley, D. A., Manktelow, P. T., Chipperfield, M. P., Pickering, S. J. and Johnson, C. E.: Description and evaluation of GLOMAP-mode: A modal global aerosol microphysics model for the UKCA composition-climate model, Geosci. Model Dev., 3(2), 519–551, doi:10.5194/gmd-3-519-2010, 2010.

Mann, G. W., Carslaw, K. S., Ridley, D. A., Spracklen, D. V., Pringle, K. J., Merikanto, J., Korhonen, H., Schwarz, J. P., Lee, L. A., Manktelow, P. T., Woodhouse, M. T., Schmidt, A., Breider, T. J., Emmerson, K. M., Reddington, C. L., Chipperfield, M. P. and Pickering, S. J.: Intercomparison of modal and sectional aerosol microphysics representations within the same 3-D global chemical transport model, Atmos. Chem. Phys., 12(10), 4449, doi:10.5194/acp-12-4449-2012, 2012.

Manning, J. G., Ludlow, F., Stine, A. R., Boos, W. R., Sigl, M. and Marlon, J. R.: Volcanic suppression of Nile summer flooding triggers revolt and constrains interstate conflict in ancient Egypt, Nat. Commun., 8(1), 900–900, doi:10.1038/s41467-017-00957-y, 2017.

Marshall, L., Johnson, J. S., Mann, G. W., Lee, L., Dhomse, S. S., Regayre, L., Yoshioka, M., Carslaw, K. S. and Schmidt, A.: Exploring How Eruption Source Parameters Affect Volcanic Radiative Forcing Using Statistical Emulation, J. Geophys. Res. Atmos., 124(2), 964–985, doi:10.1029/2018JD028675, 2019.

Marshall, L. R.: Effects of Volcanic Eruption Source Parameters on Radiative Forcing and Sulfate Deposition, University of Leeds. [online] Available from: http://etheses.whiterose.ac.uk/22551/, 2018.

McConnell, J. R., Sigl, M., Plunkett, G., Burke, A., Kim, W. M., Raible, C. C., Wilson, A. I., Manning, J. G., Ludlow, F., Chellman, N. J., Innes, H. M., Yang, Z., Larsen, J. F., Schaefer, J. R., Kipfstuhl, S., Mojtabavi, S., Wilhelms, F., Opel, T., Meyer, H. and Steffensen, J. P.: Extreme climate after massive eruption of Alaska's Okmok volcano in 43 bce and effects on the late roman republic and ptolemaic kingdom, Proc. Natl. Acad. Sci. U. S. A., 117(27), 15443–15449, doi:10.1073/pnas.2002722117, 2020.

McCormick, M. P., Thomason, L. W. and Trepte, C. R.: Atmospheric effects of the Mt Pinatubo eruption, Nature, 373(6513), 399–404, doi:10.1038/373399a0, 1995.

McElroy, C. T. and Fogal, P. F.: Ozone: From discovery to protection, Atmos. - Ocean, 46(1), 1–13, doi:10.3137/ao.460101, 2008.

Mcelroy, M. B., Salawitch, R. J., Wofsy, S. C. and Logan, J. A.: Reductions of Antarctic ozone due to synergistic interactions of chlorine and bromine, Nature, 321(6072), 759–762, doi:10.1038/321759a0, 1986.

Meul, S., Dameris, M., Langematz, U., Abalichin, J., Kerschbaumer, A., Kubin, A. and Oberländer-Hayn, S.: Impact of rising greenhouse gas concentrations on future tropical ozone and UV exposure, Geophys. Res. Lett., 43(6), 2919–2927, doi:10.1002/2016GL067997, 2016.

Mie, G.: Beiträge zur Optik trüber Medien, speziell kolloidaler Metallösungen, Ann. Phys., 330(3), 377–445, doi:10.1002/andp.19083300302, 1908.

Mills, M. J., Schmidt, A., Easter, R., Solomon, S., Kinnison, D. E., Ghan, S. J., Neely, R. R., Marsh, D. R., Conley, A., Bardeen, C. G. and Gettelman, A.: Global volcanic aerosol properties derived from emissions, 1990–2014, using CESM1(WACCM), J. Geophys. Res., 121(5), 2332–2348, doi:10.1002/2015JD024290, 2016.

Ming, A., Winton, V. H. L., Keeble, J., Abraham, N. L., Dalvi, M. C., Griffiths, P., Caillon, N., Jones, A. E., Mulvaney, R., Savarino, J., Frey, M. M. and Yang, X.: Stratospheric Ozone Changes From Explosive Tropical Volcanoes: Modeling and Ice Core Constraints, J. Geophys. Res. Atmos., 125(11), doi:10.1029/2019JD032290, 2020.

Molina, L. T. and Molina, M. J.: Production of Cl2O2 from the self-reaction of the ClO radical, J. Phys. Chem., 91(2), 433–436, doi:10.1021/j100286a035, 1987.

Molina, M. J. and Rowland, F. S.: Stratospheric sink for chlorofluoromethanes: Chlorine atomc-atalysed destruction of ozone, Nature, 249(5460), 810–812, doi:10.1038/249810a0, 1974.

Montzka, S. A., Reimann, S., Engel, A., Kruger, K., Sturges, W. T., Blake, D., Dorf, M., Fraser, P., Froidevaux, L., Jucks, K., Kreher, K., Kurylo, M. J., Mellouki, A., Miller, J., Nielsen, O.-J., Orkin, V. L., Prinn, R. G., Rhew, R., Santee, M. L., Stohl, A., Verdonik, D. and Krummel, P. B.: Ozone-Depleting Substances (ODSs) and Related Chemicals (Chapter 1), edited by Oceanic And Atmospheric Administration; National Aeronautics And Space Administration; United Nations Environment Programme; World Meteorological Organization; European Commission (Sponsor), E. (Collaborator) Atlas, P. (Collaborator) Bernath, T. (Collaborator) Blumenstock, J. H. (Collaborator) Butler, A. (Collaborator) Butz, B. (Collaborator) Connor, P. (Collaborator) Duchatelet, G. (Collaborator) Dutton, F. (Collaborator) Hendrick, P. B. (Collaborator) Krummel, L. J. M. (Collaborator) Kuijpers, E. (Collaborator) Mahieu, A. (Collaborator) Manning, J. (Collaborator) Muhle, K. (Collaborator) Pfeilsticker, B. (Collaborator) Quack, M. (Collaborator) Ross, R. J. (Collaborator) Salavitch, S. (Collaborator)

Schauffler, I. J. (Collaborator) Simpson, D. (Collaborator) Toohey, M. K. (Collaborator) Vollmer, T. J. (Collaborator) Wallington, H. J. R. (Collaborator) Wang, R. F. (Collaborator) Weiss, M. (Collaborator) Yamabe, Y. (Collaborator) Yokouchi, and S. (Collaborator) Yvon-Lewis., 2011.

Mulcahy, J., Johnson, C., Jones, C., Povey, A., Scott, C., Sellar, A., Turnock, S., Woodhouse, M., Abraham, N. L., Andrews, M., Bellouin, N., Browse, J., Carslaw, K., Dalvi, M., Folberth, G., Glover, M., Grosvenor, D., Hardacre, C., Hill, R., Johnson, B., Jones, A., Kipling, Z., Mann, G., Mollard, J., O'Connor, F., Palmieri, J., Reddington, C., Rumbold, S., Richardson, M., Schutgens, N., Stier, P., Stringer, M., Tang, Y., Walton, J., Woodward, S. and Yool, A.: Description and evaluation of aerosol in UKESM1 and HadGEM3-GC3.1 CMIP6 historical simulations, Geosci. Model Dev. Discuss., 1–59, doi:10.5194/gmd-2019-357, 2020.

Naik, V., Horowitz, L. W., Daniel Schwarzkopf, M. and Lin, M.: Impact of volcanic aerosols on stratospheric ozone recovery, J. Geophys. Res. Atmos., 122(17), 9515–9528, doi:10.1002/2016JD025808, 2017.

National Research Council: Climate intervention: Reflecting sunlight to cool earth, The National Academies Press, Washington, District of Columbia., 2015.

Neu, J. L. and Plumb, R. A.: Age of air in a "leaky pipe" model of stratospheric transport, J. Geophys. Res. Atmos., 104(D16), 19243–19255, doi:10.1029/1999JD900251, 1999.

Newhall, C., Self, S. and Robock, A.: Anticipating future Volcanic Explosivity Index (VEI) 7 eruptions and their chilling impacts, Geosphere, 14(2), 572–603, doi:10.1130/GES01513.1, 2018.

Niemeier, U. and Schmidt, H.: Changing transport processes in the stratosphere by radiative heating of sulfate aerosols, Atmos. Chem. Phys., 17(24), 14871–14886, doi:10.5194/acp-17-14871-2017, 2017.

Niemeier, U. and Timmreck, C.: What is the limit of climate engineering by stratospheric injection of SO2?, Atmos. Chem. Phys., 15(16), 9129–9141, doi:10.5194/acp-15-9129-2015, 2015.

O'Connor, F. M., Luke Abraham, N., Dalvi, M., Folberth, G. A., Griffiths, P. T., Hardacre, C., Johnson, B. T., Kahana, R., Keeble, J., Kim, B., Morgenstern, O., Mulcahy, J. P., Richardson, M., Robertson, E., Seo, J., Shim, S., Teixeira, J. C., Turnock, S. T., Williams, J., Wiltshire, A. J., Woodward, S. and Zeng, G.: Assessment of pre-industrial to present-day anthropogenic climate forcing in UKESM1, Atmos. Chem. Phys., 21(2), 1211–1243, doi:10.5194/acp-21-1211-2021, 2021.

O'Neill, B. C., Tebaldi, C., Van Vuuren, D. P., Eyring, V., Friedlingstein, P., Hurtt, G., Knutti, R., Kriegler, E., Lamarque, J. F., Lowe, J., Meehl, G. A., Moss, R., Riahi, K. and Sanderson, B. M.: The Scenario Model Intercomparison Project (ScenarioMIP) for CMIP6, Geosci. Model Dev., 9(9), 3461–3482, doi:10.5194/gmd-9-3461-2016, 2016.

Oberländer, S., Langematz, U. and Meul, S.: Unraveling impact factors for future changes in the Brewer-Dobson circulation, J. Geophys. Res. Atmos., 118(18), 10,296-10,312, doi:10.1002/jgrd.50775, 2013.

Osipov, S., Stenchikov, G., Tsigaridis, K., LeGrande, A. N. and Bauer, S. E.: The Role of the SO 2 Radiative Effect in Sustaining the Volcanic Winter and Soothing the Toba Impact on Climate, J. Geophys. Res. Atmos., 125(2), n/a-n/a, doi:10.1029/2019JD031726, 2020.

Osprey, S. M., Gray, L. J., Hardiman, S. C., Butchart, N. and Hinton, T. J.: Stratospheric variability in twentieth-

century CMIP5 simulations of the met office climate model: High top versus low top, J. Clim., 26(5), 1595–1606, doi:10.1175/JCLI-D-12-00147.1, 2013.

Pearson, P. N.: Increased atmospheric CO2 during the middle Eocene, Science (80-.)., 330(6005), 763–764, doi:10.1126/science.1197894, 2010.

Pitari, G., Aquila, V., Kravitz, B., Robock, A., Watanabe, S., Cionni, I., Luca, N., Genova, G., Mancini, E. and Tilmes, S.: Stratospheric ozone response to sulfate geoengineering: Results from the geoengineering model intercomparison project (GeoMip), J. Geophys. Res., 119(5), 2629–2653, doi:10.1002/2013JD020566, 2014.

Plumb, R. A.: A "tropical pipe" model of stratospheric transport, J. Geophys. Res. Atmos., 101(D2), 3957–3972, doi:10.1029/95JD03002, 1996.

Plumb, R. A.: Stratospheric transport, J. Meteorol. Soc. Japan, 80(4 B), 793–809, doi:10.2151/jmsj.80.793, 2002.

Pollack, J. B., Toon, O. B., Sagan, C., Summers, A., Baldwin, B. and Van Camp, W.: Volcanic explosions and climatic change: A theoretical assessment, J. Geophys. Res., 81(6), 1071–1083, doi:10.1029/jc081i006p01071, 1976.

Prata, A. J., Carn, S. A., Stohl, A. and Kerkmann, J.: Long range transport and fate of a stratospheric volcanic cloud from Soufrière Hills volcano, Montserrat, Atmos. Chem. Phys., 7(19), 5093–5103, doi:10.5194/acp-7-5093-2007, 2007.

Pumphrey, H. C., Read, W. G., Livesey, N. J. and Yang, K.: Observations of volcanic SO2 from MLS on Aura, in Atmospheric Measurement Techniques, vol. 8, pp. 195–209., 2015.

Punge, H. J., Konopka, P., Giorgetta, M. A. and Müller, R.: Effects of the quasi-biennial oscillation on low-latitude transport in the stratosphere derived from trajectory calculations, J. Geophys. Res. Atmos., 114(3), n/a-n/a, doi:10.1029/2008JD010518, 2009.

Rap, A., Richards, N. A. D., Forster, P. M., Monks, S. A., Arnold, S. R. and Chipperfield, M. P.: Satellite constraint on the tropospheric ozone radiative effect, Geophys. Res. Lett., 42(12), 5074–5081, doi:10.1002/2015GL064037, 2015.

Rasch, P. J., Crutzen, P. J. and Coleman, D. B.: Exploring the geoengineering of climate using stratospheric sulfate aerosols: The role of particle size, Geophys. Res. Lett., 35(2), doi:10.1029/2007GL032179, 2008.

Read, W., Froidvaux, L., Santee, M. and Livesey, N.: Observations of volcanic SO2 and HCl from Aura MLS, in Read, W., Froidvaux, L., Santee, M., and Livesey, N.: Observationsof volcanic SO2and HCl from Aura MLS, American Geophys-ical Union, Fall Meeting 2009, abstract number V24B-03, 14–18 December 2009., 2009.

Robock, A.: Volcanic eruptions and climate, Rev. Geophys., 38(2), 191–219, doi:10.1029/1998RG000054, 2000.

Robock, A. and Matson, M.: Circumglobal transport of the El Chichón volcanic dust cloud, Science (80-.)., 221(4606), 195–197, doi:10.1126/science.221.4606.195, 1983.

Robock, A., Ammann, C. M., Oman, L., Shindell, D., Levis, S. and Stenchikov, G.: Did the Toba volcanic eruption of ~74 ka B.P. produce widespread glaciation?, J. Geophys. Res. Atmos., 114(10), n/a-n/a, doi:10.1029/2008JD011652, 2009.

Rose, W. I., Millard, G. A., Mather, T. A., Hunton, D. E., Anderson, B., Oppenheimer, C., Thornton, B. F., Gerlach, T. M., Viggiano, A. A., Kondo, Y., Miller, T. M. and Ballenthin, J. O.: Atmospheric chemistry of a 33-34 hour old volcanic cloud from Hekla Volcano (Iceland): Insights from direct sampling and the application of chemical box modeling, J. Geophys. Res. Atmos., 111(20), doi:10.1029/2005JD006872, 2006.

Rosenfield, J. E.: Effects of volcanic eruptions on stratospheric ozone recovery, Geophys. Monogr. Ser., 139, 227–236, doi:10.1029/139GM14, 2003.

Royer, D. L.: CO 2-forced climate thresholds during the Phanerozoic, Geochim. Cosmochim. Acta, 70(23), 5665–5675, doi:10.1016/j.gca.2005.11.031, 2006.

Rüdiger, J., Gutmann, A., Bobrowski, N., Liotta, M., Maarten De Moor, J., Sander, R., Dinger, F., Tirpitz, J. L., Ibarra, M., Saballos, A., Martínez, M., Mendoza, E., Ferrufino, A., Stix, J., Valdés, J., Castro, J. M. and Hoffmann, T.: Halogen activation in the plume of Masaya volcano: Field observations and box model investigations, Atmos. Chem. Phys., 21(5), 3371–3393, doi:10.5194/acp-21-3371-2021, 2021.

Schmidt, A. and Carn, S.: Aerosols and Climate: 17. Volcanic emissions, aerosol processes and climatic effects (in press), edited by K. Carslaw, Elsevier., n.d.

Schmidt, A., Skeffington, R. A., Thordarson, T., Self, S., Forster, P. M., Rap, A., Ridgwell, A., Fowler, D., Wilson, M., Mann, G. W., Wignall, P. b. and Carslaw, K. S.: Selective environmental stress from sulphur emitted by continental flood basalt eruptions, Nat. Geosci., 9(1), 77–82, doi:10.1038/ngeo2588, 2016.

Schmidt, A., Mills, M. J., Ghan, S., Gregory, J. M., Allan, R. P., Andrews, T., Bardeen, C. G., Conley, A., Forster, P. M., Gettelman, A., Portmann, R. W., Solomon, S. and Toon, O. B.: Volcanic Radiative Forcing From 1979 to 2015, J. Geophys. Res. Atmos., 123(22), 12,491-12,508, doi:10.1029/2018JD028776, 2018.

Self, S., Zhao, J.-X., Holasek, R., Torres, R. and K, A.: The atmospheric impact of the 1991 Mount Pinatubo eruption., in Fire and Mud: Eruptions and lahars of Mount Pinatubo, Phillipines, University of Washington Press., 1996.

Self, S., Zhao, J.-X., Holasek, R. E., Torres, R. C. and King, A. J.: The Atmospheric Impact of the 1991 Mount Pinatubo Eruption, in U.S. Geological Survey, University of Washington Press., 1999.

Sellar, A. A., Jones, C. G., Mulcahy, J. P., Tang, Y., Yool, A., Wiltshire, A., O'Connor, F. M., Stringer, M., Hill, R., Palmieri, J., Woodward, S., de Mora, L., Kuhlbrodt, T., Rumbold, S. T., Kelley, D. I., Ellis, R., Johnson, C. E., Walton, J., Abraham, N. L., Andrews, M. B., Andrews, T., Archibald, A. T., Berthou, S., Burke, E., Blockley, E., Carslaw, K., Dalvi, M., Edwards, J., Folberth, G. A., Gedney, N., Griffiths, P. T., Harper, A. B., Hendry, M. A., Hewitt, A. J., Johnson, B., Jones, A., Jones, C. D., Keeble, J., Liddicoat, S., Morgenstern, O., Parker, R. J., Predoi, V., Robertson, E., Siahaan, A., Smith, R. S., Swaminathan, R., Woodhouse, M. T., Zeng, G. and Zerroukat, M.: UKESM1: Description and Evaluation of the U.K. Earth System Model, J. Adv. Model. Earth Syst., 11(12), 4513–4558, doi:10.1029/2019MS001739, 2019.

Sellar, A. A., Walton, J., Jones, C. G., Wood, R., Abraham, N. L., Andrejczuk, M., Andrews, M. B., Andrews, T., Archibald, A. T., de Mora, L., Dyson, H., Elkington, M., Ellis, R., Florek, P., Good, P., Gohar, L., Haddad, S., Hardiman, S. C., Hogan, E., Iwi, A., Jones, C. D., Johnson, B., Kelley, D. I., Kettleborough, J., Knight, J. R., Köhler, M. O., Kuhlbrodt, T., Liddicoat, S., Linova-Pavlova, I., Mizielinski, M. S., Morgenstern, O., Mulcahy, J.,

Neininger, E., O'Connor, F. M., Petrie, R., Ridley, J., Rioual, J. C., Roberts, M., Robertson, E., Rumbold, S., Seddon, J., Shepherd, H., Shim, S., Stephens, A., Teixiera, J. C., Tang, Y., Williams, J., Wiltshire, A. and Griffiths, P. T.: Implementation of U.K. Earth System Models for CMIP6, J. Adv. Model. Earth Syst., 12(4), doi:10.1029/2019MS001946, 2020.

Sigl, M., Winstrup, M., Mcconnell, J. R., K. C. Welten, G. Plunkett, F. Ludlow, U. Büntgen, M. Caffee, N. Chellman, D. Dahl-Jensen, H. Fischer, S. Kipfstuhl, C. Kostick, O. J. Maselli, F. Mekhaldi, R. Mulvaney, R. Muscheler, D. R. Pasteris, J. R. Pilcher, M. Salzer, S. Schüpbach, J. P. Steffensen, B. M. Vinther and T. E. Woodruff: Timing and climate forcing of volcanic eruptions for the past 2,500 years, Nature, 523(7562), 543–549, doi:10.1038/nature14565, 2015.

Sigurdsson, H., Houghton, B. F., Mcnutt, S. R., Rymer, H., Stix, J. and Mcbirney, A. R.: Encyclopedia of volcanoes, Encycl. volcanoes., 53(10), 84–85, doi:10.1063/1.1325206, 2000.

Sinnhuber, B. M., Sheode, N., Sinnhuber, M., Chipperfield, M. P. and Feng, W.: The contribution of anthropogenic bromine emissions to past stratospheric ozone trends: A modelling study, Atmos. Chem. Phys., 9(8), 2863–2871, doi:10.5194/acp-9-2863-2009, 2009.

Soden, B. J., Wetherald, R. T., Stenchikov, G. L. and Robock, A.: Global cooling after the eruption of Mount Pinatubo: A test of climate feedback by water vapor, Science (80-.)., 296(5568), 727–730, doi:10.1126/science.296.5568.727, 2002.

Solomon, S.: Stratospheric ozone depletion: A review of concepts and history, Rev. Geophys., 37(3), 275–316, doi:10.1029/1999RG900008, 1999.

Solomon, S., Garcia, R. R., Rowland, F. S. and Wuebbles, D. J.: On the depletion of Antarctic ozone, Nature, 321(6072), 755–758, doi:10.1038/321755a0, 1986.

Solomon, S., Portmann, R. W., Garcia, R. R., Thomason, L. W., Poole, L. R. and McCormick, M. P.: The role of aerosol variations in anthropogenic ozone depletion at northern midlatitudes, J. Geophys. Res. Atmos., 101(D3), 6713–6727, doi:10.1029/95JD03353, 1996.

Son, S. -W., Gerber, E. P., Perlwitz, J., Polvani, L. M., Gillett, N. P., Seo, K. -H., Eyring, V., Shepherd, T. G., Waugh, D., Akiyoshi, H., Austin, J., Baumgaertner, A., Bekki, S., Braesicke, P., Brühl, C., Butchart, N., Chipperfield, M. P., Cugnet, D., Dameris, M., Dhomse, S., Frith, S., Garny, H., Garcia, R., Hardiman, S. C., Jöckel, P., Lamarque, J. F., Mancini, E., Marchand, M., Michou, M., Nakamura, T., Morgenstern, O., Pitari, G., Plummer, D. A., Pyle, J., Rozanov, E., Scinocca, J. F., Shibata, K., Smale, D., Teyssdre, H., Tian, W. and Yamashita, Y.: Impact of stratospheric ozone on Southern Hemisphere circulation change: A multimodel assessment, J. Geophys. Res. Atmos., 115(19), n/a-n/a, doi:10.1029/2010JD014271, 2010.

Staehelin, J., Petropavlovskikh, I., De Mazière, M. and Godin-Beekmann, S.: The role and performance of ground-based networks in tracking the evolution of the ozone layer, Comptes Rendus - Geosci., 350(7), 354–367, doi:10.1016/j.crte.2018.08.007, 2018.

Staunton Sykes, J., Aubry, T. J., Shin, Y. M., Weber, J., Marshall, L., Luke Abraham, N., Archibald, A. T. and Schmidt, A.: Co-emission of volcanic sulfur and halogens amplifies volcanic effective radiative forcing, Atmos. Chem. Phys., 21, 9009–9029 [online] Available from: https://doi.org/10.5194/acp-21-9009-2021, 2021.

Steinfeld, J. I.: Atmospheric Chemistry and Physics: From Air Pollution to Climate Change, Third edit., Hoboken., 1998.

Stenchikov, G., Delworth, T. L., Ramaswamy, V., Stouffer, R. J., Wittenberg, A. and Zeng, F.: Volcanic signals in oceans, J. Geophys. Res. Atmos., 114(16), n/a-n/a, doi:10.1029/2008JD011673, 2009.

Stolarski, R. S. and Cicerone, R. J.: Stratospheric Chlorine: a Possible Sink for Ozone, Can. J. Chem., 52(8), 1610–1615, doi:10.1139/v74-233, 1974.

Swindles, G. T., Watson, E. J., Savov, I. P., Lawson, I. T., Schmidt, A., Hooper, A., Cooper, C. L., Connor, C. B., Gloor, M. and Carrivick, J. L.: Climatic control on Icelandic volcanic activity during the mid-Holocene, Geology, 46(1), 47–50, doi:10.1130/G39633.1, 2018.

Symons. G.: The Eruption of Krakatoa and Subsequent Phenomena, Q. J. R. Meteorol. Soc., 14(68), 301–307, doi:10.1002/qj.4970146809, 1888.

Szopa, S., Thiéblemont, R., Bekki, S., Botsyun, S. and Sepulchre, P.: Role of the stratospheric chemistry-climate interactions in the hot climate conditions of the Eocene, Clim. Past, 15(4), 1187–1203, doi:10.5194/cp-15-1187-2019, 2019.

Telford, P. J., Abraham, N. L., Archibald, A. T., Braesicke, P., Dalvi, M., Morgenstern, O., O'Connor, F. M., Richards, N. A. D. and Pyle, J. A.: Implementation of the Fast-JX Photolysis scheme (v6.4) into the UKCA component of the MetUM chemistry-climate model (v7.3), Geosci. Model Dev., 6(1), 161–177, doi:10.5194/gmd-6-161-2013, 2013.

Textor, C., Graf, H. F., Herzog, M. and Oberhuber, J. M.: Injection of gases into the stratosphere by explosive volcanic eruptions, J. Geophys. Res. Atmos., 108(19), doi:10.1029/2002jd002987, 2003.

Thomason, L. and Peter, T.: Assessment of stratospheric aerosol properties (ASAP). [online] Available from: http://www.atmosp.physics.utoronto.ca/people/sparc/News18/18_TextsFigures.pdf#page=9, 2006.

Thomason, L. W., Ernest, N., Millán, L., Rieger, L., Bourassa, A., Vernier, J. P., Manney, G., Luo, B., Arfeuille, F. and Peter, T.: A global space-based stratospheric aerosol climatology: 1979-2016, Earth Syst. Sci. Data, 10(1), 469–492, doi:10.5194/essd-10-469-2018, 2018.

Tie, X. X. and Brasseur, G.: The response of stratospheric ozone to volcanic eruptions: Sensitivity to atmospheric chlorine loading, Geophys. Res. Lett., 22(22), 3035–3038, doi:10.1029/95GL03057, 1995.

Timmreck, C.: Modeling the climatic effects of large explosive volcanic eruptions, Wiley Interdiscip. Rev. Clim. Chang., 3(6), 545–564, doi:10.1002/wcc.192, 2012.

Timmreck, C., Lorenz, S. J., Crowley, T. J., Kinne, S., Raddatz, T. J., Thomas, M. A. and Jungclaus, J. H.: Limited temperature response to the very large AD 1258 volcanic eruption, Geophys. Res. Lett., 36(21), n/a-n/a, doi:10.1029/2009GL040083, 2009.

Timmreck, C., Graf, H. F., Lorenz, S. J., Niemeier, U., Zanchettin, D., Matei, D., Jungclaus, J. H. and Crowley, T. J.: Aerosol size confines climate response to volcanic super-eruptions, Geophys. Res. Lett., 37(24), n/a-n/a, doi:10.1029/2010GL045464, 2010.

Toohey, M., Krüger, K., Bittner, M., Timmreck, C. and Schmidt, H.: The impact of volcanic aerosol on the Northern Hemisphere stratospheric polar vortex: Mechanisms and sensitivity to forcing structure, Atmos. Chem. Phys., 14(23), 13063–13079, doi:10.5194/acp-14-13063-2014, 2014.

Trepte, C. R. and Hitchman, M. H.: Tropical stratospheric circulation deduced from satellite aerosol data, Nature, 355(6361), 626–628, doi:10.1038/355626a0, 1992.

Varekamp, J. C., Luhr, J. F. and Prestegaard, K. L.: The 1982 eruptions of El Chichón Volcano (Chiapas, Mexico): Character of the eruptions, ash-fall deposits, and gasphase, J. Volcanol. Geotherm. Res., 23(1–2), 39–68, doi:10.1016/0377-0273(84)90056-8, 1984.

Vernier, J. P., Fairlie, T. D., Deshler, T., Natarajan, M., Knepp, T., Foster, K., Wienhold, F. G., Bedka, K. M., Thomason, L. and Trepte, C.: In situ and space-based observations of the Kelud volcanic plume: The persistence of ash in the lower stratosphere, J. Geophys. Res., 121(18), 11,104-11,118, doi:10.1002/2016JD025344, 2016.

Vidal, C. M., Métrich, N., Komorowski, J. C., Pratomo, I., Michel, A., Kartadinata, N., Robert, V. and Lavigne, F.: The 1257 Samalas eruption (Lombok, Indonesia): The single greatest stratospheric gas release of the Common Era, Sci. Rep., 6, doi:10.1038/srep34868, 2016.

Visioni, D., Pitari, G., Aquila, V., Tilmes, S., Cionni, I., Di Genova, G. and Mancini, E.: Sulfate geoengineering impact on methane transport and lifetime: Results from the geoengineering model intercomparison project (GeoMIP), Atmos. Chem. Phys., 17(18), 11209–11226, doi:10.5194/acp-17-11209-2017, 2017.

Visioni, D., Pitari, G., Tuccella, P. and Curci, G.: Sulfur deposition changes under sulfate geoengineering conditions: Quasi-biennial oscillation effects on the transport and lifetime of stratospheric aerosols, Atmos. Chem. Phys., 18(4), 2787–2808, doi:10.5194/acp-18-2787-2018, 2018.

van Vuuren, D. P., Edmonds, J., Kainuma, M., Riahi, K., Thomson, A., Hibbard, K., Hurtt, G. C., Kram, T., Krey, V., Lamarque, J. F., Masui, T., Meinshausen, M., Nakicenovic, N., Smith, S. J. and Rose, S. K.: The representative concentration pathways: An overview, Clim. Change, 109(1), 5–31, doi:10.1007/s10584-011-0148-z, 2011.

Wade, D. C., Vidal, C. M., Luke Abraham, N., Dhomse, S., Griffiths, P. T., Keeble, J., Mann, G., Marshall, L., Schmidt, A. and Archibald, A. T.: Reconciling the climate and ozone response to the 1257 CE Mount Samalas eruption, Proc. Natl. Acad. Sci. U. S. A., 117(43), 26651–26659, doi:10.1073/pnas.1919807117, 2020.

Wallace, L. and Livingston, W.: The effect of the Pinatubo cloud on hydrogen chloride and hydrogen fluoride, Geophys. Res. Lett., 19(12), 1209–1209, doi:10.1029/92GL01112, 1992.

Wang, M., Fu, Q., Solomon, S., White, R. H. and Alexander, B.: Stratospheric Ozone in the Last Glacial Maximum, J. Geophys. Res. Atmos., 125(21), n/a-n/a, doi:10.1029/2020JD032929, 2020.

Watt, S. F. L., Pyle, D. M. and Mather, T. A.: The volcanic response to deglaciation: Evidence from glaciated arcs and a reassessment of global eruption records, Earth-Science Rev., 122, 77–102, doi:10.1016/j.earscirev.2013.03.007, 2013.

Weber, J., Shin, Y. M., Staunton Sykes, J., Archer-Nicholls, S., Abraham, N. L. and Archibald, A. T.: Minimal Climate Impacts From Short-Lived Climate Forcers Following Emission Reductions Related to the COVID-19 Pandemic, Geophys. Res. Lett., 47(20), n/a-n/a, doi:10.1029/2020GL090326, 2020.

WMO (World Meteorological Organization): Scientific Assessment of Ozone Depletion: 2014, Geneva. [online] Available from: http://www.wmo.int/pages/prog/arep/gaw/ozone/, 2014.

Woods, D. C., Chuan, R. L. and Rose, W. I.: Halite particles injected into the stratosphere by the 1982 El Chichón eruption, Science (80-.)., 230(4722), 170–172, doi:10.1126/science.230.4722.170, 1985.

World Health Organization.: Ultraviolet radiation : an authoritative scientific review of environmental and health effects of UV, with reference to global ozone layer depletion, World Health Organization, Geneva., 1994.

World Health Organization. and International Programme on Chemical Safety.: Ultraviolet radiation : an authoritative scientific review of environmental and health effects of UV, with reference to global ozone layer depletion., 1994.

World Meteorological Organization, W.: Executive summary: scientific assessment of ozone depletion: 2018, World Meteorological Organization, global ozone research and monitoring project—report no. 58, Geneva., 2018.

Zdanowicz, C. M., Zielinski, G. A. and Germani, M. S.: Mount Mazama eruption: Calendrical age verified and atmospheric impact assessed, Geology, 27(7), 621–624, doi:10.1130/0091-7613(1999)027<0621:MMECAV>2.3.CO;2, 1999.

Zhu, Y., Toon, O. B., Jensen, E. J., Bardeen, C. G., Mills, M. J., Tolbert, M. A., Yu, P. and Woods, S.: Persisting volcanic ash particles impact stratospheric SO2 lifetime and aerosol optical properties, Nat. Commun., 11(1), doi:10.1038/s41467-020-18352-5, 2020.

Zhuo, Z., Kirchner, I., Pfahl, S. and Cubasch, U.: Climate impact of volcanic eruptions: the sensitivity to eruption season and latitude in MPI-ESM ensemble experiments, Atmos. Chem. Phys. Discuss. [preprint] [online] Available from: https://doi.org/10.5194/acp-2021-260, 2021.

Zuev, V. V. and Savelieva, E.: The cause of the spring strengthening of the Antarctic polar vortex, Dyn. Atmos. Ocean., 87, doi:10.1016/j.dynatmoce.2019.101097, 2019.